

2011

Model Electrocatalytic Surfaces: Structure, Reactivity and Nanotemplating

Xiaofang Yang
Lehigh University

Follow this and additional works at: <http://preserve.lehigh.edu/etd>

Recommended Citation

Yang, Xiaofang, "Model Electrocatalytic Surfaces: Structure, Reactivity and Nanotemplating" (2011). *Theses and Dissertations*. Paper 1250.

This Dissertation is brought to you for free and open access by Lehigh Preserve. It has been accepted for inclusion in Theses and Dissertations by an authorized administrator of Lehigh Preserve. For more information, please contact preserve@lehigh.edu.

Model Electrocatalytic Surfaces: Structure, Reactivity and Nanotemplating

by

Xiaofang Yang

A Dissertation

Presented to the Graduate and Research Committee

of Lehigh University

in Candidacy for the Degree of

Doctor of Philosophy

in

Department of Chemistry

Lehigh University

May, 2011

© Copyright
Xiaofang Yang

Approved and recommended for acceptance as a dissertation in partial fulfillment
of the requirements for the degree of Doctor of Philosophy

Xiaofang Yang

Model electrocatalytic surfaces: Structure, reactivity and nanotemplating

April 26, 2011

Defense Date

Bruce E. Koel

Dissertation Director

Approved Date

Committee Members:

Israel Wachs

Jim Roberts

Tianbo Liu

Dedication

To my wife Xiaolin Peng

谨以此论文献给我亲爱的妻子：彭晓琳

ACKNOWLEDGMENTS

First, I want to express my great gratitude toward Professor, Bruce E. Koel, my dissertation advisor, for his tremendous support, guidance and patience during the years of my Ph. D. study at Lehigh University. I am fortunate and honored to have the opportunity to study under one of the leading scientists in surface science. I cherish the time spent with him. His dedication to science will be a life-long inspiration for me.

I greatly appreciate that Professors Tianbo Liu, Jim Roberts, and Israel Wachs agreed to serve on my dissertation committee.

I am indebted to Dr. Jun Hu and Professor Runqian Wu, at University of California, Irvine for their DFT calculations of stability of Pd adatoms and oxygen adsorption and dissociation at the $\text{Pd}_3\text{Fe}(111)$ surface, Dr. Wenhua Chen at Rutgers University for her help and collaboration in the faceting of $\text{Re}(11\bar{2}1)$, Dr. Hao Wang at Columbia University for the LEED simulations, and Dr. Qinggang He in Berkeley National Laboratory for his friendship and for helping familiarizing with electrochemical analysis.

I am grateful to Dr. Guangzhi Liu for teaching me about UHV instruments. I also thank my labmates, Jie Fu, Lindsey Welch and Mauricio Ramos for helping me set up and test the UHV instruments.

TABLE OF CONTENTS

List of Figures	viii
List of Tables	ix
Abstract	1
Chapter 1 Introduction	5
1.1 Principle of fuel cells	6
1.2 Technique difficulties	10
1.3 Review of fundamental studies of the oxygen reduction reaction (ORR)	13
1.4 Research objectives	16
1.5 Experimental methods and equipment design and construction	18
1.5.1 Construction of a UHV system with easy sample transfer between the UHV chamber and an electrochemical cell	18
1.5.2 Metal films and surface alloys of interest	20
1.5.3 Characterization of bimetallic surfaces with a multi-technique, surface science approach	22
1.5.3.1 X-ray Photoelectron Spectroscopy (XPS)	22
1.5.3.2 Low Energy Ion scattering (LEIS)	23
1.5.3.3 Scanning Tunneling Microscope (STM)	24
1.5.4 Theoretical studies of adsorption of O ₂ and intermediates such as OH on single crystal alloy catalysts with density functional theory (DFT)	26
1.5.5 Nanotemplating for Pt as electrocatalysts for the	27

	hydrogen evolution reaction (HER)	
	1.5.6 Study of ORR kinetics: Origin of overpotential in ORR and Tafel analysis	28
	1.6 Experimental methods	30
	1.7 STM measurements	40
	1.8 References	44
Chapter 2	Formation of Pd monomers and Dimers on a Single Crystal Pd ₃ Fe(111)	
	2.1 Introduction	47
	2.2 Experimental details	48
	2.3 Results and discussion	50
	2.3.1 Surface characterizations by LEED, LEIS and STM	50
	2.3.2 Origin of Pd adatoms studied by DFT calculations	62
	2.4 Conclusions	75
	2.5 References	76
	2.6 Appendix: Pd Segregation on Pd ₃ Fe (111) surface	79
	2.7 References for appendix	87
Chapter 3	Determination of Atomic Structure of Ultra-thin Metal Oxides: Oxidation of single Crystal Pd ₃ Fe(111) Surface	
	3.1 Introduction	88
	3.2 Experiments	89
	3.3 Results	91
	3.3.1 LEED	91
	3.3.2 LEIS	93
	3.3.3 XPS	98
	3.3.4 STM	101
	3.4 Discussion	103
	3.4.1 FeO(111) on Pd ₃ Fe(111)	103
	3.4.2 Fe ₃ O ₄ clusters	109
	3.4.3 Fe ₂ O ₃ (0001)	115

3.5	Conclusions	119
3.6	References	120
3.7	Appendix	122
3.7.1	Moiré patterns	122
3.7.2	Un-identified STM images	123
3.7.3	Model structure of Fe oxides	124
Chapter 4	Role of Surface Fe in Enhanced Activity for the Oxygen Reduction Reaction on a Pd ₃ Fe(111) Single Crystal Alloy	
4.1	Introduction	125
4.2	Experiments	126
4.2.1	Surface Preparation and Characterization in UHV	126
4.2.2	Electrochemical Measurements	127
4.2.3	DFT calculations	128
4.2.4	ORR data and kinetic analysis	128
4.3	Results and discussion	129
4.4	Conclusions	141
4.5	References	142
4.6	Appendix	145
4.6.1	Surface stability	145
4.6.2	Data of oxygen reduction reaction	148
4.6.3	Oxygen reacts on O pre-adsorbed Pd ₃ Fe(111) surface	155
Chapter 5	High Activity Sub-monolayer Au at Pd ₃ Fe(111), for the Oxygen Reduction Reaction	
5.1	Introduction	156
5.2	Experimental details	158
5.3	Results and discussions	161
5.3.1	Constructing Au monolayer by physical vapor deposition (PVD)	161
5.3.2	Cyclic voltammetry(CV) measurements	166

	5.3.3 ORR Kinetics	170
	5.3.4 Surface characterization after electrochemical analysis	174
	5.3.5 Importance of reactive sites and oxygen spillover in the reaction mechanism for the ORR on Au _x /Pd/Pd ₃ Fe(111) surfaces	178
	5.4 Conclusions	181
	5.5 References	182
Chapter 6	Investigation of a Pt monolayer on C-induced Faceted Re(11 $\bar{2}$ 1) for the Hydrogen Evolution Reaction (HER)	
	6.1 Introduction	185
	6.2 Experimental details	187
	6.2.1 Preparation of Pt monolayer on faceted Re(11 $\bar{2}$ 1)	187
	6.2.2 Electrochemical measurements	188
	6.3 Results and discussion	189
	6.3.1 Preparation and characterization of C/Re(11 $\bar{2}$ 1)	189
	6.3.2 Preparation of a Pt monolayer on C/Re(11 $\bar{2}$ 1)	198
	6.3.3 Catalytic activity of Pt ML-C/Re(11 $\bar{2}$ 1)	200
	6.4 Conclusions	202
	6.5 References	203
Chapter 7	Summary	205
Vita		209

LIST OF FIGURES

Figure 1.1 Production Technologies for hydrogen gas	5
Figure 1.2 Schematic view of a phosphoric acid fuel cell	8
Figure 1.3 Schematic view of the UHV chamber used in this work, showing the attached high-pressure reaction cell (A) and sample holder and sample stage (B)	19
Figure 1.4 Hard sphere model of a three-layer (111) structure: Pd(top); Au(middle); and Fe (substrate)	21
Figure 1.5 Schematic view of an STM tip and the tip scanning on surface	25
Figure 1.6 Diagram of the three-electrode cell system	32
Figure 1.7 Pictures of electrochemical instruments	33
Figure 1.8 Construction of a reversible hydrogen electrode	35
Figure 1.9 Schematic view of the crystal surface before (left) and after (after) contacting with electrolyte	39
Figure 1.10 Schematic view of the STM Chamber	42
Figure 1.11 RHK sample holder with six contact pins (C- type thermocouple, label 6, K-type thermocouple, label 4 and two heat wires, label 15.)	43
Figure 2.1 LEIS of Pd ₃ Fe(111) after annealing at several temperatures	52
Figure 2.2 Top-layer composition of Pd ₃ Fe (111) measured with LEIS as a function of temperature	53
Figure 2.3 Pd segregation at a Pd ₃ Fe(111) surface. STM constant current topography with atomic resolution	57
Figure 2.4 Two STM images of Pd ₃ Fe(111) obtained during sequential scans	59
Figure 2.5 Pd adatoms at Pd ₃ Fe(111) surface with frizzy appearance	60
Figure 2.6 Constant-current STM topography with atomic resolution	61
Figure 2.7 Theoretical modeling of the origin and surface structure of Pd adatoms	65
Figure 2.8 Configurations of 32 Pd adatoms on Pd ₃ Fe (111) and a corresponding schematic model including the structure of the first layer	68
Figure 2.9 Surface composition of Fe deposited on Pd(111) studied by LEIS	69
Figure 2.10 Surface composition of Fe deposited on Pd(111) and sputtering effect studied by LEIS	70
Figure 2.11 XPS spectra for Pd 3d core levels	72
Figure 2.12 XPS spectra for Fe 2p core levels	73
Figure 2.13 XPS spectra of the Fe 2p _{3/2} peak for Pd ₃ Fe(111) after oxidation	74
Figure 3.1 Left: Comparison of LEED patterns at E _p =55 eV of clean and oxidized Pd ₃ Fe(111) surfaces. Right: Simulated LEED patterns	92
Figure 3.2 Surface compositions of clean and oxidized Pd ₃ Fe(111) surfaces studied by LEIS	94
Figure 3.3 Oxygen accumulation curves Pd ₃ Fe(111) at 300 and 500 K measured by the oxygen peak intensity in LEIS	95
Figure 3.4 Influence of O ₂ exposure on Pd ₃ Fe(111) at 300 and 500 K on the Fe peak intensity in LEIS	96

Figure 3.5 Influence of O ₂ exposure on Pd ₃ Fe(111) at 300 and 500 K on the Pd peak intensity in LEIS	97
Figure 3.6 A. Fe 2p _{3/2} peak in XPS after oxidation of Pd ₃ Fe(111) at several temperatures. B. Fe 2p _{3/2} peak in XPS after oxidation of Pd ₃ Fe(111) at 800 K, 15L O ₂ , and 950 K, 15L O ₂	100
Figure 3.7 Constant current STM images of Pd ₃ Fe(111) after oxidation	102
Figure 3.8 Structure and composition of an FeO(111) monolayer on Pd ₃ Fe(111)	108
Figure 3.9 Constant current STM image of FeO _x /Pd ₃ Fe(111) after FeO(111)/Pd ₃ Fe(111) was annealed at 950 K	112
Figure 3.10 Small area of FeO _x /Pd ₃ Fe(111) shown by an atomically resolved STM image	113
Figure 3.11 A. XPS of Fe 2p _{3/2} peaks in the FeO film (green) and annealed FeO(111) film (red) (950 K for 2 min). B. STM image of the FeO _x amorphous clusters after FeO(111) annealed at 950 K for 2 min	114
Figure 3.12 Constant current STM image of FeO _x /Pd ₃ Fe(111)	117
Figure 3.13 Constant current STM image of Fe ₂ O ₃ cluster with sizes of 2-5 nm	118
Figure 4.1 Constant current STM images of clean Pd ₃ Fe(111) surfaces illustrating the importance of annealing temperature on surface structure	131
Figure 4.2 A. Comparison of LEIS spectra obtained for the Pd ₃ Fe(111) surfaces used prior to the electrochemical measurements. B. Voltammetry curves for four different Pd ₃ Fe(111) surfaces at 300 K in an Ar-purged 0.1 M HClO ₄ solution	133
Figure 4.3 A. Comparison of the ORR polarization curves for several Pd ₃ Fe(111), Pd(111) and Pt(111) surfaces B. Comparison of the kinetic current at 0.9 V for five surfaces	134
Figure 4.4 Top view of O ₂ adsorption configuration (left top panel) and O ₂ dissociation configuration (left bottom panel) on Surface I	140
Figure 5.1 Schematic view of a gold doser on a 2.5-in. feedthrough	159
Figure 5.2 Au film growth on Pd ₃ Fe(111) monitored by XPS and LEIS	165
Figure 5.3 Linear sweep voltammetry curves for Au _x /Pd/Pd ₃ Fe(111) surfaces in Ar-saturated 0.1 M HClO ₄ before (black) and after measurements of the ORR kinetics (colored)	168
Figure 5.4 Comparison of CV curves for Au _x /Pd/Pd ₃ Fe(111) surfaces in Ar-saturated 0.1 M HClO ₄ solution after polarization curves were obtained for measuring the ORR	169
Figure 5.5 Comparison of ORR polarization curves for Au _x /Pd/Pd ₃ Fe(111), Pd/Pd ₃ Fe(111) and Au (111) surfaces	172
Figure 5.6 Influence of the Au film coverage on Pd/Pd ₃ Fe(111) on the ORR kinetic current at 0.9 V (vs. RHE)	173
Figure 5.7 Characterization of Au _x /Pd/Pd ₃ Fe(111) surfaces by A. Au4f _{7/2} /Pd3d _{5/2} XPS peak area ratio, B. Au peak area measured by LEIS	176
Figure 5.8 Schematic depictions of two possible reconstructions for Au _x /Pd/Pd ₃ Fe(111) surfaces with 0.6 ML Au induced by polarization measurements of the ORR activity	177

Figure 5.9 Schematic representation of the importance of reactive sites and oxygen spillover in the reaction mechanism of oxygen reduction on $\text{Au}_x/\text{Pd}/\text{Pd}_3\text{Fe}(111)$ surfaces	180
Figure 6.1 LEED patterns from $\text{Re}(11\bar{2}1)$. A. Planar $\text{Re}(11\bar{2}1)$ at $E_i = 60$ eV. B. Partially faceted $\text{C}/\text{Re}(11\bar{2}1)$ at $E_i = 90$ eV. C. Fully faceted $\text{C}/\text{Re}(11\bar{2}1)$ at $E_i = 90$ eV	190
Figure 6.2 AES spectra of planar and C-induced faceted $\text{Re}(11\bar{2}1)$. A. Planar $\text{Re}(11\bar{2}1)$. B. Faceted $\text{Re}(11\bar{2}1)$ after 0.3 L C_2H_2 exposure at 700 K followed by annealing in vacuum at 1100 K for 1 min	191
Figure 6.3 STM images of faceted $\text{Re}(11\bar{2}1)$ induced by exposure of $\text{Re}(11\bar{2}1)$ at 700 K to 0.3 L C_2H_2 and then heating to 1100 K in vacuum for 3 min. A. (200×200) nm^2 . B. (60×60) nm^2 , -2.08 V, 434 pA	193
Figure 6.4 Constant current STM images of faceted $\text{Re}(11\bar{2}1)$ induced by exposure of $\text{Re}(11\bar{2}1)$ at 700 K to 0.3 L C_2H_2 and then heating to 1100 K in vacuum for 3 min. A. (200×200) nm^2 . B. (60×60) nm^2 , -2.08 V, 434 pA	194
Figure 6.5 Constant current STM images of faceted $\text{Re}(11\bar{2}1)$ induced by exposure of $\text{Re}(11\bar{2}1)$ at 700 K to 0.3 L C_2H_2 and then heating to 1100 K in vacuum for 5 min. A. (150×150) nm^2 . B. (50×50) nm^2 , -1.95 V, 330 pA	195
Figure 6.6 Schematic illustrations providing top views of a hard-sphere model of A. a planar $\text{Re}(11\bar{2}1)$ surface with three geometrical layer exposed, top view and side view, Green-1st layer, Red-2nd layer and Blue-3rd layer and B. a single pyramid from a faceted $\text{Re}(11\bar{2}1)$ surface	197
Figure 6.7 Surface characterization of Pt monolayer by LEIS and XPS. A. Red-Clean $\text{Re}(11\bar{2}1)$ and Blue-Pt ML on $\text{Re}(11\bar{2}1)$. 4.5 keV Ar^+ , 3 nA, pass energy: 1127.1 eV B. Pt ML on $\text{Re}(11\bar{2}1)$	199
Figure 6.8 A. Hydrogen evolution polarization curves in 0.1 M HClO_4 , B. Tafel plots for (1) $\text{Re}(11\bar{2}1)$, (2) $\text{Pt}(111)$ and (3) $\text{Pt ML-C}/\text{Re}(11\bar{2}1)$	201

LIST OF TABLES (REMOVE IF NO TABLES)

Table 1.1 Three proposed oxygen reduction reaction (ORR) mechanisms	9
Table 1.2 Natural abundance and prices of precious metals	10
Table 5.1 Kinetic parameters for the ORR of Pd ML-Pd ₃ Fe(111), Pt(111), and Au _x /Pd/Pd ₃ Fe(111) surfaces at 900 rpm	174

ABSTRACT

Fundamental study of electrocatalysis in energy related applications such as fuel cells and hydrogen production is important because it impacts and possibly defines the future energy technology picture. Platinum-based electrocatalysts are widely used for their exemplary performance, but these catalysts suffer from drawbacks, e.g., cost, undesired catalytic properties, and low durability, which limit fuel cell development. In this research, non-Pt electrocatalysts or ultrathin-Pt film electrocatalysts have been studied to gain insight and discover materials that can replace costly Pt electrocatalysts or greatly reduce Pt loadings while retaining or even increasing activity with improved stability. The research focus is on using model electrocatalysts with well-defined surface composition and structure to simplify the system and exert control to improve the understanding of the surface phenomena that control electrocatalytic reactions. Specifically, three types of model electrocatalysts were prepared in ultrahigh vacuum and characterized using multiple surface science techniques, and then their electrocatalytic activity for the oxygen reduction reaction (ORR) and the hydrogen evolution reaction (HER) was measured: (i) Pd₃Fe(111), (ii) Au/Pd₃Fe(111), and (iii) Pt on a faceted C/Re(11 $\bar{2}$ 1) nanotemplate.

Significant surface segregation of Pd was discovered after clean Pd₃Fe(111) was annealed at high temperatures in Ultrahigh vacuum(UHV). The surface structure strongly depends on the annealing temperature, with the formation of an atomically smooth, random substitutional alloy by heating to 1000 K, and the formation of Pd monomer and dimer adatoms by heating to 1250 K. The adatom feature is not observed for other binary alloys. The annealed Pd₃Fe(111) surface exhibits higher ORR

electrocatalytic reactivity than pure Pt. When a submonolayer amount of Au was deposited on Pd₃Fe(111), the Au/Pd₃Fe(111) surface was found highly active for the ORR and the activity was strongly dependent on the Au coverage. The surface with ~0.6 monolayer of Au was twice as active as Pt(111). A Pt monolayer deposited on a nanofaceted C/Re(11 $\bar{2}$ 1) was studied for the HER and EO electrocatalysis and found that the catalytic performance was the higher activity than Pt. In summary, we have investigated a range of non-Pt and ultrathin-Pt film model electrocatalysts that are more active than pure Pt bulk material, gaining new insights and pointing to new materials that could be used to reduce cost and improve activity by nanoengineering novel electrocatalysts.

Chapter 1 Introduction

As the global community considers how to develop alternative energy sources to supplement, extend, and replace traditional fossil-based energy resources, fuel cells have drawn much attention due to their large inherent efficiency for energy conversion.¹ Fuel cells are technologies to transfer the chemical energy in fuels such as hydrogen, methanol, and other hydrocarbons directly into electrical energy through electrical “burning” of these fuels. Fuel cells can not only generate electrical power with high efficiencies, up to 60%, but also can utilize non-fossil or renewable fuels and thus reduce the impact on the environment. The automobile manufacturing industry is very interested in further developing fuel cells because of the potential for this technology to bring revolutionary change to the industry.² For example, fuel cells not only provide quiet power, but also greatly increase fuel efficiency and reduce harmful emissions. The hydrogen-based fuel cell does not have any toxic emissions since water is the only product.¹ Fuel cells have their critics who point out that this technology would currently be heavily dependent on the fossil resources to generate fuels such as hydrogen and methanol, and a large increase in the use of ethanol from corn would cause food prices to rise.³ This latter problem could bring disaster to people living in developing countries, where the food supply is heavily dependent on imports from the United States.³⁻⁴ So, while many people believe that the final solutions to the world’s energy and environmental challenges are solar energy and nuclear energy, it is still worth considering the role of fuel cells in supplying the energy needs, especially if further improvements to the technology can be made.

The looming “energy crisis” not only refers to a potential shortage of energy supplies, but is also related to the absence of energy devices that can convert or store energy efficiently for transportation applications such as vehicles, airplanes and boats. Fuel cells and battery technologies are much closer term prospects for supplying this capability than other energy technologies such as solar cells and nuclear energy. Polymer electrolyte membrane fuel cells (PEM-FCs) can run at low temperatures ($<70\text{ }^{\circ}\text{C}$) and are attractive for portable devices such as laptops, cell phones, and digital cameras.

The primary fuel in PEM-FCs is hydrogen gas (H_2), which provides the highest energy conversion efficiency and most stable performance for the fuel cell.⁵ The sources of hydrogen are very important considerations for cost and sustainability issues. The production technologies for hydrogen along a timeline are illustrated in Figure 1.1. Extensive application of solar energy to produce hydrogen in the future will significantly lower our dependence on petroleum production if PEM-FCs are utilized.

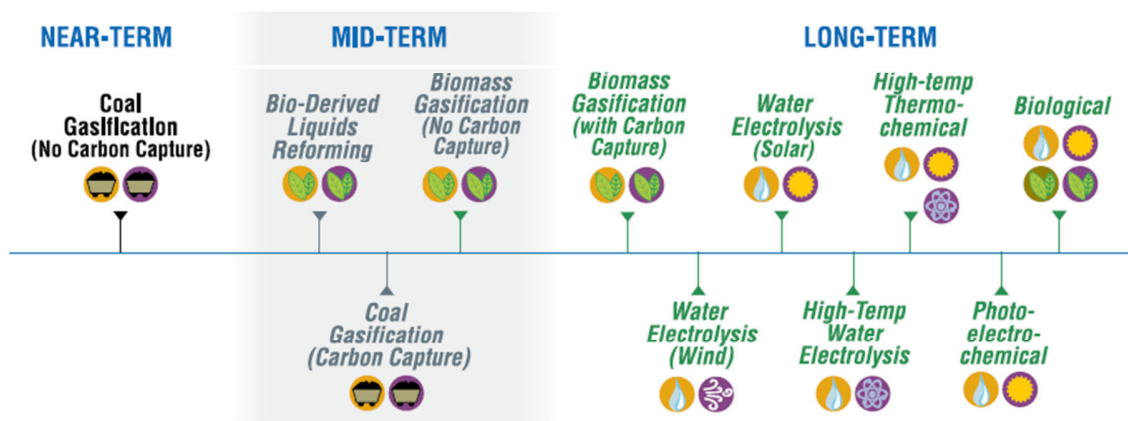
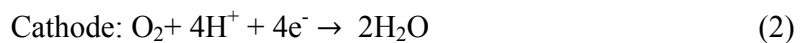


Figure 1.1 Production technologies for hydrogen gas. In the near-term, the coal is the primary source. In the mid-term, the biomass will be introduced to supply hydrogen gas. In the future, wide range of energy sources will be considered such as solar energy, thermal energy, wind energy and etc.⁵

1.1 Principles of fuel cells

Figure 1.2 illustrates the basic structure and function of different components in a phosphoric acid fuel cell (PAFC).⁶ In general, hydrogen fuel flows into the anode where it dissociates and loses electrons and is converted to protons. These electrons flow through the external load to furnish power and drive appliances and then return to the cathode where oxygen molecules (O₂) combine with protons transported by the electrolyte and these electrons to produce water (H₂O).

The total reaction is given by the two half cell reactions:



Even though the overall process is simple, the detailed (atomic level) reaction mechanism is complicated. The reaction at the interface between the electrolyte and electrodes is influenced by several factors such as water, solvent ions, potentials, and the details of composition and structure of the electrode catalysts. It is also difficult to carry out fundamental studies of the reaction intermediates. For example, oxygen species adsorbed at the electrode surfaces are hard to differentiate from the oxygen species in the electrolytes by surface science techniques and vibrational spectroscopies such as FT-IR and Raman. However, it is important to know the details of the reaction mechanism so that we can develop optimized catalysts for these reactions. Currently, Pt and Pt-based electrodes/electrocatalysts are utilized and because of the cost and limited supplies of Pt, it is desirable to reduce the amount of Pt needed to operate the fuel cell or eliminate Pt entirely. One of the primary limiting factors in fuel cell efficiency and lifetime is the poor

performance of electrocatalysts for the oxygen reduction reaction (ORR) given in Eq. (2).

Further details of this reaction are discussed below.

With the help of theoretical calculations based on density functional theory (DFT), three ORR mechanisms have been proposed as shown in Table 1.1.⁷⁻⁸

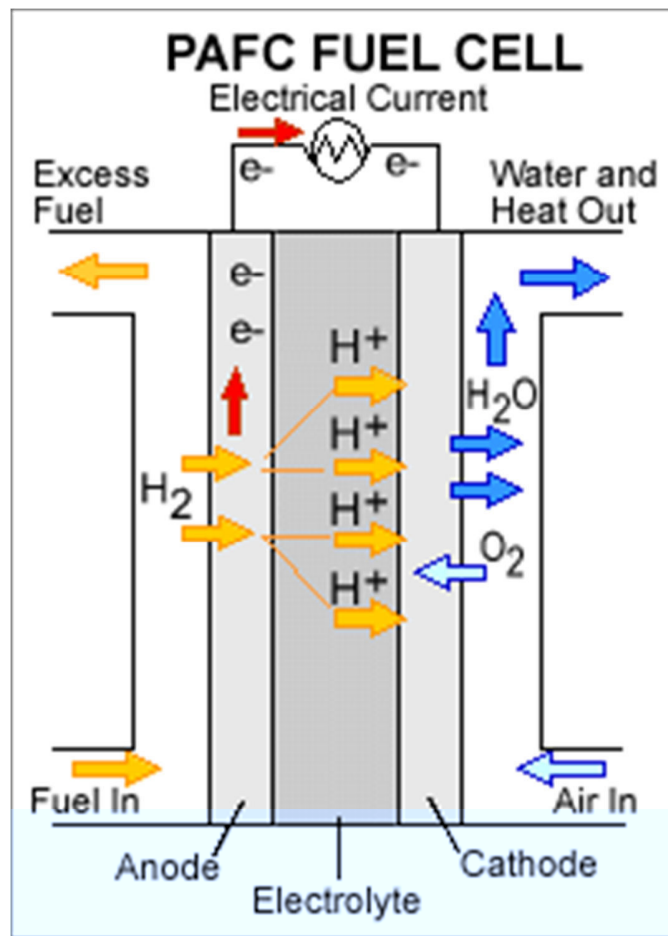


Figure 1.2 Schematic view of a phosphoric acid fuel cell. Hydrogen fuel flows into the anode where it dissociates and loses electrons and is converted to protons. These electrons flow through the external load to furnish power and drive appliances and then return to the cathode where oxygen molecules (O_2) combine with protons transported by the electrolyte and these electrons to produce water (H_2O).⁶

Table 1.1. Three proposed oxygen reduction reaction (ORR) mechanisms ⁸

Mechanism 1		Mechanism 2		Mechanism 3	
$O_2+* \rightarrow O_2^*$	1	$O_2+* \rightarrow O_2^*$	1	$O_2+* \rightarrow O_2^*$	1
$O_2^*+* \rightarrow 2 O^*$	2	$O_2^*+(H^++e^-) \rightarrow HOO^*$	3	$O_2^*+(H^++e^-) \rightarrow HOO^*$	3
$2 O^*+(H^++e^-) \rightarrow HO^*$	7	$HOO^*+* \rightarrow O^*+HO^*$	5	$HOO^*+(H^++e^-) \rightarrow HOOH^*$	4
$HO^*+(H^++e^-) \rightarrow H_2O+*$	8	$2 O^*+(H^++e^-) \rightarrow HO^*$	7	$HOOH^* \rightarrow 2HO^*$	6
		$HO^*+(H^++e^-) \rightarrow H_2O+*$	8	$HO^*+(H^++e^-) \rightarrow H_2O+*$	8

Mechanism **1** is called the dissociative mechanism, which entails O-O bond breakage (step 2) at the surface, followed by proton/electron transfer to produce water. Mechanisms **2** and **3** are associative mechanisms, which entail proton/electron transfer to form OOH*(step 3) or HOOH* (step 4) at the surface, followed by O-O bond breakage to produce OH*, and subsequent hydrogenation of OH* to produce water. Pioneering work by Nørskov and coworkers calculated the oxygen reduction reaction mechanisms on extended model surfaces of a large number of transitional metals and found that the ORR activity was strongly dependent on the oxygen binding energy.⁹ The reaction barrier on Pt(111) mainly comes from the first proton and electron transfer (step 3), and the barrier is changed by the applied bias on the electrode.¹⁰ Theoretical studies of ORR at novel proposed electrodes consisting of platinum monolayers coating transition metals found

that the rate determining step is either the removal of OH* in cases of strong oxygen binding to the surface or the breaking of the O-O bond in cases of weak oxygen binding to the surface.⁸ The binding strength of oxygen on the surface is affected by the surface Pt lattice constant, which is modified by the substrate atoms. For example, the lattice constant of a Pt monolayer is compressed 3.5% by an Ir substrate. This compression shifts the *d*-band center down (to higher binding energy) and weakens the bond strength of oxygen on the Pt monolayer.⁸

Table 1.2. Natural abundance and prices of precious metals.

Natural	Ru	Rh	Pd	Ir	Pt	Au
abundance*	9.9×10^{-7}	7.0×10^{-8}	6.3×10^{-7}	4.4×10^{-8}	3.6×10^{-6}	3.1×10^{-7}
Price, \$/oz**	460	6500	884	450	1880	1377

* Wolfram Research, Inc.

** www.metalprices.com at March. 1 2011

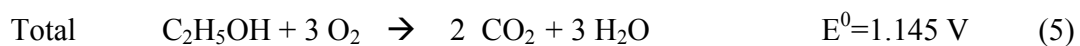
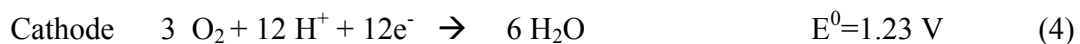
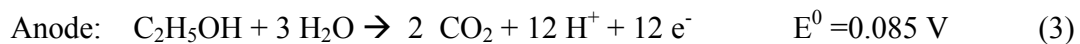
1.2 Technical difficulties

Extensive research and development efforts, along with a large number of fundament research studies, have enabled continued development of fuel cells. For example, major automobile companies such as GM and Toyota, have completed a series of successful tests on fuel cell powered vehicles and pronounced that by 2011 some models would be available in the marketplace.¹¹ However, there are still major drawbacks that limit further development and applications of fuel cells on a large scale. First, fuel

cells are expensive partly due to the use of costly Pt-based catalysts, and the natural abundance of Pt is too low to support large scale use of fuel cells with Pt as an electrocatalyst, as shown in Table 1.2. Second, Pt-based catalysts are poisoned by impurities such as CO, H₂S, and NH₃, in fuels, and these impurities seriously reduce the activity of catalysts, thus shortening their lifespan. Third, the sluggish oxygen reduction reaction (ORR) kinetics at the cathode (due to the large overpotential) causes relatively low current density and thus limits the power of fuel cells. Without significant breakthrough that solves these problems, fuel cells are still far from useful in large applications.¹²

Solutions to these problems rely on the discovery and tailoring of an optimal catalyst with attributes of high activity, durability, low cost, and resistance to negative effects of impurities in the fuel. Many current studies of fuel cells focus on how to improve the ORR kinetics, since 80% of the over-potential (lost potential causing low efficiency) comes from the ORR. Major breakthroughs in fuel cell efficiency are heavily dependent on improving ORR kinetics.

Take direct ethanol oxidation as an example:¹³



Under reversible conditions, the total cell energy efficiency (ϵ_{rev}) is 97%:¹³

$$\varepsilon_{\text{rev}} = \frac{nFE_{\text{eq}}^{\circ}}{-\Delta H_{\text{r}}^{\circ}} = \frac{12 \times 96500 \times 1.145}{1366.8 \times 1000} = 97\% \quad (6)$$

where n is the number of electrons transferred (theoretically), F is the Faraday constant ($96485 \text{ C. mol}^{-1}$), E_{eq}° is the cell voltage under reversible conditions, and $-\Delta H_{\text{r}}^{\circ}$ is the reaction enthalpy.

However, under actual operating conditions, the following Eq. must be used and the energy efficiency (ε) is much lower than the theoretical value:¹³

$$\varepsilon = \frac{n_{\text{exp}}FE(j)}{-\Delta H_{\text{r}}^{\circ}} = \frac{nFE_{\text{eq}}^{\circ}}{-\Delta H_{\text{r}}^{\circ}} \times \frac{E(j)}{E_{\text{eq}}^{\circ}} \times \frac{n_{\text{exp}}}{n} \quad (7)$$

where n_{exp} is the number of electrons transferred (experimentally), $E(j)$ is the cell voltage under current value j .

where

$$E(j) = E_2 - E_1 = E_{\text{eq}}^{\circ} - (\eta_a + \eta_c + \eta_{\text{Xover}} + R_i j) \quad (8)$$

where E_2 and E_1 are the potentials of cathode and anode respectively, η_{Xover} is the potential loss of fuel crossover, and R_i is the cell internal resistance. The system suffers a huge loss in output potential (E_j) due to the over-potential at the cathode (η_c), the anode (η_a), and other factors. The total number of electrons (n_{exp}) involved in the reaction is also smaller than the theoretical value (n).

1.3 Review of fundamental studies of the oxygen reduction reaction (ORR)

Most basic research deals with bimetallic (or more complex multimetallic) electrocatalysts. Thus it is useful to briefly review related background material from the more extensively investigated field of the bimetallic catalysts for used in gas phase heterogeneous catalysis. For example, Pd based alloys are found to be highly selective in the hydrogenation of alkynes to alkenes.¹⁴ Usually, the bimetallic catalysts are either mixtures of two (3d, 4d and 5d) transition metals or one transition metal doped by other non-transition metals. Basically, the enhanced catalytic properties in the bimetallic catalysts are discussed as arising from two different effects: electronic effects and geometric effects. For electronic effects, the electronic structure of the first metal is modified by the second metal. In particular, the filling of *d*-band is changed, so the chemical and physical properties are affected by the depletion or addition of *d*-electrons.¹⁵ For geometric effects, active sites on the surface are changed due to dilution by the second less-active metal.¹⁶ However, it is not easy to separate these two effects since some change in electronic properties by alloying with other metals always occurs and the small size (a few atoms) of active sites also makes it difficult to probe this influence.

Researchers in electrocatalysis also extensively explore bimetallic catalysts to improve performance. So far, a wide range of bimetallic catalysts (Pt/M, M=Ni, Co, Au, Sn, Ru, etc.; Pd/N, N=Co, Ni, Fe, etc.) have been studied for their catalytic performance as cathode and anode materials.¹⁷⁻²¹ The fundamental idea behind investigating Pt-based alloys is that the loading of Pt can be significantly reduced in alloys, lowering the cost of

fuel cells. In some cases, the catalytic activity remains the same or becomes higher. Recently, the study of non-Pt based bimetallic electrocatalysts has gained much popularity. The costs of these catalysts are further reduced when cheap metals such as Fe, Co and Ni are used. Surprisingly, these catalysts can be even better than Pt-based catalysts in reducing the cathode over potential and increasing ORR kinetics. Particularly, Adzic's group at Brookhaven National Laboratory is leading research and development of Pd-based catalysts.¹³⁻¹⁹ Pd/M (M=Fe, Co and Ni) nanoparticles are found to be comparable to Pt electrocatalysts in the ORR at the cathode. Much higher electrocatalytic activity is also found when these bimetallic nanoparticles act as the support of a Pt or Pd monolayer. Here again, *d*-band theory is used to explain the origin of the activity.^{8, 13} In order to have fast ORR kinetics, the binding between oxygen and the active sites should be neither too strong nor too weak. On one hand, strong binding helps electron transfer between adsorbed oxygen and the surface, but on the other hand it hinders oxygen desorption from the surface and blocking effects due to this adsorbed oxygen slows down the ORR kinetics.^{8, 22} Weak binding helps the removal of oxygen, but causes slow electron transfer. The localized *d*-band position is mainly responsible for the binding of oxygen on the surface. Higher *d*-band electron filling is correlated to stronger binding to oxygen. Therefore, the *d*-band center has been used as a yardstick to understand and predict ORR properties. Theoretical calculations have found that the ORR kinetics of bimetallic catalysts correlates very well with the *d*-band center position. These findings are very important because they provide a strategy for screening candidates for bimetallic catalysts.⁸ For example, one notices that a good catalyst may be synthesized by mixing late transition metals with early transition metals.

Markovic has developed a new approach for improving the ORR performance of Pt.²³ Instead of focusing on the detailed reaction mechanism, he emphasizes that the free sites accessible to oxygen molecules at the surface determine the reactivity. He modified the Pt surface by partially covering it with strongly bonded cyanide (CN) species, so that the anions (SO_4^{2-} , PO_4^{3+} , *etc.*) in the electrolyte were blocked by adsorbed CN, but retaining enough sites for oxygen adsorption. Experimentally, the ORR activity of Pt(111) modified by CN was found to be improved enormously.²³

Some non-precious metal catalysts have been synthesized and evaluated for their ORR performance. Representatives of this category are metal-organic complexes such as Cu- and Fe- porphyrins, However, so far, electrocatalysts prepared from this type of material are much less active than Pt –base catalysts and their stability is questionable.²⁴

The morphology of Pt nanostructures was found to be important for the ORR activity. The ORR activity of Pt single crystal surfaces is structure-sensitive, and in the order of Pt(100) \ll Pt(111) < Pt(110) due to the different OH adsorption properties on these surfaces. By controlling the exposure of the (111, 110) facets of nanoclusters, the reactivity was improved five times higher than Pt-black catalysts.²⁰

In yet another direction, carbon nanotubes modified by nitrogen were found to be active for ORR. This metal-free electrode is attractive due to its low cost and potentially high stability. However, its ORR performance needs to be greatly improved to be comparable to that for Pt-based catalysts.²⁵

The stability of cathode catalysts is extremely important for developing stable fuel cells with long lifespans. Cathodes suffer from corrosion by oxygen at oxidative

potentials, so the cathode materials need to be very stable. Pt catalysts are dissolved in the electrolyte slowly under running conditions, which decreases the performance of the catalysts and shortens the lifetime of the cell. It was found that adding Au to Pt catalysts improved the stability significantly.²⁶ This was interpreted as due to Au adsorption at defect sites of Pt, which prevented the dissolution of Pt.

1.4 Research objectives

The current research focuses on the study of non-Pt catalysts and Pt monolayer (ML) model electrocatalysts relevant for advanced electrodes for fuel cells. This work seeks insights and the discovery of new materials by establishing clear structure-activity relationships in electrocatalysis. Catalyst surface structures and electronic properties are characterized by employing multiple surface science techniques such as low energy electron diffraction (LEED), Auger electron spectroscopy (AES), low energy ion scattering (LEIS), X-ray photoelectron spectroscopy (XPS), and scanning tunneling microscopy (STM) under ultrahigh vacuum (UHV) conditions. Electrochemical measurements on these same surfaces determine electrocatalytic reactivity for the ORR, and hydrogen evolution reaction (HER). Alloy single-crystal model catalysts have been synthesized in UHV by physical vapor deposition (PVD) of a second metal, strictly controlling the deposited film for the thickness, composition and structure at an atomic level. Importantly, a multifunctional sample holder has been constructed to work in conjunction with a high-pressure reaction cell directly attached to the UHV surface analysis chamber to be able to bridge the UHV conditions and the liquid electrochemical environment to overcome the “pressure gap” between these two conditions. Metal vapor

deposition in the UHV system provides fast, well-controlled synthesis of model catalysts of thin films and surface alloys. These surfaces are well-suited for not only the study of catalytic properties of well-known electrocatalysts, but also for the development of new highly active, durable, and low cost electrocatalysts. By using this approach, we hope to gain a more thorough understanding of the origin of catalytic activity of existing catalysts and to lay the foundation for the designed modification of catalyst properties for the optimization of catalytic performance.

1.5 Experimental methods - equipment design and construction

1.5.1 Construction of a UHV system with easy sample transfer between the UHV chamber and an electrochemical cell

Preparation of a single crystal surface in UHV provides a clean, well-ordered surface with a well-characterized composition and structure. However, it is often difficult to transfer the sample between the UHV chamber and an electrochemical cell rapidly while keeping the surface free of contamination. We have designed a simple sample holder which is able to fit both the sample support rod in the UHV chamber and the electrode connector in an electrochemical cell, as shown in Figure 1.3. This device facilitates clean transfer of the sample between the high-pressure reaction cell attached to the UHV chamber and external cell suitable for electrochemical measurements by enabling a simple decoupling to remove the sample holder under an ambient inert atmosphere. As it is shown in Figure 1.3, the crystal is attached to a ceramic sample holder by four tantalum (0.25 in. long, 0.01 in. diameter, 99.98%, ESPI) heating wires. The threaded hole in the center of the ceramic sample holder is designed to couple with the rotating rod of the electrochemical cell apparatus. The sample holder is placed on the sample stage by sliding two metal pieces (0.2×0.3 sq. in., 0.01 in. thick, tantalum, 99.98%, ESPI) on the two sides of the ceramic body (0.5×0.5 sq. in and 0.125 in. thick, Ultra-High Temp Machinable Glass-Mica Ceramic, McMaster) in between the two clips (0.3×1.0 sq. in. molybdenum, 99.98% ESPI) on the sample stage. After that, the thermocouple pins (0.1×0.2 sq. in, K-type) on both the sample holder and the sample stage will contact each other. The sample transfer between UHV and the electrochemical cell is trivial with this special device. More details are described in Section 1.7.

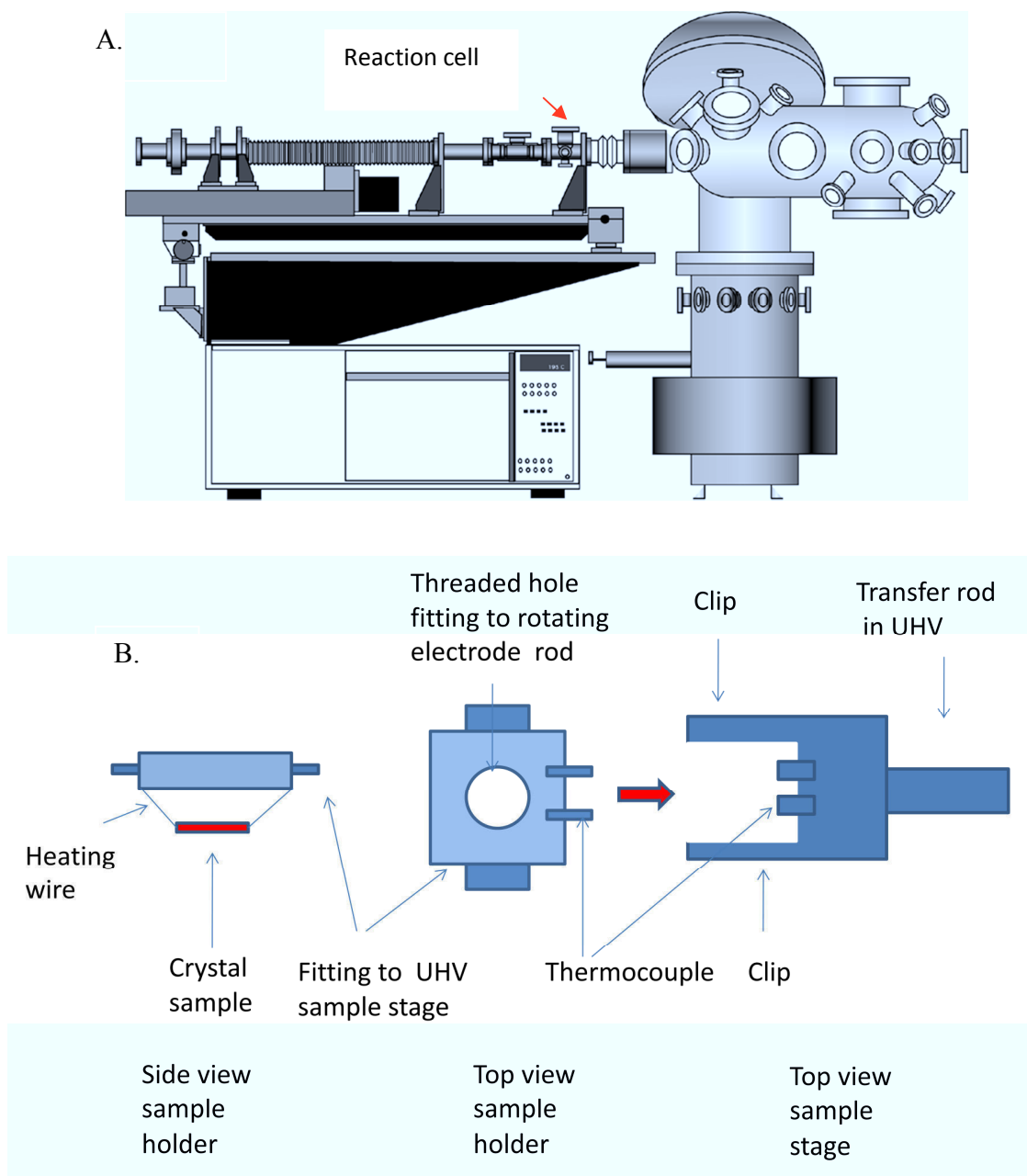


Figure 1.3 Schematic view of the UHV chamber used in this work, showing the attached high-pressure reaction cell (A) and sample holder and sample stage (B). The red arrow in B indicates how the sample holder is transferred to the sample stage.

1.5.2 Metal films and surface alloys of interest

In the UHV chamber, we are able to deposit metal atoms to form a monolayer film on various substrates and to synthesize surface alloys by subsequently heating the sample. Because of that, we are able to study a wide range of bimetallic and ternary alloy catalysts prepared by deposition of Pd, Pt, Au, Ir, Fe, Ni, and Co, and Pt on Pd or Pd alloy single crystals. Specifically, this research also investigated a new type of model catalyst inspired by the core-shell structure of nanoparticles. Such a system has a three-layer structure as shown in Figure 1.4 for one particular example. In addition to the traditional two-layer core-shell structure, the introduction of a middle layer not only modifies the electronic properties of the top layer, but also should offer protection to the active substrate from oxidation. The strong interaction between active metals in the substrate and oxygen could pull substrate atoms out of the bulk if there was no extra blocking effect by the middle layer. The middle layer consists of one or two monolayers of inert metal atoms (Au, Ir, *etc*). The electronic properties of the top layer are influenced by bonding to the middle layer and indirectly by the deeper layers of the substrate, which potentially allows for greater possibilities to tune the surface properties.

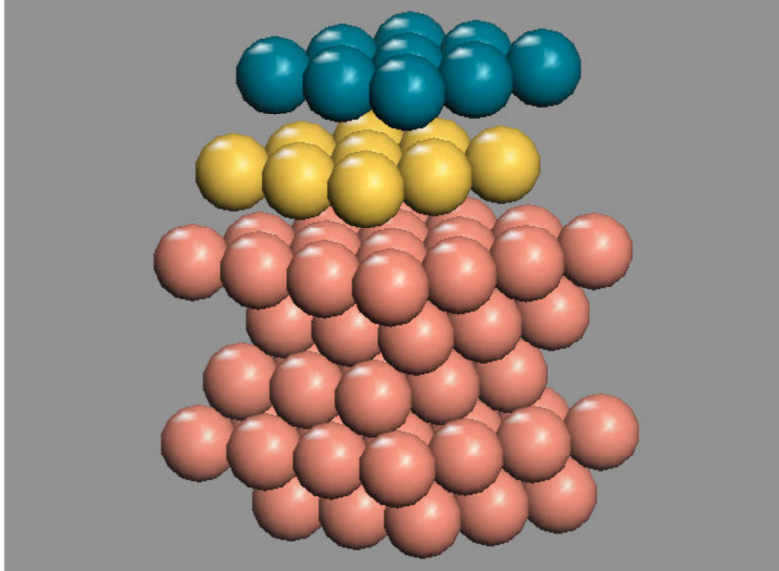


Figure 1.4 Hard sphere model of a three-layer (111) structure: Pd(top); Au(middle); and Fe (substrate). The introduction of a middle layer not only modifies the electronic properties of the top layer, but also should offer protection to the active substrate from oxidation.

1.5.3 Characterization of bimetallic surfaces with a multi-technique, surface science approach

In heterogeneous electrochemical reactions, the catalytically active sites are located at the electrode surface. Therefore, it is important to understand the geometric arrangement and surface elemental composition of these surfaces. Experimental studies of these surfaces by XPS, LEIS, and STM are able to provide comprehensive information on surface structure and composition at the atomic level. The valence electronic structure of each element in the alloy is modified by the other components due to electron transfer between the components and/or rehybridization due to alloying. These changes cause alterations in the adsorption properties and surface reactivity, and thus affect the catalytic properties.

1.5.3.1 X-ray Photoelectron Spectroscopy (XPS)

X-ray Photoelectron Spectroscopy (XPS) is a surface sensitive analysis technique, which is used to study elements quantitatively in the near surface region by measuring the core level electron binding energies of atoms in the solid. The basic principle is expressed by:²⁷

$$E_B = h\nu - KE \quad (9)$$

where E_B is the binding energy of an electron in an atom, $h\nu$ is the energy of the incident X-ray source (Al $K\alpha$, 1486.6 eV and Mg $K\alpha$, 1253.4 eV), and KE is the kinetic energy of the photoelectron, which is measured by an electron energy analyzer.

Since the E_B values of the atom are modified by the chemical environment, XPS is an effective probe of the oxidation state of the metals present by measuring shifts in

these core level binding energies. It is also used extensively to follow surface adsorbate coverage and identify surface intermediates that reveal reaction mechanisms.

Experimentally, the XPS system includes an X-ray source and an energy analyzer, which control both sensitivity and resolution of XPS measurements. High-resolution XPS analysis usually refers to use of a monochromatic X-ray source.

1.5.3.2 Low Energy Ion Scattering (LEIS)

Low Energy Ion Scattering (LEIS) is a monolayer-sensitive analyzing technique, which is able to obtain the outermost atomic layer element compositions. Basically, the ion beam (He^+ , Ne^+ and Ar^+ , 0.5~5.0 keV) is directed to the surface and the energy of scattered ions after interacting with the surface is measured. According to two-body elastic scattering, the energy of a scattered ion is dependent on atomic mass of the target atom and the scattering angle. The kinematic factor K defined by the energy ratio:²⁸

$$K = E_2/E_1 = \left(\frac{\cos \theta_1 + (A^2 - \sin^2 \theta_1)^{\frac{1}{2}}}{1+A} \right)^2 \quad (10)$$

where E_2 is the projectile energy after scattering, E_1 is the projectile initial energy, and θ_1 is the scattering angle, A is the mass ratio given by:

$$A = M_2/M_1 \quad (11)$$

where M_2 is the target atomic mass, and M_1 is the projectile atomic mass. Experimentally, the energies of the scattering ions are measured by an electron energy analyzer (operated with reversed polarities) and the identification of the targeted mass is based on Eq. 10.

1.5.3.3 Scanning Tunneling Microscope (STM)

Scanning Tunneling Microscope (STM) is a topographic technique with the potential to obtain images of the surface with an atomic resolution. The schematic view of STM is shown in Figure 1.5. In principle, electron can tunnel through the vacuum gap between the tip and the surface when a voltage is applied. The tunneling current is controlled by the applied voltage and the distance from the tip to the surface. The surface topography is obtained by scanning the tip over the surface and recording the tunneling current. . Usually the current and voltage are kept constant and the image is generated by recording the voltage on a power supply as it moves the tip up and down to follow the contours of the surface to satisfy this requirement.

The tunneling current (I) is given by: ²⁹

$$I \propto e^{-2kd} \quad (12)$$

where d is the separation between the tip and the surface and k is related to the local work function by: ²⁹

$$k = (2m\phi/h^2)^{1/2} \quad (13)$$

where ϕ is the work function of the surface, h is the Planck constant, and m is the mass of the electron.

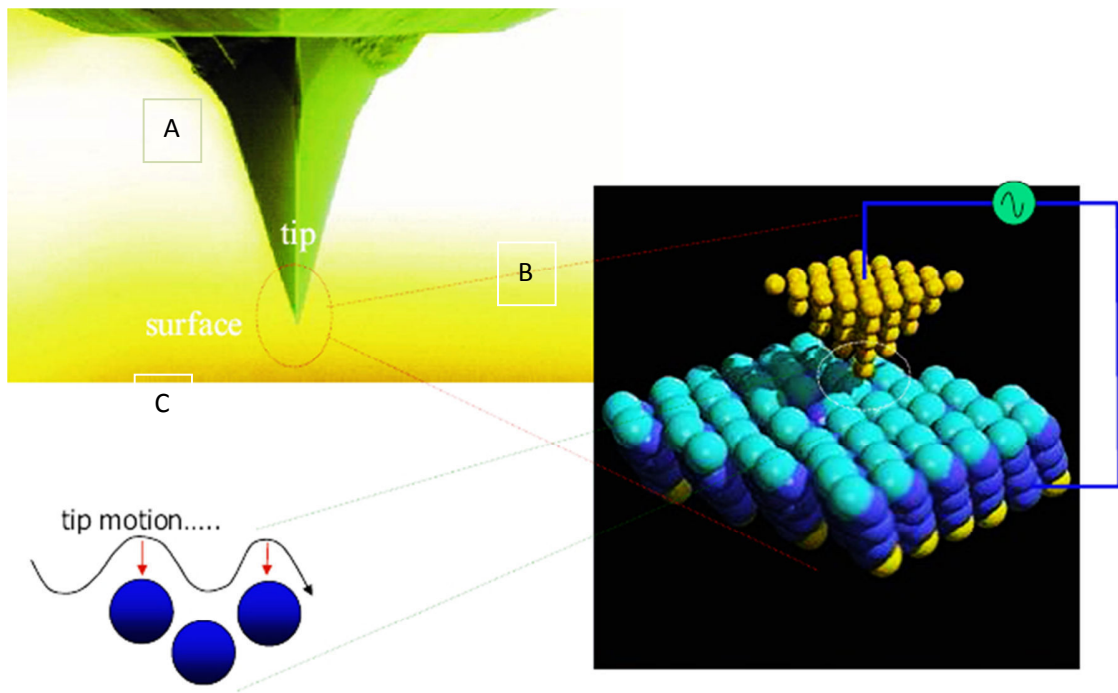


Figure 1.5 Schematic views of an STM tip and the tip scanning on surface. A. STM tip, B. STM Tip scanning on surface, C. Tip motion during scanning. [Taken from ref.: <http://nanohub.org/>] The STM images are taken by scanning the tip over the surface and the tunneling current is collected and converted into image.

The use of XPS, LEIS, and STM provides powerful approach to characterization needed for the controlled and reliable construction of model catalyst surfaces.

Importantly, XPS and LEIS provide a direct link between the compositions and aspects of the structure of well-defined single crystal model catalysts and the practical nanoparticle catalysts being developed for use as electrodes in working fuel cells. These fundamental studies and comparisons are critical to establishing new structure/composition-reactivity correlations and improve our understanding of enhanced ORR activity by alloy catalysts.

1.5.4 Theoretical studies of adsorption of O₂ and intermediates such as OH on single crystal alloy catalysts with density functional theory (DFT)

Understanding the adsorption of O₂ and identifying reactive intermediates is an important part of establishing the mechanisms of reactions on the surfaces of electrodes.

Major progress in understanding of the ORR theoretically has been made by using extended model surfaces as surrogates to the actual electrochemical interface.¹²

Theoretical studies of the ORR at platinum monolayer on several transition metals found that the rate determining step(rds) is either the removal of OH* for a strong oxygen binding to the surface, or the breaking O-O bond for weak oxygen binding to the surface.⁸ The first proton and electron transfer was identified as a possible rds through the calculations of relevant intermediates formation energy on Pt(111) in multiple possible mechanisms.⁹⁻¹⁰ A very important contribution by DFT was that the interaction between the metal surface and oxygen species (O, OH) was identified as an effective yardstick for predicting relative ORR rates.¹⁰ It is difficult to prove these proposed ORR mechanisms experimentally, but improved understanding of oxygen adsorption on these surfaces is an essential step to elucidate such mechanisms. We collaborated with Prof. Ruqian Wu of

the University of California at Irvine to design and carry out first principles calculations using DFT to explore O₂ adsorption and dissociation mechanisms at these model catalyst surfaces.

1.5.5 Nanotemplating for Pt as electrocatalysts for the hydrogen evolution reaction (HER)

Fundamental study of reactions on extended surfaces such as a single crystal flat surface do not represent the state of practical catalysts because Pt catalysts are often supported on some inactive materials. Here, a new concept is introduced in which a well-ordered nanotemplate serving as the support for active metals (Pt, Pd) bridges an important materials gap. The morphology of surface elements is confined by the nanotemplate, which also modifies the electronic properties. This approach allows us to explore the catalytic activity of such special template surfaces for different reactions and understand the various effects (size, orientation, and low-coordination sites) that are induced by the nanoscale template. Specifically, HER on a Pt monolayer on faceted Re(11 $\bar{2}$ 1) was studied in this thesis.

Hydrogen evolution by electrochemical water splitting is of great interest since the product, H₂, is an important energy carrier for fuel cells with high mass energy density. One of the challenges for this reaction is costly catalysts based on Pt. Our studies emphasize the synthesis of cheaper model catalysts for HER by using ultra-low levels of Pt metal that can be realized by using Pt monolayers.

1.5.6 Study of ORR kinetics: Origin of overpotential in ORR and Tafel analysis

The oxygen reduction reaction at the cathode can be described by the Eq. (2).¹² This reaction involves a four electron transfer and has a standard potential of 1.23 V. Unfortunately, oxygen reduction kinetics on all-Pt catalysts suffer significant overpotential loss. The overpotential is the difference between the thermodynamically determined reduction potential (1.23 V) and the observed potential (0.8~0.9 V) for this reaction to take place. The overpotential of Eq.(2) mainly originates from the activation energy for electron transfer at the surface and the blocking of surface sites by adsorbed OH at higher potentials (0.75~0.95 V).⁹ The ORR rate expression considering the blocking of active sites by surface oxide can then be written as:¹²

$$J_{ORR} = J_0(1 - \theta_{OX})exp\left(\frac{E^o - E}{b_{int}}\right) \quad (14)$$

where, J_{ORR} is the observed current, J_0 is the exchange current at E^o , E is the cathode potential, E^o is the redox potential for the O_2/H_2O couple under the relevant operation conditions, θ_{ox} is the coverage by chemisorbed oxygen at potential, E , and b_{int} is the “intrinsic” value of the ORR Tafel slope for a surface free of oxygen. The variation of the observed current to the change of overpotential is:¹²

$$Apparent\ Tafel\ slope = \frac{d(\log J_{ORR})}{d(E^o - E)} = \frac{1}{b_{int}} + \frac{1}{1 - \theta_{OX}} \frac{d\theta_{OX}}{dE} \quad (15)$$

The *apparent Tafel slope* for ORR is expected to be smaller than the intrinsic slope b_{int} from Eq. (15).

Experimentally, the ORR kinetics are studied by analysis of ORR polarization curves, which are I-V curves obtained in an electrochemical cell with a three-electrode system, controlled by a potentiostat. O_2 is dissolved in the electrolyte and diffuses to the electrode surface. The energy levels are different for the electron in O_2 and at the electrode surface, which causes the electron transfer from the electrode to the O_2 . Macroscopically, current is generated and recorded by the potentiostat. The kinetics of this process are changed by the applied potential on the electrode, which changes the relative positions of the energy levels of the electrode and O_2 . The applied potential also affects the adsorption capability of O-containing species. Experimental setups are shown in Figures 1.4 and 1.5, and more experimental details are described in Section 1.6

The bimetallic and ternary alloy catalysts studied included Pd, Pt, and Au monolayers and alloys formed after depositing these metals on Pd, Pd_3Fe , and Re single crystal surfaces.

The specific model catalysts reported on herein are:

- (1) Pd monolayer deposited on a $Pd_3Fe(111)$ substrate
- (2) Au monolayer deposited on a $Pd_3Fe(111)$ substrate
- (3) Pt monolayer deposited on a (carbon-induced) faceted surface of $Re(11-21)$.

1.6 Experimental methods

Ensuring the quality of the experimental results requires strict procedures in passing from the sample preparation under UHV conditions to the electrochemical analysis in the electrochemical cell. The quality of the crystal surfaces prepared in UHV must be evaluated by LEED, XPS, AES and LEIS to ensure the right surface composition and structure with minimum contamination. The base pressure of the UHV chamber was below 3.0×10^{-10} torr. If possible, STM is used to study the surface structure at an atomic level to examine structural defects. The most common impurities for a Pd crystal surface are carbon and sulfur. Cycles of sputtering by 500-eV Ar^+ ions and annealing at 1000 K in vacuum can reduce these impurities to below a detectable level ($<0.1\%$). The high pressure cell, where the sample can be transferred between UHV and the electrochemical cell, is pumped by a turbomolecular pump. The gas lines connected to the UHV chamber should also be pumped by a turbomolecular pump to ensure that they are free of contamination from mechanical pump oil. The sample should not be exposed to air because impurities in the air such as oil-containing aerosols can irreversibly adsorb on the clean surface and ruin the experiment. Because only the crystal surface has a well-defined composition and structure, the edge of the crystal must not contact the electrolyte. This is possible as long as the crystal is lowered into the electrolyte slowly and carefully. Ultra-high purity electrolytes (Perchloric acid, 70%, 99.999% trace metals basis and HPLC water, Fisher) must be used and the glassware needs to be cleaned by HPLC water in all electrochemical experiments. The three-electrode cell system includes a reference electrode (hydrogen electrode or AgCl electrode, 66-EE009 "No Leak" Ag/AgCl,

Cypress) and a counter electrode (pure Pt wire, 99.99%, ESPI) and a working electrode (the crystal surface under investigation). The electrochemical setup is displayed in Figures 1.6 and 1.7. During polarization experiments, the working electrode potential is scanned relative to the reference electrode and the current between the working electrode and the counter electrode is recorded. Scanning is controlled by an EG&G Potentiostat (PAR-263A). The current range setting is: 10 mA for ORR and HER polarization curves and 0.1mA for CVs.

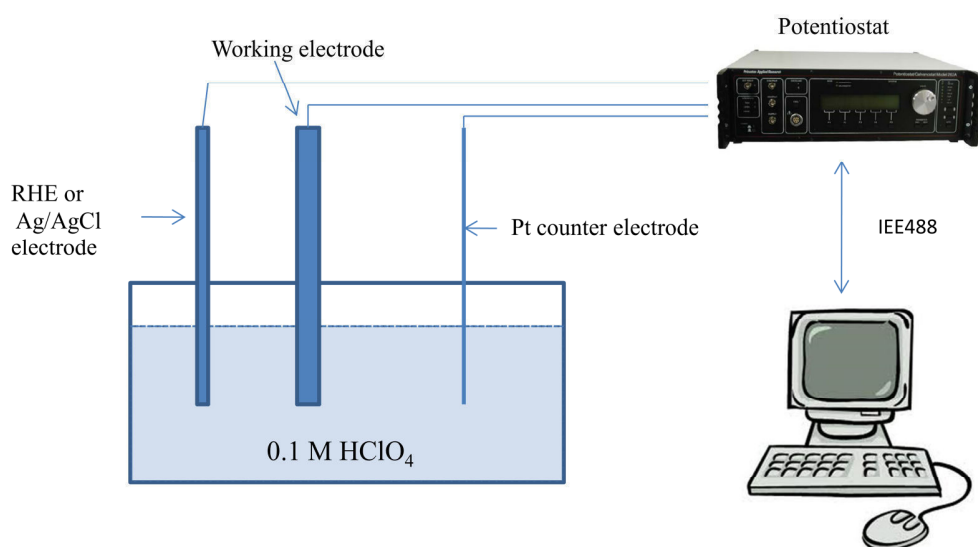
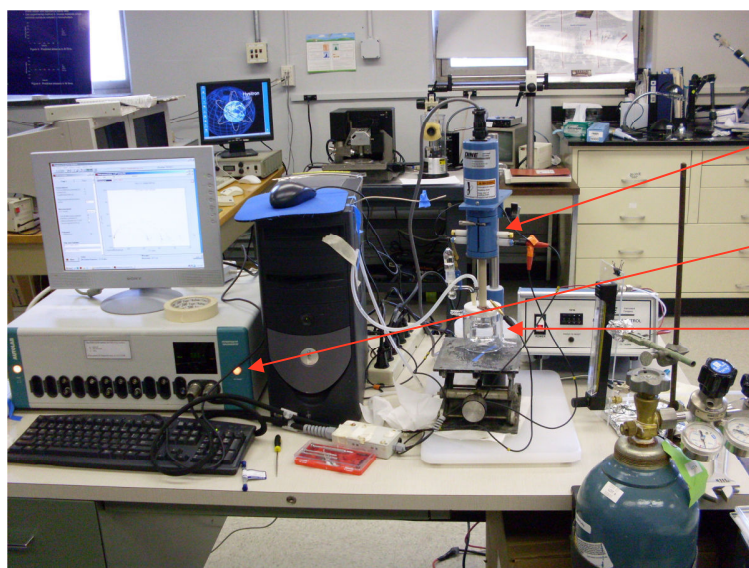


Figure 1.6 Diagram of the three-electrode cell system. In a CV or ORR experiment, the potential of the working electrode is scanned linearly relative to the reference electrode in cycles at a certain potential range. The current between the working electrode and counter electrode is corrected.

A.

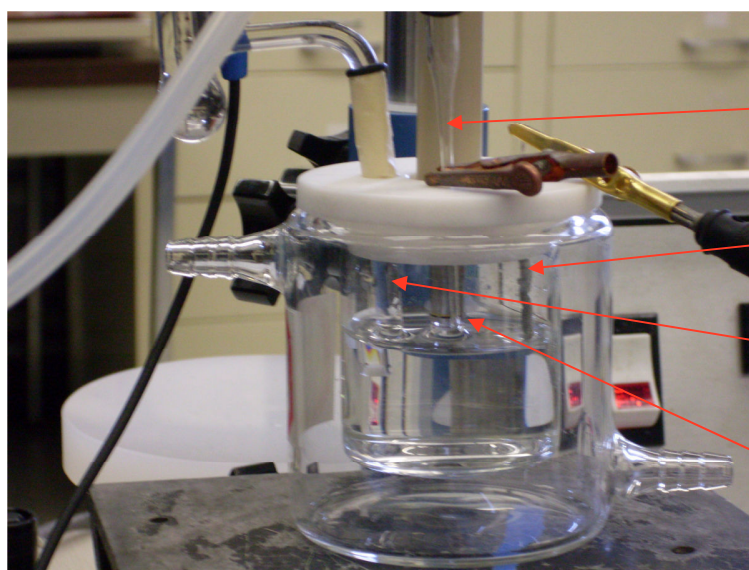


Rotator

Potentiostat

Electrochemical cell

B.



Reference electrode

Counter electrode (Pt)

Purging gas tube

Crystal (working electrode)

Figure 1.7 Pictures of electrochemical instruments. A. Set-up of the electrochemical analysis system, B. Three-electrode electrochemical cell. The major components are indicated by arrows. See the text for more details.

The construction of a hydrogen electrode is shown in Figure 1.8. The reversible hydrogen electrode is a practical electrode with reproducible potential. The potential is given by the Nernst equation:

$$E = E^0 - \frac{RT}{2F} \ln P(H_2)/\alpha(H^+)^2 \quad (16)$$

where E^0 is the standard hydrogen potential, which is defined as zero, R is the gas constant, T is the absolute temperature, P is the pressure of hydrogen gas above the solution, α is the activity of H^+ in the solution, and F is the Faraday constant.

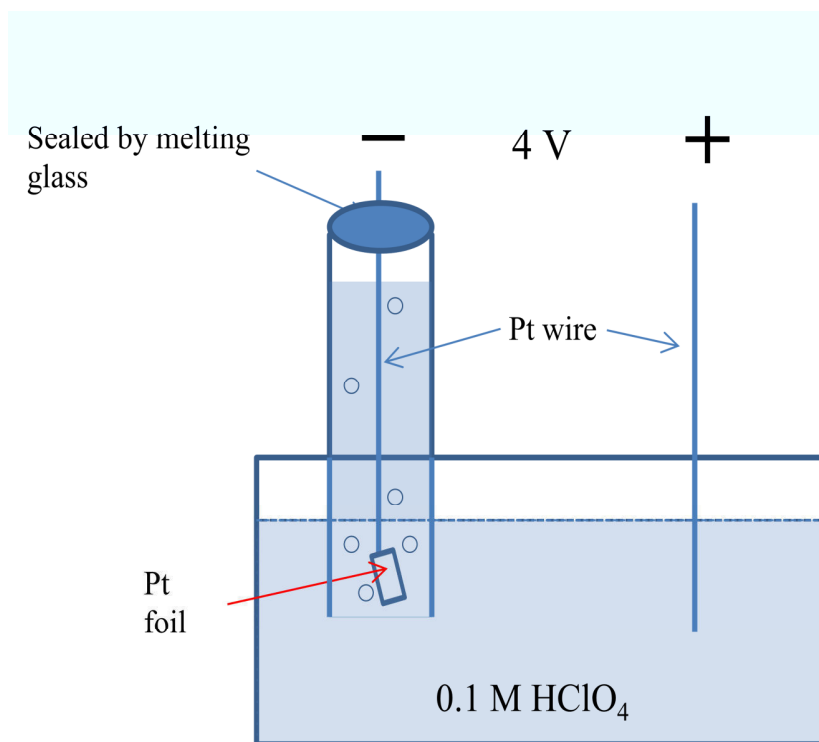


Figure 1.8 Construction of a reversible hydrogen electrode. The electrode is constructed by inserting a piece of Pt foil (5mm×5mm) into a 0.1M HClO₄ solution bubbling with hydrogen gas. Hydrogen gas is generated by electro-hydrolyzing water with an external DC power supply (4 Volts) and the hydrogen gas is contained on the top of the glass tube. The top of the glass tube is sealed by flame annealing.

The overall experimental procedure for electrochemical measurements can be given as:

1. Install a crystal on the sample holder

High purity crystals (99.99%), 6.5mm diameters, 3 mm thick, and one side polished, were purchased from Metal and Metal Oxides Ltd. A Pd₃Fe(111) crystal was also loaned by Dr. Radoslav Adzic at Brookhaven National Laboratory. The crystal sample was mounted on the sample holder by spot-welding four Ta wires (0.01 in. dia) at the edge of the crystal as shown in Figure 1.3. To avoid edge-wetting problems in the electrochemical measurements, the welding position should be close to the unpolished side. The center of the crystal surface should align to the center of the sample holder, so that it can rotate up to 1600 rpm stably during the polarization experiments.

2. Prepare clean metal films and alloy surfaces by sputtering, annealing, and vapor deposition of metal under UHV conditions.

After the sample is transferred into the high pressure cell, the cell is first pumped by a turbomolecular pump until the pressure is below 1.0×10^{-7} torr. Degassing is carried out by heating the crystal and the sample holder to about 200 °C. The high pressure cell is also baked out for 10 hours. Then the crystal is moved to the main UHV chamber. The crystal is cleaned by cycles of Ar⁺ sputtering (500eV, 0.3 μA) and annealing at 850 K in 1.0×10^{-7} torr O₂ for 2 mins, followed by flashing the crystal to 1100 K. The surface cleanliness is checked by XPS and AES to ensure there is no-detectable carbon and sulfur at

the surface. The surface ordering is checked by LEED. The other elements are evaporated onto the surface by physical vapor deposition (PVD). The construction detail of an Au doser is described in Chapter 5.

3. Transfer the sample to the high pressure cell.

After the sample is prepared in the UHV, it is moved to the high pressure cell. Then the gate valve between the UHV chamber and the high pressure cell is closed. The high pressure cell is pressurized and back-filled with high purity nitrogen gas (slightly exceeding 1 atm). The sample is disassembled from the sample stage by sliding the sample holder off the clips. A drop of ultra-high purity water is added to the crystal surface, so that the surface is fully covered by the water. This water drop can protect the surface from contamination in the atmosphere, which allows for the exposure of the crystal in air for a short time safely.

4. Transfer the sample from the high pressure cell to the electrochemical cell.

After the sample is removed from the high pressure cell, it is moved to the electrochemical cell. The sample is installed on the rotator (Compact Pine Rotator) by connecting the rotator rod to the center hole of the sample holder. In this procedure, the sample surface should be kept downward to hold the water drop all the time. Then, the sample is moved into the electrochemical cell by lifting the electrochemical cell carefully until the electrolyte surface contacts with the water drop on the sample surface. (See Figure 1.9) The potential is controlled at zero *versus* the potential of a reversible hydrogen electrode (RHE) in this procedure.

5. Carry out electrochemical measurements including cyclic voltammetry (CV) and the polarization curves for ORR and HER kinetics.

Pure Ar gas (99.98%, Airgas) is purged into the 0.1 HClO₄ solution (10 mL/s, 10min) to remove dissolved O₂ before CV and HER measurements. Oxygen gas is purged into the solution (10 mL/s, 10 min) to remove dissolved Ar and saturate into the solution with O₂ before the ORR experiments and O₂ flows above the solution during the ORR measurements. The potential of the sample (working electrode) is scanned from 0 to 1000 mV in cycles at 20 mV/s during the CV and ORR experiments. A potential range of -400 to 100 mV is scanned at 2 mV/s during the HER experiments. In the ORR polarization measurements, the sample is rotated by the Compact Pine Rotator. Rotating speeds are 100, 225, 400, 625, 900, 1250 and 1600 rpm.

6. Surface analysis after electrochemical measurements.

After the electrochemical measurements are finished, the sample surface is cleaned by ultra-high purity water and dried with high purity helium gas, and transferred back to the high pressure cell quickly. The cell is pumped by a turbomolecular pump to the pressure below 1.0×10^{-7} torr, before the crystal is moved to the UHV chamber for surface analysis using spectroscopic techniques.

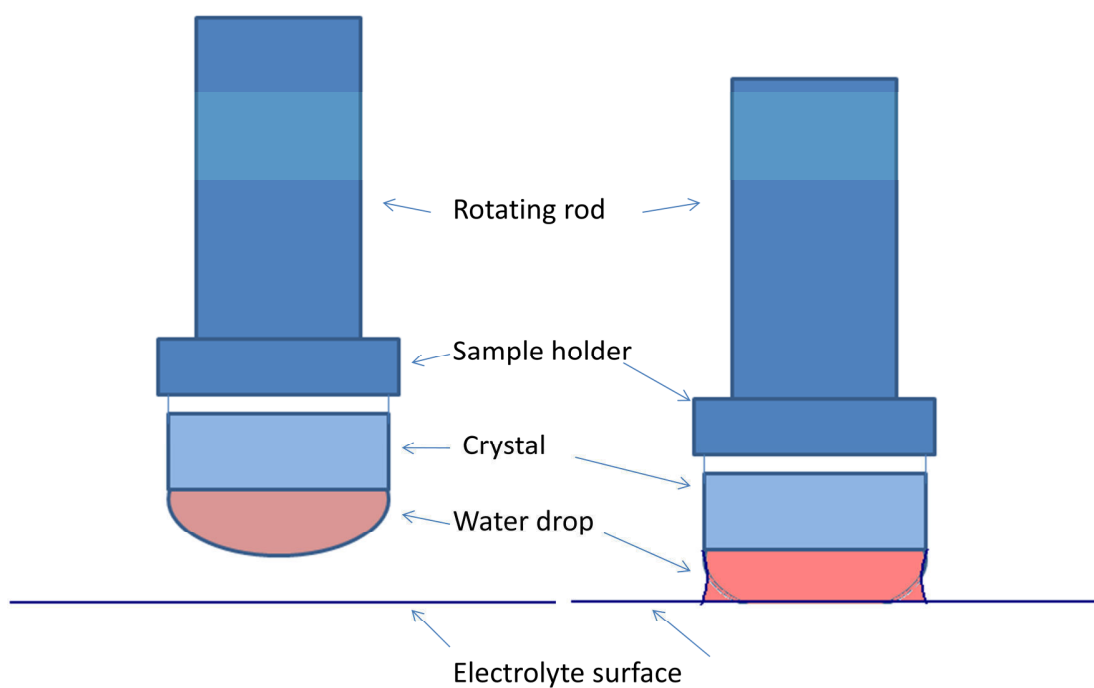


Figure 1.9 Schematic view of the crystal surface before (left) and after (after) contacting with electrolyte. The side or the back of the crystal should not contact the solution.

1.7 STM measurements

A custom apparatus designed around a commercial STM instrument (RHK UHV 3000, SPM 1000) was used to study surface structure under UHV conditions. A schematic view of the UHV STM chamber is shown in Figure 1.10. The RHK STM system consists of two main chambers, a preparation chamber equipped with XPS, LEIS, LEED and AES, and an analysis chamber equipped with STM, both pumped by ion pumps (Gamma Vacuum) and a load-lock pumped by a turbo pump (TW 70H, Leybold Vacuum Equipment). The RHK STM sample holder with 6 contact pins is shown in Figure 1.11. The sample is annealed by an electron-beam(e-beam) heating method. The sample is mounted to be electrically insulated with respect to the sample holder by two sapphire disks (labeled as 19 in Figure 1.11). The thermocouple is spot-welded on the edge of the crystal edge. In e-beam heating, a positive bias (300-400 V) is applied to the sample while the sample holder and the filament are grounded. This heating method is better than using a negative bias on the filament with the sample holder and the sample grounded. The high voltage is applied through the thermocouple. *Caution:* avoid electrical shorting when measuring the temperature. The sample mounted on the RHK sample holder can be transferred between the preparation chamber and analyzing chamber conveniently.

STM tips were prepared by dipping a small W diameter (0.01 in., 99.98%, ESPI Metals) metal wire into a 2.0 M NaOH solution in which a counter electrode is sitting to apply an AC voltage. The tungsten tip is easily oxidized into tungsten oxide, which is removed by dipping it into a HF solution (48%, Fisher) for 5 seconds before transferring into the UHV chamber. During STM scanning, the whole UHV chamber is floated on

three air-legs (35 psi, Newport Corporation). Both the dry pump and turbo pump are shut off to reduce vibrations. The power supply of the ion gauge in the analysis chamber and the baking system are also shut down to minimize electric noise. STM images of the best quality were often obtained at a small negative bias.

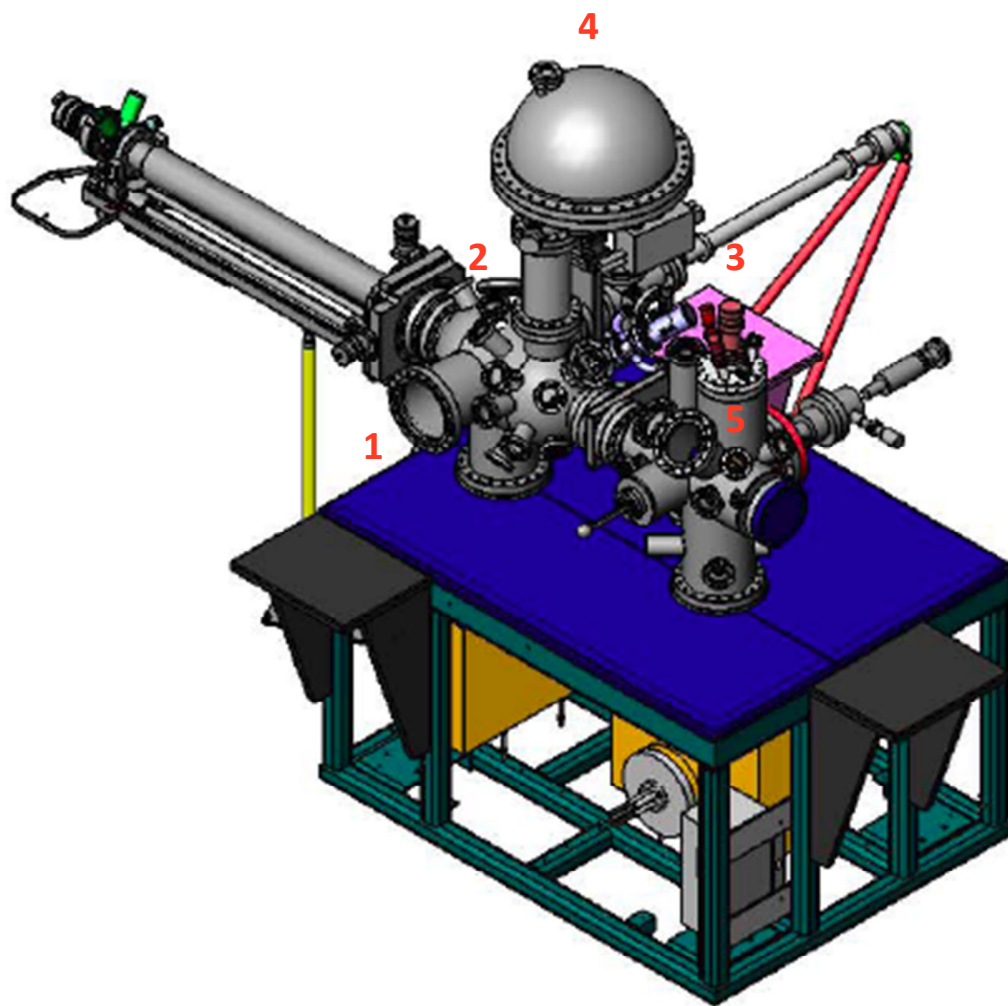


Figure 1.10 Schematic view of the STM Chamber. 1. LEED, 2. X-Ray source(Perkin Elmer dual anode, Model 04-548), 3. Ion gun (Perkin Elmer, Model 04-303), 4. PHOIBOS 100 Energy Analyzer, and 5. STM SPM 1000 system.

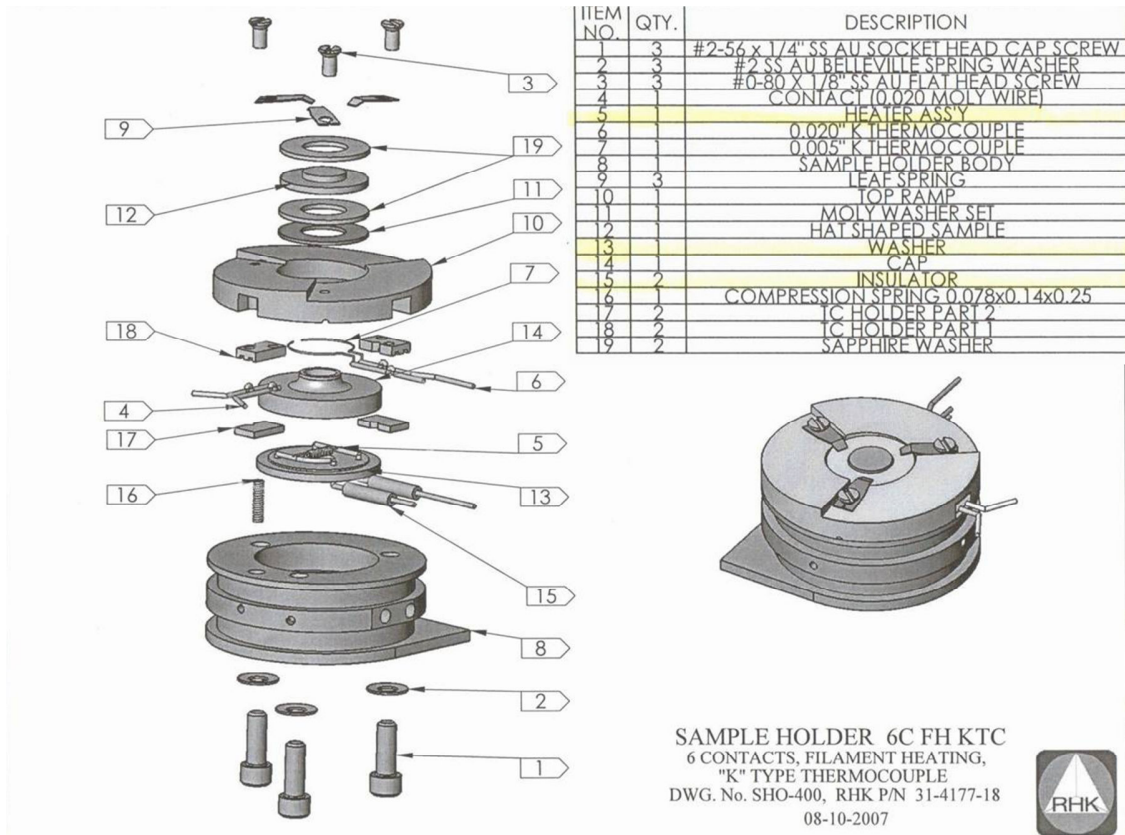


Figure 1.11 RHK sample holder with six contact pins (C- type thermocouple, label 6, K-type thermocouple, label 4 and two heating wires, label 15.)

1. 8 References

1. Kordesch, K. V.; Simader, G. R., Environmental impact of fuel cell technology. *Chem. Rev.* **1995**, *95* (1), 191-207.
2. Trimm, D. L.; Önsan, Z. I., Onboard fuel conversion for hydrogen-fuel-cell-driven vehicles *Catalysis Reviews: Science and Engineering* **2001**, *43* (1), 31 - 84.
3. Johnson, J., Ethanol—Is It Worth It? *Chem. Eng. News* **2007**, *85*, 19-21.
4. Patzek, T. W., Ch. 2 Can the earth deliver the biomass-for-fuel we demand? In *Biofuels, Solar and Wind as Renewable Energy Systems*, Pimentel, D., Ed. Springer: New York, 2008.
5. http://www1.eere.energy.gov/hydrogenandfuelcells/pdfs/h2_tech_roadmap.pdf.
6. <http://www1.eere.energy.gov/hydrogenandfuelcells/>.
7. Rossmeisl, J.; Nørskov, J. K., Electrochemistry on the computer: Understanding how to tailor the metal overlayers for the oxygen reduction reaction. *Surf. Sci.* **2008**, *602* (14), 2337-2338.
8. Nilekar, A. U.; Mavrikakis, M., Improved oxygen reduction reactivity of platinum monolayers on transition metal surfaces. *Surf. Sci. Lett.* **2008**, *602*, L89.
9. Nørskov, J. K.; Rossmeisl, J.; Logadottir, A.; Lindqvist, L.; Kitchin, J. R.; Bligaard, T.; Jónsson, H., Origin of the overpotential for oxygen reduction at a fuel-cell cathode. *J. Phys. Chem. B* **2004**, *108* (46), 17886-17892.
10. Panchenko, A.; Koper, M. T. M.; Shubina, T. E.; Mitchell, S. J.; Roduner, E., Ab initio calculations of intermediates of oxygen reduction on low-Index platinum surfaces. *J. Electrochem. Soc.* **2004**, *151* (12), A2016-A2027.
11. Kresse, G.; Furthmüller, J., Efficiency of ab-initio total energy calculations for metals and semiconductors using a plane-wave basis set. *Comput. Mater. Sci.* **1996**, *6* (1), 15-50.
12. Gottesfeld, S., Ch. 1 Electrocatalysis of oxygen reduction in polymer electrolyte fuel cells: A brief history and a critical examination of present theory and diagnostics. In *Fuel Cell Catalysis: A Surface Science Approach*, Wieckowski, A., Ed. John Wiley & Sons, Inc.: Hoboken, New Jersey, 2009.

13. Xu, Y.; Shao, M.; Mavrikakis, M.; Adzic, R. R., Ch. 9 Recent developments in the electrocatalysis of the O₂ reduction reaction. In *Fuel cell catalysis - a surface science approach*, Wieckowski, A., Ed. John Wiley & Sons, Inc., Hoboken, New Jersey, 2009.
14. Varga, M.; Mulas, G.; Cocco, G.; Molnár, Á.; Lovas, A., Binary and ternary amorphous palladium alloys: Characterization, activity and selectivity in hydrogenation of dienes. *Mater. Sci. Eng., A* **2001**, *304-306*, 462-466.
15. Rodriguez, J. A., Chapter 12 Electronic and chemical properties of palladium in bimetallic systems: How much do we know about heteronuclear metal-metal bonding? In *The Chemical Physics of Solid Surfaces*, Woodruff, D. P., Ed. Elsevier: 2002; Vol. Volume 10, pp 438-465.
16. Bertolini, J. C.; Jugnet, Y., Chapter 11 Surface structure and catalytic reactivity of palladium overlayers for 1,3-butadiene hydrogenation. In *The Chemical Physics of Solid Surfaces*, Woodruff, D. P., Ed. Elsevier: 2002; Vol. Volume 10, pp 404-437.
17. Shao, M.-h.; Liu, P.; Adzic, R. R., Superoxide anion is the intermediate in the oxygen reduction reaction on platinum electrodes. *J. Am. Chem. Soc.* **2006**, *128* (23), 7408-7409.
18. Paulus, U. A.; Wokaun, A.; Scherer, G. G.; Schmidt, T. J.; Stamenkovic, V.; Radmilovic, V.; Markovic, N. M.; Ross, P. N., Oxygen reduction on carbon-supported Pt–Ni and Pt–Co alloy catalysts. *J. Phys. Chem. B* **2002**, *106* (16), 4181-4191.
19. Stamenkovic, V. R.; Fowler, B.; Mun, B. S.; Wang, G.; Ross, P. N.; Lucas, C. A.; Markovic, N. M., Improved oxygen reduction activity on Pt₃Ni(111) via Increased surface site availability *Science* **2007**, *315*, 493-497.
20. Lim, B.; Jiang, M.; Camargo, P. H. C.; Cho, E. C.; Tao, J.; Lu, X.; Zhu, Y.; Xia, Y., Pd-Pt Bimetallic Nanodendrites with High Activity for Oxygen Reduction. *Science* **2009**, *324* (5932), 1302-1305.
21. Xing, Y.; Cai, Y.; Vukmirovic, M. B.; Zhou, W.-P.; Karan, H.; Wang, J. X.; Adzic, R. R., Enhancing oxygen reduction reaction activity via Pd–Au alloy sublayer mediation of Pt monolayer electrocatalysts. *J. Phys. Chem. Lett.* **2010**, 3238-3242.

22. Lima, F. H. B.; Zhang, J.; Shao, M. H.; Sasaki, K.; Vukmirovic, M. B.; Ticianelli, E. A.; Adzic, R. R., Catalytic activity–*d*-band center correlation for the O₂ reduction reaction on platinum in alkaline solutions. *J. Phys. Chem. C* **2006**, *111* (1), 404-410.
23. Strmcnik, D.; Escudero-Escribano, M.; Kodama, K.; StamenkovicVojislav, R.; Cuesta, A.; Marković, N. M., Enhanced electrocatalysis of the oxygen reduction reaction based on patterning of platinum surfaces with cyanide. *Nat. Chem.* **2010**, *2* (10), 880-885.
24. Lefèvre, M.; Proietti, E.; Jaouen, F.; Dodelet, J.-P., Iron-based vatalysts with improved oxygen reduction activity in polymer electrolyte fuel cells. *Science* **2009**, *324* (5923), 71-74.
25. Gong, K.; Du, F.; Xia, Z.; Durstock, M.; Dai, L., Nitrogen-doped carbon nanotube arrays with high electrocatalytic activity for oxygen reduction. *Science* **2009**, *323* (5915), 760-764.
26. Zhang, J.; Sasaki, K.; Sutter, E.; Adzic, R. R., Stabilization of platinum oxygen-reduction electrocatalysts using gold clusters. *Science* **2007**, *315* (5809), 220-222.
27. Ratner, B. D.; Castner, D. G., Ch. 3 Electron Spectroscopy for Chemical Analysis. In *Surface Analysis–The Principal Techniques, 2nd Edition*, Vickerman, J. C.; Gilmore, I. S., Eds. John Wiley & Sons Ltd: Chichester, UK, 2009.
28. Taglauer, E., Ch. 6 Low-Energy Ion Scattering and Rutherford Backscattering. In *Surface Analysis -The Principal Techniques, 2nd Edition*, Vickerman, J. C.; Glimore, I. S., Eds. JohnWiley & Sons Ltd: Chichester, UK, 2009.
29. Leggett, G. J., Ch. 9 Scanning Probe Microscopy. In *Surface Analysis –The Principal Techniques, 2nd Edition*, John, C. V.; Glimore, I. S., Eds. JohnWiley & Sons Ltd: Chichester, UK, 2009.

Chapter 2 Formation of Pd Monomers and Dimers on a Single Crystal Pd₃Fe(111) Surface

2.1 Introduction

Palladium-iron bimetallic catalysts have been widely studied in heterogeneous catalysis for reactions such as selective hydrogenation of unsaturated hydrocarbons,¹⁻² production of methanol from synthesis gas³ and improved oxygen reduction at the cathode in PEM fuel cells.⁴⁻⁶ It is well known that the enhanced catalytic properties of bimetallic catalysts originate from both ligand effects and geometric effects.⁷⁻⁸ Ligand effects arise from modification of the electronic structure of the first metal by the second metal, in particular the filling and shifting of their *d*-states. Geometric effects are induced by changes in the arrangement of active sites (ensembles) that alter the transition states and hence the reaction kinematics. Basic information on composition and structure of bimetallic surfaces, and how segregation in alloys influences their surface properties, is of great importance for the control of catalytic properties.⁹

Herein, we show that the Pd₃Fe(111) surface may exhibit an unusual surface morphology, with Pd adatoms atop a Pd-enriched alloy surface, after a particular annealing procedure. This surface structure is different from other well-studied (111) surfaces of *3d* and *4d* alloys, such as Pd/M (M=Ni, Co) and Pt/M (M=Fe, Ni, Cu, Rh),¹⁰ which are comprised of flat and complete terraces after high temperature annealing. The discovery of such a special structure for the Pd₃Fe(111) surface raises an interesting

question of how to control the distribution of Pd adatoms for the optimization of catalytic properties of this alloy.

2.2 Experimental details

A Pd₃Fe(111) single crystal (6-mm dia., 3-mm thick) was mounted on a sample holder and then transported into a UHV chamber with a base pressure of 1×10^{-10} torr. This UHV system was equipped for AES, XPS, LEIS, LEED, TPD and STM. Sample cleaning was performed by several cycles of 500-eV Ar⁺ ion sputtering at 2×10^{-5} torr (0.4 μ A, 5 min) and heating to 1100 K in vacuum for 60 sec. Residual carbon was removed by heating the sample in 5×10^{-8} torr O₂ at 700 K for 2 min. The sample was then heated to 1200 K in vacuum for 30 sec to remove oxygen and obtain a well-ordered surface. The cleanliness of the alloy surface was evaluated by XPS and LEIS and no detectable amount of carbon, oxygen, sulfur or chlorine remained prior to experiments. In temperature-dependent studies, the surface was cooled directly to room temperature after annealing to a specified temperature, and all LEED, LEIS and STM measurements were obtained at room temperature (300 K).

Typically, abruptly stopping heating at 1200 K causes the sample to cool to 500 K in about 2 min and then to continue to cool to room temperature more slowly *via* heat transfer from the sample to the surroundings. We report here only results obtained from “quenched” samples that were prepared by heating the sample to a certain temperature and then cooling it directly and rapidly to room temperature prior to measurements. Some measurements were also made (not reported here) on surfaces prepared using a different,

stepwise-cooling procedure, which leads to different surface compositions and surface structures.

The surface composition was studied by LEIS spectra, taken at a 50° incident angle from the normal of the sample surface and a normal detection angle to give a 130° scattering angle. The helium ion source was differentially pumped with a He pressure of 1×10^{-7} torr in the source region and 1×10^{-9} torr in the analysis chamber. The incident He⁺ ion energy was 1000 eV. These experimental conditions generated a 3 nA ion current on the sample. Sensitivity factors for Fe and Pd were calculated based on measurements using pure (99.999%) Fe foil and pure (99.999%) Pd foil standards. Sensitivity factors obtained using these samples as standards are valid for our single crystal samples because the surface morphologies of the two are similar enough considering the small sensitivity of LEIS to small values of surface roughness. Using our measured relative sensitivity factors to determine $S_{\text{Pd}}/S_{\text{Fe}} = 2.1$, we found that the initial state of the Pd₃Fe(111) alloy surface after sputtering had the expected bulk Pd:Fe ratio of 3:1. This result indicates that preferential sputtering expected for the lighter Fe atoms caused no significant change in the surface composition of these surfaces.

The surface structure was studied by STM and the STM images were taken in an attached chamber at a base pressure of 6×10^{-11} torr. After the sample was cleaned, it was annealed to 1200 K for 2 min in the STM chamber prior to imaging. The STM images were acquired with an electrochemically etched tungsten tip at a tip voltage of -1 mV to -300 mV and a tunneling current of 0.3 – 2.5 nA.

Theoretical calculations based on DFT were carried out with the Vienna ab-initio simulation package (VASP) at the level of the spin-polarized generalized-gradient

approximation (GGA).¹¹ We used the projector augmented wave (PAW) method for the description of core-valence interactions. As a benchmark, we calculated that the optimized lattice constant of bulk Pd₃Fe was 3.877 Å, and the magnetic moments of Fe and Pd were 3.33 and 0.32 μB, respectively. These results agree excellently with both experimental measurement and previous density functional calculations.¹² We used slab models with 5 monolayers of Pd and Fe atoms along with a 15 Å vacuum space in between to study surface segregation in Pd₃Fe(111). To allow for sufficient freedom, we used a (2×2) supercell (or 16 atoms per layer) in the lateral plane for most calculations and a (7×2) supercell (or 56 atoms per layer) for simulations of step edges. The convergence of calculated energies against the number of *k*-points was carefully monitored. More details on the DFT calculations are listed in the appendix of this chapter.

2.3 Results and discussion

2.3.1 Surface characterization by LEED, LEIS and STM

Segregation in polycrystalline Pd₁Fe₉₉ and Pd₅Fe₉₅ alloy samples was studied previously by LEIS,¹³ which is a powerful technique for determining the surface composition with absolute top-layer sensitivity. Segregation of Pd to the surface and formation of an ordered Pd₅₀Fe₅₀ surface phase was found for polycrystalline Pd₁Fe₉₉, while Pd segregation without formation any ordered surface phase was found for polycrystalline Pd₅Fe₉₅. Our investigation of a Pd₃Fe(111) single crystal is a rare probe of a bulk alloy with high Pd concentration (75 at.%). LEIS spectra obtained after heating to

increasing temperatures are shown in Figure 2.1. Similar to that for the polycrystalline Pd/Fe alloy, Pd segregates to the surface of Pd₃Fe(111). The Pd concentration on the surface increases with increased annealing temperature, reaching the highest Pd concentration of 91% at ~1130 K. Further increase of the annealing temperature above 1130 K lowers the Pd concentration slightly, which is indicative of Langmuir-McLean behavior as the phase-transition temperature is reached.¹⁴ The LEIS spectra were obtained after cooling the sample to room temperature, and so these data do not necessarily represent the surface in its equilibrium state at the elevated annealing temperature. A good Langmuir-McLean relationship was found (Figure 2.2) when LEIS spectra were obtained with the surface held at the annealing temperature. This Langmuir-McLean relationship shows that segregation, an exothermic process, is able to disrupt the bulk alloy structure and break energetically favorable Pd-Fe bonds. A simple interpretation of the LEIS data with the assumption of large flat terraces leads to the conclusion that the outmost layer contains 91% Pd and 9% Fe. However, as we now show, STM reveals that segregation of Pd on Pd₃Fe(111) is very different from that on Pd/Ni single crystals and an unusual segregation mechanism occurs. The clean Pd₃Fe(111) surface prepared by Ar⁺ ion sputtering and annealing to 1100 K exhibits a sharp and bright (1×1) hexagonal LEED pattern (Figure 2.1a insert). This simple pattern indicates that the surface atoms are ordered, although the arrangement between Fe and Pd is not ordered. This (1×1) hexagonal pattern is similar to LEED observations of the Pd₂₅Ni₇₅(111) alloy surface,¹⁵ but different from that of the Pt₈₀Fe₂₀(111) alloy, which shows a (2x2) superstructure caused by an ordered intermetallic arrangement in the second layer.¹⁶

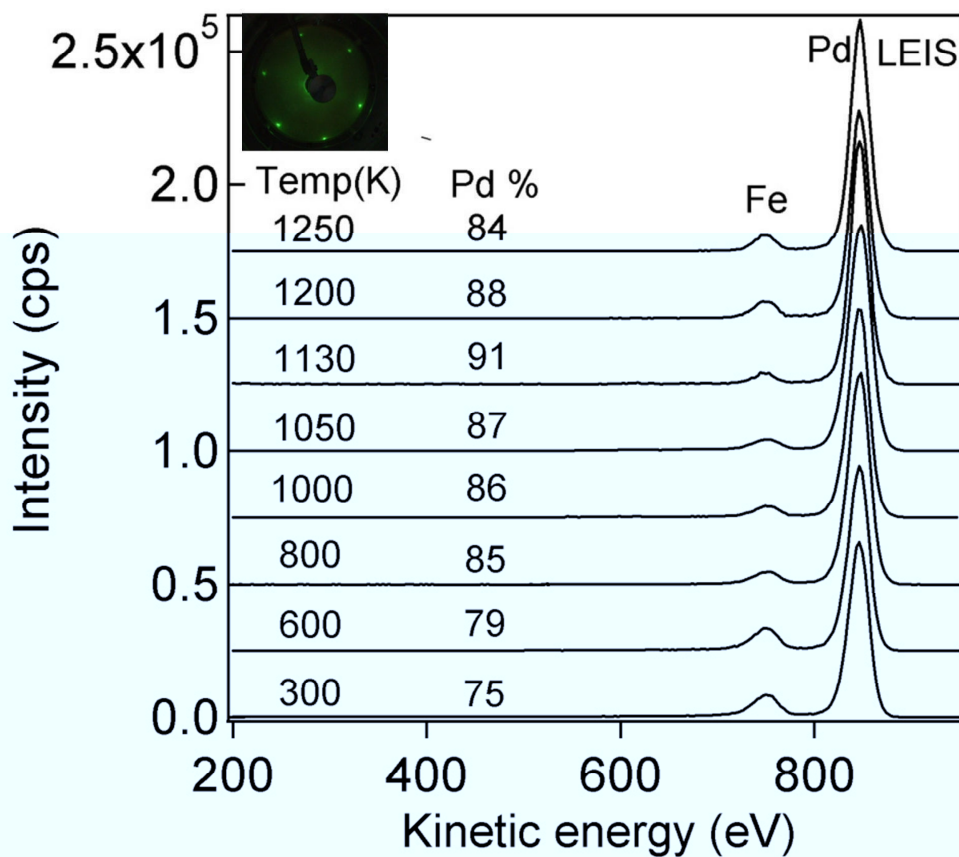


Figure 2.1 LEIS of Pd₃Fe(111) after annealing at several temperatures. $E_i = 1000$ eV He⁺, 3.0 nA. Insert: LEED at $E_p = 55$ eV. Increasing temperature enhances Pd segregation, with a maximum of 91% Pd after heating to 1130 K.

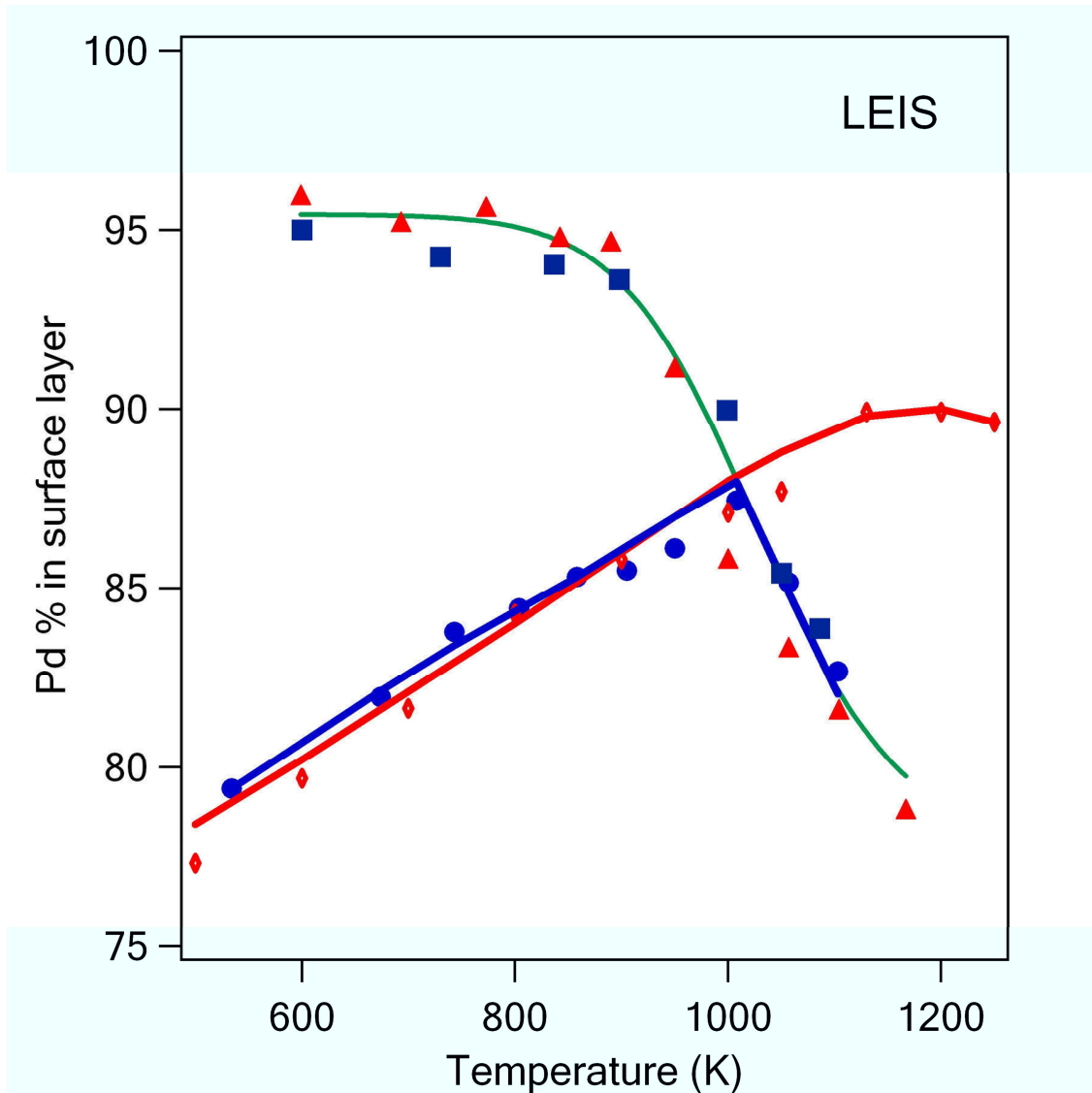
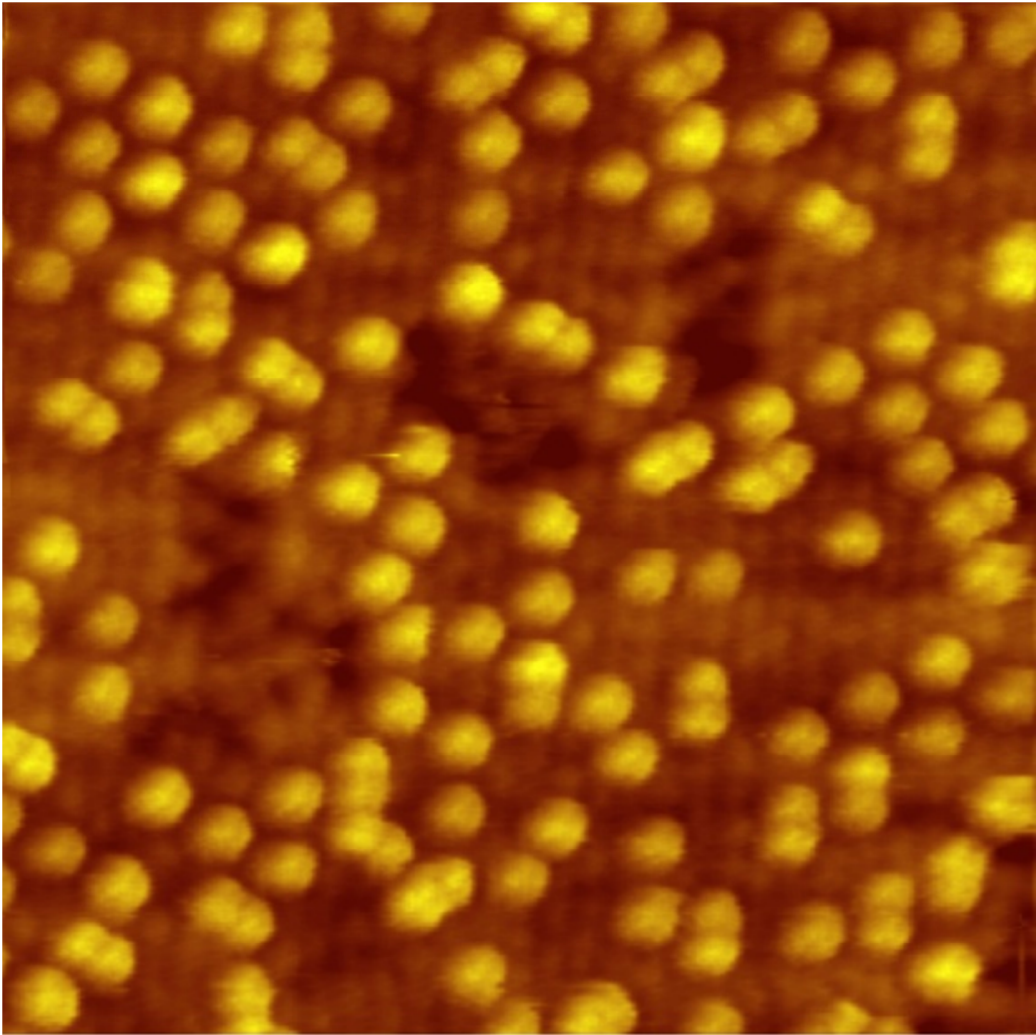


Figure 2.2 Top-layer composition of Pd₃Fe (111) measured with LEIS as a function of temperature. The surface was prepared with a stepwise annealing and cooling procedure. This procedure entails holding the surface at a certain temperature for 2 min before measurement by LEIS at this temperature. The surface Pd is in equilibrium with Pd in the bulk at high temperature. The filled circle markers denote the Pd enrichment when heating a sputter-cleaned surface stepwise to 1100 K. The Pd enrichment reaches a maximum at 1000 K, and then decreases at more elevated temperatures (filled circles). The square and triangle markers show the composition after subsequently heating and

cooling the surface between 550 K and 1150 K. The LEIS data obtained after direct cooling is also plotted here as the filled diamond markers for comparison. The first annealing cycle (filled circles) caused the Pd surface concentration to increase until a maximum Pd concentration, 85%, was reached at 1000 K. Further raising the temperature lowered the Pd concentration, with 75% Pd at 1150 K. The surface Pd concentration equal to the Pd concentration in the bulk is due to the completely disordered (solution) state of Pd₃Fe(111) at 1150 K. The following cooling cycle (filled squares) caused the Pd concentration to increase continuously and reached a maximum of 95% at 900 K. There was no change in the Pd concentration below 900 K (due to a kinetic barrier). The final annealing cycle (filled triangles) recovered the same Pd surface concentration as that in the cooling cycle (filled squares). Therefore, there was a reversible surface composition profile between 900 and 1120 K, indicative of Langmuir-McLean behavior as the phase-transition temperature was reached. The surface prepared by stepwise annealing and cooling showed a diffuse (2×2) pattern.

STM images were obtained at room temperature after the Pd₃Fe(111) surface was sputtered and annealed to 1200 K. A small-area (8.0 nm × 8.0 nm) STM image with atomic resolution and a large-area STM image showing steps and terraces (125.0 nm × 65.0 nm) are shown in Figures 2.3A and 2.3B. Bright spot features arise from mostly monomers and dimers, with a very small amount of trimers and tetramers. The STM image was independent of the bias on the tip (-1.0 to +1.0 V). The smallest distance between adjacent single isolated bright spots is twice the nearest neighbor spacing (0.273 nm) of Pd₃Fe(111) and the distance between two spots in a dimer is 0.273 nm. Thus the bright spots in this STM image are single atoms, even though they appear larger than an atomic diameter. Short-range ordering forms small domains of (2×2) structures. The apparent height of the bright spots is about 1.2 Å. STM may show very strong chemical contrast on alloy surfaces, such as in the study of Pt₂₅Ni₇₅(111).¹⁵ This is attributed to an adsorbate on the STM tip, which interacts strongly with one of the components in the alloy. However, the large apparent height of the bright spots on the Pd₃Fe(111) surface is not only from the chemical contrast, but mainly due to a topographic effect indicative of adatoms (and in this case Pd adatoms, as discussed below).

A.



B.

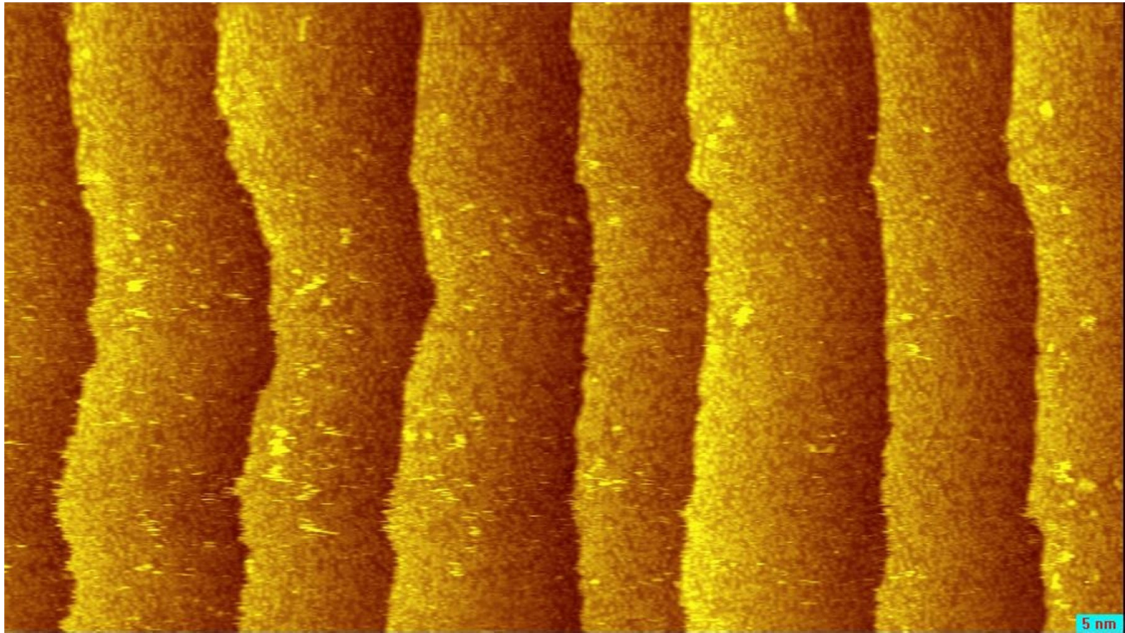


Figure 2.3 Pd segregation at a Pd₃Fe(111) surface. A. STM constant current topography with atomic resolution is obtained. Bright yellow spots are primarily due to segregated Pd monomers and dimers. Image size: 8.0 nm × 8.0 nm. B. Large area showing terraces and steps. Image size: 120.0 nm × 65.0 nm. Imaging conditions for both A and B: 1.03 mV, 2.04 nA, 0.50 M ohm.

We observed single Pd adatoms to move across the surface, jumping from one adsorption site to the next, as they followed the trajectory of the tip (in a “pulling mode”).¹⁷ This is shown by atoms labeled with an arrow in Figure 2.4. Examination of these atomic resolution STM images shows that the bright spots are located at positions different from the lattice positions of the first layer, which eliminates the possibility that these bright spots are embedded within the first layer. Figure 2.5 shows some fuzzy appearance on the right of the bright spots due to tip-induced diffusion. This diffusion is often seen on step edges when the tip jumps from a high terrace to a low terrace, which is similar to the tip scanning over the adatoms on the top layer. Therefore, STM provides solid evidence that the bright spots are due to single atoms, dimers, trimers and tetramers present in an adlayer. Statistical analysis of STM images in Figure 2.6 reveals that the bright spot coverage is 17%, which excludes the possibility that these bright spots are Fe adatoms, since the Fe concentration is only 9% on the surface as determined by LEIS. The coverage of 0.91-ML (monolayer) Pd determined by LEIS is due to the total number of Pd atoms in the topmost (first) alloy layer and the coverage of 0.17-ML Pd present as adatoms. Atoms within the first alloy layer can be seen by LEIS because of the open structure of the adlayer. The assignment of these adatoms as Pd is consistent with the lower surface energy of Pd compared to Fe, which is because of the lower number of unpaired *d* electrons in Pd.¹⁸ Thus, the clean annealed Pd₃Fe(111) alloy crystal terminates in an unusual surface structure comprised of 0.17-ML Pd adatoms segregated on the outmost layer of a Pd-enriched alloy surface.

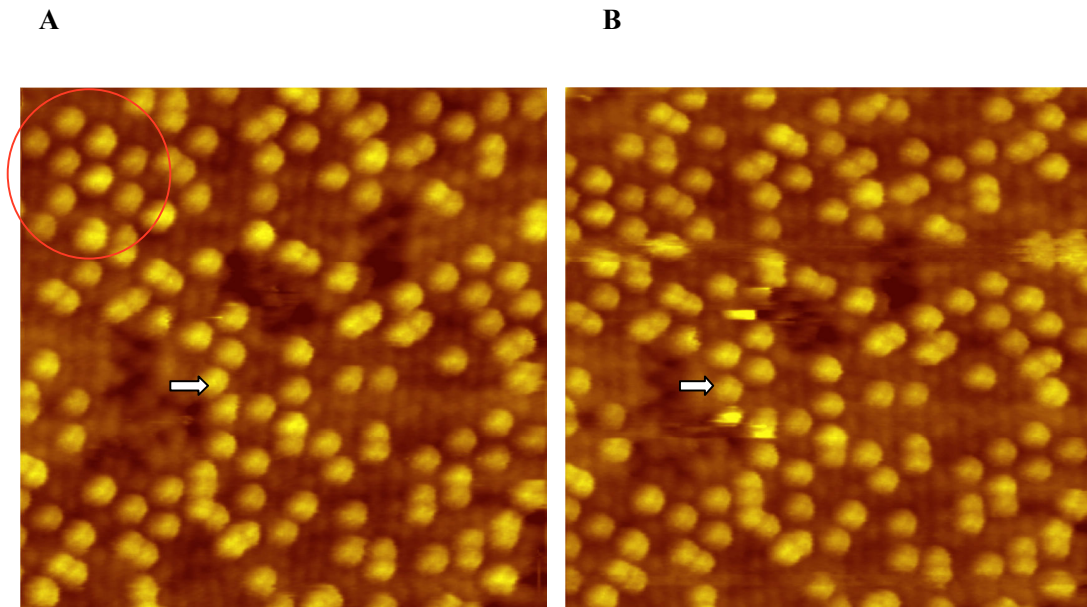


Figure 2.4 Two STM images of Pd₃Fe(111) obtained during sequential scans. A. Image obtained with the STM tip scanned from right to left, top to bottom. B. Image obtained with the STM tip scanned from right to left, bottom to top. There is a small drift noticeable between images. The atom labeled by the arrow was induced by the scanning STM tip to shift to a neighboring site. Single Pd atoms and dimers are the main species of the bright adatoms imaged in STM. The red circled region in the upper-left corner of (A) illustrates short-range ordering of Pd adatoms to form (2×2) structures (referenced to the Pd(111) lattice). Image sizes: 8.0 nm × 8.0 nm. The possibility that these adatoms are due to impurities such as C, O or CO accumulated prior to or during scanning can be excluded since the adatom features are very stable and the heights of these features are more than 1 Å, which is larger than the heights of adsorbed C, O or CO.

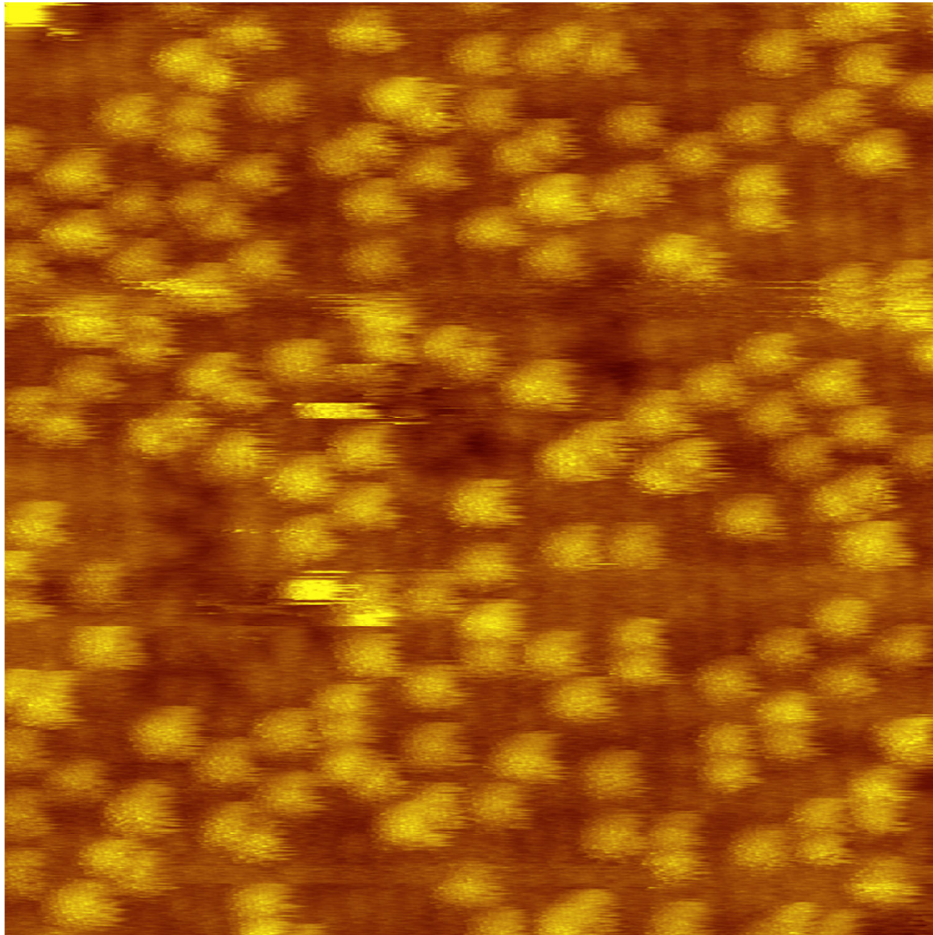


Figure 2.5 Pd adatoms at Pd₃Fe(111) surface with frizzy appearance. Tip is scanning from left to right. Right side of the adatoms appears diffuse. This fuzzy appearance is artificial because the tip didn't response quickly enough to the height change when it moved from the adatoms to the below layer.

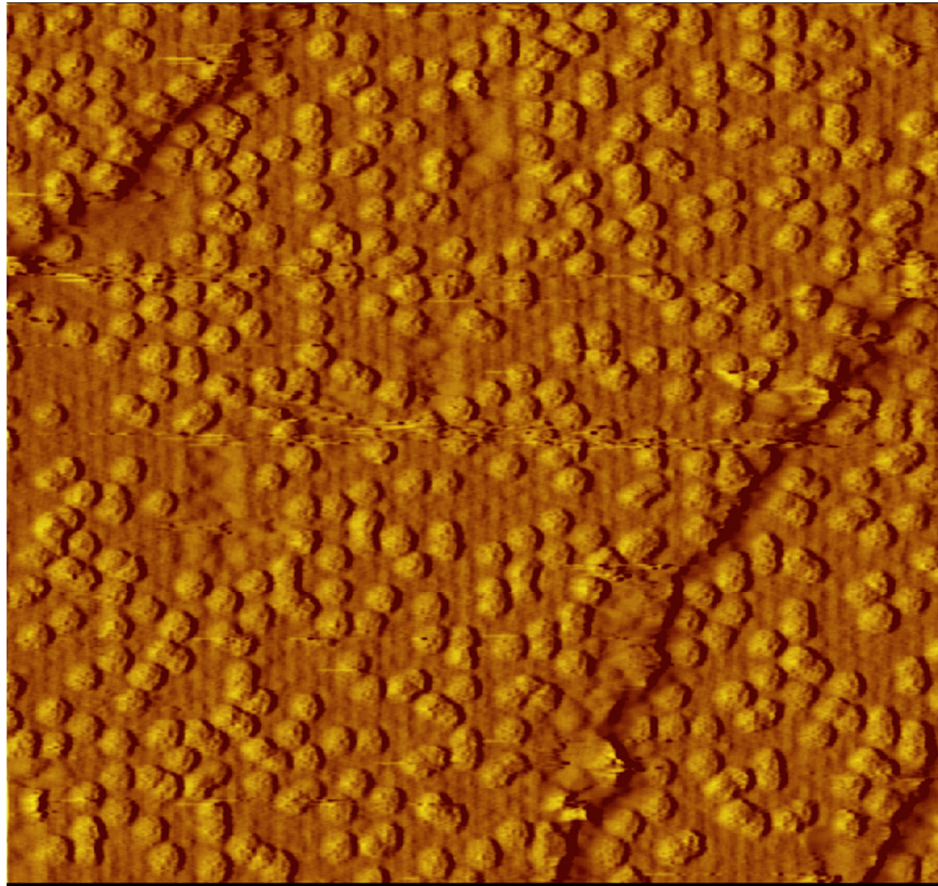


Figure 2.6 Constant-current STM topography with atomic resolution. Image size: 15.0 nm×14.0 nm. Imaging conditions: 1.03 mV, 2.04 nA, 0.50 M ohm. In this image, the total number of atoms in the first complete layer is 3260 and the total number of adatoms is 538, which includes 270 single atoms, 123 dimers, 6 trimers and 1 tetramer. The atom-percentage coverage of Pd adatoms is 17%.

2.3.2 Origin of Pd adatoms studied by DFT calculations

The formation of Pd adatoms at the Pd₃Fe(111) surface is surprising. The mobility of metal adatoms is expected to be high at the high temperatures used for annealing, and so the adatoms might be expected to diffuse easily on terraces and form islands or accumulate at step edges to cause step-flow growth because of the higher number of nearest neighbors. The latter does occur extensively on the Pd₃Fe(111) surface, since high temperature annealing removes much of the roughness induced by ion sputtering, smoothes the surface and forms the large flat terraces imaged by STM. In order to understand the experimental findings regarding the segregation and distribution of Pd atoms, we performed DFT calculations and directly investigated the energetics of several possible segregation pathways and diffusion barriers for Pd adatoms moving from atop sites to step edges at room temperature. At temperature T and pressure p , the stability of an ensemble is determined by its Gibbs free energy, $G(T,p)$, which is defined as.¹⁹

$$G(T,P) = \Delta E + F_{vib} - TS_{conf} + pV \quad (1)$$

where ΔE is the total energy difference, which can be conveniently obtained from DFT calculations, F_{vib} is the vibrational free energy that includes vibrational energy and vibrational entropy, S_{conf} is the configurational entropy, and V is the volume. The vibrational free energy at temperature T for a phonon with vibrational frequency ω is determined by the following Eq.¹⁹

$$F_{vib}(T, \omega) = \frac{1}{2} \hbar \omega + k_B T \ln \left(1 - e^{-\hbar \omega / k_B T} \right), \quad (2)$$

where \hbar and k_B are the Planck and Boltzmann constants, respectively. The configurational entropy for n defects on a surface with N sites is expressed as

$$S_{conf} = k_B \ln \left(\frac{N!}{n!(N-n)!} \right)^{10}$$

Since the experiments were conducted under ultrahigh vacuum, the contribution of the last term in Eq. (A1) is negligible. We considered four possible processes for Pd segregation, as shown in Figure 2.7a. In process **I**, a Pd atom segregates from the subsurface layer to the surface layer by exchanging its position with a surface Fe atom. This leads to Pd enrichment in the surface layer as observed in our experiment. Processes **II**, **III** and **IV** are designed to understand the formation of ensembles of Pd adatoms on the terraces by taking Pd atoms from the bulk, surface and step edge, respectively.

First, we found that the change of total energy per Pd atom through process **I** is $\Delta E_I = -0.23$ eV, which indicates an exothermic process. The surface energy of Fe is much higher than that of Pd¹⁸ and segregation of Pd to the surface layer reduces the surface energy of the system. By minimizing $G(T,p)$ in Eq. (A1), we obtained the temperature dependence of the Fe concentration (θ_{Fe}) in the surface layer as

$\theta_{Fe} = [\exp(\Delta E_A + F_{vib})/k_B T + 1]^{-1}$, which is plotted as the black line in Figure 2.7c. In the temperature range of 900-1500 K, we see that θ_{Fe} increases almost linearly from 5 to 14%. At 1200 K, the calculated value of θ_{Fe} is about 0.11 ML, which is consistent with that observed in the experimental measurements. When Pd adatoms are present, the interaction between Pd and Fe decreases the surface energy of Fe, causing θ_{Fe} to increase.

In order to address the energetics of processes **II**, **III** and **IV**, we first investigated the stability of a Pd monomer and dimer on the Pd₃Fe(111) surface, considering cases with 0 to 3 Fe atom(s) under the Pd adatom(s). We found that a Pd monomer prefers a bridge site between two neighboring surface Fe atoms as shown in Figure 2.7b. For this

case, we found that formation of a Pd monomer through all three processes is endothermic. Particularly, the energy costs for processes **II** and **III** are as high as $\Delta E_{\text{II}} = 2.0$ eV and $\Delta E_{\text{III}} = 1.57$ eV, respectively. Therefore, these processes should hardly occur even at high temperature. In contrast, the energy cost for an edge Pd atom to become an adatom through process **IV** is $\Delta E_{\text{IV}} = 0.75$ eV and the probability for an edge Pd atom to dissociate is already reasonably high at 1200 K. This energy is further reduced by about 0.04 eV/atom when two Pd monomers bind together to form a dimer (see Figure 2.7b). Therefore, we believe that Pd adatom ensembles observed in our STM images are formed mainly through process **IV** as depicted in Figure 2.7a. Using the calculated total energies for a Pd monomer and dimer with configurations shown in Figure 2.7b, we estimate from Eq. (A1) that the equilibrium concentration of Pd adatoms on Pd₃Fe(111), including Pd monomers and dimers, is about 0.21 ML at 1200 K. This is slightly larger than the experimental measurement of 0.17-ML Pd, as might be expected because some Pd adatoms may aggregate to the step edge again during cooling. In Figure 2.7c, one can see that the population of Pd adatoms is a steep function of temperature around 1200 K, mainly due to the enhanced contributions of vibrational free energy and configurational entropy at high temperature.

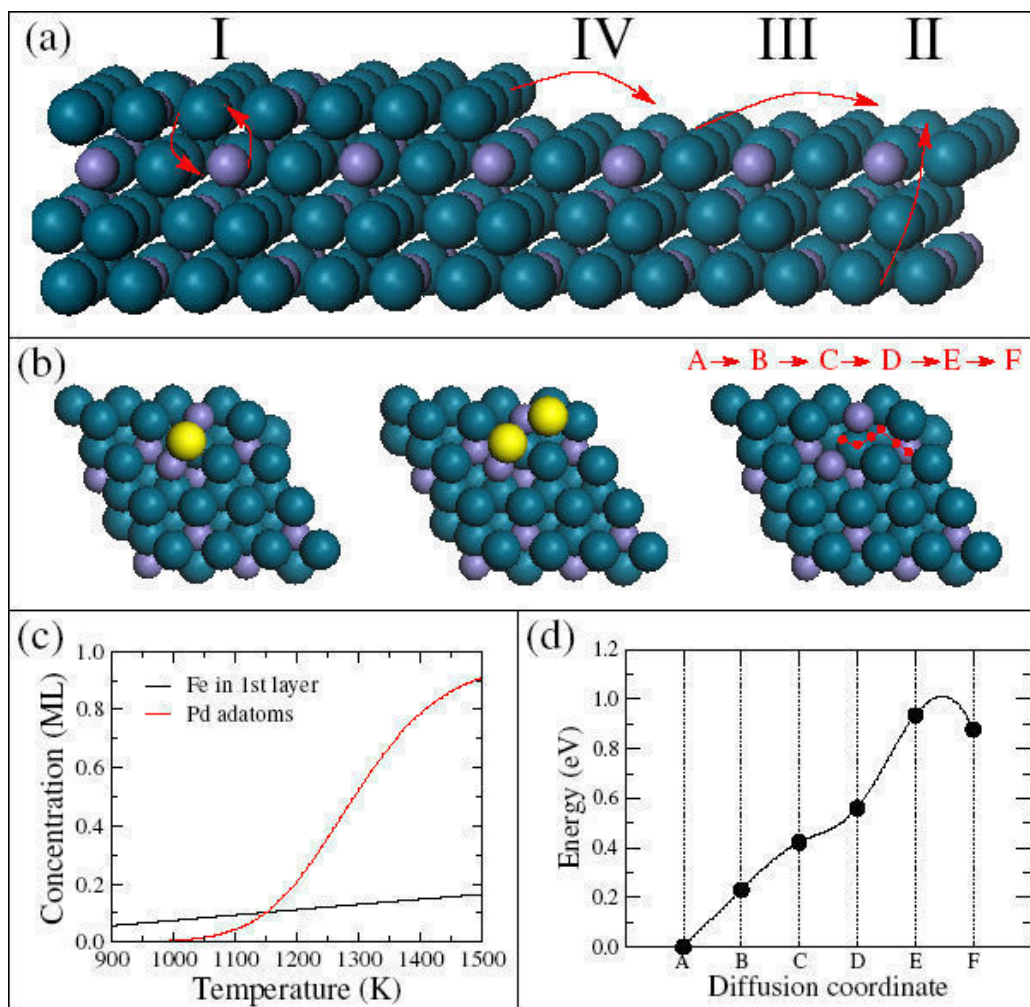


Figure 2.7 Theoretical modeling of the origin and surface structure of Pd adatoms. (a) Schematic of the segregation processes considered here. Dark cyan and medium purple balls correspond to Pd and Fe atoms, respectively. (b) Schematic view of the adsorption configurations of Pd adatoms as a monomer (left) and dimer (middle). The right schematic shows the diffusion path of the Pd monomer moving from site **A** to site **F**. The red dots from left to right correspond to sites **A**, **B**, **C**, **D**, **E** and **F** in sequence. Yellow balls correspond to Pd adatoms. (c) Optimal concentration of Fe in the surface layer and Pd adatoms on the surface as a function of temperature. (d) Total energy changes when a Pd monomer adatom diffuses along the path shown in (b). Dark filled circles show the calculated energies and the line is a curve obtained by using cubic spline interpolation.

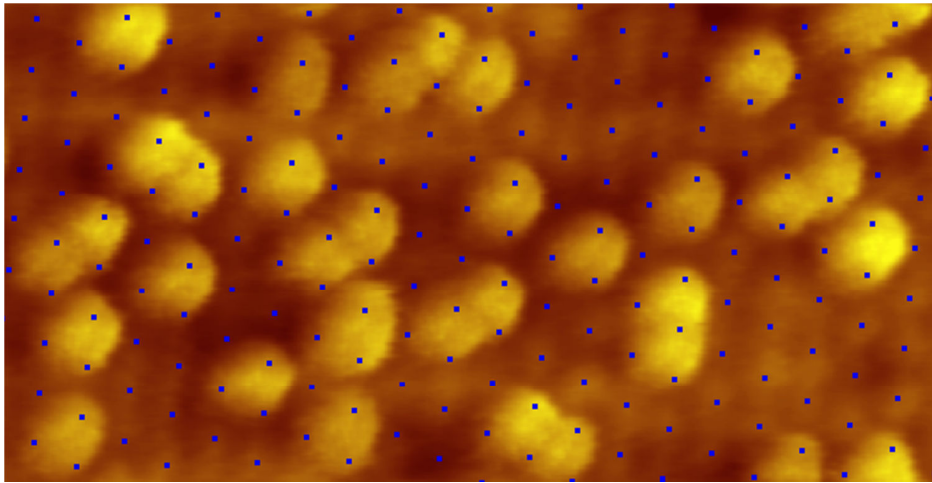
It is known that metal atoms are mobile on close-packed metal surfaces at elevated temperatures. Hence, the stability of Pd adatoms on Pd₃Fe(111) during cooling to room temperature is another important experimental observation to understand by using DFT calculations. Since the diffusion energy barrier of Pd adatoms on Pd(111) is just 0.35 eV,²⁰ the stability of Pd adatoms on Pd₃Fe(111) at room temperature is mainly governed by the diffusion of Pd adatoms out of the vicinity of surface Fe. This process can be represented by the diffusion from the ground-state site (A) to a hollow site over three surface Pd atoms (F), as shown in Figure 2.7b. Interestingly, the energy barrier for this diffusion is about 1.0 eV, which means that diffusion of the Pd monomer is "blocked" at room temperature. In addition, diffusion of a Pd dimer is harder than that of a Pd monomer, so Pd dimers are even more stable during the cooling process. This high stability of Pd adatoms on the Pd₃Fe(111) surface hinders the back diffusion of Pd toward step edges, as occurs on other surfaces. The origin of this "blocking" effect should be assigned to the large difference between Pd-Pd and Pd-Fe interactions.

Nearly quantitative agreement between theory and experiment validates our models. One can see that the exact structure and composition of a bimetallic surface, such as for Pd₃Fe(111) here, might be governed by small energy differences, *e.g.*, ~0.23 eV/atom. Synergistic exploration using experimental and theoretical approaches as described here are essential for the identification of segregation pathways and provide opportunities for the fabrication of optimized bimetallic surfaces for practical applications.

We propose a schematic model, which is shown in Figure 2.8B, to help visualize the surface structure of the adatoms and top alloy layer. As we have discussed, all

adatoms are Pd, and so 0.1-ML Fe as determined by LEIS must be within the topmost (first) alloy layer. Figure 2.7b shows the two most stable configurations for a Pd monomer and Pd dimer, as determined by DFT total energy calculations. In each case, there are two Fe atoms in the first layer contacting the Pd adatoms, so the Fe concentration in the first layer should be slightly larger than the concentration of Pd adatoms (0.17 ML). We know that shadowing and blocking effects by Pd adatoms reduce the Fe signal in LEIS, and the measured value of only 0.1-ML Fe must reflect this. The schematic model shown in Figure 2.8B directly corresponds to the STM image shown in Figure 2.8A with 32 Pd adatoms and satisfies the requirement that all Pd adatoms contact Fe atoms in the first layer. This model illustrates that the surface energy of Pd₃Fe(111) with Pd adatoms is lowered by heteroatomic interactions between Pd and Fe at the surface. Observations that Fe prefers to be in the second layer after annealing Fe films deposited on a pure Pd(111) crystal, as shown in Figures 2.9 and 2.10, provide additional support for this conclusion. Strong heteroatomic interactions are also found in other more extensively studied Pd alloy systems, *e.g.*, Pd/Ni alloys, where Pd segregation increases the amount of Pd in the first (topmost) layer on the (111) and (100) surfaces and Ni enrichment occurs in the second layer. The oscillating interlayer chemical ordering is caused by attractive Ni–Pd interactions.^{21,22} A high stability of metal adatoms caused by such heteroatomic interactions has also been reported for Ir-Rh²³ and Pd-Pt systems.²⁴

A.



B.

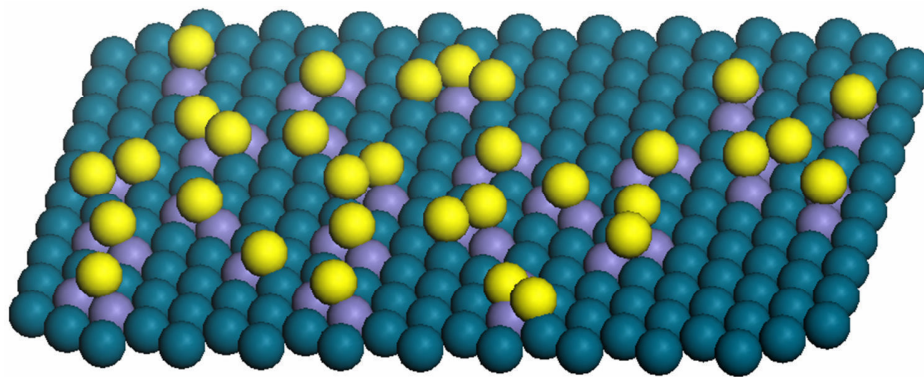


Figure 2.8 Configurations of 32 Pd adatoms on Pd₃Fe (111) and a corresponding schematic model including the structure of the first layer. A. An *fcc* lattice is superimposed on the STM image to show the positions of first-layer atoms B. Schematic view of an incomplete adlayer that corresponds to the STM image, with bright yellow balls representing Pd adatoms and dark cyan and medium purple balls corresponding to first-layer Pd and Fe atoms, respectively. We are unable to determine Fe atom concentration and position in the first layer directly from the STM image, but the Fe positions indicated are optimized, based on DFT calculations, to fit the Pd adatoms configurations in A.

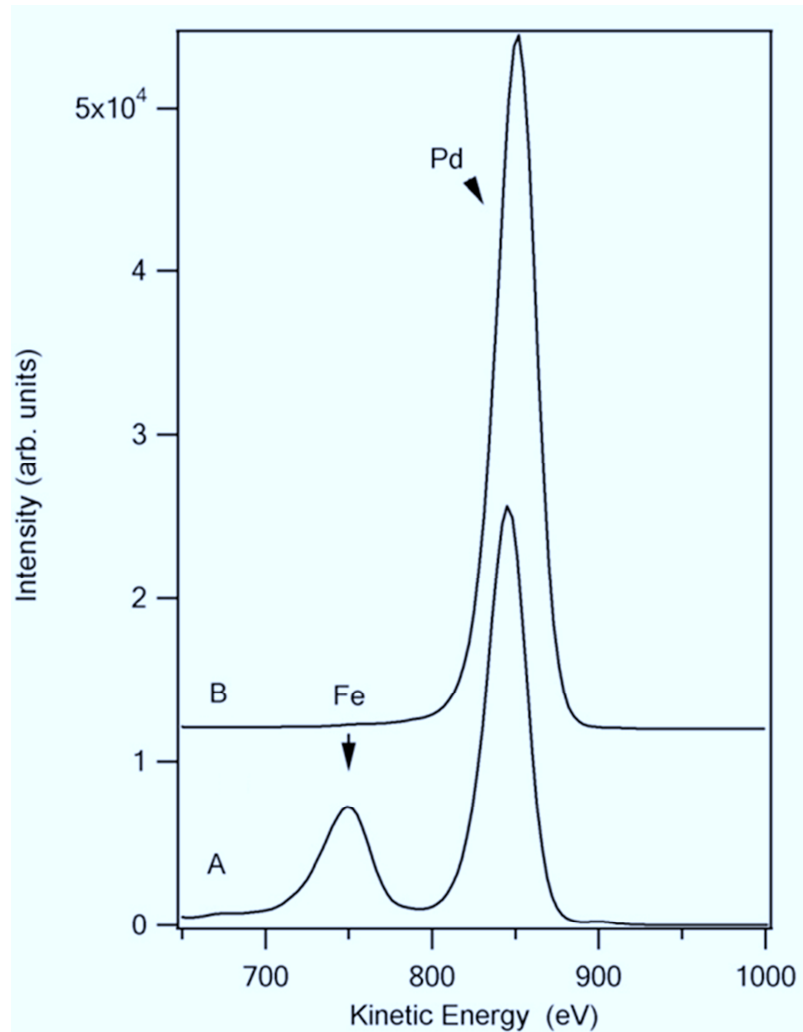


Figure 2.9 Surface composition of Fe deposited on Pd(111) studied by LEIS. A. After dosing 0.5-ML Fe on Pd(111) at 300K. B. After sample in (A) was annealed to 1100 K. The Fe peak disappeared due to Fe diffusion into the subsurface region to produce a pure-Pd top layer. LEIS spectra obtained with $E_i=1000$ eV, 3 nA.

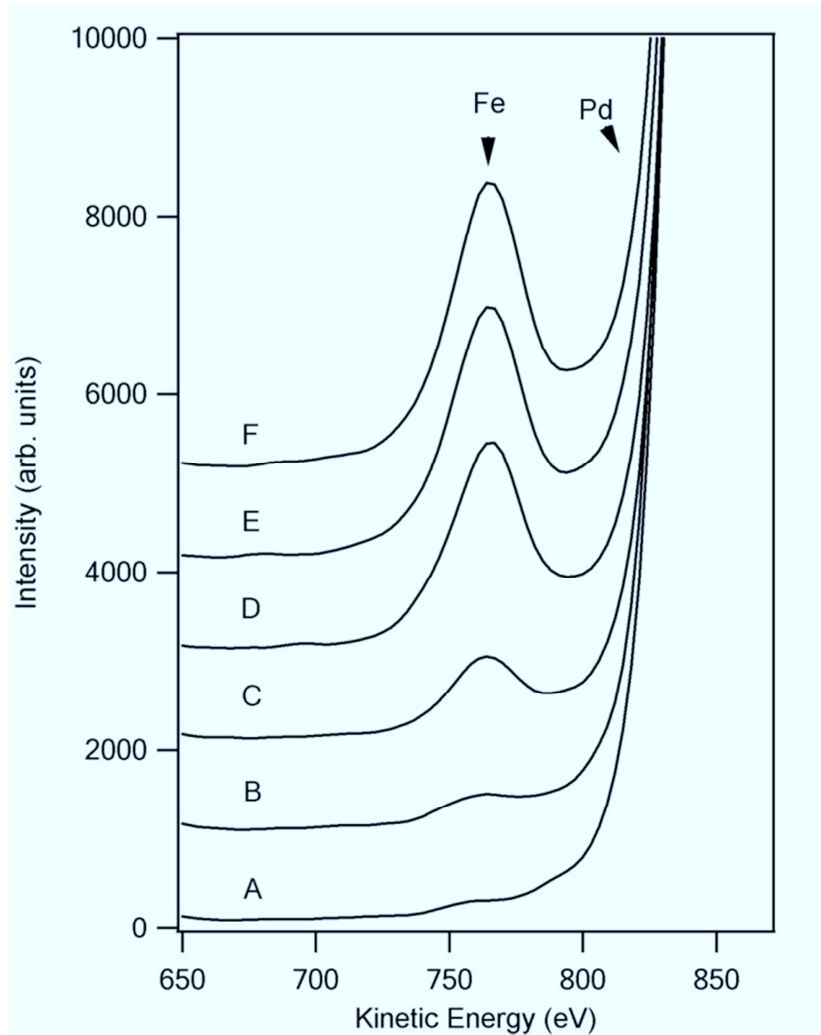


Figure 2.10 Surface composition of Fe deposited on Pd(111) and sputtering effect studied by LEIS. A. After dosing 0.5-ML Fe on Pd(111) at 300K and then annealing to 1100 K. All Fe diffused into the subsurface region. LEIS curves in B to F were obtained for increasing He^+ ion exposures with the sample at room temperature: B. 5 min, B. 10 min, C. 20 min, E. 40 min, and F. 80 min. The amount of surface sputtering by the incident He^+ beam increases with time and caused Fe peaks to appear and increase in intensity. These results show that the Fe that was initially deposited on the surface diffused into the near surface region, mostly likely in the second layer. The LEIS spectra obtained with $E_i=1000$ eV, 3 nA.

Pd 3d and Fe 2p core levels in the XPS spectra, shown in Figures 2.11, 2.12, reveals that the surface electronic structure is altered after segregation. We believe that both ensemble effects and modification of electronic properties should contribute to its enhanced electrocatalytic activity to ORR reaction.

In addition, studies of the interactions of oxygen at these surfaces are vital to improving our understanding of the improved ORR performance for these alloys and are reported in a Chapter 3. Critical steps in the oxygen reduction process are the adsorption of an oxygen molecule and cleavage of the O-O bond. The surface Fe beneath Pd adatoms is a relatively active metal and beneficial to breaking the O-O bond. Our measurements of oxidation of Pd₃Fe (111) in UHV show that only Fe is oxidized, as shown in Figure 2.13 It seems reasonable that adsorbed oxygen adatoms at an Fe site, O_{ads,Fe}, can migrate to Pd adatom sites and be reduced to water in electrochemical environments. Since Fe atoms are partly protected by Pd adatoms, they should be less affected by dissolution in acidic electrolytes, and this may also be a factor in why the annealed Pd-Fe alloy electrode is stable in acidic media^{5,25}.

A.

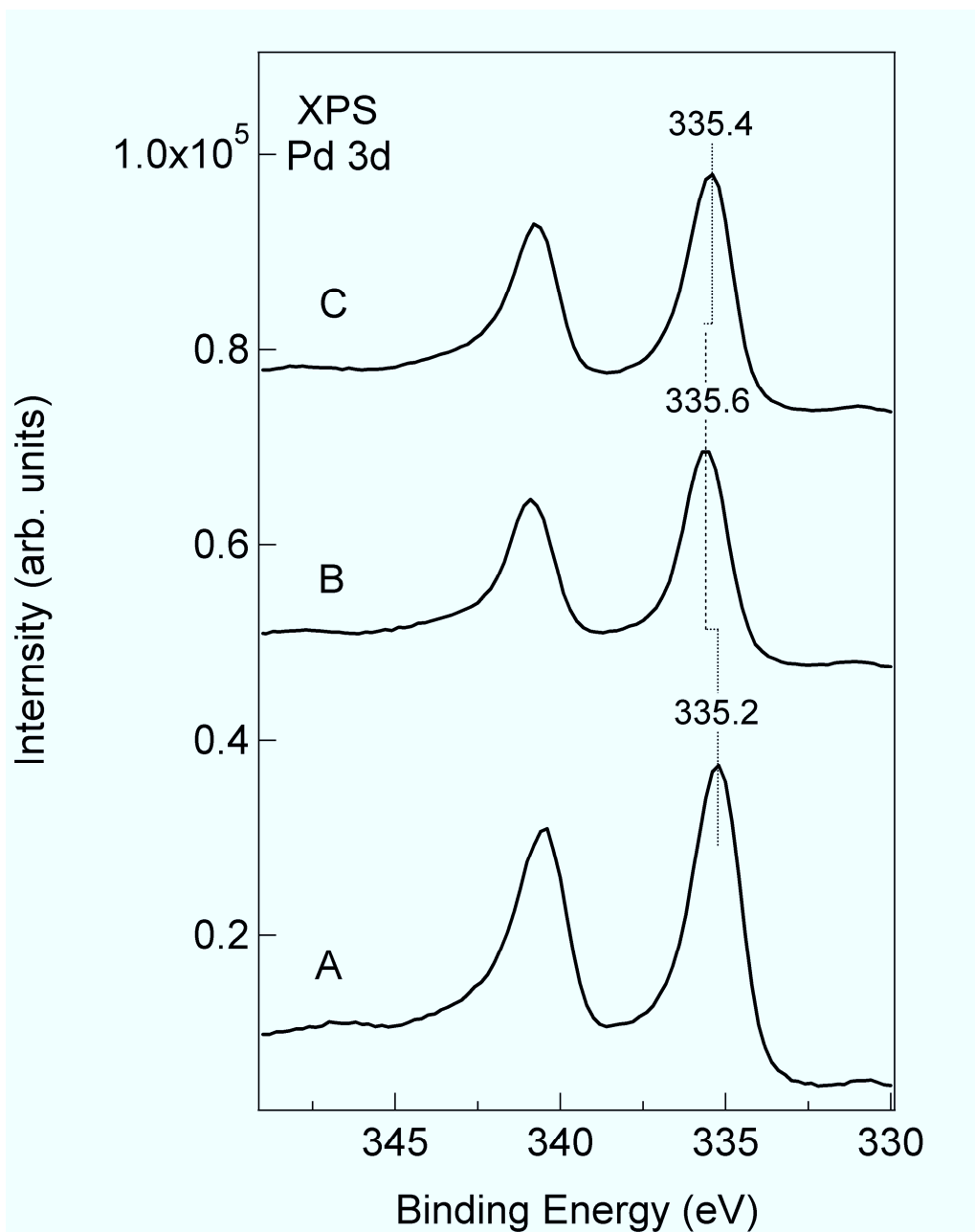


Figure 2.11 XPS spectra for Pd 3d core levels. A. Pure metal Pd, B. Pd₃Fe(111) after sputtering, and C. Pd₃Fe(111) after annealing at 1200K. XPS conditions are: X-ray: 20 mA, 15 kV Al K α , pass energy: 20 eV, energy step: 0.2 eV, dwell time: 0.5s and 2 scans.

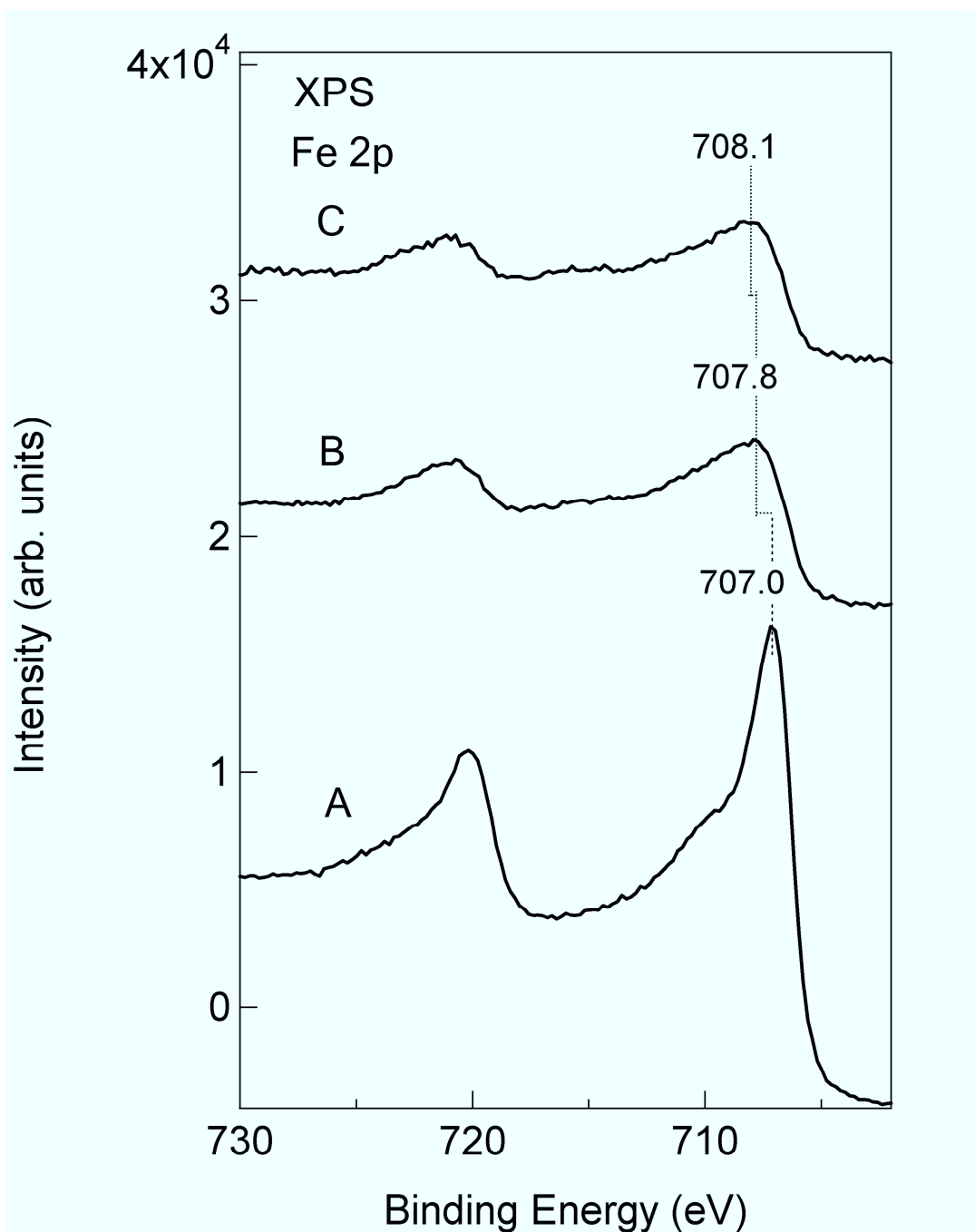


Figure 2.12 XPS spectra for Fe $2p$ core levels. A. Pure metal Pd or Fe, B. $\text{Pd}_3\text{Fe}(111)$ after sputtering, and C. $\text{Pd}_3\text{Fe}(111)$ after annealing at 1200K. XPS conditions are: X-ray: 20 mA, 15 kV Al $K\alpha$, pass energy: 20 eV, energy step: 0.2 eV, dwell time: 0.5s and 5 scans.

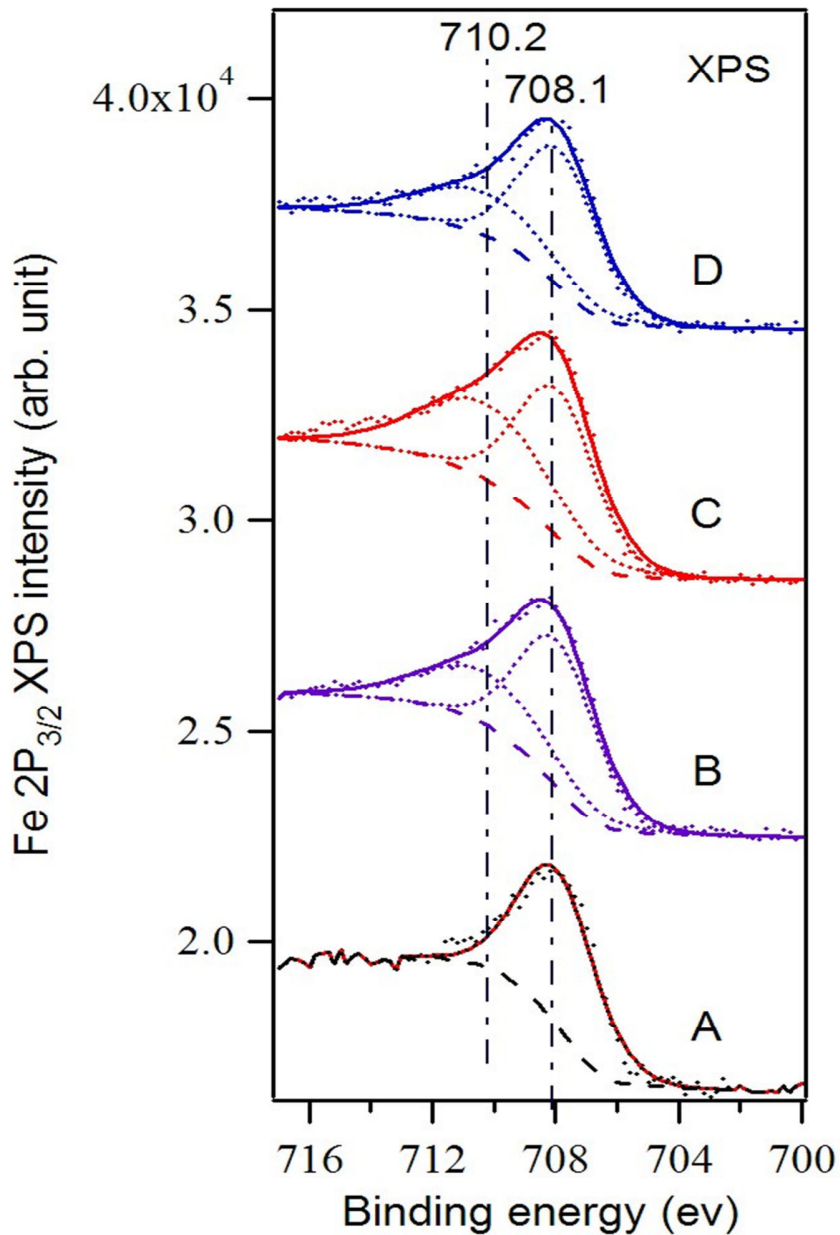


Figure 2.13 XPS spectra of the Fe $2p_{3/2}$ peak for $\text{Pd}_3\text{Fe}(111)$ after oxidation. A. clean surface B. after 15L O_2 at 800 K; C. after 15L O_2 at 950 K; D. after 15L O_2 at 800 K, and flashed to 1000 K. The peak at 710.2 eV is due to oxidation of Fe. No oxidized Pd peak was observed in Pd 3d spectra. XPS conditions are: X-ray: 20 mA, 15 kV Al $K\alpha$, pass energy: 20 eV, energy step: 0.2 eV, dwell time: 0.5s and 5 scans.

2.4 Conclusions

We have discovered an unusual structure for the clean, annealed Pd₃Fe(111) surface by using a combination of LEED, LEIS and STM. Palladium atoms segregate to the surface during annealing to 1200 K and cooling to room temperature forms a surface with Pd monomers and dimers on top of the first layer. Such a Pd adatom structure is unusual, but is thought to stem from the low surface free energy of Pd and an increased stability of Pd adatoms through localized heteroatomic interactions between Pd and Fe. Theoretical calculations by DFT were used to account for the stability and formation of Pd adatoms on this surface, identifying that the most likely sources of Pd adatoms are edge atoms of terraces. The specific chemistry and catalysis at this surface deserves more attention in order to explore the possible chemical and physical properties of these Pd monomers and dimers. Observation of this unusual surface structure should contribute to an improved understanding of heterogeneous catalysis by Pd-based alloys.

2.5 References

1. Bertolini, J. C.; Rousset, J. L.; Miegge, P.; Massardier, J.; Tardy, B., On the large Pd surface segregation and reactivity of Pd₁Fe₉₉ and Pd₅Fe₉₅ dilute alloys. *Surf. Sci.* **1993**, *287/288*, 346-349.
2. Bachir, R.; Marecot, P.; Didillon, B.; Barbier, J., Isoprene hydrogenation on supported Pd-Fe catalysts: Influence of the catalyst preparation procedure. *Appl. Catal., A* **1997**, *164*, 313-322.
3. Guzzi, L., Structural effect of bimetallic catalysts in the Co+H₂ reaction. *Stud. Surf. Sci. Catal.* **1988**, *38*, 85-96.
4. Shao, M.-H.; Sasaki, K.; Adzic, R. R., Pd-Fe nanoparticles as electrocatalysts for oxygen reduction. *J. Am. Chem. Soc.* **2006**, *128* (11), 3526-3527.
5. Zhou, W.-P.; Yang, X.; Vukmirovic, M. B.; Koel, B. E.; Jiao, J.; Peng, G.; Mavrikakis, M.; Adzic, R. R., Improving electrocatalysts for O₂ reduction by fine-tuning the Pt -support interaction: Pt monolayer on the surfaces of a Pd₃Fe(111) single-crystal alloy. *J. Am. Chem. Soc.* **2009**, *131* (35), 12755-12762.
6. Shao, M.; Liu, P.; Zhang, J.; Adzic, R., Origin of enhanced activity in palladium alloy electrocatalysts for oxygen reduction reaction. *J. Phys. Chem. B* **2007**, *111* (24), 6772-6775.
7. Bertolini, J. C.; Jugnet, Y., Chapter 11 Surface structure and catalytic reactivity of palladium overlayers for 1,3-butadiene hydrogenation. In *The Chemical Physics of Solid Surfaces*, Woodruff, D. P., Ed. Elsevier: 2002; Vol. Volume 10, pp 404-437.
8. Rodriguez, J. A., Chapter 12 Electronic and chemical properties of palladium in bimetallic systems: How much do we know about heteronuclear metal-metal bonding? In *The Chemical Physics of Solid Surfaces*, Woodruff, D. P., Ed. Elsevier: 2002; Vol. Volume 10, pp 438-465.
9. Baddeley, C. J., Chapter 14 Adsorbate induced segregation at bimetallic surfaces. In *The Chemical Physics of Solid Surfaces*, Woodruff, D. P., Ed. Elsevier: 2002; Vol. Volume 10, pp 495-526.

10. Schmid, M.; Varga, P., Chapter 4 Segregation and surface chemical ordering--an experimental view on the atomic scale. In *The Chemical Physics of Solid Surfaces*, Woodruff, D. P., Ed. Elsevier: 2002; Vol. Volume 10, pp 118-151.
11. Kresse, G.; Furthmüller, J., Efficiency of ab-initio total energy calculations for metals and semiconductors using a plane-wave basis set. *Comput. Mater. Sci.* **1996**, *6* (1), 15-50.
12. Winterrose, M. L.; Lucas, M. S.; Yue, A. F.; Halevy, I.; Mauger, L.; Munoz, J. A.; Hu, J.; Lerche, M.; Fultz, B., Pressure-induced invar behavior in Pd₃Fe. *Phys. Rev. Lett.* **2009**, *102*, 237.
13. Creemers, C., Dual mode segregation of Pd to the surface of polycrystalline Fe₉₉Pd₁. *Surf. Sci.* **1996**, *360*, 10-20.
14. Schmid, M.; Varga, P., *Segregation and surface chemical ordering an experimental view on the atomic scale ch.4*. Elsevier Science B.V.: Amsterdam, The Netherlands, 2002; Vol. 10, p 118-151.
15. Schmid, M.; Stadler, H.; Varga, P., Direct observation of surface chemical order by scanning tunneling microscopy. *Phys. Rev. Lett.* **1993**, *70*, 1441-1444.
16. Creemers, C.; Deurinck, P., Platinum segregation to the (111) surface of ordered Pt₈₀Fe₂₀ : LEIS results and model simulations. *Surf. Interface Anal.* **1997**, *25*, 177-189.
17. Bartels, L.; Meyer, G.; Rieder, K. H., Basic steps of lateral manipulation of single atoms and diatomic clusters with a scanning tunneling microscope tip. *Phys. Rev. Lett.* **1997**, *79*, 697-700.
18. Ruban, A. V.; Skriver, H. L.; Nørskov, J. K., Surface segregation energies in transition-metal alloys. *Phys. Rev. B: Condens. Matter* **1999**, *59*, 15990.
19. Reuter, K.; Scheffler, M., Composition, structure, and stability of RuO₂(110) as a function of oxygen pressure. *Phys. Rev. B: Condens. Matter* **2001**, *65*, 035406.
20. Steltenpohl, A.; Memmel, N., Self-diffusion on Pd(111). *Surf. Sci.* **2000**, *454-456*, 558-561.
21. Derry, G. N.; McVey, C. B.; Rous, P. J., The surface structure and segregation profile of Ni₅₀Pd₅₀(100): a dynamical LEED study. *Surf. Sci.* **1995**, *326* (1-2), 59-66.

22. Derry, G. N.; Wan, R., Comparison of surface structure and segregation in AgAu and NiPd alloys. *Surf. Sci.* **2004**, 566-568 (Part 2), 862-868.
23. Kellogg, G. L., Direct observation of substitutional-atom trapping on a metal surface. *Phys. Rev. Lett.* **1994**, 72 (11), 1662.
24. Fallis, M. C.; Wright, A. F.; Fong, C. Y.; Daw, M. S., Trapping of a diffusing adatom by a substitutional surface defect. *Surf. Sci.* **1994**, 311 (3), L717-L723.
25. Koper, M. T. M., *Fuel cell catalysis - a surface science approach ch.9*. John Wiley & Sons, Inc.; Hoboken, New Jersey, 2009.

2.6 Appendix

Pd Segregation on Pd₃Fe (111) surface: Two-stage model

All the calculations were carried out with the Vienna ab initio simulation program (VASP)¹ using the projector augmented wave (PAW) method² and the generalized-gradient approximation (GGA) in parameterization by Perdew, Burke and Ernzerhof (PBE)³. The cutoff energy of plane waves was set to 300 eV. Spin polarization was considered for all cases. The optimized lattice constant was calculated to be 3.877 Å, and the magnetic moments of Fe and Pd was calculated to be 3.33 and 0.32 μ_B respectively. These results are consistent with both experimental measurement and LDA calculations.⁴

We first calculate the surface segregation energy (E_{segr}) following the conventional concept of segregation in metal alloys^{5,6} by exchanging the surface Fe atoms with the Pd atoms in the inner layer. E_{segr} is defined as:⁶

$$E_{segr} = E(111),\lambda - E(111), \quad (A1)$$

where $E(111),\lambda$ is the total energy of a Pd₃Fe (111) slab with a surface Fe atom exchanged with a Pd atom of the λ^{th} layer, while $E(111)$ is the total energy of unchanged slab. From the definition, we can see that a negative (positive) E_{segr} suggests the exchange is favorable (unfavorable). Employing a 6-ML slab, the value of E_{segr} for $\lambda = 2$ and 3 are -0.23 and 0.06 eV, respectively. Therefore, the Fe atoms in the surface (1st) layer prefer to exchange with the Pd atoms in the second (2nd) layer, but do not like to exchange with the Pd atoms in the third (3rd) layer. In other words, the Pd atoms in the 2nd layer tend to segregate to the 1st layer, and the segregation occurs within the two topmost atomic layers. Given that a Fe atom in the 1st layer leads to increment of total energy of 0.23 eV,

for an N -atom surface layer with n Fe atoms, the increment of Gibbs free energy at temperature T , $T[\Delta G(T,n)]$, is given by ⁶

$$\Delta G(T, n) = 0.23n - k_B T \cdot \ln \left(\frac{N!}{(N-n)!n!} \right) \quad (\text{A2})$$

where k_B is the Boltzmann constant, The last term of Eq. (A2) is the contribution of configurational entropy. The equilibrium condition requires that the derivative of $\Delta G(T,n)$ with respect to n equals zero. Then we obtain the equilibrium concentration of Fe atoms in the 1st layer at temperature T as ⁶

$$\frac{n}{N} = \frac{1}{\exp(0.23/k_B + 1)} \quad (\text{A3})$$

The results are consistent with the experimental observation: 0.1 ML of Fe atoms in the 1st layer after annealing at 1200 K. Note that from Eq. (A3) the concentration of Fe atoms in the 1st layer increases as temperature increases, which is opposite to experimental observations. This is because in Eq. (A3) the system is assumed to be in equilibrium. But in our experiments, equilibrium conditions may not be achieved at the low temperatures involved.

We calculate Pd adatom adsorption sites on a Pd₃Fe (111) surface using a 5ML slab. The most favorable configurations of Pd monomer, dimer and trimer are shown in Figure A1. Taking Pd gas as the source of the adatoms, the adsorption energies (E_{ad}) of Pd monomer, dimer and trimer in the sequence shown in Fig. A1 are -2.84, -3.04, -3.03 and -3.14 eV per Pd atom, respectively. Note that the energy difference between the two configurations of Pd dimers in Fig. A1 (b) and (c) is just 10 meV per Pd atom, so we

deem that these configurations exist at comparable concentrations at room temperature.

Moreover, the calculations indicate that the Pd adatoms tend to congregate.

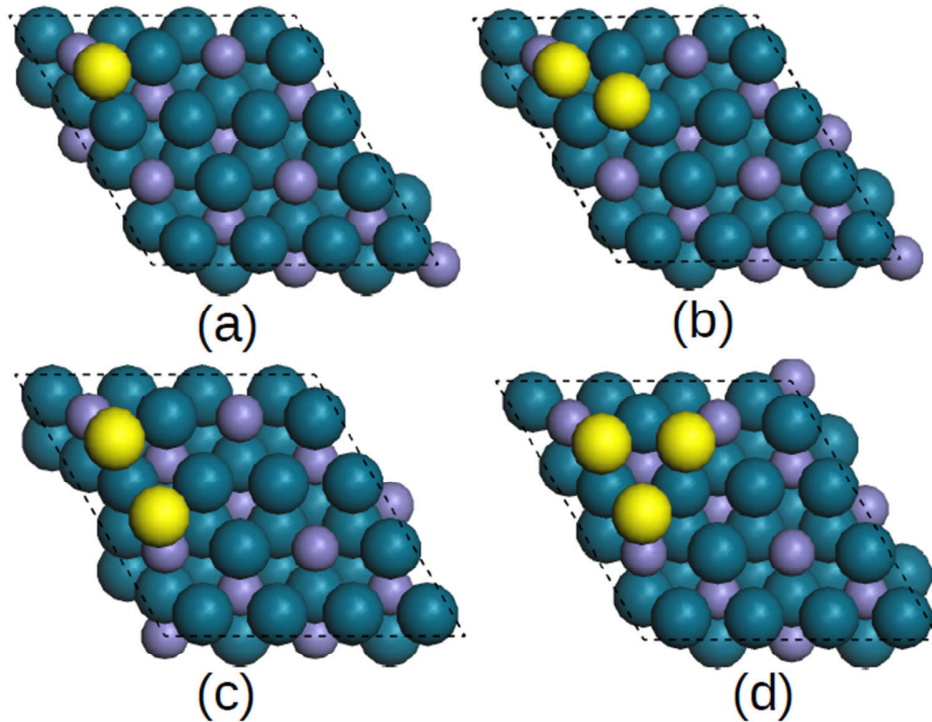


Fig .A1 Configurations of Pd monomer, dimer and trimer adsorbed on a Pd₃Fe (111) surface.

The dark cyan, medium purple and yellow balls correspond to Pd and Fe in the surface layers and adsorbed Pd atoms, respectively.

One may speculate that the Pd adatoms come from a bulk or surface layer, leaving a vacancy there. Consequently, we calculate the formation energies (E_{form}) of bulk and surface vacancies. Values of E_{form} for these vacancies as well as that for a single Pd adatom on a Pd₃Fe (111) surface are plotted in Fig. A2. The total energy cost to move a bulk or surface Pd atom to an adsorption site is as large as 2.24 or 1.81 eV, respectively,

which implies that this process is not likely even at high temperature (such as 1200 K in the experiment). Therefore, there must be another source of the Pd adatoms observed experimentally.

It is notable that there are terraces in a real sample used in the experiments. The edge atoms of a terrace may also be a source of Pd adatoms. Therefore, we constructed a 7×2 slab and removed one-half of the surface atoms to model a terrace, as shown in Fig. A3. Then we calculate E_{form} to remove edge Pd atoms, *i.e.*, E_{form} of edge vacancies. To prevent creating an edge Fe atom after removing the edge Pd atoms, we replace all Fe atoms by Pd atoms in the second atomic row of the terrace. Note that in an unit cell of the terrace, there are four Pd atoms. Hence removing one Pd atom results in 25% vacancies in the edge row, while removing four Pd atoms leads to 100% vacancies. As shown in Fig. A3, removing an entire row of the terrace is more favorable than removing part of the row. Furthermore, the total energy cost for an edge-Pd atom diffusing to the terrace to form an adatom is at least 0.99 eV. This reasonably low energy greatly increases the likelihood of this process. Therefore, we conclude that the edge of a terrace is the most probable source of Pd adatoms.

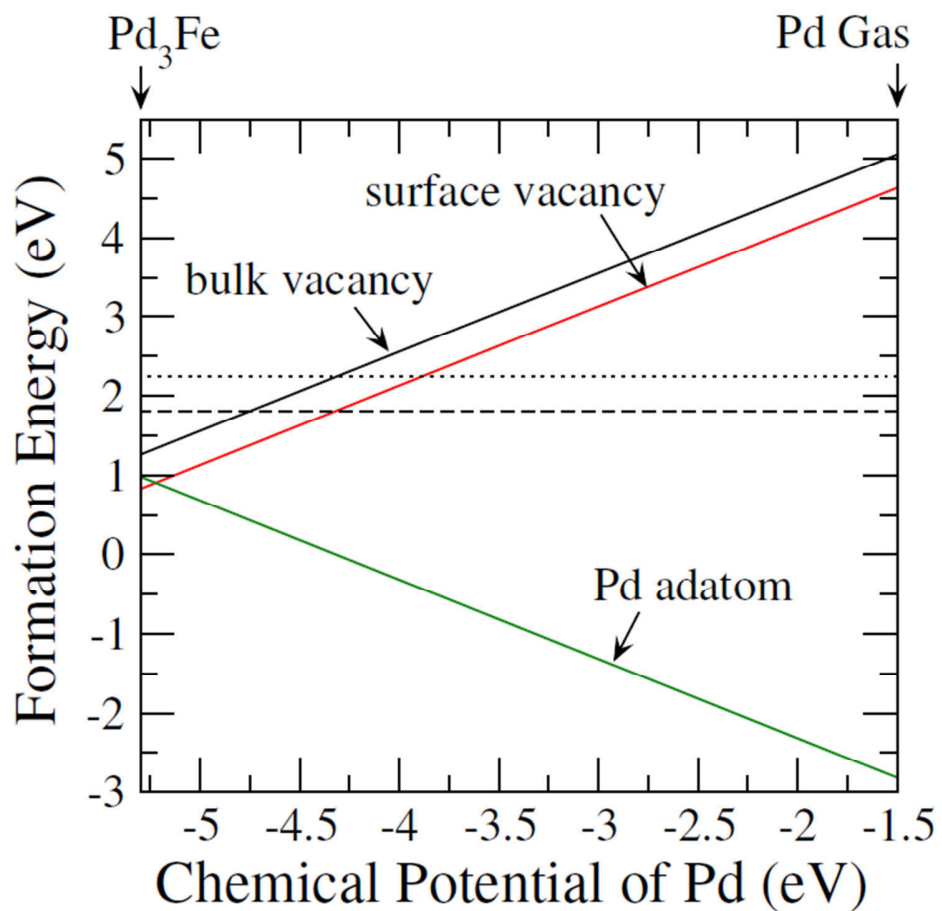


Fig. A2. Formation energies of bulk and surface vacancies, as well as a single Pd adatom on Pd₃Fe (111) surface. The Pd chemical potential varies between Pd₃Fe bulk and Pd gas. The dotted (dashed) horizontal line is the sum of the formation energy of a bulk (surface) vacancy and a Pd adatom.

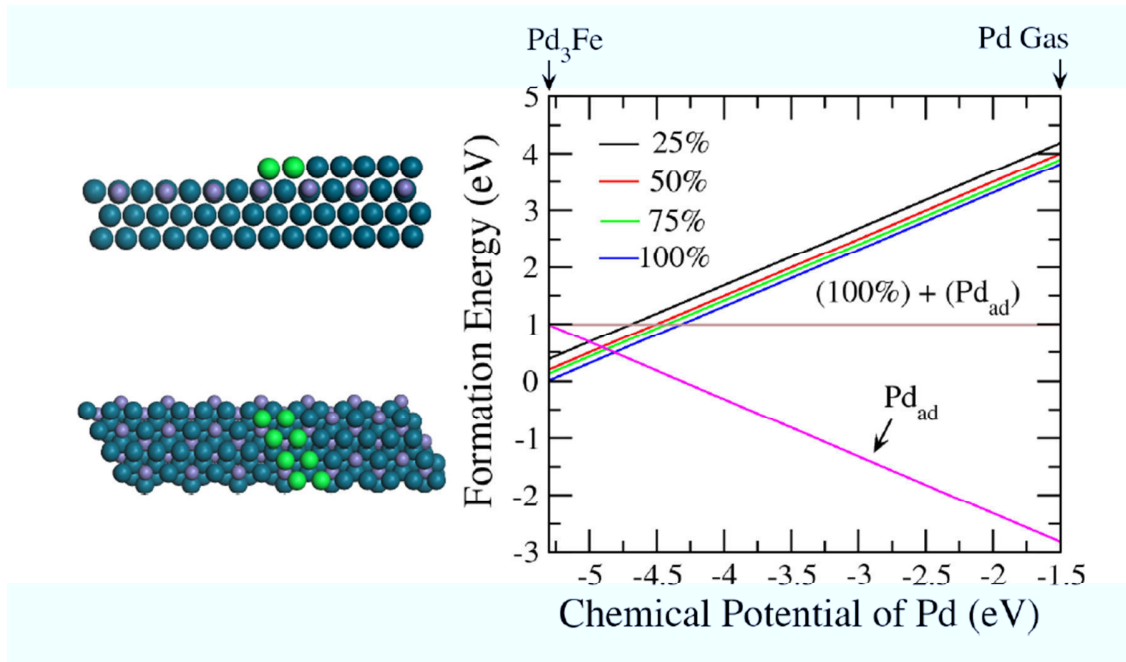


Fig. A3. Left top and left bottom are side and top views, respectively, of a structural model of a terrace. The dark cyan, medium purple and light green balls denote host Pd, host Fe and edge Pd atoms, respectively. The plot on the right gives the formation energies of edge vacancies as well as a single Pd adatom on a Pd₃Fe (111) surface.

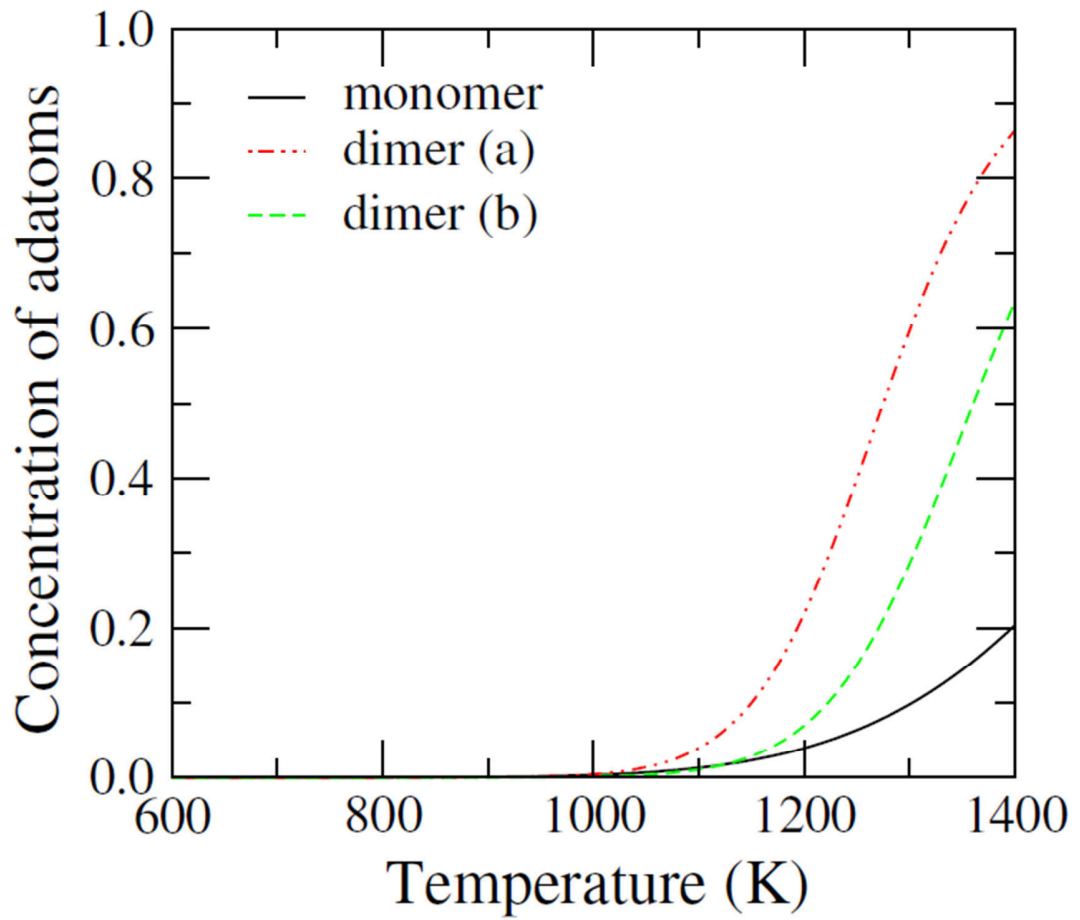


Fig. A4. The concentrations of Pd adatoms as function of temperature. The monomer, dimer (a) and dimer (b) correspond to the configurations shown in Fig. 1 (a), (b) and (c), respectively.

Considering n edge-Pd atoms become Pd adatoms, the change of Gibbs free energy of the system can be expressed as

$$\Delta G(T, n) = \Delta E_{tot} + \Delta F_{vib}(T) - TS_{conf} \quad (\text{A4})$$

Where, ΔE_{tot} and ΔF_{vib} are the changes in the total energy and vibrational free energy, respectively, and last term is the contribution of the configurational entropy. Similar to Eq. (A3), we can obtain the equilibrium concentration of Pd adatoms as

$$\frac{n}{N} = \frac{1}{\exp(\varepsilon_1 + \varepsilon_2)/k_B T + 1} \quad (\text{A5})$$

where N is total number of surface atom, n is the total of Fe surface atoms, and ε_1 and ε_2 are the contributions of each Pd adatom to the total energy and the vibrational free energy.

We used Eq. (A5) to calculate the concentrations of Pd monomers and dimers on the Pd₃Fe(111) surface as shown in Fig. A4. We presume that the Pd trimer will be dissociated at high temperatures, so we did not consider it. It can be seen that almost no Pd adatoms exist on the surface under 1000 K, while at higher temperature the concentrations of Pd adatoms, especially the Pd dimers, increase very fast. At 1200 K, the concentrations of monomer, dimer (a) and dimer (b) are 0.039, 0.218 and 0.069, respectively. Note that these concentrations were obtained by assuming that there is just one type of Pd adatoms. Actually, these adatoms may coexist, given by the probabilities, p_i , where

$$p_i = \frac{\exp(-\varepsilon_i/k_B T)}{\sum_j \exp(-\varepsilon_j/k_B T)} \quad (\text{A6})$$

where i is the total energy of the i th configuration. Finally, the total concentration of Pd adatoms at 1200 K is 0.139, which agrees with the experimental measurements of 0.165 ML of Pd adatoms.

In summary, the experimental observation of unusual Pd segregation can be explained by the two-stage model proposed in this work. This two-stage model consists of conventional segregation occurring within the two topmost layers and unconventional segregation occurring at the edge of terraces. Conventional segregation results in ~ 0.1 ML Fe in the surface layer at 1200 K, while unconventional segregation leads to ~ 0.14 ML Pd adatoms on the surface.

2.7 References for appendix

1. Kresse, G.; Furthmüller, J., Efficiency of ab-initio total energy calculations for metals and semiconductors using a plane-wave basis set. *Comput. Mater. Sci.* **1996**, *6* (1), 15-50.
2. Bl; ouml; chl, P. E., Projector augmented-wave method. *Phys. Rev. B* **1994**, *50* (24), 17953; (b)
3. Perdew, J. P.; Burke, K.; Ernzerhof, M., Generalized Gradient Approximation Made Simple. *Phys. Rev. Lett.* **1996**, *77* (18), 3865.
4. Winterrose, M. L.; Lucas, M. S.; Yue, A. F.; Halevy, I.; Mauger, L.; Mu; ntilde; oz, J. A.; Hu, J.; Lerche, M.; Fultz, B., Pressure-Induced Invar Behavior in Pd₃Fe. *Phys. Rev. Lett.* **2009**, *102* (23), 237202.
5. Ruban, A. V.; Skriver, H. L.; oslash; rskov, J. K., Surface segregation energies in transition-metal alloys. *Phys. Rev. B* **1999**, *59* (24), 15990.
6. Løvvik, O. M., Surface segregation in palladium based alloys from density-functional calculations. *Surf. Sci.* **2005**, *583* (1), 100-106.

Chapter 3 Determination of the Atomic Structure of Ultra-thin Metal

Oxides: Oxidation of a Single Crystal Pd₃Fe(111) Surface

3.1 Introduction

Noble metals (Pd, Pt) supported on reducible oxides (TiO₂, CeO₂, FeO_x) are important model catalysts to study strong metal–support interaction (SMSI), which modifies the electronic properties of the noble metals and affects their catalytic activities. Wetting and dewetting of metals oxides often occurs on metal surfaces, which has prompted people to study “inverted” catalysts, *i.e.*, thin film metal oxides supported on noble metals. Interestingly, these inverted catalysts can exhibit greatly enhanced catalytic activity comparing to the noble metals alone. For example, FeO_x/Pt(111) has been found to be highly active for selective CO oxidation,¹⁻² the oxygen reduction reaction³ and the water–gas shift reaction.⁴⁻⁵ A review paper on surface chemistry and catalysis on well-defined epitaxial iron-oxide layers is available.⁶ Inspired by the discoveries on FeO_x/Pt(111), it is of great interest to study the properties of FeO_x/Pd(111). To the best of our knowledge, there is no literature on FeO_x/Pd(111). The reason for that may be partially due to the difficulty in preparing FeO_x films on Pd surfaces. We found vapor-deposited Fe easily diffused into the bulk of the Pd(111) crystal upon annealing. To avoid this problem, a different way to prepare thin FeO_x films on Pd(111) is to take advantage of the segregation property of Fe in a bulk alloy of Pd₃Fe(111) in an oxidizing environment.

In this study, oxidation of Pd₃Fe(111) has been investigated by XPS, LEIS, LEED and STM. The objective of this work is not only to investigate the surface structure in an oxygen environment, but also to understand how the surface structure affects the chemical properties. We explored the atomic structure of a FeO(111) film on Pd₃Fe(111). A Moiré pattern from a superstructure with a periodicity of 19.74 Å was observed with STM. Upon annealing, ordered defects, possible missing Fe or O, were formed. The location of these defects coincided with specific locations in the Moiré superlattice of the FeO(111) layer. Oxygen vacancy defects are often the active sites for catalytic reactions, *e.g.*, CO oxidation on FeO/Pt(111).² Understanding the structure and formation mechanism for these defects should also be interesting for other catalytic reactions as well, such as water-gas shift reaction and Fischer-Tropsch reaction. Specifically, knowledge of the interaction between oxygen and the Pd₃Fe(111) surface may be useful to better understand the ORR mechanism in electrochemical environments.

3.2 Experimental methods

A custom UHV system (based on an STM instrument from RHK Technology, Inc.) consisting of two UHV chambers was used in this study. A base pressure of 2×10^{-10} torr was achieved before experiments. The preparation chamber, equipped with LEED, XPS, and LEIS, was used to clean and prepare the sample. STM measurements were done in the STM chamber after the surface was prepared. In LEED, which is used to study the surface structure of crystalline materials, a collimated beam of low energy electrons (20-200 eV) impinges on the crystal surface and the diffracted electrons appear as spots on a fluorescent screen. In this experiment, LEED patterns were measured and compared

before and after the sample oxidization. The incident electron beam energy was set to 55 eV and the emission current was set to 15 mA. XPS was used with an Al K α X-ray source with a photon-energy of 1486.7 eV. The settings of the energy analyzer were: pass energy = 20 eV, step size = 0.2 eV, and a full open iris aperture. The sample surface was perpendicular to the analyzer, which resulted in a 90 ° detection angle. The binding energy (BE) of all peaks was calibrated to Pt 4f_{5/2} at 71.3 eV BE. In the LEIS experiment, the geometrical position of the sample was same as it was in the XPS measurement. The ion source was 1 keV He⁺ with 3.0 nA incident current. The scattering angle of 130° and a normal detection angle were used. All measurements are done at room temperature (300 K). A homemade tungsten tip was used in the STM measurements. Tips are prepared by chemically etching a 1-cm long, 0.01 in. diameter tungsten wire in 2M NaOH electrolyte at 4 V for several seconds until a sharp tip was formed. The fresh tips were examined by optical microscopy ($\times 100$) and rinsed with deionized water, acetone and 30% HF acid before mounting onto the STM tip head. STM images were taken at room temperature (300 K) all the time except when otherwise noted. Typical scanning parameters were in the range of -50 mV to -2.0 V for the bias and 0.5 -1.0 nA for tunneling current.

The details of preparation of the clean Pd₃Fe(111) surface were the same as described in Chapter 2. The clean, annealed Pd₃Fe(111) surfaces were oxidized by exposing them to O₂ by back-filling the UHV chamber with O₂. The effects of temperature and oxygen exposure were investigated. After oxidation, the chemical states of surface Fe and Pd were characterized by XPS. Oxygen-induced Fe segregation was studied by LEIS. The surface structures of Fe oxide films were studied by LEED and

STM. O₂ exposures were made by leaking O₂ into the UHV using a leak valve (Variable leak valve 1000, Varian). The O₂ exposure was calculated by using the oxygen pressure measured by the ion gauge, uncorrected for ion gauge sensitivity, multiplied by the exposure time. Exposures are recorded in units of Langmuir (L), which is defined as 1 L = 1.0 × 10⁻⁶ torr · s

3.3 Results

3.3.1 LEED

The clean Pd₃Fe(111) surface after heating to 1150 K showed a (1 × 1) hexagonal pattern in LEED, shown in Panel A in Figure 3.1, which is similar to the pattern observed for Pd(111). We have discussed in Ch. 2 that this surface is characterized by 0.9 ML Pd segregation to the Pd₃Fe(111) surface. Exposure of Pd₃Fe(111) at elevated temperatures to O₂ causes formation of several ordered surface structures. After 15 L O₂ exposure at 700 K, as shown in Panel B in Figure 3.1, LEED showed six closely spaced hexagons of spots. This so-called Moiré pattern is due to a film superstructure on top of the substrate. The inner spot of each of the spot arrays originates from the substrate surface. The outer ring of spots is due to an FeO overlayer (discussed below) which has a larger lattice (unit cell vector) than the substrate surface. Additional information about Moiré patterns is discussed in the appendix. A different LEED pattern, ($\sqrt{3} \times \sqrt{3}$) R30°, as shown in D, was formed after 15 L O₂ exposure at 1000 K, we will show later that this corresponds to formation of an incomplete Fe₂O₃(111) monolayer on the surface. At intermediate temperature, mixtures of patterns B and D were observed, as shown in C.

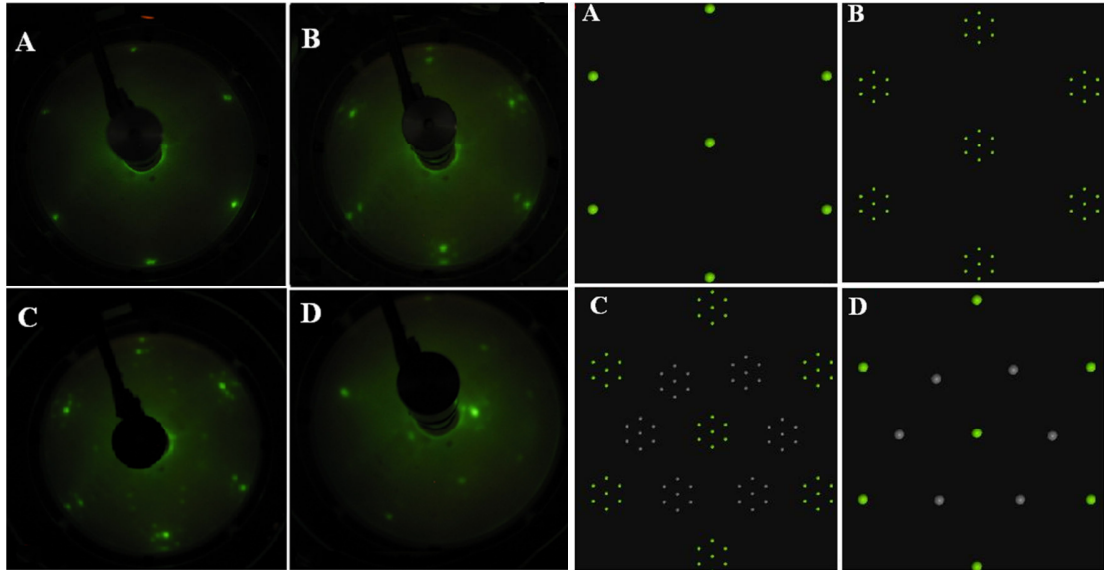


Figure 3.1 Left: Comparison of LEED patterns at $E_p=55$ eV of clean and oxidized $\text{Pd}_3\text{Fe}(111)$ surfaces. A. clean surface (1×1); B. Moiré pattern formed by a $\text{FeO}(111)$ monolayer on the substrate after 15 L O_2 exposure at 700 K; C. Mixed pattern comprised of spots from the patterns of B and D after 15 L O_2 exposure at 900K; and D. $(\sqrt{3}\times\sqrt{3})$ $R30^\circ$ pattern after 15 L O_2 exposure at 1000K. Right: Simulated LEED patterns.

3.3.2 LEIS

Figure 3.2 illustrates LEIS spectra of clean and oxidized Pd₃Fe(111). Oxidation of the surface causes the oxygen peak to increase and the Pd peak to greatly decrease in intensity, but hardly affects the Fe peak. The O, Fe, and Pd peak intensities are plotted in Figures 3.3, 3.4 and 3.5 to provide quantitative assessments of the effect of substrate temperature and oxygen exposure level. For O₂ exposures with the substrate at 300 K, the oxygen LEIS signal initially increases linearly with increasing O₂ exposure, but eventually increases more slowly until it reaches a maximum after 50 L. Both the oxidation rate and the maximum oxygen signal are influenced by the substrate temperature during exposure. As shown in Figure 3.3, both values are larger with the substrate at 500 K than at 300 K. An interesting phenomenon is observed for the Fe peak intensity in LEIS, as shown Figure 3.4. At 300 K, the Fe peak initially sharply decreases after low O₂ exposures, but then slowly increases with increasing O₂ exposures, however never recovering the initial value. At 500 K, the Fe peak increases as the oxygen exposure increases for all amounts. This result indicates two different oxidation mechanisms. At 300 K, only surface Fe is oxidized. At 500 K, near surface Fe is pulled out to the surface layer by the strong interaction between Fe and O. O₂ exposures in all cases causes the Pd peak intensity in LEIS to decrease.

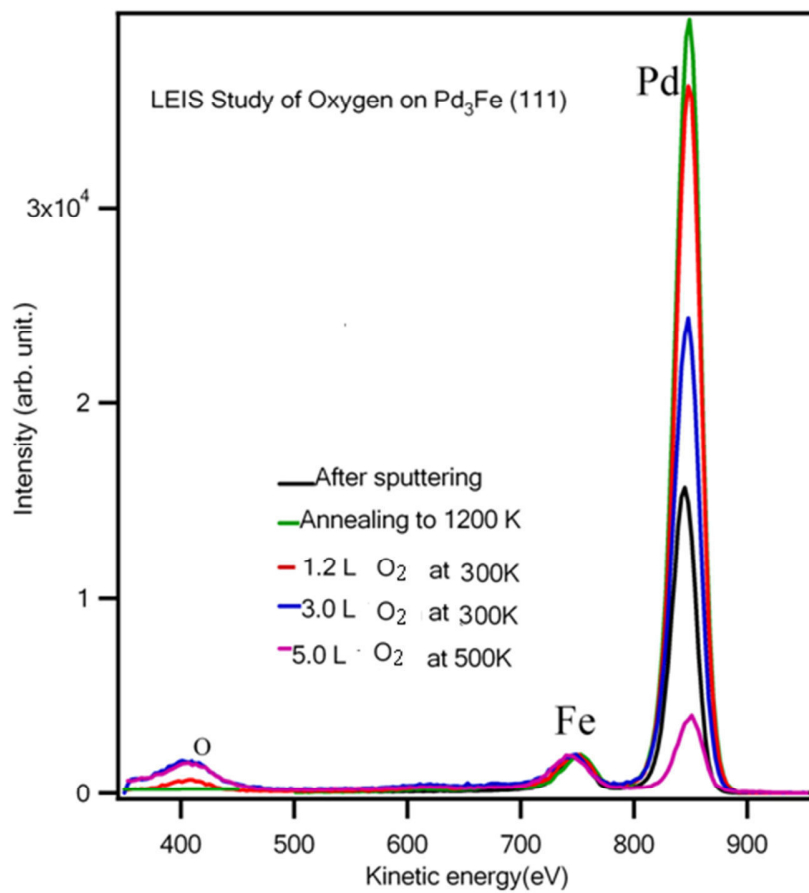


Figure 3.2 Surface compositions of clean and oxidized Pd₃Fe(111) surfaces studied by LEIS. LEIS parameters: $E_i=1000$ eV. 3.0 nA He⁺, Scattering angle: 130°.

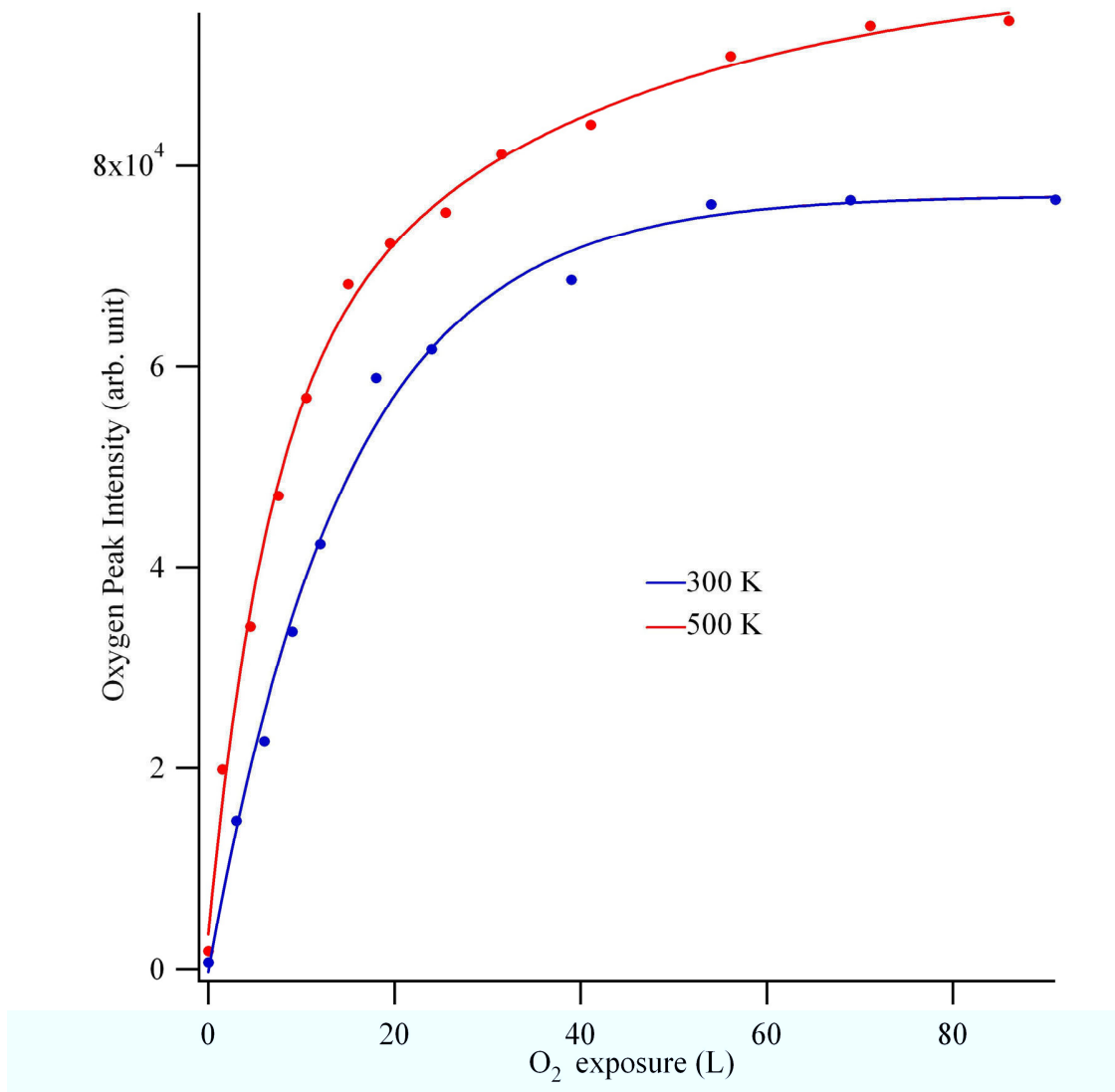


Figure 3.3 Oxygen accumulation curves Pd₃Fe(111) at 300 and 500 K measured by the oxygen peak intensity in LEIS. LEIS parameters: $E_i=1000$ eV, 3.0 nA He⁺. Scattering angle: 130°.

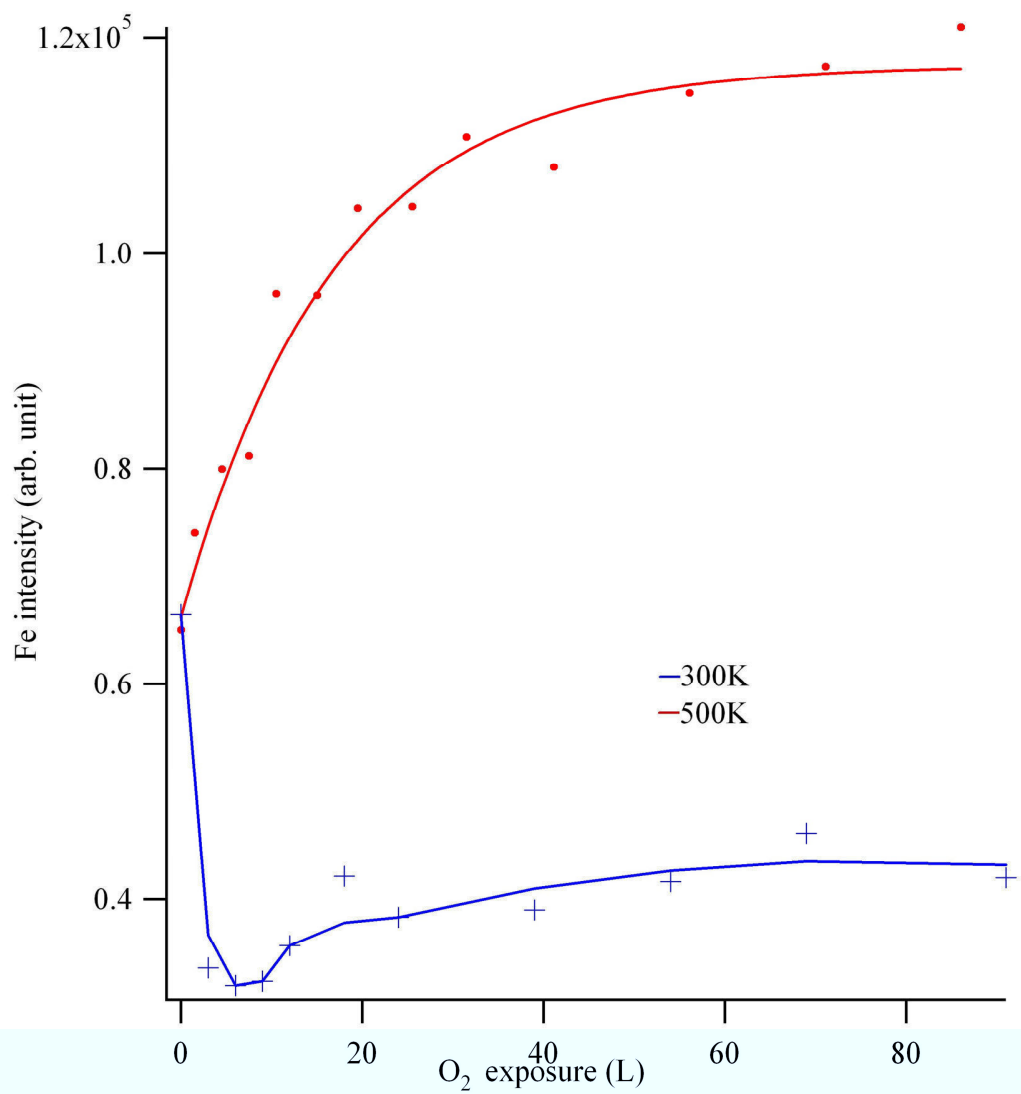


Figure 3.4 Influence of O₂ exposure on Pd₃Fe(111) at 300 and 500 K on the Fe peak intensity in LEIS. LEIS parameters: E_i=1000 eV, 3.0 nA He⁺. Scattering angle: 130°.

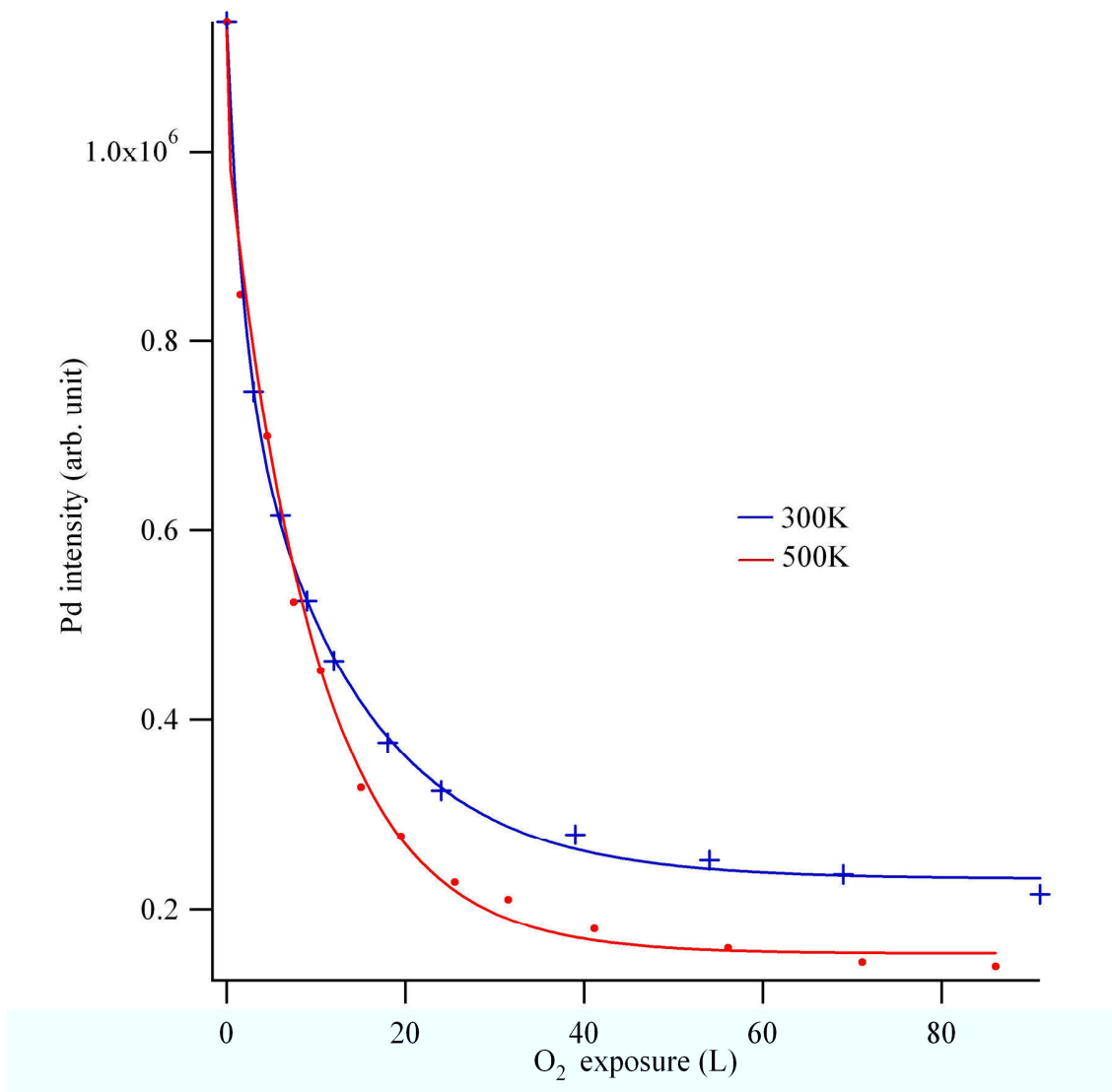


Figure 3.5 Influence of O₂ exposure on Pd₃Fe(111) at 300 and 500 K on the Pd peak intensity in LEIS. LEIS parameters: E_i=1000 eV, 3.0 nA He⁺. Scattering angle: 130°.

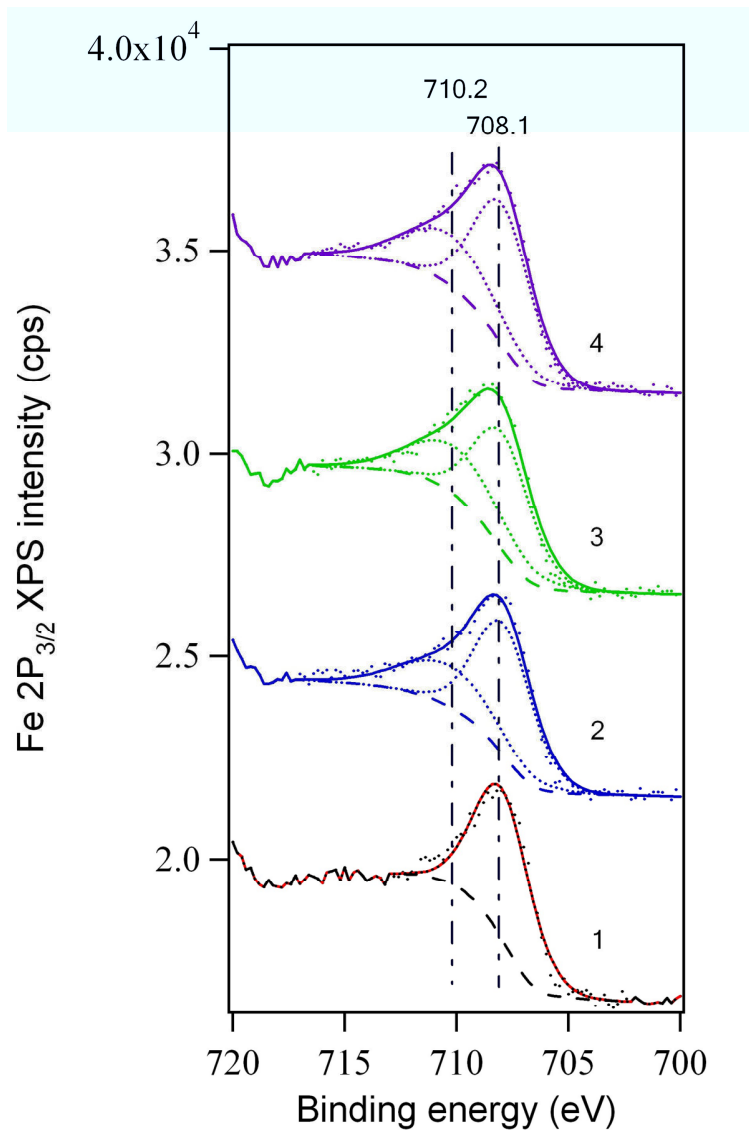
3.3.3 XPS

Figure 3.6 shows XPS spectra of the Fe $2p_{3/2}$ core level after 15 L O₂ exposures on Pd₃Fe(111) at different temperatures. Before oxidation, the surface was cleaned by Ar⁺ sputtering at 500 eV and annealing at 1100 K for 60 sec. All the oxidized surfaces were prepared by exposing O₂ at different temperatures on a clean surface. Fe $2p$ peaks in XPS in oxidized states appear as multiple peaks and are complicated to fit.⁷ In this study, the fitting of Fe $2p_{3/2}$ in the oxidized Pd₃Fe(111) is simplified by taking the Fe $2p_{3/2}$ peak in the alloy as the standard for the peak position and the component of metallic Fe. The full width at half maximum (FWHM) is 3.5 eV.

The peak at 708.1 eV binding energy (BE) is due to the metallic Fe alloyed with Pd. A new Fe $2p_{3/2}$ peak at 710.2 eV appears following O₂ exposure and increases in intensity as the temperature increases. This new peak is assigned to Fe(II)⁸ and attributed to the formation of an FeO(111) monolayer film at the surface. Figure 3.6 B compares the Fe $2p_{3/2}$ peaks after the surface oxidized at 950 K and 800 K. The background was subtracted. Satellite peaks are observed at about 715 eV, which are attributed to Fe²⁺.⁷

Oxidation at 950 K caused the Fe $2p_{3/2}$ to become broad and the Fe²⁺ satellite peak to decrease in intensity. This result indicates the presence of Fe₂O₃, which was transformed by oxidation of FeO. The Fe³⁺ satellites in Fe₂O₃ usually appear at about 719 eV,⁷ which overlaps with Fe $2p_{1/2}$ of the metallic Fe in this study. No chemical shift was observed for Pd $3d$ peaks.

A.



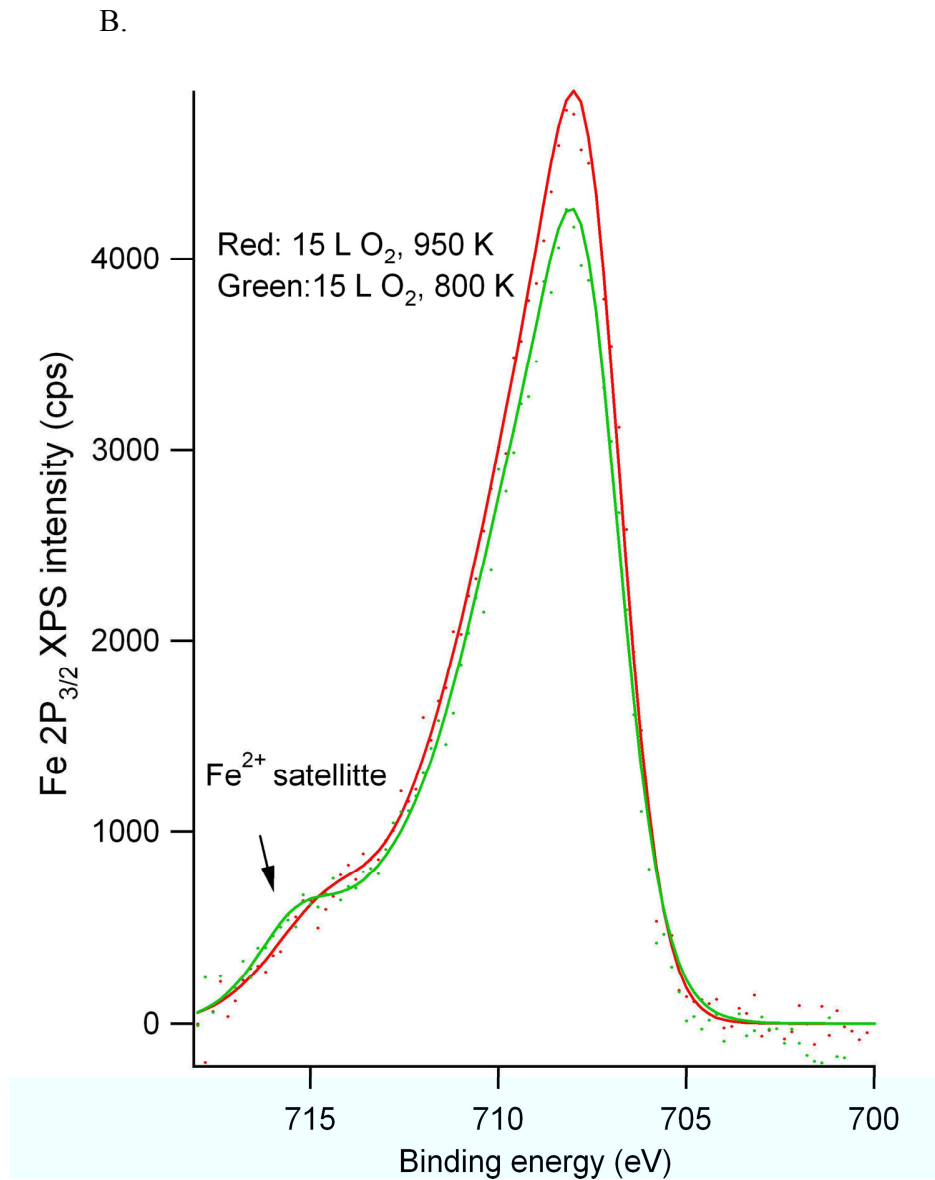


Figure 3.6 A. Fe $2p_{3/2}$ peak in XPS after oxidation of Pd₃Fe(111) at several temperatures. 1) Clean surface. 2) 300 K, 15L O₂. 3) 500 K, 15L, O₂. 4) 800 K, 15L O₂. B. Comparison of Fe $2p_{3/2}$ peak in XPS after oxidation of Pd₃Fe(111) at 800 K, 15L O₂, and 950 K, 15L O₂. A Shirley background has been subtracted from the spectra.

3.3.4 STM

STM images obtained after 15 L O₂ exposures on Pd₃Fe(111) at different temperatures are shown in Figure 3.7. The ordered structures identified in STM correspond to those identified by the LEED patterns shown in Figure 3.2.

A 15 L O₂ exposure on Pd₃Fe(111) at 800 K caused the surface to form a well-ordered structure, corresponding to the LEED pattern of Figure 3.1B. This surface displays a superstructure and two different unit cells can be identified with lattice constants of 3.15 Å and 19.84 Å. Later discussion will show that this structure was a FeO(111) monolayer on Pd₃Fe(111). A 15 L O₂ exposure on Pd₃Fe(111) at 900 K produced a structure of ($\sqrt{3}\times\sqrt{3}$) R30° that existed as small islands above the Moiré superstructure, which causes the mixed LEED pattern of these two structures (Figure 3.1C). High temperature annealing (1100K) causes dissociation of Fe oxide at the surface and the (1x1) structure is recovered, as shown in Figure 3.7 C.

However, more complicated structures were discovered by STM when the oxidation temperatures and O₂ exposure were changed or after the oxidized surface was annealed, which will be discussed later. The stability of PdO(111) film will also be addressed in the discussion section.

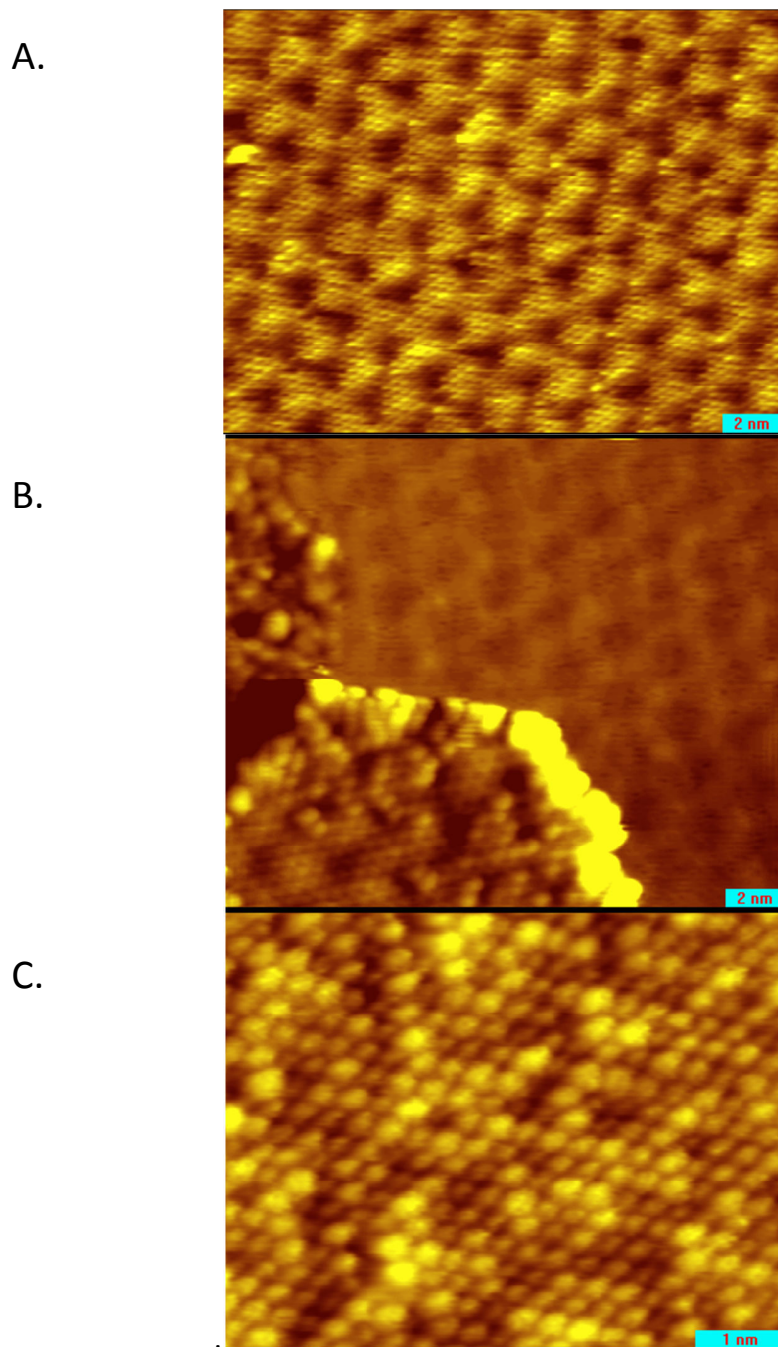


Figure 3.7 Constant current STM images of Pd₃Fe(111) after oxidation. A. ($14.0 \times 11.0 \text{ nm}^2$), Moiré structure formed after 15 L O₂ at 800 K. B. ($15.0 \times 14.0 \text{ nm}^2$), $(\sqrt{3} \times \sqrt{3})R30^\circ$ and Moiré structures after 15 L O₂ at 950 K. C. ($6.0 \times 4.0 \text{ nm}^2$), Clean, ordered (1×1) Pd₃Fe(111) surface produced after 15 L O₂ at 800 K followed by vacuum-annealing at 1050 K for 1 min. STM conditions: A. -0.99 mV, 0.60 nA. B. -350 mV, 340 pA. C. -500 mV, 0.5 nA.

3.4 Discussion

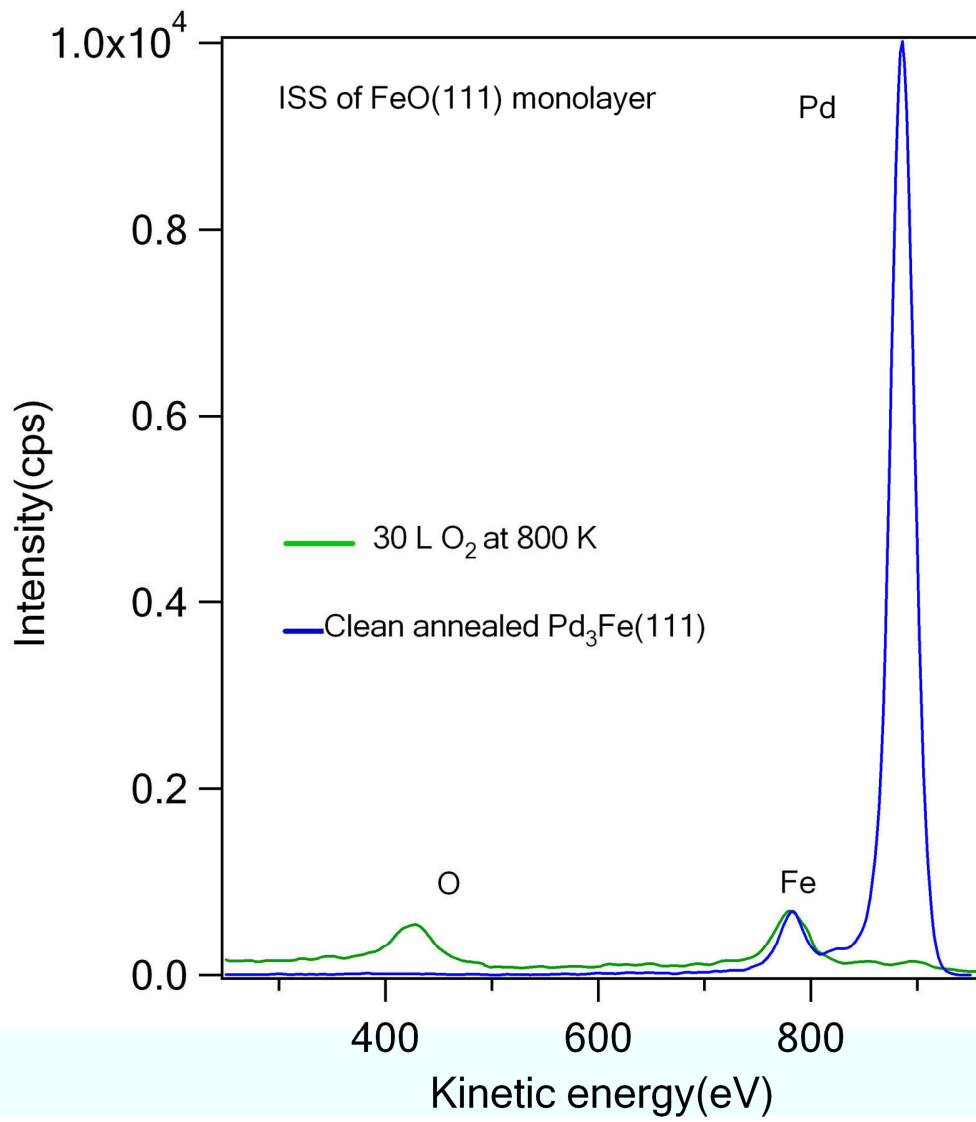
3.4.1 FeO(111) on Pd₃Fe(111)

It has been well-established that an FeO(111) monolayer forms a Moiré pattern on Pt(111) due to the mismatch of the lattice constants of Pt(111) and FeO(111).⁹⁻¹⁰ The FeO(111) monolayer has a bilayer structure, which consists of an Fe atomic layer and an O atomic layer. In this study, a similar structure was formed on Pd₃Fe(111) after oxidation, which causes us to assign the structure as FeO(111) ML/Pd₃Fe(111). The details are discussed below.

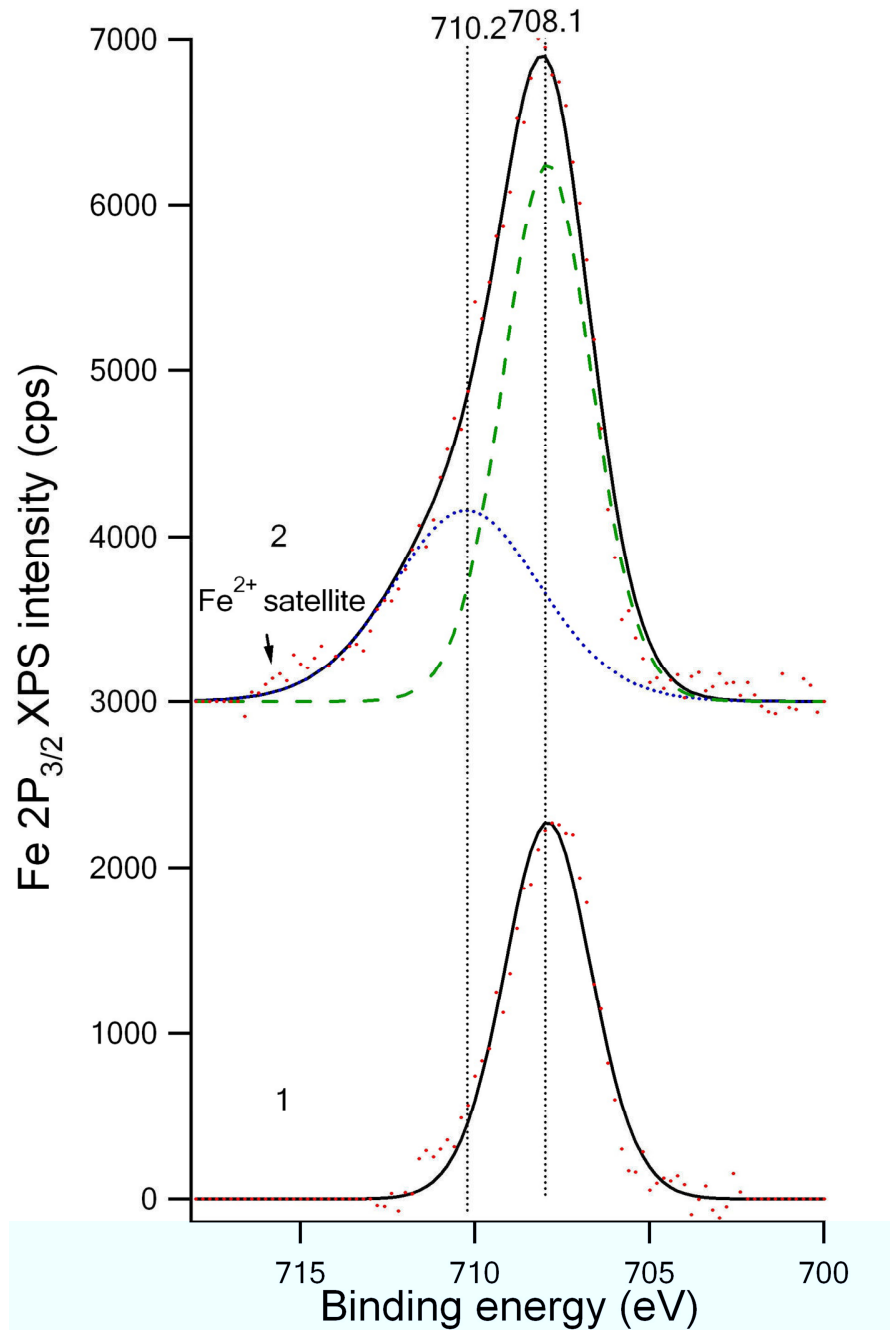
Figure 3.8 shows XPS of Fe *2p* core level, LEIS, LEED pattern and STM images with atomic resolution of Pd₃Fe(111) surface after it was oxidized by 30 L O₂ at 800 K. The surface elemental profile was shown by LEIS in Figure 3.8A. Analysis of the surface composition by LEIS revealed no Pd but only oxygen and Fe on the surface layer, indicating a complete FeO layer was formed. The oxygen-induced segregation of an active metal has been reported for other alloys, e.g., Pt-Fe alloys,¹¹ and was attributed to the strong attractive interactions between Fe and oxygen. The corresponding XPS of Fe *2p*_{3/2} of this surface was shown in Figure 3.8B. This peak can be deconvoluted into two components, one at 708.1 eV and the other at 710.2 eV. The peak at 708.1 eV is due to metallic Fe alloyed with Pd in the near surface layer since this peak is shown on the clean Pd₃Fe(111). The peak at 710.2 eV can be assigned as Fe(II) since no satellite peaks at about 719 eV due to Fe(III) were observed.⁷ A possible assignment of the Fe oxides film is FeO(111) monolayer. This assignment is supported by the LEED and STM observations. Figure 3.8C shows the LEED pattern exhibiting the principal spots as well as satellite spots arising from the Moiré structure. A Moiré pattern is often observed

when an ordered layer with a slightly different lattice constant is formed on top of an ordered surface. More discussion of the Moiré superstructure is included in the appendix. Consistent with the LEED observations, Figure 3.8D displays atomically resolved STM images of the FeO thin film on the surface of Pd₃Fe(111). The ordered surface was characterized by hexagonal structures with two different unit vectors: 3.15 Å and 19.84 Å. These two vectors are not in the same direction. The unit cell dimensions of the annealed, clean Pd₃Fe(111) surface are 2.73 Å (Figure 3.7 C), which is not simply related to the ordered structure observed for the oxidized surface. By comparing to the ordered surfaces of Fe oxides in the appendix 3.7.3, we believe that the ordered surface must be due to an FeO(111) monolayer. And the only explanation of the large unit cell size (19.84 Å) is that a Moiré superstructure was formed due to the lattice mismatch between the substrate (possibly Pd(111)) and the surface FeO(111) layer. To better view the surface structure, Figure 3.8E displays a 2D model of the Moiré superstructure corresponding to the STM image (Figure 3.8D). It consists of a laterally expanded O-terminated FeO(111) monolayer on top of the Pd(111) surface. The Fe atoms are separated by 3.15 Å and form rows that are rotated by 2.2° from the underlying Pd atom rows along the ($\bar{1}10$) and ($01\bar{1}$) directions. This corresponds to a lattice expansion of 3.6 % compared to the cubic sodium chloride structure of bulk FeO, which has an interatomic distance of 3.04 Å. The large superstructure unit cell is 19.84 Å. A similar Moiré superstructure of an FeO layer on Pt(111) has been studied.¹²⁻¹³ It is of interest to know the layer structure directly under the FeO film. The Moiré superstructure that we observed by LEED is similar to the structure of FeO/Pt(111).⁹

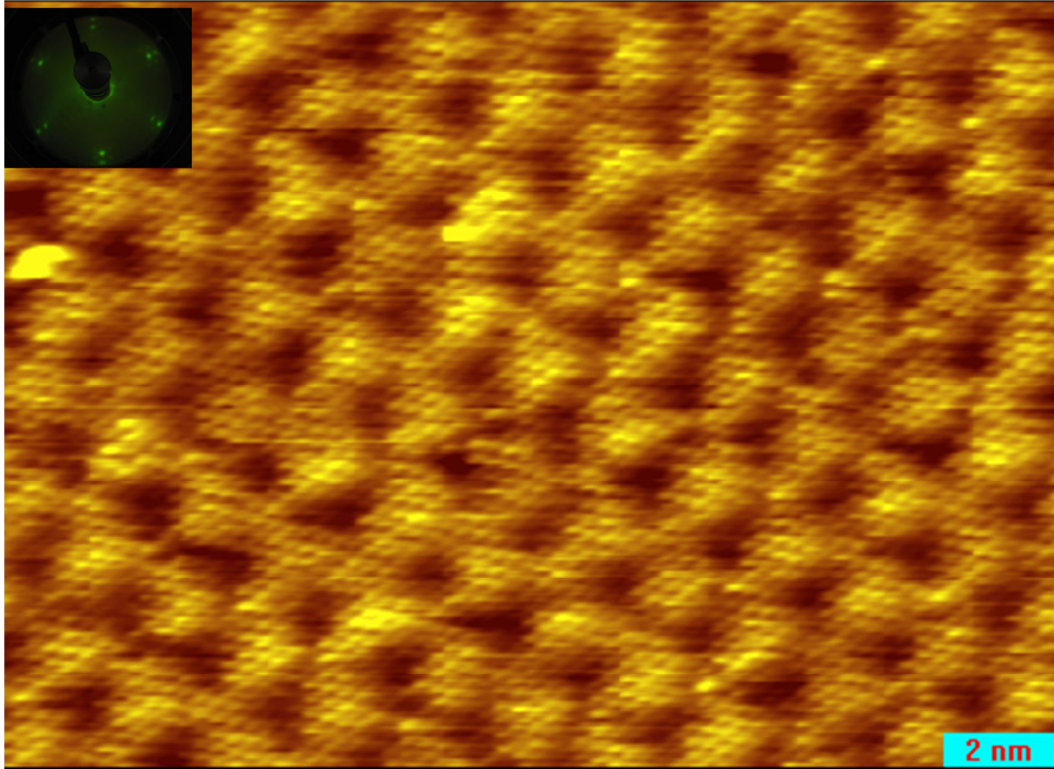
A.



B.



C.



D.

E.

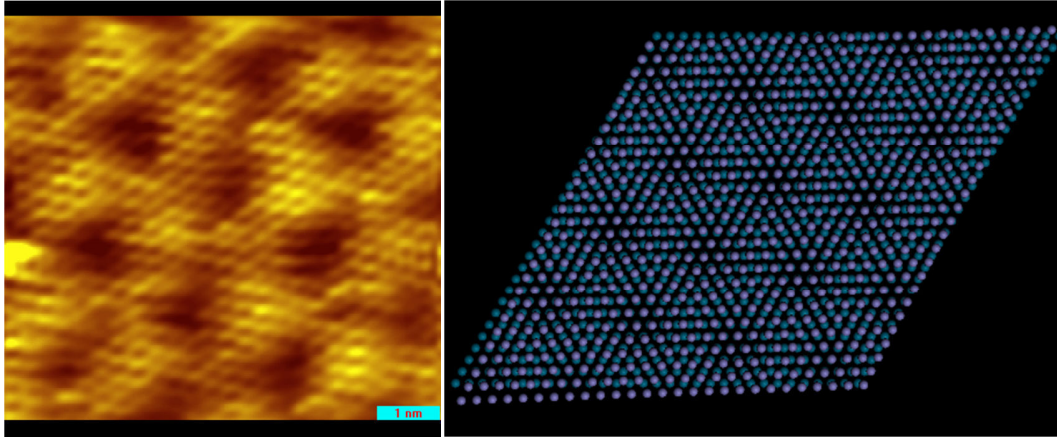


Figure 3.8 Structure and composition of an FeO(111) monolayer on Pd₃Fe(111). A. LEIS of FeO film and clean Pd₃Fe(111) after annealing to 1100 K. B. XPS of Fe $2p_{3/2}$ peaks in (1) FeO film and (2) clean Pd₃Fe(111). A Shirley background has been subtracted. C. Atomically resolved STM image of FeO(111) layer. Insert: LEED pattern of same surface. D. Constant current STM image of small area of the FeO(111) layer. E. Proposed model of iron oxide monolayer on Pd₃Fe(111). This model is built by one layer of oxygen, one layer of iron, one layer of Pd and the bulk Pd₃Fe(111). The model is terminated with oxygen, which is supported by LEIS data. Only Fe (purple) and Pd (blue) are shown in the model. Detailed structure parameters are given in the text. Image sizes: C. (14×11) nm², D. (5×5) nm². Tunneling condition: -0.99 mV, 0.60 nA.

3.4.2 Fe₃O₄ clusters

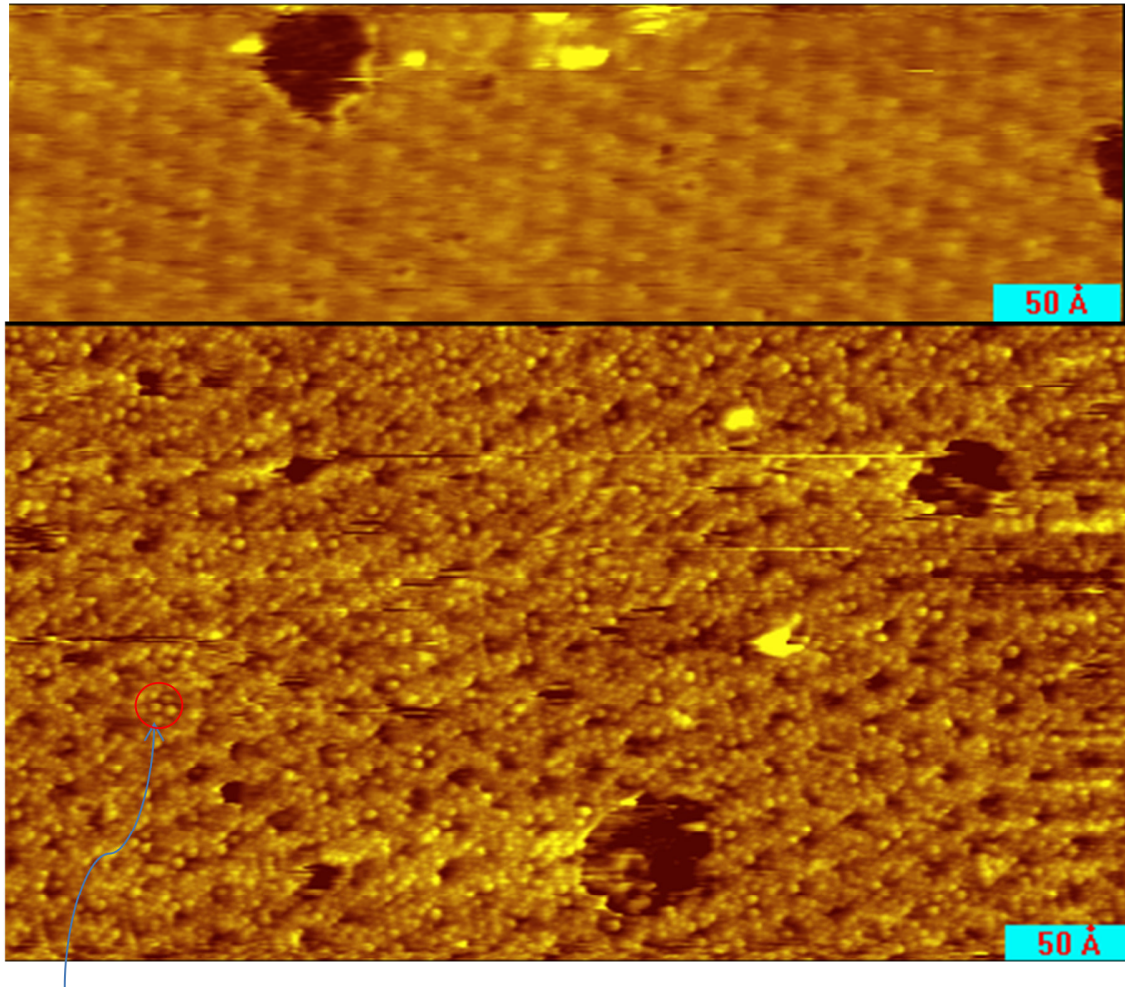
Figure 3.9 exhibits an STM image after the Pd₃Fe(111) was oxidized at 850 K using 1×10^{-7} torr O₂ for 5 min (30L). The STM image displayed different chemical contrasts between the upper and lower panels, which was caused by a sudden change of the tip condition during scanning. An ordered structure with a unit cell of 19.84 Å can be found in the lower part of the STM image. This result indicates that the structure is correlated to the FeO(111)/Pd₃Fe(111) with a Moiré superlattice of 19.84 Å. Very importantly, this structure was also formed when FeO(111)/Pd₃Fe(111) was annealed at 850 K under an oxygen environment. The lower panel displays much higher resolution and some interesting features can be identified. First, the surface displays many defects with apparent depths of 1.0 Å, which is much larger than the chemical contrast (~0.25 Å) only due to the Moiré structure of FeO(111)/Pd₃Fe(111). Interestingly, these defects are located at the Moiré structure lattice registry. Second, a number of small clusters consisting of 3 or 4 large spots can be found at or near the defect sites, exhibiting shapes of an acute triangle or a rhombus, as indicated by the arrows in Figure 3.9-lower panel. Image analysis found that the distance between two neighboring spots in the cluster was about twice the lattice constant of Pd(111) and coincidentally identical to the lattice constant of Fe₃O₄(111). The apparent heights of these spots were about 1.2 Å, referenced to the defects and 0.25 Å referenced to the surrounding FeO_x film. It has been found that Fe₃O₄(111) can be formed on Pt(111) by oxidizing FeO(111)/Pt(111), and a (2×2) superstructure is formed.¹⁴ However, we didn't observe any (2×2) structure by LEED on the oxidized Pd₃Fe(111) structure even by widely changing preparation conditions such as oxygen dosing levels (up to 100 L O₂) and annealing temperatures (800-1050 K).

Since the cluster has a localized structure similar to the $\text{Fe}_3\text{O}_4(111)$ surface, we still assign the cluster as Fe_3O_4 and it could be formed by a disproportionation reaction, such as $4 \text{FeO} \rightarrow \text{Fe}_3\text{O}_4 + \text{Fe}$.

Figure 3.10 is a high resolution STM image of oxidized $\text{Pd}_3\text{Fe}(111)$ showing the Fe_3O_4 clusters and defects. The ordered regions have unit cells of 3.12 \AA , which is identical to that of the intact $\text{FeO}(111)$ monolayer on $\text{Pd}_3\text{Fe}(111)$. This result suggests that the ordered region is the $\text{FeO}(111)$ film without disproportionation reactions. Again, the defects are only located at the lattice registry of the Moiré superstructure, indicating that the reactivity originates from the formation of the Moiré superstructure and it is dependent on the localized structure. In the simulated structure shown in Figure 3.8E, the Moiré superstructure displays the relative geometrical positions of Pd atoms (blue) in the substrate to the Fe atom layer (purple). Two possible geometrical configurations for the lattice registry of the Moiré superstructure can be found in this model. One is with the Fe atom directly above a Pd atom, the other is with the Fe atom sitting at the FCC sites by three Pd atoms. We believe that the atop Fe configuration is less stable than the FCC Fe configuration and the defects should preferentially form at these Fe site with atop configurations by annealing.

The stability of the Moiré superstructure of $\text{FeO}(111)$ on $\text{Pd}_3\text{Fe}(111)$ was explored by annealing the $\text{FeO}(111)$ film at 950 K for 2 min. The Moiré superstructure of the $\text{FeO}(111)$ film disappeared and the original (1×1) LEED pattern was regained but was more diffuse. There was no oxygen desorption from the surface as measured by mass spectroscopy. This result indicates that the ordered FeO film was disordered by the

annealing treatment at 950 K. XPS in Figure 3.11A shows that Fe oxidation state is changed with formation of Fe^{3+} . Therefore, annealing at 950 K caused oxidation and reduction of FeO through the reaction of $\text{FeO} \rightarrow \text{FeO}_x + \text{Fe}$. These FeO_x species are stable at the surface as amorphous clusters, as displayed in Figure 3.11 B. The Fe after decomposition of FeO diffused into the subsurface region during annealing at 950 K, which creates ordered Pd (111) domains.



Fe_3O_4 clusters

Figure 3.9 Constant current STM image of $\text{FeO}_x/\text{Pd}_3\text{Fe}(111)$ after $\text{FeO}(111)/\text{Pd}_3\text{Fe}(111)$ was annealed at 950 K. ($45 \text{ nm} \times 45 \text{ nm}$, -302 mV , 335 pA) The change in the nature of the image in the top panel and bottom panel was caused by a change in the STM tip. A Moiré superstructure is formed with a unit cell of 19.84 \AA , which is identical to the structure of an FeO monolayer on $\text{Pd}_3\text{Fe}(111)$. The dark regions in the bottom panel image are not due to chemical contrast in a flat FeO layer on $\text{Pd}_3\text{Fe}(111)$. Instead, they are holes due to missing atoms. The apparent depth of these features in STM is 1.2 \AA , which is much larger than the chemical contrast of dark features in the FeO bilayer of the Moiré pattern, 0.25 \AA . Large defects are also shown. The arrow indicates a small Fe_3O_4 cluster.

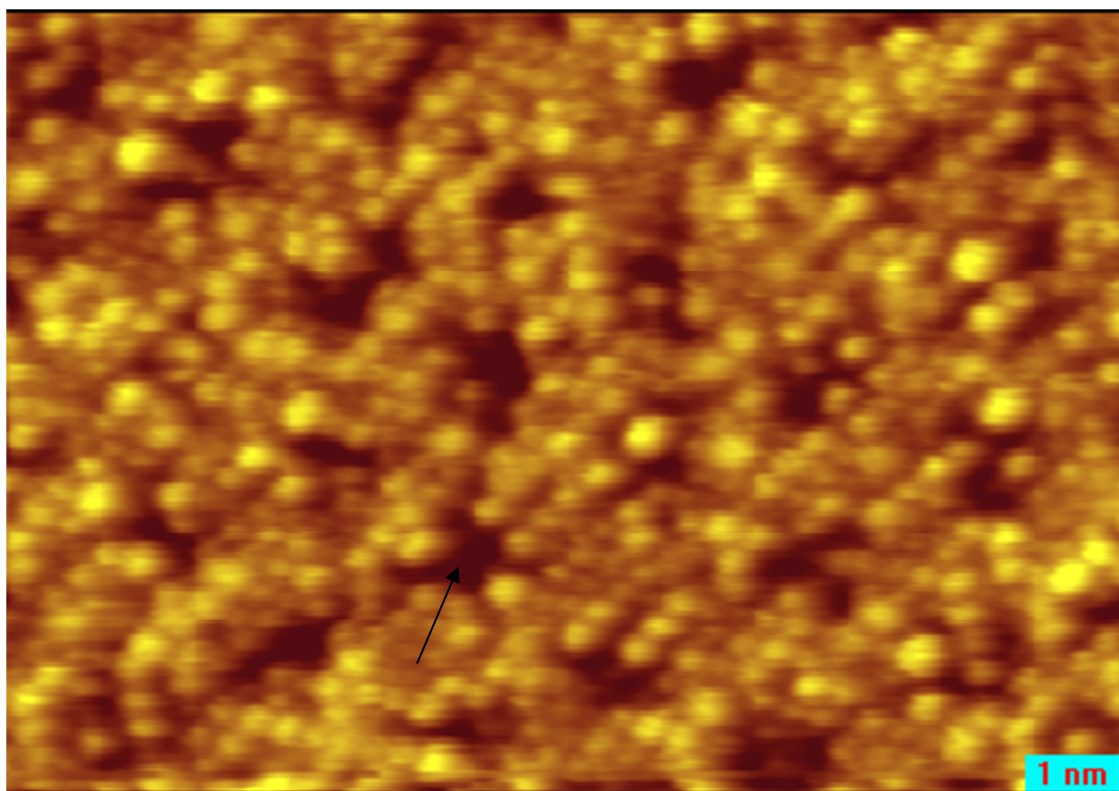


Figure 3.10 Small area of FeO_x/Pd₃Fe(111) shown by an atomically resolved STM image. This surface was obtained after the FeO(111)/Pd₃Fe(111) was annealed at 950 K. The spot features corresponds to oxygen atoms. The surface was still ordered but defects due to missing Fe or O atom appeared. The arrow shows a hole-like defect. Ordered regions are still the FeO(111) film as the lattice constant is identical to that of FeO(111) shown in Figure 3.8. Image size: 14×10 nm², -302 mV, 343 pA.

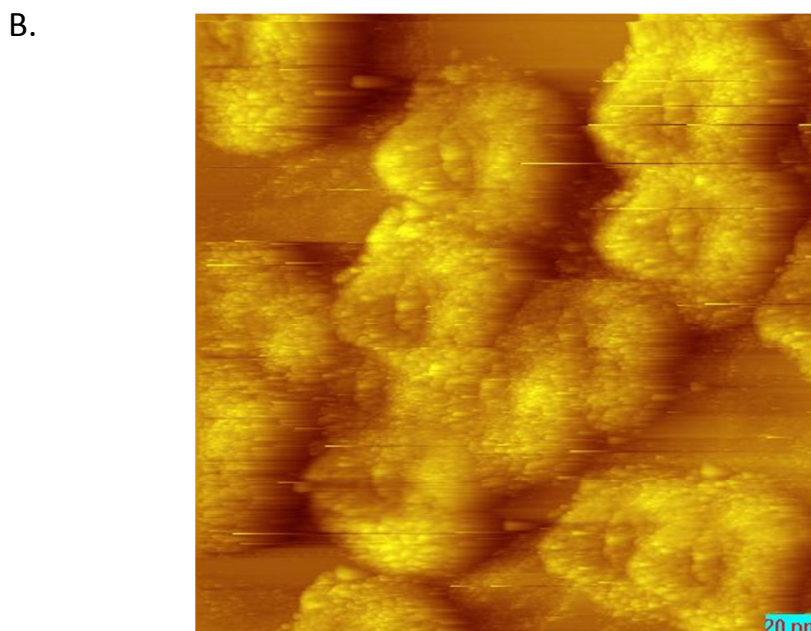
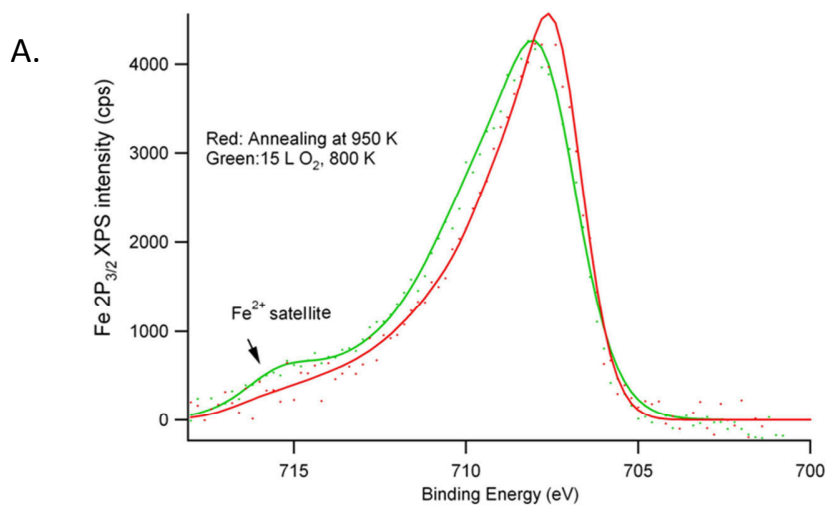


Figure 3.11 A. XPS of Fe $2p_{3/2}$ peaks in the FeO film (green) and annealed FeO(111) film (red) (950 K for 2 min). A Shirley background has been subtracted. The Fe^{2+} satellite peak disappeared after annealing and the peak shifts to lower binding energy, indicating the reaction $\text{FeO} \rightarrow \text{FeO}_x + \text{Fe}$. The surface is still covered partially by Fe oxides (Fe_2O_3) since the peak shape is different from that of a clean $\text{Pd}_3\text{Fe}(111)$ (See Figure 3.8B). B. STM image of the FeO_x amorphous clusters after FeO(111) was annealed at 950 K for 2 min. This surface had a diffuse (1×1) LEED pattern, indicating the substrate was comprised of Pd(111)-like domains. Image size: $160 \times 160 \text{ nm}^2$. STM conditions: -302 mV, 343 pA.

3.4.3 Fe₂O₃(0001)

A structure of ($\sqrt{3}\times\sqrt{3}$)R30° was found by LEED when the FeO(111) film or Pd₃Fe(111) was oxidized at 950-1050 K using 15 L O₂. The STM image of this surface is shown in Figure 3.12. Cluster sizes of 2-5 nm with heights of 1.8 Å and a ($\sqrt{3}\times\sqrt{3}$)R30° structure can be identified. It has been found that Fe₂O₃(0001) on Pt(111) displayed a structure of ($\sqrt{3}\times\sqrt{3}$)R30° (See appendix 3.7.3). Therefore, we believe that these ordered clusters are small islands of Fe₂O₃(0001). The FeO(111) film and Fe₂O₃(0001) islands were found to co-exist when the annealing temperature was 800-950K, which is shown in Figure 3.13. Interestingly, Moiré superstructures were found on both terraces. The lower terrace is FeO(111)/Pd₃Fe(111). The higher terrace is Fe₂O₃(0001)/Pd₃Fe(111) with a structure of ($\sqrt{3}\times\sqrt{3}$)R30°. The formation of Fe₂O₃(0001) Moiré superstructures has not been observed on any other substrate before but on the Pd₃Fe(111) surface in this study. The terrace height of the ($\sqrt{3}\times\sqrt{3}$)R30° regions in Figure 3.12 is 2.0 Å. But this height is not the thickness of Fe₂O₃ islands since it is referenced to the FeO film at the lower terrace. Smaller Fe₂O₃(0001) clusters can also be found in other regions of the surface. The STM image of Fe₂O₃(0001) clusters of 2~5 nm is shown in Figure 3.1. Moiré structure was not found in the surrounding area of the Fe₂O₃(0001) clusters, indicating the FeO film starts to decompose at 950 K. Theoretically, two different planes of Fe₂O₃(0001) can be exposed, O- terminated and Fe-terminated (See appendix 3.7.3). The termination of the Fe₂O₃(0001) cluster cannot be identified easily without more studies and/or theoretical calculations. The different appearances of Fe₂O₃ clusters in the STM images in Figure 3.12 and Figure 3.13 may indicate that the Fe₂O₃(0001) are terminated

by different atoms, such as oxygen terminated or Fe terminated and FeO_x layer structures, such as Fe-O-Fe or O-Fe-O.

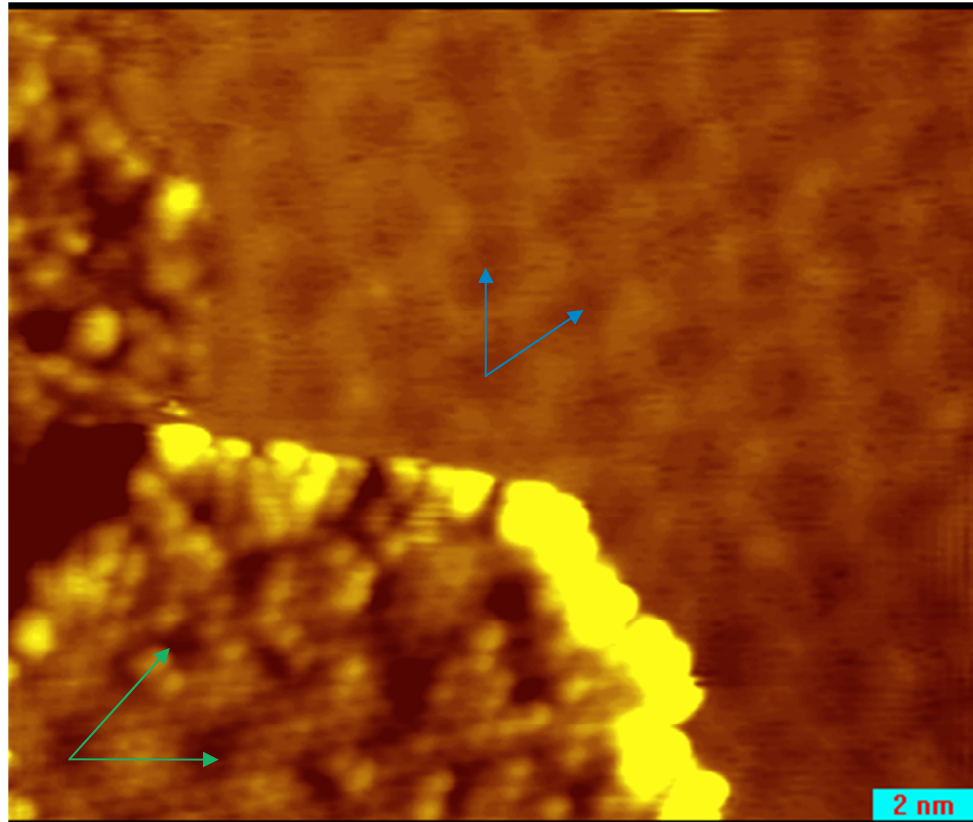


Figure 3.12 Constant current STM image of FeOx/Pd₃Fe(111). This structure was obtained by annealing the Pd₃Fe(111) surface at 950 K in oxygen. The lower terrace is still FeO(111) with a Moiré structure with a unit vector of 19.84 Å (blue). The higher terrace (left corner) is Fe₂O₃(0001) with a structure of ($\sqrt{3}\times\sqrt{3}$)R30°. Surprisingly, a different Moiré structure was formed by the Fe₂O₃(0001) layer. The green arrow indicates the lattice vector (24.2 Å). 15.0 × 14.0 nm², 350 mV, 340 pA.

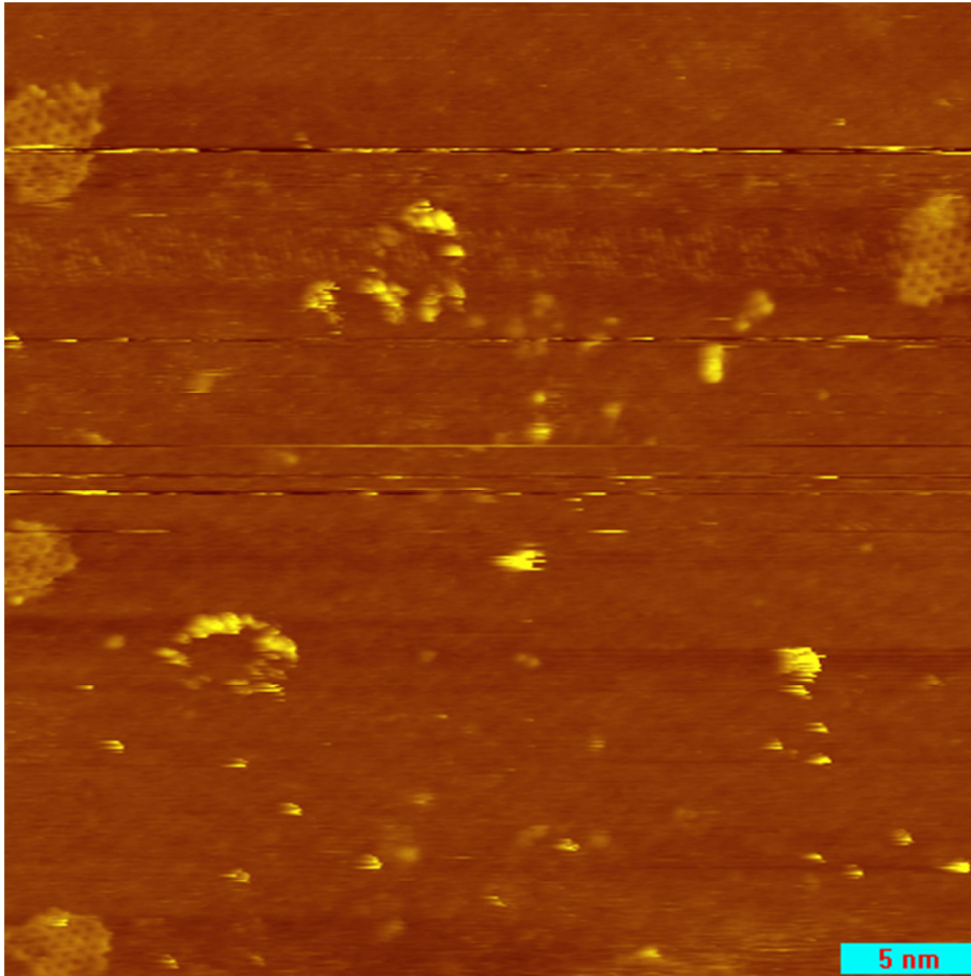


Figure 3.13 Constant current STM image of Fe₂O₃ clusters with sizes of 2-5 nm. The Moiré structure of FeO(111) disappeared. Image size: 46.2 × 46.2 nm². STM: -350 mV, 336 pA.

3.5 Conclusions

Oxygen adsorption reverses the segregation trend and causes Fe atoms to accumulate on the surface. XPS shows that Fe at the surface is oxidized by oxygen. Oxygen dosing at elevated temperatures causes formation of well-organized surface structures, such as FeO(111) with a Moiré structure at 700 K, FeO(111) + ($\sqrt{3} \times \sqrt{3}$) R30° at 700 -950K, and ($\sqrt{3} \times \sqrt{3}$) R30° at 1000 K. Ordered defects were formed when FeO(111)/Pd₃Fe(111) was annealed at 950 K. Formation of a Moiré pattern of the FeO(111) monolayer on the Pd substrate causes some regions of the FeO film to be very active. Oxygen can further oxidize these regions to higher oxidation states or FeO in this region can be decomposed to leave atomic defects on the surface.

3.6 References

1. Sun, Y. N.; Qin, Z. H.; Lewandowski, M.; Carrasco, E.; Sterrer, M.; Shaikhutdinov, S.; Freund, H. J., Monolayer iron oxide film on platinum promotes low temperature CO oxidation. *J. Catal.* **2009**, *266* (2), 359-368.
2. Sun, Y.-N.; Giordano, L.; Goniakowski, J.; Lewandowski, M.; Qin, Z.-H.; Noguera, C.; Shaikhutdinov, S.; Pacchioni, G.; Freund, H.-J., The Interplay between structure and CO oxidation catalysis on metal-supported ultrathin oxide films. *Angew. Chem. Int. Ed.* **2010**, *49* (26), 4418-4421.
3. Fu, Q.; Li, W.-X.; Yao, Y.; Liu, H.; Su, H.-Y.; Ma, D.; Gu, X.-K.; Chen, L.; Wang, Z.; Zhang, H.; Wang, B.; Bao, X., Interface-confined ferrous centers for catalytic oxidation. *Science* **2010**, *328* (5982), 1141-1144.
4. Basińska, A.; Maniecki, T. P.; Józwiak, W. K., Catalytic activity in water-gas shift reaction of platinum group metals supported on iron oxides. *React. Kinet. Catal. Lett.* **2006**, *89* (2), 319-324.
5. Knudsen, J.; Merte, L. R.; Grabow, L. C.; Eichhorn, F. M.; Porsgaard, S.; Zeuthen, H.; Vang, R. T.; Lægsgaard, E.; Mavrikakis, M.; Besenbacher, F., Reduction of FeO/Pt(1 1 1) thin films by exposure to atomic hydrogen. *Surf. Sci.* **2010**, *604* (1), 11-20.
6. Weiss, W.; Ranke, W., Surface chemistry and catalysis on well-defined epitaxial iron-oxide layers. *Prog. Surf. Sci.* **2002**, *70* (1-3), 1-151.
7. Grosvenor, A. P.; Kobe, B. A.; Biesinger, M. C.; McIntyre, N. S., Investigation of multiplet splitting of Fe 2p XPS spectra and bonding in iron compounds. *Surf. Interface Anal.* **2004**, *36* (12), 1564-1574.
8. Schedel-Niedrig, T.; Weiss, W.; Schlögl, R., Electronic structure of ultrathin ordered iron oxide films grown onto Pt(111). *Phys. Rev. B: Condens. Matter* **1995**, *52* (24), 17449.
9. Giordano, L.; Lewandowski, M.; Groot, I. M. N.; Sun, Y. N.; Goniakowski, J.; Noguera, C.; Shaikhutdinov, S.; Pacchioni, G.; Freund, H. J., Oxygen-induced transformations of an FeO(111) film on Pt(111): A combined DFT and STM study. *J. Phys. Chem. C* **2010**, *114* (49), 21504-21509.

10. Ritter, M.; Ranke, W.; Weiss, W., Growth and structure of ultrathin FeO films on Pt(111) studied by STM and LEED. *Phys. Rev. B: Condens. Matter* **1998**, *57* (12), 7240.
11. Baddeley, C. J., Chapter 14 Adsorbate induced segregation at bimetallic surfaces. In *The Chemical Physics of Solid Surfaces*, Woodruff, D. P., Ed. Elsevier: 2002; Vol. Volume 10, pp 495-526.
12. Kim, Y. J.; Westphal, C.; Ynzunza, R. X.; Galloway, H. C.; Salmeron, M.; Van Hove, M. A.; Fadley, C. S., Interlayer interactions in epitaxial oxide growth: FeO on Pt(111). *Phys. Rev. B: Condens. Matter* **1997**, *55* (20), R13448.
13. Giordano, L.; Pacchioni, G.; Goniakowski, J.; Nilus, N.; Rienks, E. D. L.; Freund, H.-J., Interplay between structural, magnetic, and electronic properties in a FeO/Pt(111) ultrathin film. *Phys. Rev. B: Condens. Matter* **2007**, *76* (7), 075416.
14. Ritter, M.; Weiss, W., Fe₃O₄(111) surface structure determined by LEED crystallography. *Surf. Sci.* **1999**, *432* (1-2), 81-94.
15. N'Diaye, A. T.; Coraux, J.; Plasa, T. N.; Busse, C.; Michely, T., Structure of epitaxial graphene on Ir(111) *New J. Phys.* **2008**, *10* 043033.
16. Weiss, W.; Ritter, M., Metal oxide heteroepitaxy: Stranski-Krastanov growth for iron oxides on Pt(111). *Phys. Rev. B: Condens. Matter* **1999**, *59* (7), 5201.

3.7 Appendix

3.7.1 Moiré patterns

The unit vector of the surface layer is \vec{k}_2 and the substrate vector is \vec{k}_1 , and the Moiré vector is expressed by the following Eq.

$$\vec{k}_{Moiré} = \vec{k}_2 - \vec{k}_1 \quad (\text{A1})$$

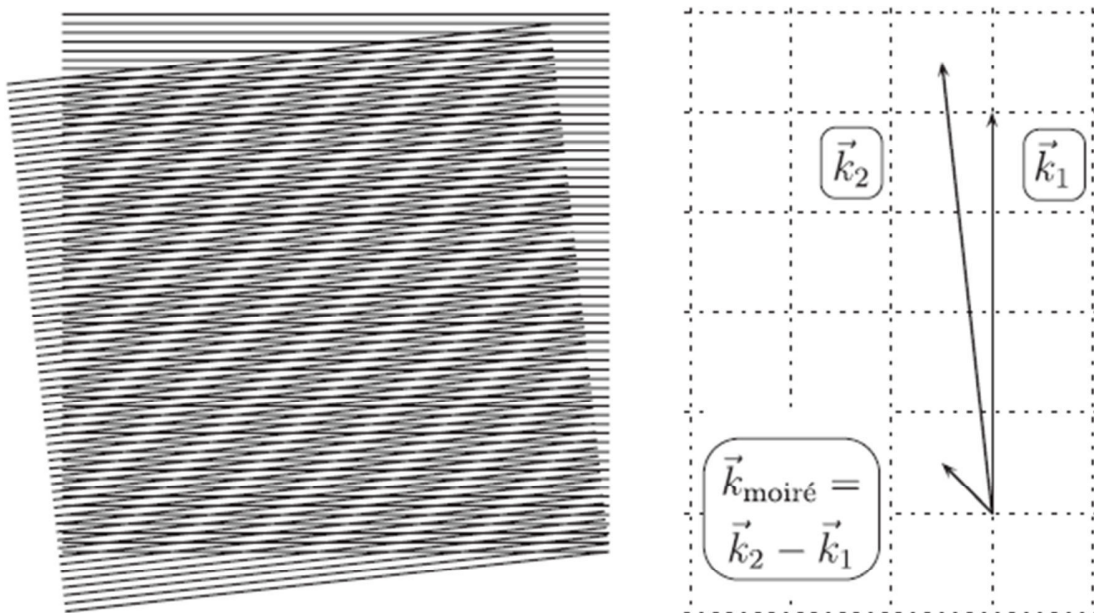


Fig. 3. A1. Moiré pattern formed by overlapping two ordered structures. ¹⁵

3.7.2 Un-identified STM images

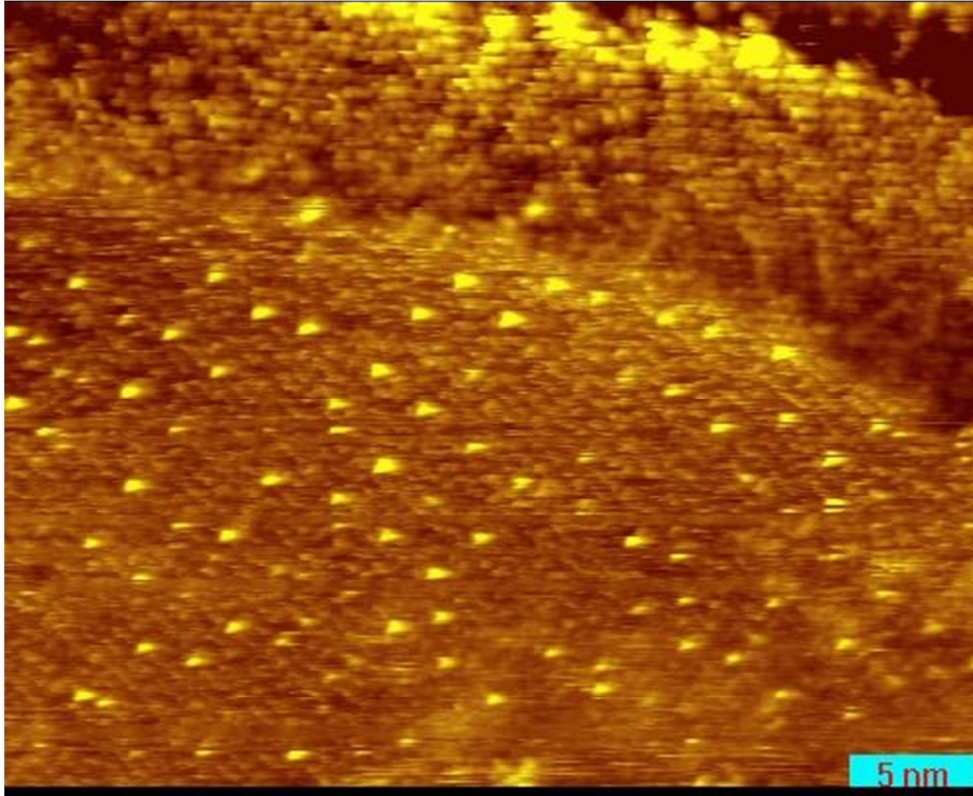


Fig. 3.A2 Oxides on Pd₃Fe(111) after oxidation under 15 L O₂ at 800 K. This structure was found to co-exist with the FeO(111) film occasionally. Clusters with triangle shapes can be seen. Since FeO nanoislands were identified on Pt(111), the clusters in this image could be FeO clusters and they may represent the beginning of surface oxidation.

3.7.3 Model structure of Fe oxides

Three main Fe oxides are FeO, Fe₃O₄ and Fe₂O₃. Below are the low index faces of the crystals of Fe oxides.

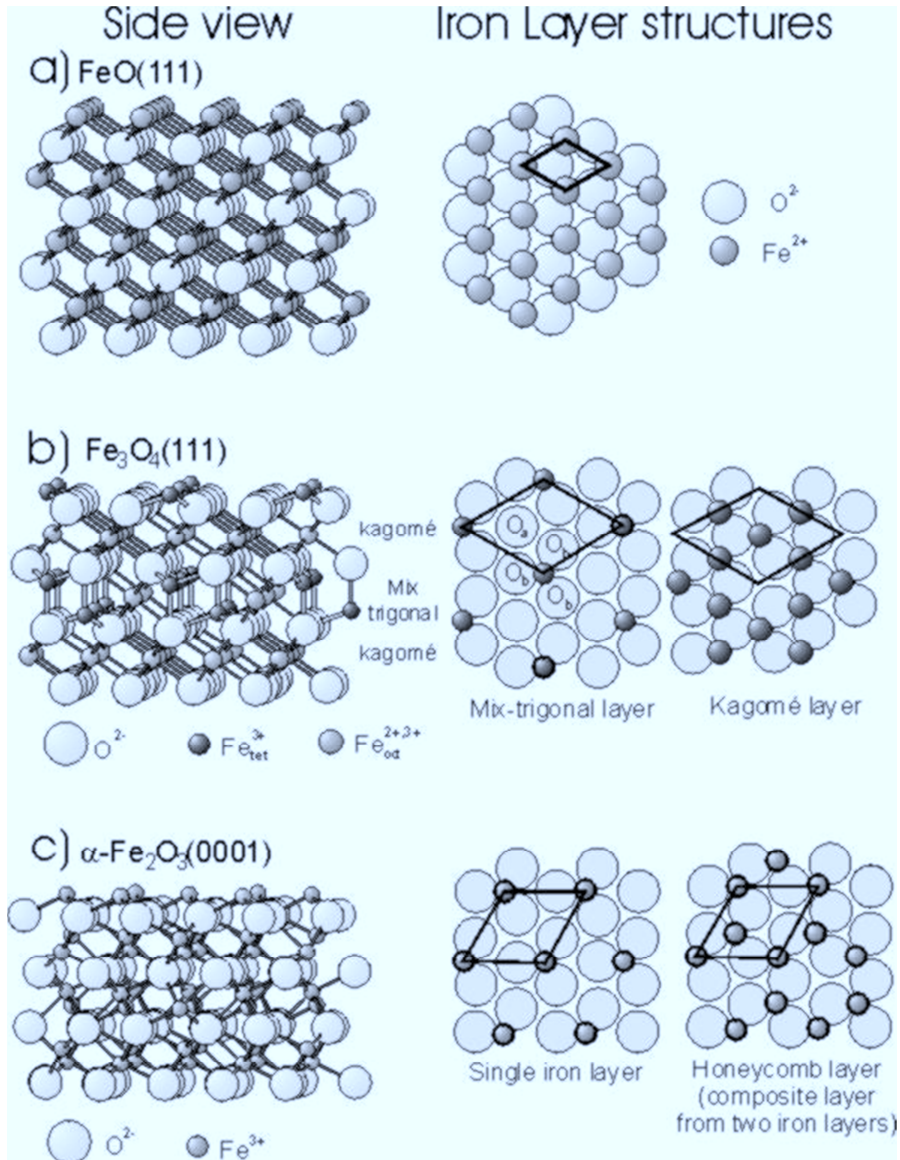


Fig. 3.A3 Structural models of three common Fe oxides and the surface structures of some low index surfaces.¹⁶

Chapter 4 Role of Surface Fe in Enhanced Activity for the Oxygen Reduction Reaction on a Pd₃Fe(111) Single Crystal Alloy

4.1 Introduction

Applications of polymer electrolyte membrane fuel cells (PEM-FCs) require a continued search for an optimal catalyst with attributes of high activity, durability, low cost, and resistance to negative effects of impurities in the fuel. Pt-based bimetallic catalyst systems are widely utilized in PEM-FCs because of their exemplary performance as both cathode and anode.¹⁻⁷ Alloying with inexpensive metals can reduce the loading of Pt used and lower the cost of the fuel cell, but in some cases the catalytic activity is maintained or even becomes higher. Surprisingly, some non-Pt based alloy catalysts (e.g., Pd-Fe and Pd-Co) appear to have even better performance than Pt-based alloy catalysts.⁸⁻⁹ Recently, higher electrocatalytic activity and stability were found when metals or alloys were used as supports for a Pt or Pd monolayer (ML).¹⁰⁻¹⁷ Development of improved catalysts would be aided by a fundamental understanding of the ORR mechanism. However, the ORR system is complex and ultimately requires considering fully the effects of water, solvent ions, changing electrical potentials, and a detailed description of the composition and structure of all the chemical phases present at the electrode surface. Thus, progress has been limited in elucidating the origin of the enhanced performance of various bimetallic catalysts. An important factor that can be isolated is the surface composition and structure of the alloy responsible for the ORR kinetics. In this chapter, studies are described on a bimetallic alloy single crystal, Pd₃Fe(111), which combine surface

analytical techniques including low energy ion scattering (LEIS) and scanning tunneling microscopy (STM), electrochemical analysis, and quantum chemistry calculations in order to investigate at a molecular level the origin of the enhanced ORR properties of Pd-Fe alloys. We find excellent ORR performance for the Pd₃Fe(111) crystal after heating to high temperatures in ultrahigh vacuum (UHV) and establish a strong correlation of this performance to the presence of surface Fe.

4.2 Experimental methods

4.2.1 Surface Preparation and Characterization in UHV

A disk-shaped Pd₃Fe(111) single crystal sample, 6.5 mm in diameter and 4 mm in thickness, with one side polished, was obtained from Metal-Crystal and Oxide, Cambridge, England. The alloy was mounted in a special sample holder so that it could be installed on the sample stage of a UHV chamber for surface analysis and utilized for electrochemistry measurements, as described in Chapter 1. The UHV chamber was also described in Chapter 1, and was equipped with LEIS, AES, XPS, and LEED. The sample was cleaned by cycles of Ar⁺ ion sputtering and annealing at 1100 K in the UHV chamber with a base pressure of 1×10^{-10} torr. Surface cleanliness and long-range order were checked by XPS and LEED. No detectable impurity was found by XPS. A sharp and bright (1×1) LEED pattern was obtained before other experiments. This pretreatment caused Pd segregation at the surface as described in our previous study.¹⁸ LEIS was used to study the surface composition with absolute topmost layer surface sensitivity. A relative sensitivity in LEIS of Pd/Fe=2.1 was used in this study. After the crystal surface was cleaned, five different Pd₃Fe(111) surfaces were prepared in UHV: (1) an atomically

rough Pd-Fe surface with Fe:Pd=1:3 prepared by Ar⁺ ion sputtering of a clean Pd₃Fe(111) crystal with 1-keV Ar⁺ ions for 20 min in order to achieve a higher surface Fe concentration of 25%, identical to the Fe concentration in the bulk; (2) an atomically smooth Pd-Fe surface with Fe:Pd=1:3 prepared by dosing 0.8-ML Fe followed by annealing at 1000 K for 20s; (3) a Pd-Fe surface prepared by annealing the sputtered surface to 1250 K to form Pd adatoms on the surface and an 11% Fe concentration as determined by LEIS; (4) a Pd-Fe surface without Pd adatom features in STM and with an 8% Fe concentration determined by LEIS prepared by annealing the sputtered surface to 900 K; and (5) a Pd monolayer on Pd₃Fe(111), denoted as Pd ML/Pd₃Fe(111), prepared by annealing the Pd₃Fe(111) crystal to 1000 K followed by deposition of 0.5-ML Pd at 300 K and then annealing to 900 K (LEIS determined a concentration of 97% Pd at this surface).

4.2.2 Electrochemical measurements

The sample holder also enabled attachment to a rotating disc electrode rotator (RDE, Pine). A quick transfer of the sample between the main UHV chamber and the electrochemical cell was accomplished with the aid of a small high-pressure antechamber/load lock attached directly to the UHV chamber. During the sample transfer, the antechamber was filled with high purity N₂ (99.998 %, Airgas). The UHV-prepared Pd₃Fe(111) surfaces were protected by placing a droplet of pure water (HPLC grade, Fisher) on the surface in the antechamber. The crystal was then immediately transferred into an electrochemical cell and immersed in a 0.1 M HClO₄ solution for electrochemical measurements. A hanging meniscus rotating disc technique was used and the height of

the meniscus was carefully controlled to prevent wetting of the side of crystal. A standard three-electrode electrochemical cell with a Pt-wire counter electrode was used and a hydrogen electrode was used as a reference. More details of electrochemical measurements can be found in Chapter 1.

4.2.3 DFT calculations

We entered into a collaboration with Prof. Ruqian Wu of the University of California at Irvine, and his student Jun Hu, in order to obtain DFT calculations relevant to these investigations. All the calculations were carried out with the Vienna ab-initio simulation package (VASP)¹⁹⁻²⁰, at the level of spin-polarized generalized-gradient approximation (GGA). The projector augmented wave (PAW) method was used for the description of core-valence interactions. More details of the calculation methodology can be found in our previous paper.¹⁸ Two structural models with a 2×2 supercell (or 16 atoms per layer) in the lateral plane were employed: (i) one monolayer Pd was distributed on Pd₃Fe(111) (denoted as **Surface I**); and (ii) one surface Pd atom in **Surface I** was substituted by one Fe atom (denoted as **Surface II**), which leads to 6.25% Fe atoms in the outmost layer. Other experimental details regarding the DFT calculations are available in the Chapter 2-Appendix and our previous paper.¹⁸

4.2.4 ORR data and kinetic analysis

The ORR current density j is expressed by the Kotecký-Levich equation:²¹

$$\frac{1}{j} = \frac{1}{j_k} + \frac{1}{j_d} \quad (1)$$

The diffusion limiting current density for a hanging meniscus rotating disk system is

described using a modified Levich equation:²²

$$j_d = 0.620nFD^{2/3}C_0\nu^{-1/6}\omega^{1/2}[1 - 2KR_0^{-1}(\nu/\omega)^{1/2}] \quad (2)$$

where j is the measured current density, j_k is the kinetic current density, j_d is diffusion limiting current density, n is the number of exchanged electron; ω is the rotation speed, F is the Faraday constant (96485 C mol⁻¹), D is the diffusion coefficient of O₂ in 0.1 M HClO₄ solution, ν is the kinematic viscosity, C_0 is the concentration of molecular oxygen, R_0 is the geometric radius of the electrode, and K is a constant related to the meniscus height. All specific activities were calculated using the geometric surface area of the crystal sample.

4.3 Results and discussion

The lower surface energy of Pd causes significant Pd segregation to the top surface of Pd-Fe alloys, which has been studied for both polycrystalline PdFe alloys²³ and a Pd₃Fe(111) single crystal.¹⁸ Pd₃Fe(111) surfaces with different structures can be prepared by heating at different temperatures in UHV, and two surface structures are shown in Figure 4.1. Annealing at 1200 K or higher after sputtering causes Pd segregation and STM reveals a complex reconstructed surface containing 0.17-ML Pd monomer and dimer adatoms on top of the outermost alloy layer, as we reported previously.¹⁸ LEIS results gave a composition for this surface of 9% Fe and DFT calculations indicated that all Fe atoms were directly bonded to Pd adatoms. Pd adatoms are not formed by annealing at temperatures below 1000 K, as shown in Figure 4.1b. LEIS and STM analysis of this surface revealed 8% Fe in the surface layer. We assign the

bright spots in the STM image in Figure 4.1b as surface Fe atoms since the number of these bright spots is close to the Fe concentration determined by LEIS and because Fe atoms were identified as bright spots in a previous study of a PtFe alloy.²⁴ The strength of Pd-Fe bonding is such that Fe atoms in the surface layer can be isolated, with only Pd neighbors, or present as small Fe-Fe clusters or chains with a maximum of five Fe atoms that are surrounded by Pd atoms.

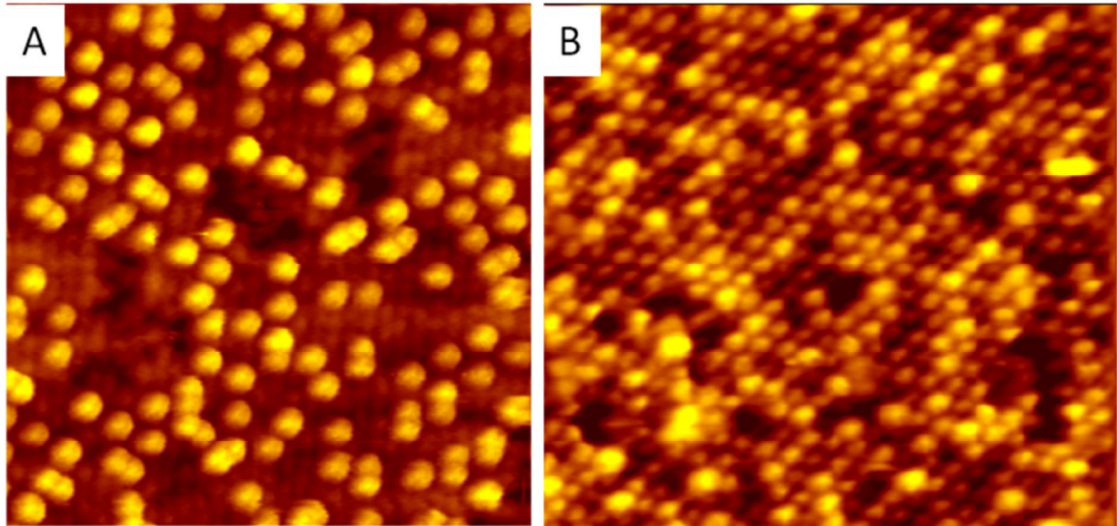
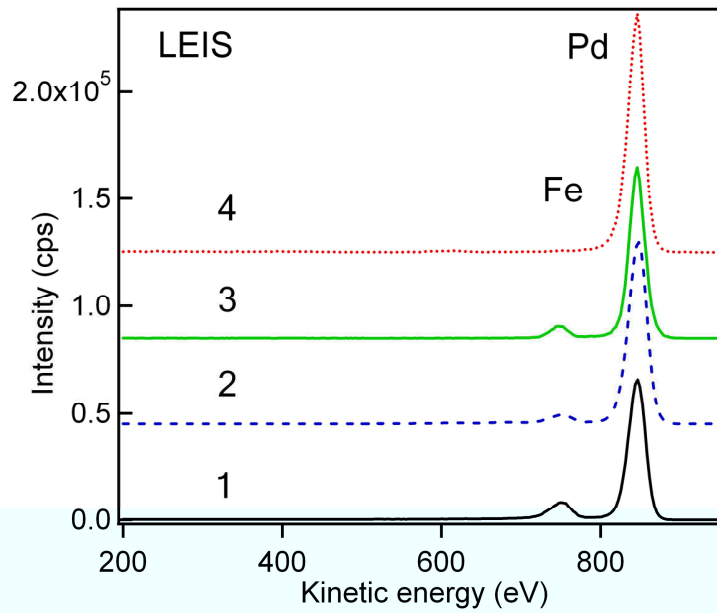


Figure 4.1 Constant current STM images of clean Pd₃Fe(111) surfaces illustrating the importance of annealing temperature on surface structure. (A) After heating to 1200 K. Image: $8.0 \times 8.0 \text{ nm}^2$. Tunneling parameters: 1.03 mV, 2.04 nA. High temperature annealing created Pd monomer and dimer adatoms at the surface. Bright yellow spots are primarily due to segregated Pd monomers and dimers. (B) After heating to 1000 K. Image: $7.0 \times 7.0 \text{ nm}^2$. Tunneling parameters: -302 mV, 340 pA. Lower temperature annealing did not result in the Pd adatom features. Two distinct corrugations are observed due to chemical contrast between Pd and Fe atoms. Bright spots are assigned to Fe atoms.

We investigated the electrochemical properties of the two surface structures for Pd₃Fe(111) for catalyzing the ORR. Curves 2 and 3 in Figure 4.2 show the cyclic voltammograms (CVs) of Pd₃Fe(111) in oxygen-free electrolyte after the crystal was annealed at 900 and 1250 K, respectively. The heating temperature caused changes in both H adsorption/desorption (H_{ads/des}) features at 200 mV and surface oxidation features at 700 mV, comparing to a rough Pd₃Fe(111) surface reported by Adzic.¹³ A larger area under the H_{ads/des} curves was obtained on Pd₃Fe(111) annealed at 1250 K. This large H_{ads/des} peak can be explained by that the presence of Pd adatoms, which increases the number of surface active sites.

The ORR activity of these two Pd₃Fe(111) surfaces were measured by sweep voltammetry in O₂-saturated HClO₄ electrolyte using a rotating disk electrode at 300 K, as shown in Figure 4.3. As discussed below, both surfaces were found to be highly active in the ORR and there was only a small difference observed between the two. This result indicates that the surface structure of Pd is not the determining factor in controlling the alloy reactivity or that Pd adatoms are not stable in acid solution and dissolve or transfer to islands or defects. We noted that both alloy surfaces had similar amounts of surface Fe, and so we proposed that this surface Fe plays an important role in the ORR kinetics.

A.



B.

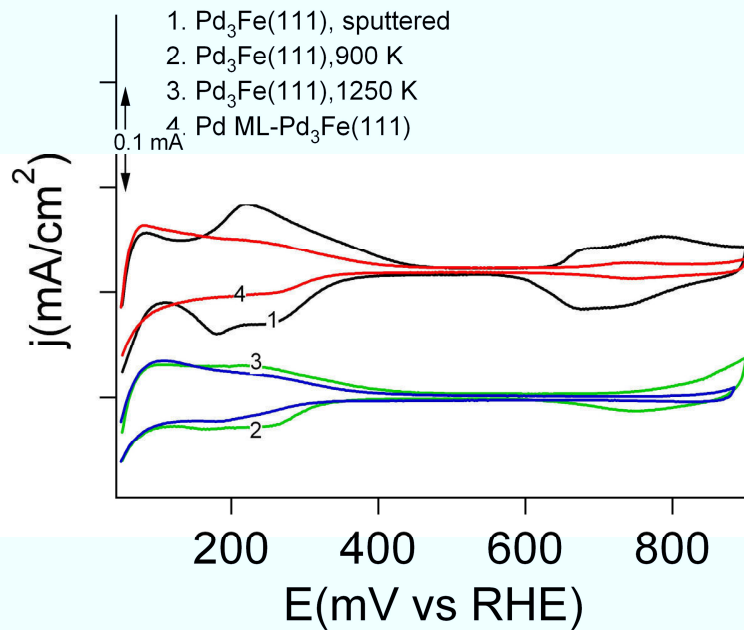
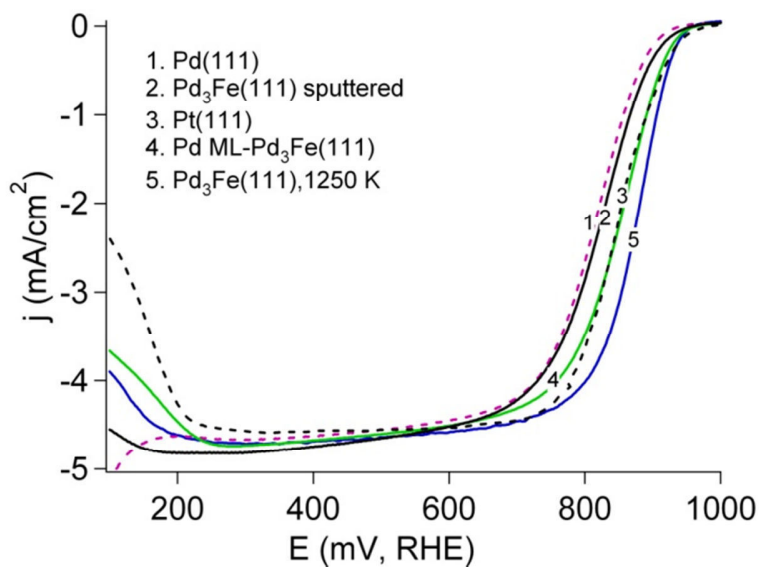


Figure 4.2 A. Comparison of LEIS spectra obtained for the Pd₃Fe(111) surfaces used prior to the electrochemical measurements. B. Voltammetry curves for four different Pd₃Fe(111) surfaces at 300 K in an Ar-purged 0.1 M HClO₄ solution. The sweep rate was 20 mV/s. ISS conditions: 3 nA, 1 keV He⁺.

A.



B.

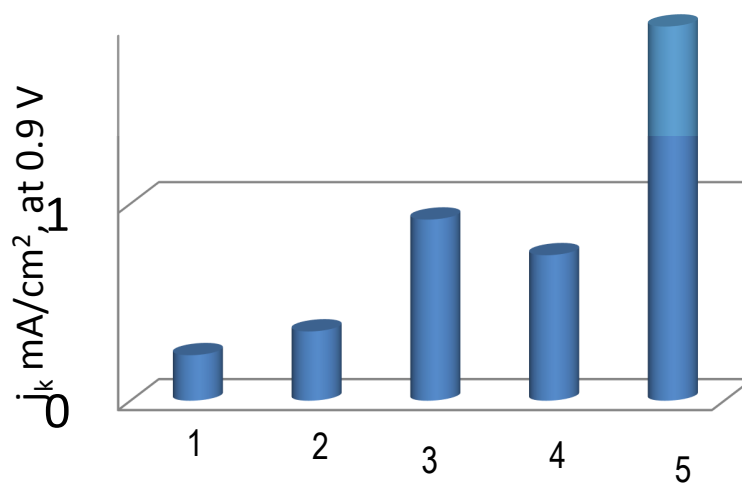


Figure 4.3 A. Comparison of the ORR polarization curves for several Pd₃Fe(111), Pd(111) and Pt(111) surfaces. Polarization curves were obtained at 300 K in an O₂-purged 0.1 M HClO₄ solution with a sweep rate of 20 mV/s and rotation rate of 900 rpm. B. Comparison of the kinetic current at 0.9 V for five surfaces: (1) clean Pd(111) annealed at 1000 K; (2) Pd₃Fe(111) sputtered at 300 K; (3) Pd ML-Pd₃Fe(111) prepared as described in the text; (4) Pt(111); and (5) Pd₃Fe(111) annealed to 1250K.

In order to more fully explore the effect of surface Fe on ORR activity, Pd-Fe surfaces with a high concentration of Fe (25%) and free of Fe were prepared in UHV. The Pd₃Fe(111) crystal has 25 % Fe in the bulk, and we have determined that mechanical polishing or sputtering produces a surface with 25% Fe. However, this surface is rough and annealing in UHV to smooth the surface causes Pd segregation to the surface. A way to prepare an atomically flat surface with 25% Fe is to add more Fe to an annealed surface by Fe vapor deposition with the crystal at 300 K, followed by controlled annealing to 900 K. The LEIS for all of Pd-Fe surfaces prepared in UHV for CV measurements are shown in Figure 4.2. The surfaces with 25% Fe were not stable in the electrochemical environment and surface Fe was dissolved slowly in the electrolyte during polarization scanning (22 % over 30 min). However, no apparent Fe dissolution was detected (< 1 %) for the annealed Pd₃Fe(111) surfaces with 10% or less surface Fe. (See Appendix Figure 4.A1 for more details on the surface Fe concentrations before and after CV and ORR experiments.) Therefore, surface geometry and composition has an important effect on the stability of surface Fe.

The onset potential is a common parameter used to describe electrochemical reactions at electrode surfaces and it refers to the potential where a chemical reaction starts and is characterized by a sudden increase in observed current. The onset potential of surface oxide formation on the sputtered Pd₃Fe(111) is at 620 mV. After formation of a Pd layer on Pd₃Fe(111), the onset potential of surface oxide formation is shifted to 680 mV, which is 60 mV more positive than that on sputtered Pd₃Fe(111). This result indicates the Pd layer is less active for forming a surface oxide. Interestingly, the onset

potentials of surface oxide formation on the annealed surfaces at high temperature further shifts positively, at 720 mV on Pd₃Fe(111) annealed at 900 K and at 810 mV on Pd₃Fe(111) annealed at 1250 K. Little change in the onset potential for H adsorption/desorption ($H_{\text{ads/des}}$) was seen on the sputtered surface, but a much larger peak of $H_{\text{ads/des}}$ compared to all other annealed surfaces. As we have discussed, surface Fe was dissolved by comparing the LEIS result before and after ORR measurements.. The Fe dissolution caused an amorphous Pd layer to form. This is why the $H_{\text{ads/des}}$ peak from the sputtered surface is much larger than that from other surfaces. Molecular oxygen electroreduction was studied on all the prepared Pd₃Fe(111) surfaces and Pd(111) and Pt(111) in an O₂ saturated, 0.1 M HClO₄ solution using a rotating disk electrode. The ORR polarization curves are generated by linearly scanning the potential of the sample at 20 mV/s in the range of 100-1000 mV and recording the corresponding current. Full sets of scanning ORR polarization curves at 100, 225, 400, 625, 900, 1225 and 1600 rpm were obtained and plotted as Appendix Figures 4.A3-6.

ORR polarization curves at 900 rpm of positive scanning (from 100 to 1000 mV) for all Pd-Fe surfaces are plotted and compared to Pd(111) and Pt(111) in Figure 4.3. All of the curves are characterized by two different regions: The well-defined limiting currents (j_D) region (0.2–0.7 V) and the mixed diffusion-kinetic control region (0.7–0.95 V). The corresponding ORR kinetic parameters from these experiments are given in Table 1. The polished Pd(111) sample had the worst ORR activity, similar to a mechanically polished Pd₃Fe(111) surface.¹³ A slight improvement was observed on the sputtered, but unannealed Pd₃Fe(111) sample. Apparently, pure Pd(111) or rough

Pd₃Fe(111) surfaces are not good ORR catalysts. However, adding more Pd on the alloy surface by Pd vapor deposition at 300 K, followed by annealing at 900 K, significantly increased the ORR activity to a level of performance comparable to Pt(111). This is consistent to a previous report by Adzic.¹³ Interestingly, the highest ORR activity was obtained on the Pd₃Fe(111) surface that had been heated to 1250 K. . The half-wave potential ($E_{1/2}$) is often used as an indicator of activity and is the potential where the current is one-half of the limiting current. The Pd₃Fe(111) surface annealed at 1250 K had a value of $E_{1/2}$ shifted to 30 mV more positive than Pt(111) and 55 mV more positive than sputtered Pd₃Fe(111). The second highest ORR activity was obtained on the Pd₃Fe(111) surface that had been heated to 900 K, with 8% Fe at the surface. The kinetic current density for the Pd₃Fe(111) alloy surface annealed at 1250 K was five times larger than that from the sputtered alloy surfaces and 6-10 times larger than that for the annealed Pd(111) in the potential range of 0.80-0.90 V. A detailed analysis of all oxygen polarization curves is provided in the appendix. These investigations strongly indicate that an optimal surface concentration of ~10% Fe is needed to have high ORR activity for Pd-Fe alloys.

In order to help understand the role of surface Fe in ORR, DFT calculations were performed to explore oxygen adsorption and reaction on two different Pd-Fe surfaces. One was a Pd ML/Pd₃Fe(111) alloy surface and the other was a Pd₃Fe(111) alloy with a low Fe concentration of 6.25% at the surface. The adsorption energies of molecular oxygen on **Surface I** and **Surface II** are 0.74 eV and 1.24 eV, respectively, which reflects a stronger interaction between Fe and O₂ than that between Pd and O₂. Interestingly, the

dissociation of O₂ on **Surface II** is much easier than that on **Surface I**, with an energy barrier of 0.28 eV *versus* 1.02 eV from the energy profiles plotted in Figure 4.4. The small barriers both for O₂ dissociation and O atom diffusion provide the phenomenal benefit of having surface Fe for ORR, and this conclusion supports our experimental observations discussed above.

There is still considerable controversy about the detailed reaction mechanism in ORR, but it has been agreed upon that the rate determining step in ORR is either molecular oxygen dissociation, the first electron and proton transfer step, or the removal of surface oxygen adspecies.²⁵ It has been recognized that the Pd monolayer on Pd₃Fe(111) has different electronic properties than pure Pd, which causes a large difference in ORR activity between these two surfaces. A Pd monolayer on Pd₃Fe(111) has a d-band center that is shifted down by 0.25 eV compared to that of Pd(111), which significantly lowers the binding energy of O and OH to the surface and thus improves the removal of O and OH by protonation.²⁶ The presence of 10% randomly distributed surface Fe at the Pd₃Fe(111) surface that was annealed at high temperatures causes an inhomogeneity in the surface structure compared to the Pd monolayer and this adds complexity in explaining the catalytic activity simply by d-band shifting. Because of the small amount of Fe and large amount of Pd on these Pd₃Fe(111) surfaces, it is possible that a synergistic effect exists that takes advantage of the capability of Fe sites for strong oxygen adsorption/ dissociation and the capability of the Pd layer for fast removal of oxygen species by protonation. This process requires the oxygen species to “spillover” from Fe sites to Pd sites, and this process would be strongly affected by the diffusion

barriers of oxygen species on the surface. Figure 4.4 shows results of calculations that show that after O₂ dissociation at the Fe site, one O atom can diffuse easily across areas with pure Pd (represented by the diffusion of **O1**) with a small energy barrier of 0.25 eV. In contrast, the barrier for the second O atom to diffuse away from the Fe atom (represented by the diffusion of **O2**) is as high as 1.25 eV. This high barrier may result in irreversible adsorption of an oxygen atom to the Fe site, causing site-blocking of further reactions. Intriguingly, this pre-adsorbed O atom does not hinder further O₂ dissociation at the corresponding Fe site and the energy barrier to O₂ dissociation is 0.40 eV. Furthermore, the subsequent O diffusion away from the surface Fe atom is significantly promoted, with the energy barrier decreasing from 1.25 to 0.75 eV, as shown in Figure 4.A7 of the appendix. Therefore, a partial coverage of O adatoms near surface Fe sites not only preserves the high activity of these sites for O₂ dissociation, but also enhances O adatom diffusion near surface Fe sites. This synergistic feature could serve to balance the O₂ dissociation and O diffusion rates, so that the ORR process can optimally proceed.

A better understanding of the ORR mechanism at this surface requires much more detailed modeling of the many possible reaction pathways and the use of a much more complex environment for these processes, which is very complicated and beyond the scope of this thesis. However, we can conclude at this time that adding active metal elements that significantly enhance O₂ adsorption, and also forming enhanced Pd surface concentrations due to segregation, are important factors that increase ORR kinetics on Pd-based alloys.

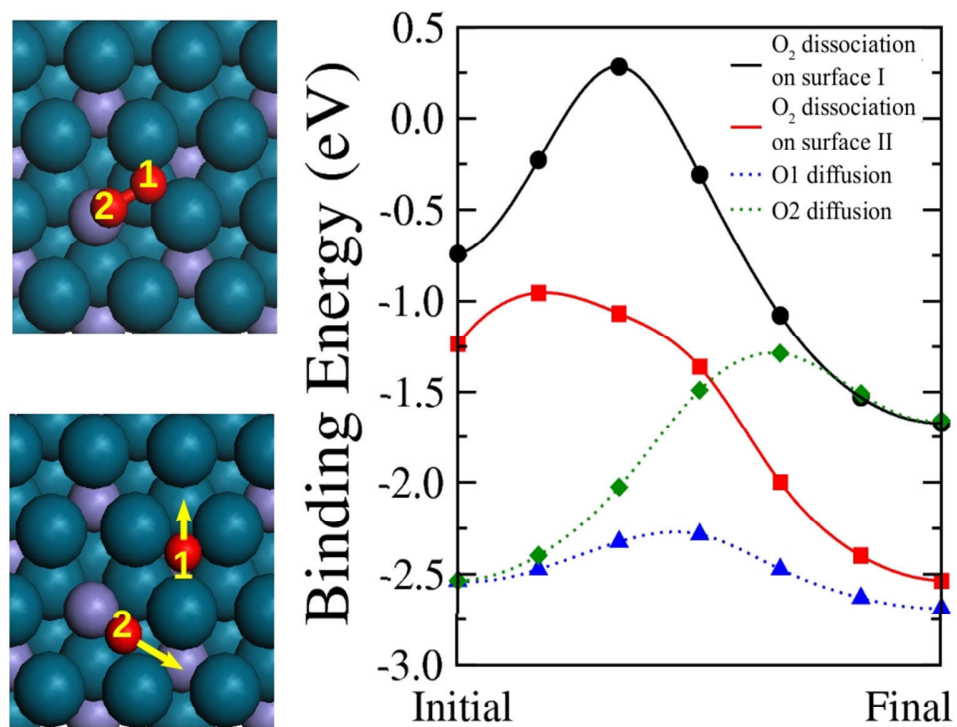


Figure 4.4 Top view of the O₂ adsorption configuration (left top panel) and the O₂ dissociation configuration (left bottom panel) on **Surface II**. Cyan, purple and red balls correspond to Pd, Fe and O atoms, respectively. Arrows indicate the diffusion pathways of the two oxygen atoms from O₂ adsorption denoted as **O1** and **O2**. The right panel plots energy profiles for dissociation of O₂ and diffusion of **O1** and **O2**.

4.4 Conclusions

In summary, we have prepared a Pd₃Fe(111) alloy single crystal in UHV with different surface compositions and morphologies and investigated the performance of these surfaces as cathode catalysts for the ORR. We observed a strong correlation of the electrocatalytic activity with the surface Fe concentration, with the highest performance at ~10% Fe. The Pd₃Fe(111) surfaces prepared by high-temperature heating in UHV were found to be 5-8 times more active than Pd(111) and 50% more active than Pt(111). This study not only demonstrates that Pd-Fe is a possible candidate to replace Pt as the cathode electrocatalyst, but also points out the important role of a small amount of active element in the alloy electrocatalysts. The presence of surface Fe atoms strongly impacts both O₂ adsorption and O₂ dissociation, which are important, perhaps rate-determining steps in ORR. While the stability of these alloys need to be evaluated by long-term studies, indications are that alloys containing significant concentrations of active metals at the surface can be prepared that show greatly improved stability over some previous results.

4.5 References

1. Paulus, U. A.; Wokaun, A.; Scherer, G. G.; Schmidt, T. J.; Stamenkovic, V.; Radmilovic, V.; Markovic, N. M.; Ross, P. N., Oxygen reduction on carbon-supported Pt–Ni and Pt–Co alloy catalysts. *J. Phys. Chem. B* **2002**, *106* (16), 4181-4191.
2. Stamenković, V.; Schmidt, T. J.; Ross, P. N.; Marković, N. M., Surface composition effects in electrocatalysis: Kinetics of oxygen reduction on well-defined Pt₃Ni and Pt₃Co Alloy surfaces. *J. Phys. Chem. B* **2002**, *106* (46), 11970-11979.
3. Stamenkovic, V. R.; Mun, B. S.; Arenz, M.; Mayrhofer, K. J. J.; Lucas, C. A.; Wang, G.; Ross, P. N.; M.Markovic, N., Trends in electrocatalysis on extended and nanoscale Pt-bimetallic alloy surfaces. *Nat. Mater.* **2007**, *6*, 241-246.
4. Chen, S.; Sheng, W.; Yabuuchi, N.; Ferreira, P. J.; Allard, L. F.; Shao-Horn, Y., Origin of oxygen reduction reaction activity on “Pt₃Co” nanoparticles: Atomically resolved chemical compositions and structures. *J. Phys. Chem. C* **2008**, *113* (3), 1109-1125.
5. Kowal, A.; Li, M.; Shao, M.; Sasaki, K.; Frenkel, A. I.; Adzic, R. R., Ternary Pt/Rh/SnO₂ electrocatalysts for oxidizing ethanol to CO₂. *Nat. Mater.* **2009**, *8*, 325-330.
6. Stamenkovic, V. R.; Fowler, B.; Mun, B. S.; Wang, G.; Ross, P. N.; Lucas, C. A.; Markovic, N. M., Improved oxygen reduction activity on Pt₃Ni(111) via increased surface site availability. *Science* **2007**, *315*, 493-497.
7. Xiong, L.; Manthiram, A., Effect of atomic ordering on the catalytic activity of carbon supported PtM (M = Fe, Co, Ni, and Cu) alloys for oxygen reduction in PEMFCs. *J. Electrochem. Soc.* **2005**, *152* (4), A697-A703.
8. Shao, M.-H.; Sasaki, K.; Adzic, R. R., Pd-Fe nanoparticles as electrocatalysts for oxygen reduction. *J. Am. Chem. Soc.* **2006**, *128* (11), 3526-3527.
9. Wang, W.; Zheng, D.; Dua, C.; Zhiqing Zoua; Zhang, X.; Xia, B.; Yang, H.; L.Akins, D., Carbon-supported Pd-Co bimetallic nanoparticles as electrocatalysts for the oxygen reduction reaction. *J. Power Sources* **2007**, *16*, 243.
10. Zhang, J.; Vukmirovic, M. B.; Xu, Y.; Mavrikakis, M.; Adzic, R. R., Controlling the catalytic activity of platinum-monolayer electrocatalysts for oxygen reduction with

different substrates. *Angew. Chem. Int. Ed.* **2005**, *44* (14), 2132-2135.

11. Zhang, J.; Lima, F. H. B.; Shao, M. H.; Sasaki, K.; Wang, J. X.; Hanson, J.; Adzic, R. R., Platinum monolayer on nonnoble metal-noble metal core-shell nanoparticle electrocatalysts for O₂ reduction. *J. Phys. Chem. B* **2005**, *109* (48), 22701-22704.

12. Adzic, R.; Zhang, J.; Sasaki, K.; Vukmirovic, M.; Shao, M.; Wang, J.; Nilekar, A.; Mavrikakis, M.; Valerio, J.; Uribe, F., Platinum Monolayer Fuel Cell Electrocatalysts. *Top. Catal.* **2007**, *46* (3), 249-262.

13. Zhou, W.-P.; Yang, X.; Vukmirovic, M. B.; Koel, B. E.; Jiao, J.; Peng, G.; Mavrikakis, M.; Adzic, R. R., Improving electrocatalysts for O₂ reduction by fine-tuning the Pt-support interaction: Pt monolayer on the surfaces of a Pd₃Fe(111) single-crystal alloy. *J. Am. Chem. Soc.* **2009**, *131* (35), 12755-12762.

14. Stamenkovic, V. R.; Mun, B. S.; Mayrhofer, K. J. J.; Ross, P. N.; Markovic, N. M., Effect of surface composition on electronic Structure, stability, and electrocatalytic properties of Pt-transition metal alloys: Pt-skin versus Pt-skeleton Surfaces. *J. Am. Chem. Soc.* **2006**, *128* (27), 8813-8819.

15. Yang, R.; Leisch, J.; Strasser, P.; Toney, M. F., Structure of dealloyed PtCu₃ thin films and catalytic activity for oxygen reduction. *Chem. Mater.* **2010**, *22* (16), 4712-4720.

16. Hirunsit, P.; Balbuena, P. B., Stability of Pt Monolayers on Ir-Co Cores with and without a Pd Interlayer. *J. Phys. Chem. C* **2010**, *114* (30), 13055-13060.

17. Sasaki, K.; Naohara, H.; Cai, Y.; Choi, Y. M.; Liu, P.; Vukmirovic, M. B.; Wang, J. X.; Adzic, R. R., Core-protected platinum monolayer shell high-stability electrocatalysts for fuel-cell cathodes. *Angew. Chem. Int. Ed.* **2010**, *49* (46), 8602-8607.

18. Yang, X.; Hu, J.; Wu, R.; Koel, B. E., Formation of Pd monomers and dimers on a single-crystal Pd₃Fe(111) surface. *J. Phys. Chem. Lett.* **2010**, *1* (16), 2493-2497.

19. Kresse, G.; Joubert, J., From ultrasoft pseudopotentials to the projector augmented-wave method. *Phys. Rev. B: Condens. Matter* **1999**, (59), 1758.

20. Anisimov, V. I.; Aryasetiawan, F.; Lichtenstein, A. I., First-principles calculations of the electronic structure and spectra of strongly correlated systems: The LDA+U method. *J. Phys. Condens. Matter.* **1997**, 767.

21. Higuchi, E.; Uchida, H.; Watanabe, M., Effect of loading level in platinum-dispersed carbon black electrocatalysts on oxygen reduction activity evaluated by rotating disk electrode. *J. Electroanal. Chem.* **2005**, *583* (1), 69-76.
22. Villullas, H. M.; Teijelo, M. L., The hanging-meniscus rotating disk (HMRD) Part 1. Dependence of hydrodynamic behavior on experimental variables. *J. Electroanal. Chem.* **1995**, *384* (1-2), 25-30.
23. Creemers, C., Dual mode segregation of Pd to the surface of polycrystalline Fe₉₉Pd₁. *Surf. Sci.* **1996**, *360*, 10-20.
24. Schmid, M.; Varga, P., Chapter 4 Segregation and surface chemical ordering--an experimental view on the atomic scale. In *The Chemical Physics of Solid Surfaces*, Woodruff, D. P., Ed. Elsevier: 2002; Vol. Volume 10, pp 118-151.
25. Nørskov, J. K.; Rossmeisl, J.; Logadottir, A.; Lindqvist, L.; Kitchin, J. R.; Bligaard, T.; Jónsson, H., Origin of the Overpotential for Oxygen Reduction at a Fuel-Cell Cathode. *J. Phys. Chem. B* **2004**, *108* (46), 17886-17892.
26. Shao, M.; Liu, P.; Zhang, J.; Adzic, R., Origin of enhanced activity in palladium alloy electrocatalysts for oxygen reduction reaction. *J. Phys. Chem. B* **2007**, *111* (24), 6772-6775.
27. Wang, J. X.; Markovic, N. M.; Adzic, R. R., Kinetic Analysis of Oxygen Reduction on Pt(111) in Acid Solutions: Intrinsic Kinetic Parameters and Anion Adsorption Effects. *J. Phys. Chem. B* **2004**, *108* (13), 4127-4133.
28. Anastasijevic, N. A.; Vesovic, V.; Adzic, R. R., Determination of the kinetic parameters of the oxygen reduction reaction using the rotating ring-disk electrode: Part II. Applications. *J. Electroanal. Chem. Interfacial Electrochem.* **1987**, *229* (1-2), 317-325.
29. Blöchl, P. E., Projector augmented-wave method. *Phys. Rev. B: Condens. Matter* **1994**, *50* (24), 17953.
30. Nørskov, J. K.; Rossmeisl, J.; Logadottir, A.; Lindqvist, L.; Kitchin, J. R.; Bligaard, T.; Jónsson, H., Origin of the overpotential for oxygen reduction at a fuel-cell cathode. *J. Phys. Chem. B* **2004**, *108* (46), 17886-17892.

4.6 Appendix

4.6.1 Surface stability

Surface elemental compositions were measured by LEIS before and after ORR experiments for each surface investigated. Significant loss of surface Fe was observed for the surface with 0.25-ML Fe that was prepared by one hour of sputtering using 1-keV Ar⁺. The annealed surface with 0.25-ML Fe was also severely dissolved by the electrolyte during ORR. This change was also reflected in the CVs obtained during continuous scanning that were shown in Figure 4.A2. The two annealed surfaces with less than 0.1-ML Fe were much more stable, showing a loss of about 1% after the CV and ORR measurements.

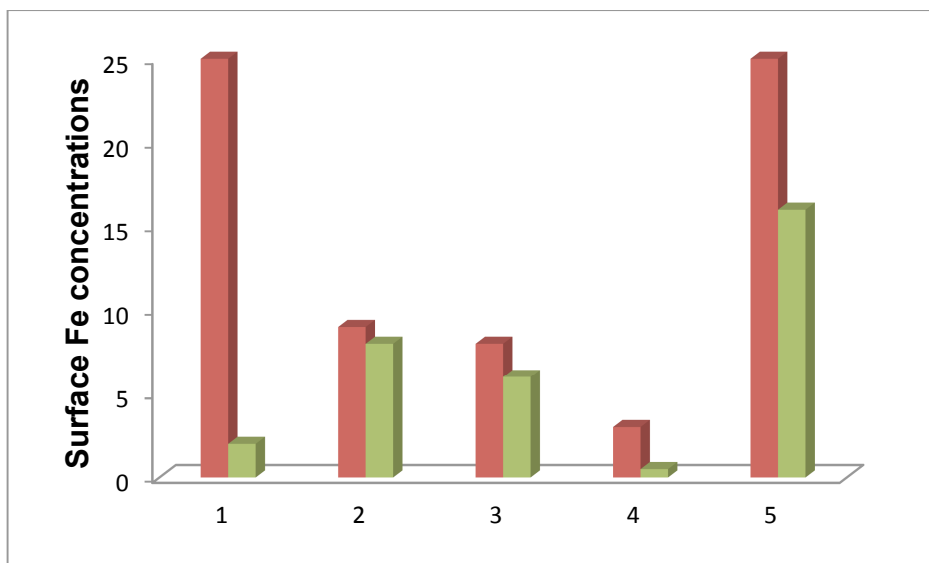


Figure 4.A1 Surface Fe concentrations before (red bar, left) and after (green bar, right) electrochemical experiments as determined by LEIS. The electrochemical experiments including both CV scanning and ORR measurements, in 0.1 M HClO₄, at 20 mV/s in the potential range of 100 mV ~1000 mV for 50 cycles. Five surfaces were prepared and investigated here: (1) sputtered Pd₃Fe(111); (2) Pd₃Fe(111) annealed at 1250 K; (3) Pd₃Fe(111) annealed at 900 K (4) Pd monolayer on Pd₃Fe(111), prepared by annealing the Pd₃Fe(111) crystal to 1000 K followed by deposition of 0.5-ML Pd at 300 K and then annealing to 900 K; and (5) smooth Pd₃Fe(111) surface with 0.25-ML Fe, prepared by annealing the Pd₃Fe(111) crystal to 1000 K followed by deposition of 0.5-ML Fe at 300 K and then annealing to 900 K, 60 sec. LEIS conditions: $E_i = 1000$ eV He⁺, 3.0 nA.

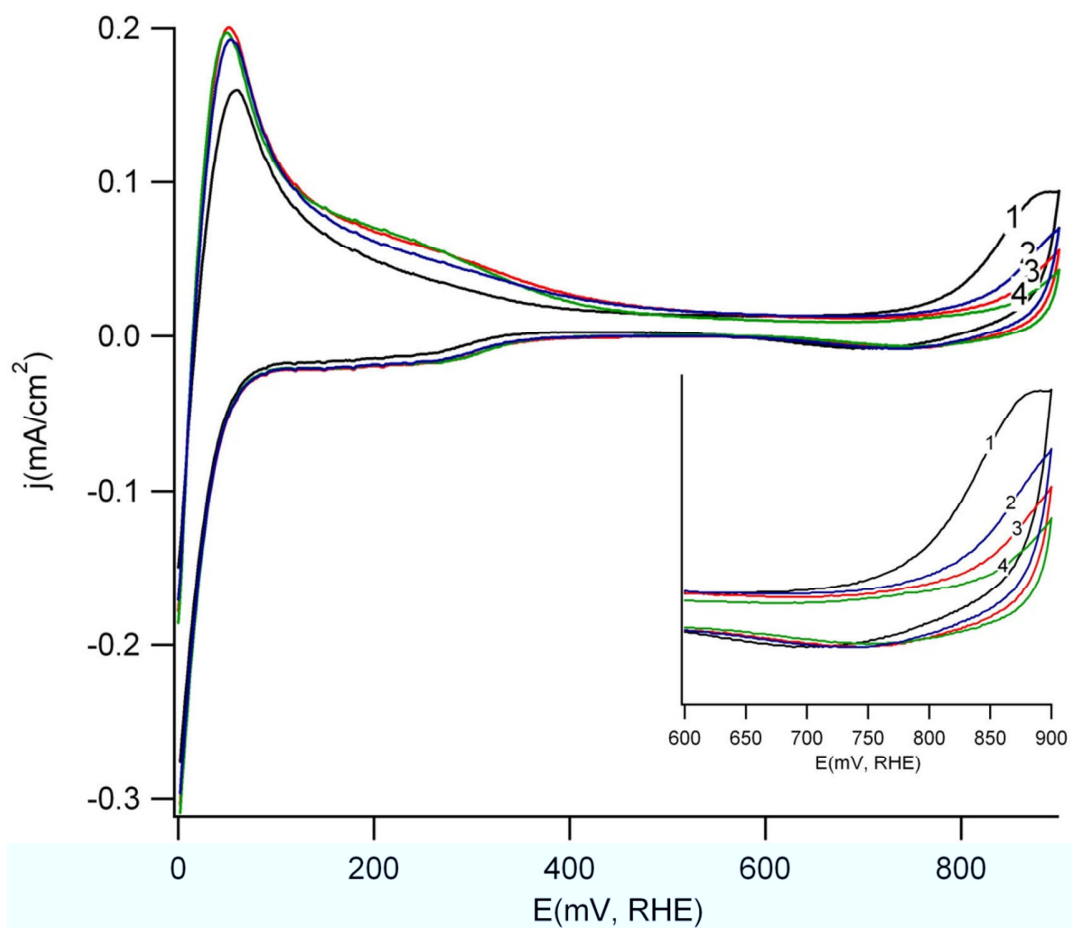


Figure 4.A2 Continuously scanned voltammetry curves for the smooth Pd₃Fe(111) surface with 0.25-ML Fe at 300 K in an Ar-purged 0.1 M HClO₄ solution. The sweep rate was 20 mV/s. Insert: Expansion of the range between 0.6 and 0.9 V.

4.6.2 Oxygen reduction reaction data

Table A1. Kinetic parameters for ORR in O₂-saturated 0.1 M HClO₄

	[Fe] _s ^a	E _{1/2} (mV)	<i>j_k</i> (mA cm ⁻²) ^b		
			@900mV	@850mV	@800mV
Annealed Pd ₃ Fe(111),1250 K	0.09	877	1.62	8.99	26.5
Annealed Pd ₃ Fe(111), 900 K	0.08	858	1.18	6.85	20.6
Pd monolayer on Pd ₃ Fe(111)	0.02	845	0.741	3.72	11.84
Pt(111)	0	850	0.921	3.94	16.2
Pd(111)	0	815	0.221	1.55	5.92
Sputtered Pd ₃ Fe(111)	0.25	822	0.372	2.03	7.02

^a [Fe]_s: Fe concentration at surface

^b *j_k*: kinetic current corrected for diffusion

The kinetic current *j_k* is calculated based on the Koutecký-Levich equation²⁷

$$\frac{1}{j_k} = \frac{1}{j} - \frac{1}{j_d} \quad (3)$$

Where *j* is the measured current in the ORR polarization experiments, *j_d* is the limiting current, calculated by Eq. (2) described in the experimental method. The current at 800, 850 and 900 mV are calculated.

The original ORR data of Pd₃Fe(111) annealed at 1250 K, Pd monolayer on Pd₃Fe(111), Pd(111) and sputtered Pd₃Fe(111) are plotted in Figures 4.A3, 4.A4, 4.A5 and 4.A5, respectively. Koutecký–Levich(K-L) plots and Tafel curve at 900 rpm are also

calculated for the 1250-K annealed Pd₃Fe(111). The K-L plots with linearity and parallelism suggest first-order kinetics with respect to molecular oxygen.²⁸

The Tafel plot is calculated based on Tafel equation for the reduction reaction:

$$j_c = j_0 \exp[-\alpha_c nF(E-E_0)/RT] \quad (4)$$

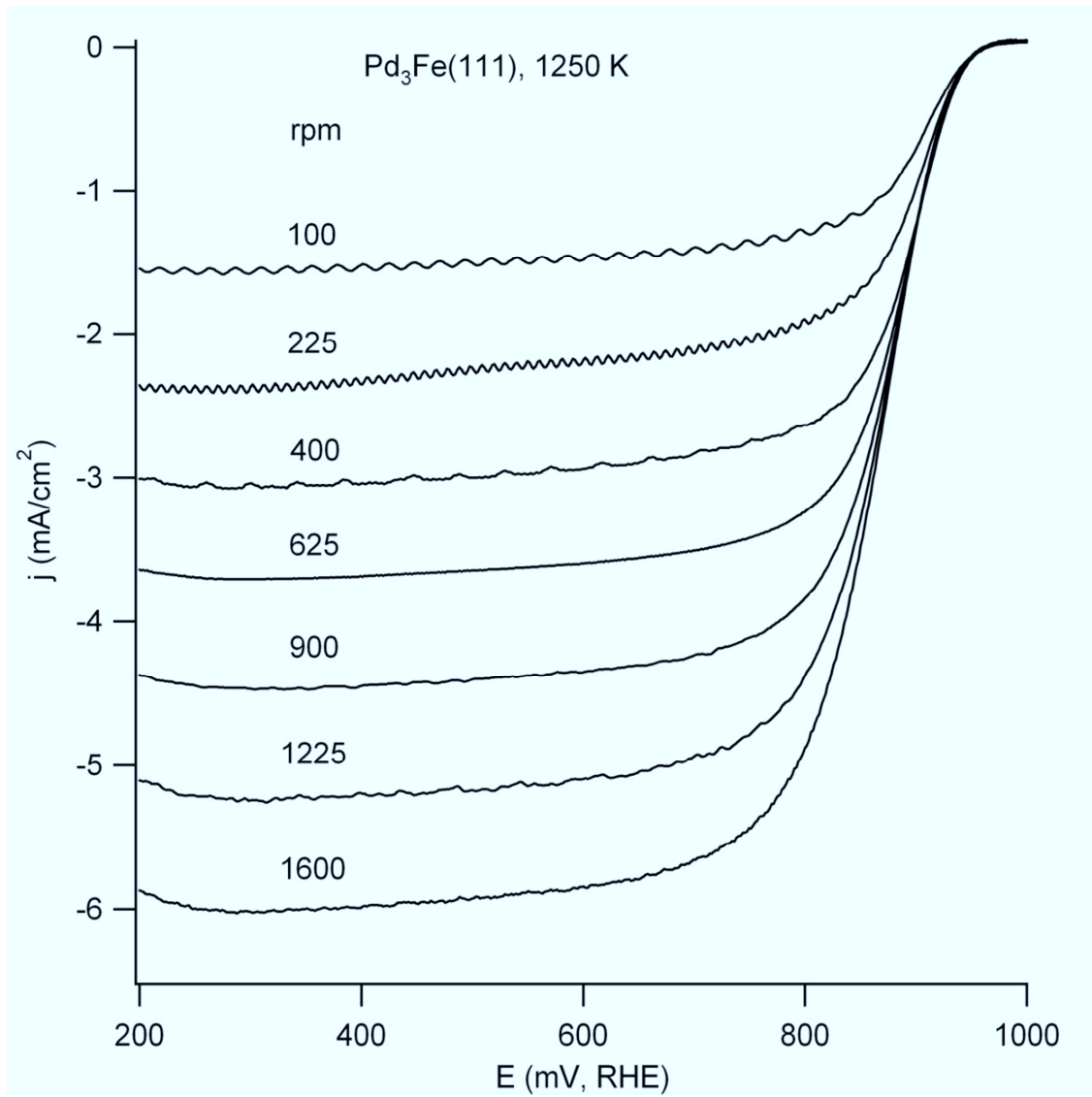
Where j_c is the cathode current density at potential (E), j_0 is the exchange current at standard potential E_0 , α_c is charge transfer coefficient and its value is 0.5,²⁹ F is Faraday constant, R is the gas constant, T is the absolute temperature (K).

There is a linear relation between $\log(j_c)$ and the applied potential and slope is $-\alpha_c nF/RT$. The theoretical value of the Tafel slope is 120 mV dec⁻¹ for a $n=4$, four electron transfer reaction.

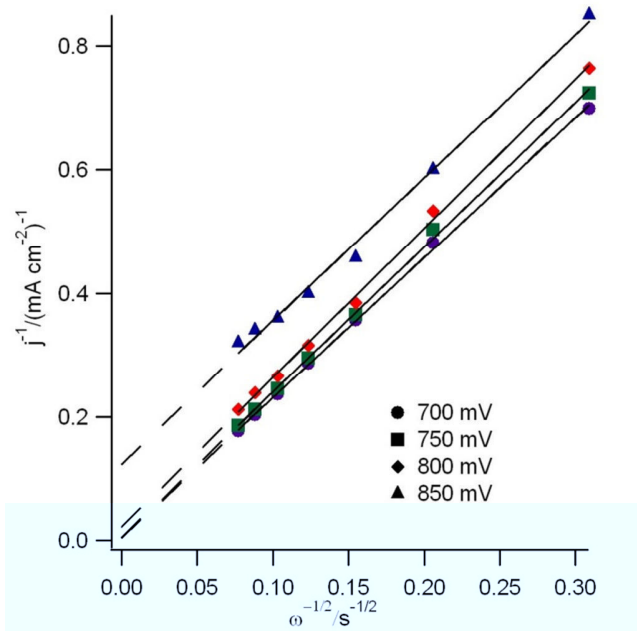
Two Tafel slopes were observed for Pd₃Fe(111) annealed at 1250 K : -56 mV dec⁻¹ in the potential range of 0.93 V > E > 0.87 V and -111 mV dec⁻¹ in the potential range of 0.86 V > E > 0.75 V. Similar Tafel slopes were also reported for Pt(111) in 0.1 M HClO₄ solution.²⁷ People still are inconsistent in explaining these two different slopes observed for ORR.²⁹ A Tafel slope of 60 mV/dec indicates a reaction order of 0.5 with respect to O₂. However, with consideration of the blocking and/or the electronic effect by the adsorbed oxygen-containing species, the apparent Tafel slope is different from the intrinsic Tafel slope, which is described in the chapter 1-Tafel analysis.

We also believe that the effect of adsorbed oxygen must be considered in the potential range of 0.75~0.86 V. Therefore, the Tafel plot of -111 mV/dec is in accordance with the first, one-electron-transfer step being the slow step in the ORR sequence, proposed by Norskov,³⁰ which is discussed in Chapter 1-Mechanism of ORR.

A.



B.



C.

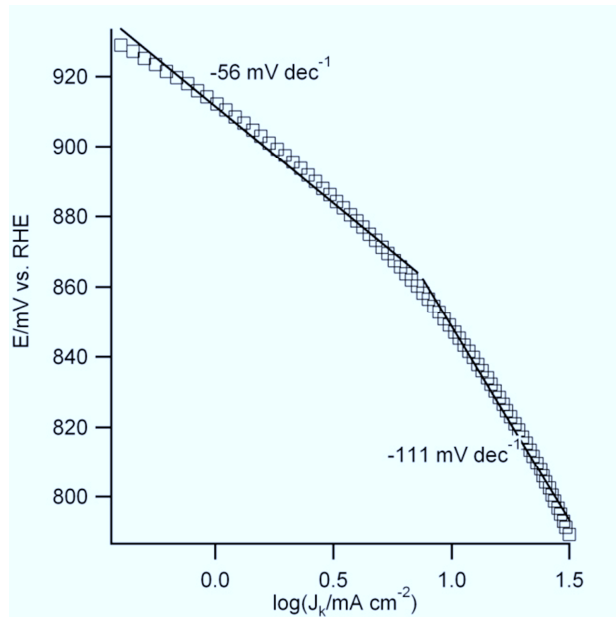


Figure 4.A3 A. RDE voltammograms for ORR on the 1250-K annealed Pd₃Fe(111) sample in O₂-saturated 0.1 M HClO₄ at different rotation rates. The current density was calculated by normalizing the voltammetric current to the geometrical area of the electrode. DC ramp 20 mV/s. B. Koutecký–Levich plot at various potentials. C. Tafel plot at 900 rpm. The two slopes are fitted linearly by dividing the data in two groups: 0.75~0.86 V and 0.86~0.95 V.

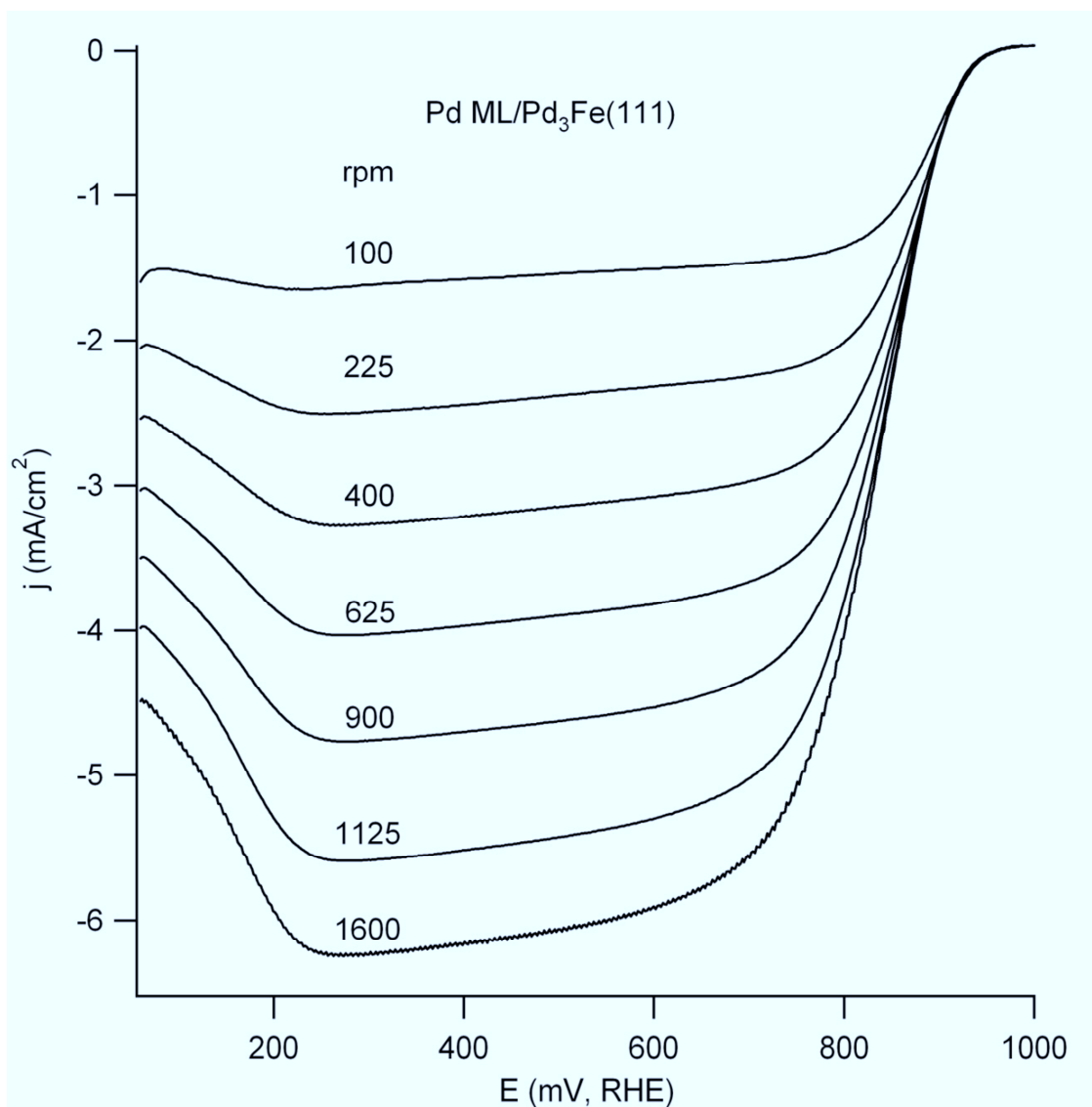


Figure 4.A3 RDE voltammograms for ORR on the PdML/Pd₃Fe(111) sample in O₂-saturated 0.1 M HClO₄ at different rotation rates. The current density was calculated by normalizing the voltammetric current to the geometrical area of the electrode.

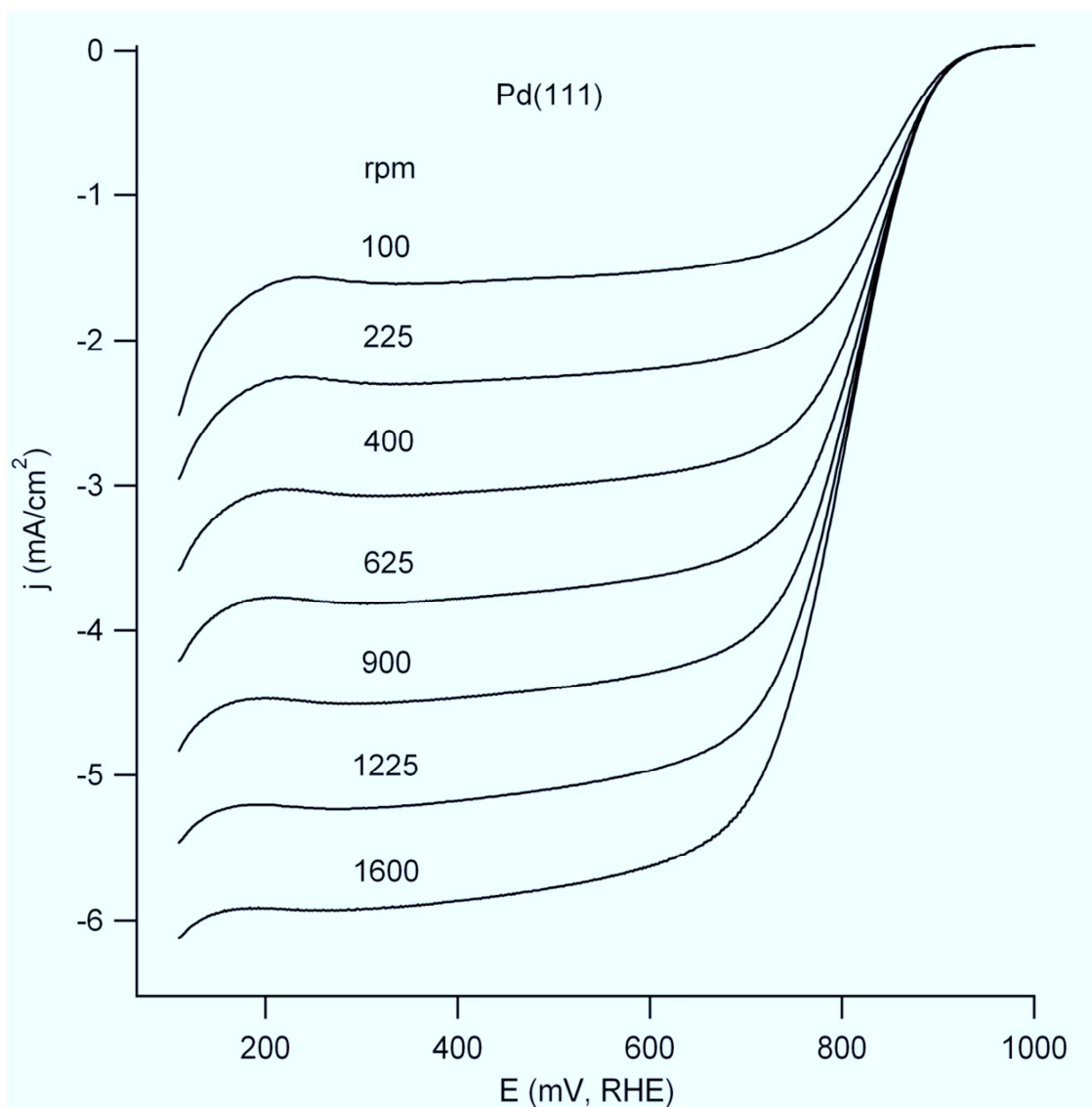


Figure 4.A5 RDE voltammograms for ORR on Pd(111) in O_2 -saturated 0.1 M HClO_4 at different rotation rates. The current density was calculated by normalizing the voltammetric current to the geometrical area of the electrode. DC ramp 20 mV/s.

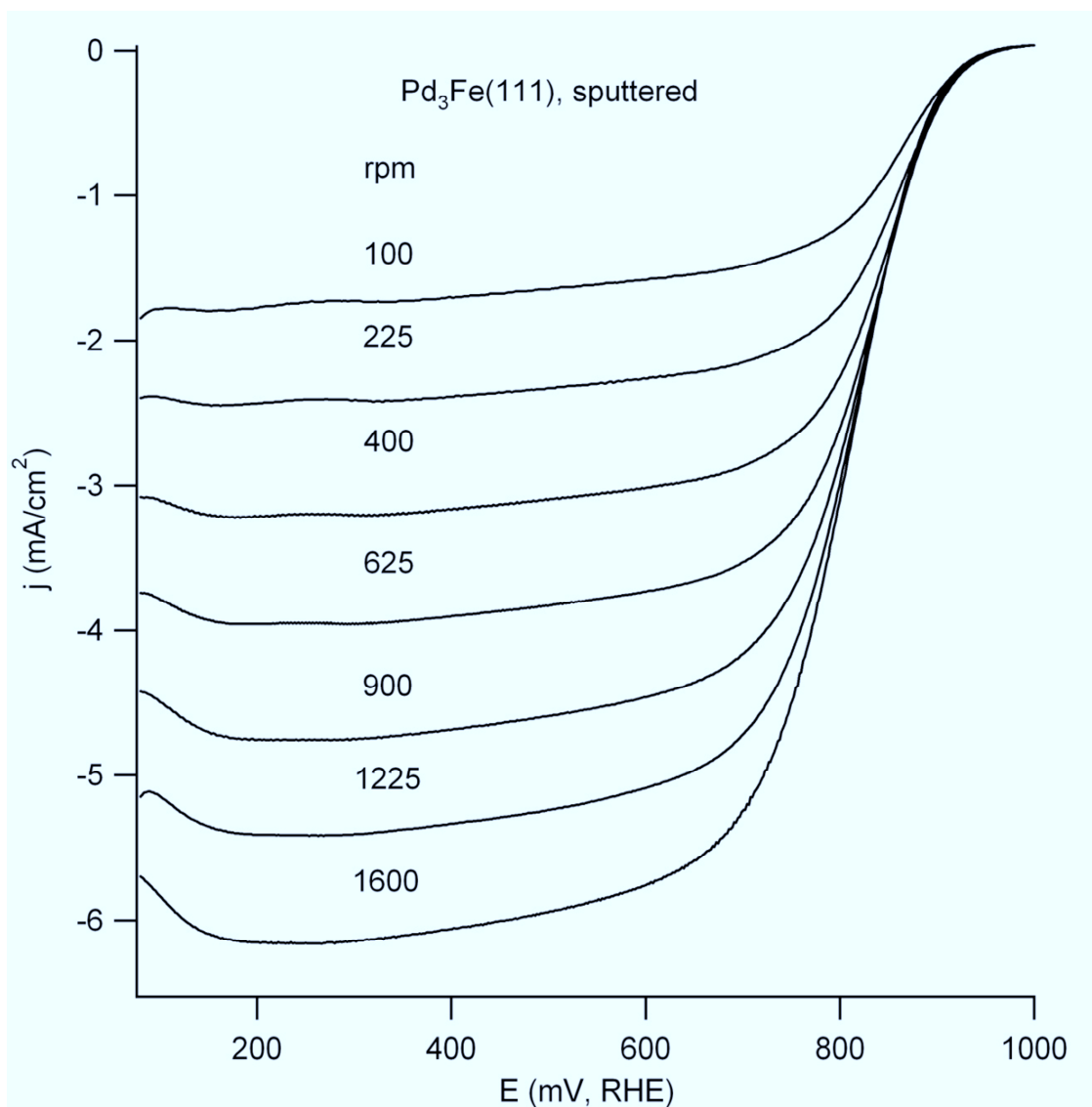


Figure 4.A6 RDE voltammograms for ORR on the sputtered Pd₃Fe (111) sample in O₂-saturated 0.1 M HClO₄ at different rotation rates. The current density was calculated by normalizing the voltammetric current to the geometrical area of the electrode. DC ramp 20 mV/s.

4.6.3 Oxygen reactions on an O-precovered Pd₃Fe(111) surface

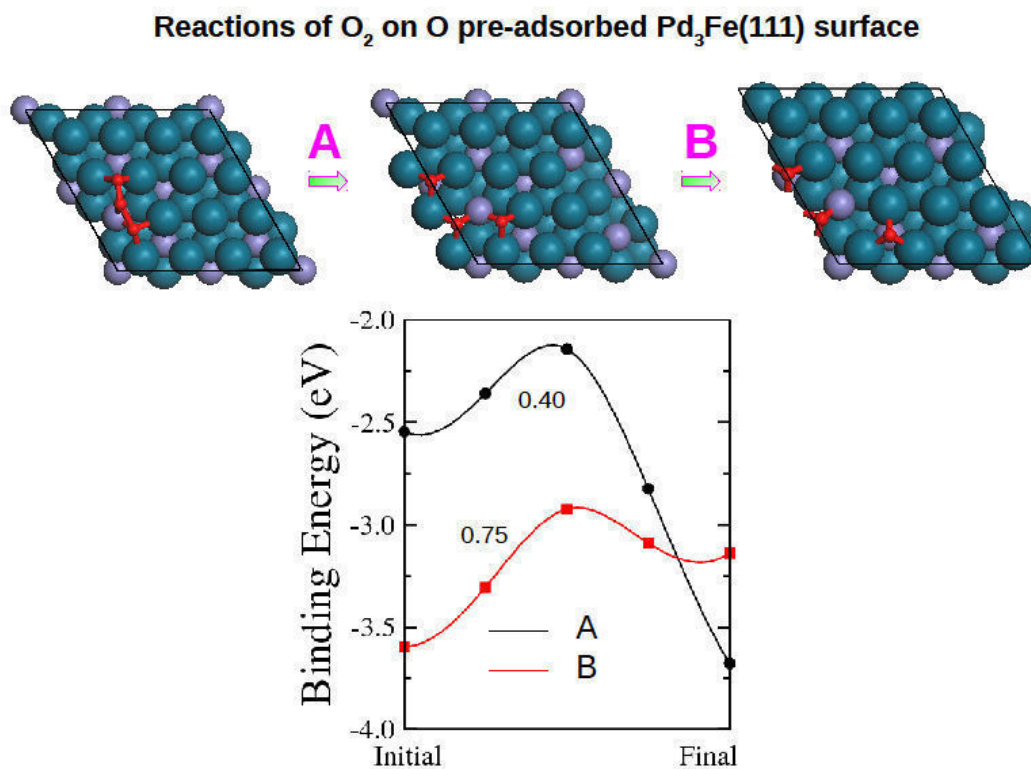


Figure 4. A7 O₂ dissociation and diffusion at the Pd-Fe surface with coadsorbed oxygen adatoms at Fe sites.

Curve A is the free energy profile of O₂ dissociation at a Fe site with a pre-adsorbed O. A small reaction barrier 0.4 eV is found for this process, indicating that this reaction can take place at room temperature easily. The blocking effect of O is studied by calculating the diffusing free energy of one O atom away from Fe site to Pd site. The barrier for this process (B) is 0.75 eV, suggesting a weak blocking effect.

Chapter 5 Identification of the High Activity of a Submonolayer Au Film on Pd₃Fe(111) For the Oxygen Reduction Reaction

5.1 Introduction

The sluggish kinetics of the electrochemical reduction of molecular oxygen in polymer electrolyte membrane fuel cells (PEM-FCs) requires continued search for proper catalysts. The cost and stability of the catalysts are also important for developing economic and long lifespan fuel cells. Ultra-low Pt-loading catalysts, such as those made from a Pt monolayer (ML) on Pd₃Fe nanoparticles, have been found that are not only more active but also more stable than Pt.¹ It is widely recognized that surface monolayers perform very differently than the bulk materials.²⁻⁶ In general, the mismatch of the lattice constant between the metal substrate and the surface layer causes tension or compression in the surface layer, and this modifies the *d*-band center of the surface layer, which determines the interaction between surface and oxygen species.⁷ As we realized that the alloying effects from mixing two elements can modify both the geometric structure and electronic properties, we also considered that the introduction of a third element would further increase the complexity but provide greater flexibility to tune the reactivity. This chapter discusses our study of a ternary surface alloy system, Au-Pd₃Fe(111), that was motivated by this concept. This alloy contains a mixture of elements that are relatively chemically inert (Au), moderately active (Pd), and active (Fe) with the aim of synthesizing a ternary alloy that will have both improved reactivity and stability over that of Pd₃Fe(111) in the ORR. We discovered that we could indeed prepare a ternary surface

alloy that exhibited twice the ORR activity as Pt (111) and an improved stability compared to Pd₃Fe(111). This work successfully demonstrated a special role of surface Au and opens new possibilities to develop highly active Au-based catalysts.

In general, bulk gold is an oxidation-resistant metal and it is regarded as a catalytically inactive material. However, Au clusters at the nanoscale (less than 10 nm in diameter) are active in a wide variety of chemical reactions, such as the oxidization of methanol,⁸ oxidation of ethanol,⁹ oxidization of CO,¹⁰ selective hydrocarbon oxidation,¹¹ water-gas shift reaction, and selective oxidation of styrene.¹² Molecular oxygen does not dissociatively adsorb at bulk Au surfaces at room temperature, but effectively does so on supported Au nanoparticles.¹³⁻¹⁴ This finding indicates a potential application for nano-Au in the cathode catalyst for the ORR. Previous investigations have shown that the ORR activity of Au was greatly affected by particle size, pH of the electrolyte, surface structure¹⁵ and support materials (Au/SnO₂, Au/MnO₂, Pd).¹⁶⁻¹⁷ Interestingly, some new applications of Au have been discovered recently. Since Au is chemically inert and selectively aggregates at defect sites, Pt catalysts modified by Au nanoclusters exhibit significant improvements in durability without lowering the activity.¹⁸ Au was also studied as a support for Pd or Pt monolayer catalysts or as a core material in core-shell catalysts.¹⁹ Even though improved reactivity was found for pure or supported Au clusters, these catalysts are still much worse than typical Pt-based catalysts and so are not viable as new cathode catalysts. Importantly, the work discussed in this chapter found that Au at sub-monolayer coverage could be very active. The activity was strongly dependent on the Au coverage, with the best results obtained for a submonolayer amount of Au (0.6 ML) on a Pd₃Fe(111) substrate showing high activity in an acid electrolyte.

5.2 Experimental details

Synthesis of the ternary alloy surface of Au/Pd₃Fe(111) was performed by physical vapor deposition of Au on a clean and annealed Pd₃Fe(111) single crystal surface at 300 K in a UHV system. The experimental details of preparing the Pd₃Fe(111) surface were described in Chapter 2. The growth of Au films was monitored by XPS and LEIS. A gold metal evaporator was constructed by wrapping pure gold wire (0.001 in. in diameter, 0.9999 purity from ESPI) around a shaped tungsten wire (0.01 in. in diameter, 0.999 purity from ESPI) filament as shown in Figure 5.1. Prior to use for Au deposition, the W wire was heated up to the melting point of gold and a gold “drop” was formed at the top of the “V” of the shaped W wire in vacuum. This procedure was necessary to achieve reproducible Au dosing. The W wire was heated slightly below the melting point of Au to degas the evaporator until the base pressure did not increase during heating (2.0×10^{-10} torr). An evaporator with a W heating wire with a suitable resistance (~0.5 ohms) and good thermal contact between the gold and W wire were important for making a reliable and repeatable doser. Spot welding could improve the thermal contact, but caution should be taken to avoid copper contamination from the spot welder tips. The dosing conditions had to be optimized and kept unchanged to have accurate and reproducible Au deposition during dosing. The dosing conditions include the precise position of the sample relative to the location of the doser, the evaporator warm-up temperature and time, and the dosing current and time. The resistance of the Au doser was observed to change after a period of time of use due to gold evaporation. The doser was recalibrated as needed if the doser performed abnormally, such as if the dosing rate became too high.

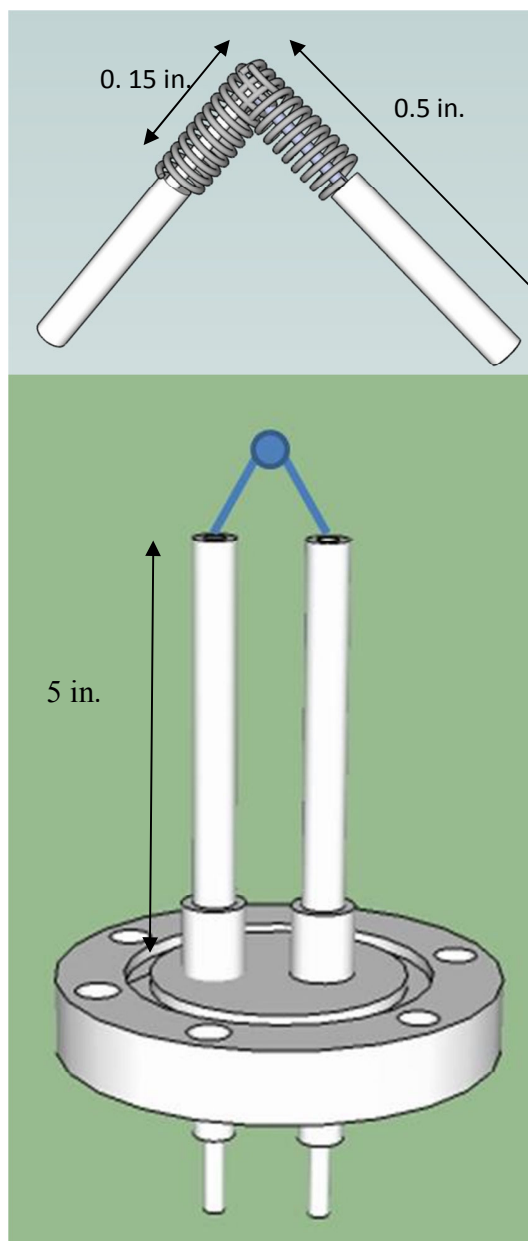


Figure 5.1 Schematic view of a gold doser on a 2.5-in feedthrough. The “V” shaped gold doser is attached at the ends of the two copper rods by set screws. Top: Expanding view of the “V” shaped gold doser. Thin gold wire is wrapped at the tip of a 0.5-in long “V” shaped tungsten heating wire. Dosing conditions: 1 ML Au is dosed in 5 min when the doser is operated at 3.0 V, 4.1 A.

The coverage of Au at the surface was determined by the ratio of the Au LEIS peak intensity to the Au LEIS peak intensity of a Au(111) single crystal sample or from a Au film surface that completely covered the substrate. If a Au(111) crystal is used as the standard, the difference in atom density between Au(111) and Pd₃Fe(111) needs to be considered, but this should not be an important difference. The surface composition of the Au/Pd₃Fe(111) sample before and after electrochemical measurements (both CV and ORR) were measured by XPS and LEIS. It is important to note that the sample surface could be covered with a full monolayer of adsorbates (OH, H, and/or H₂O) after electrochemical experiments. To be able to determine the Au and Pd surface coverage, it is necessary to carry out a light preferential sputtering of these adsorbates to remove them from the surface. Continuously obtaining LEIS spectra with the ion gun on (He⁺ ions, 1.6 keV, 10 nA, ~2 mm in diameter) lightly sputters the surface and the Pd and Au peaks should appear and increase in intensity with time. Since Pd and Au are heavy atoms, the sputtering cross section is much lower and one can realize conditions where this can be negligible and still obtain the LEIS spectra. We observed that after the adsorbates were sputtered away, the Pd and Au peak intensities would stay unchanged for quite some time (10 mins) and then the Au signal would start to decrease a small amount due to the weak sputtering effect on Au. Intensities recording in the “constant peak” region were used to calculate the surface coverages of Pd and Au.

Other experimental details regarding the electrochemical analysis are the same as those described in the experimental sections in Chs. 2 and 3. After electrochemical experiments, the potential of the sample was controlled at zero by the potentiostat versus RHE. Then, the cell was disconnected and the sample was cleaned by pure water (HPLC

grade, Fisher) and dried by high purity He gas (99.99%, Airgas), Finally, the sample was transferred back to the UHV chamber for surface analysis.

5.3 Results and discussion

5.3.1 Synthesis of an Au ML on Pd₃Fe(111) by physical vapor deposition (PVD) of Au

An Au film was grown epitaxially by physical vapor deposition (PVD) of Au on a clean Pd₃Fe(111) surface at 300 K, which had been previously annealed to 1100 K.

Figure 5.2A and B shows the Pd 3d_{5/2} and Au 4f_{7/2} core level peaks in XPS, and illustrates how these peak intensities change as the amount of deposited Au increases. LEIS spectra shown in Figure 5.2C were used to determine the Au coverages given in the labels in Figure 5.2. The absolute Au coverage was calculated as the peak area ratio of the Au LEIS peaks to that from Au(111) in Figure 5.2C.

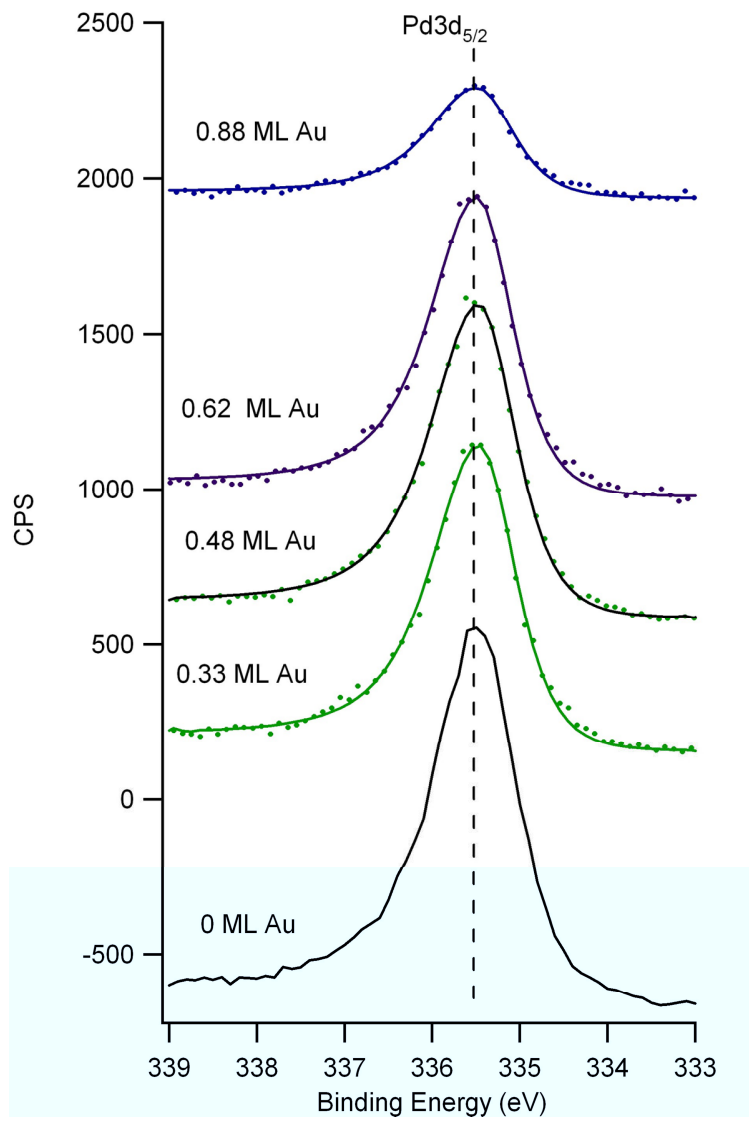
The increase in size of the Au 4f_{7/2} peak was accompanied by a reduction in the size of the Pd 3d_{5/2} peak. The Au 4f_{7/2} peak position was found to shift from 84.12 eV binding energy (BE) at Au coverages less than 0.6 ML to 83.96 eV BE at 0.9 ML Au coverage. For calibration, the Au 4f_{7/2} peak position was set to 84.10 eV BE for the clean Au(111) crystal sample. The shift with Au coverage indicates an electronic effect, probably formation of a mixed Au-Pd surface alloy layer at lower coverages.

Both Fe and Pd peaks in LEIS spectra decreased as the Au coverage increased. Deposition of Au seems to preferentially cover Fe site and we observed that the Fe LEIS peak completely disappeared at 0.9 ML Au coverage. This feature of Au film growth may indicate a capability of Au for protecting the active metal, Fe, from attack by the acid electrolyte in later electrochemical experiments.

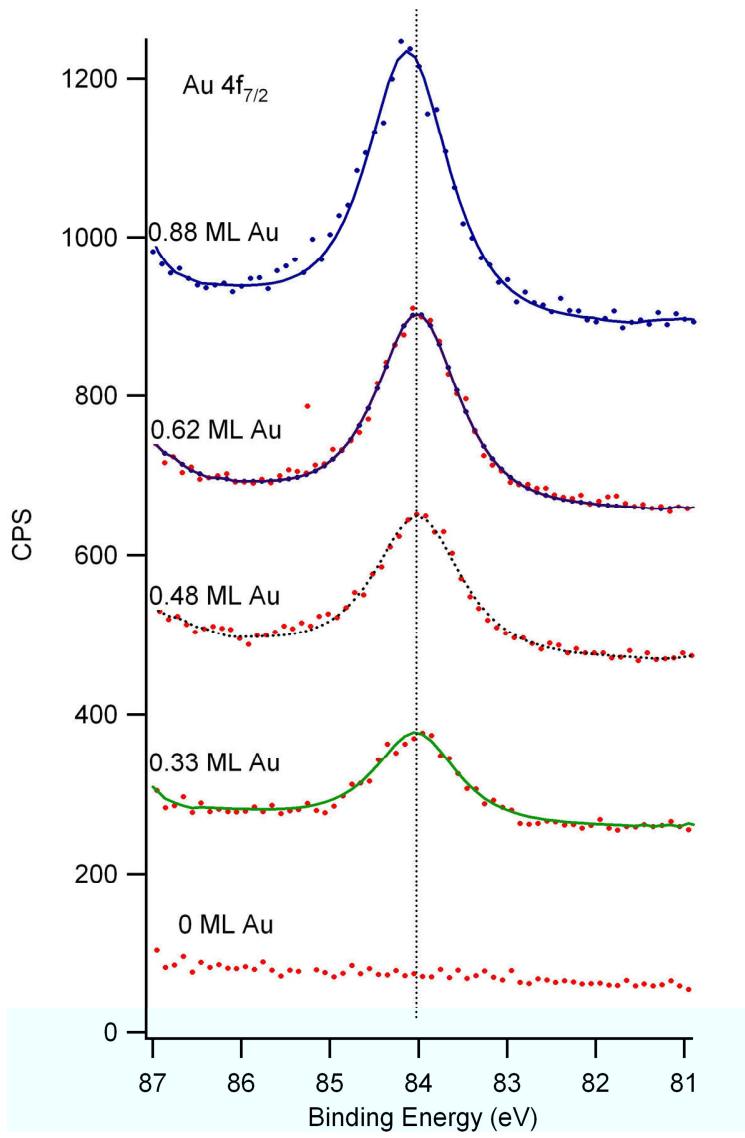
The Pd₃Fe(111) surface annealed at 1100 K has 0.9 ML Pd segregated at the surface, and so a better representation for the Au coverage surface is Au_{*x*}/Pd/Pd₃Fe(111), in which *x* is the Au coverage in units of fractional monolayer. Four surfaces with different Au coverages were prepared and electrochemical analysis including CV in Ar-purged acid (HClO₄) solution and polarization curves for the ORR in O₂-purged acid (HClO₄) solution was carried out at each surface.

The vacuum-prepared Au_{*x*}/Pd/Pd₃Fe(111) surfaces were transferred out into the electrochemistry cell for electrochemical analysis. As described in detail in Ch. 1, a special sample holder was used that fit both the manipulator in the UHV chamber and the electrode connector of the electrochemical cell, which facilitates clean transfer between the high-pressure reaction cell on the UHV chamber and external electrochemical cell.

A.



B.



C.

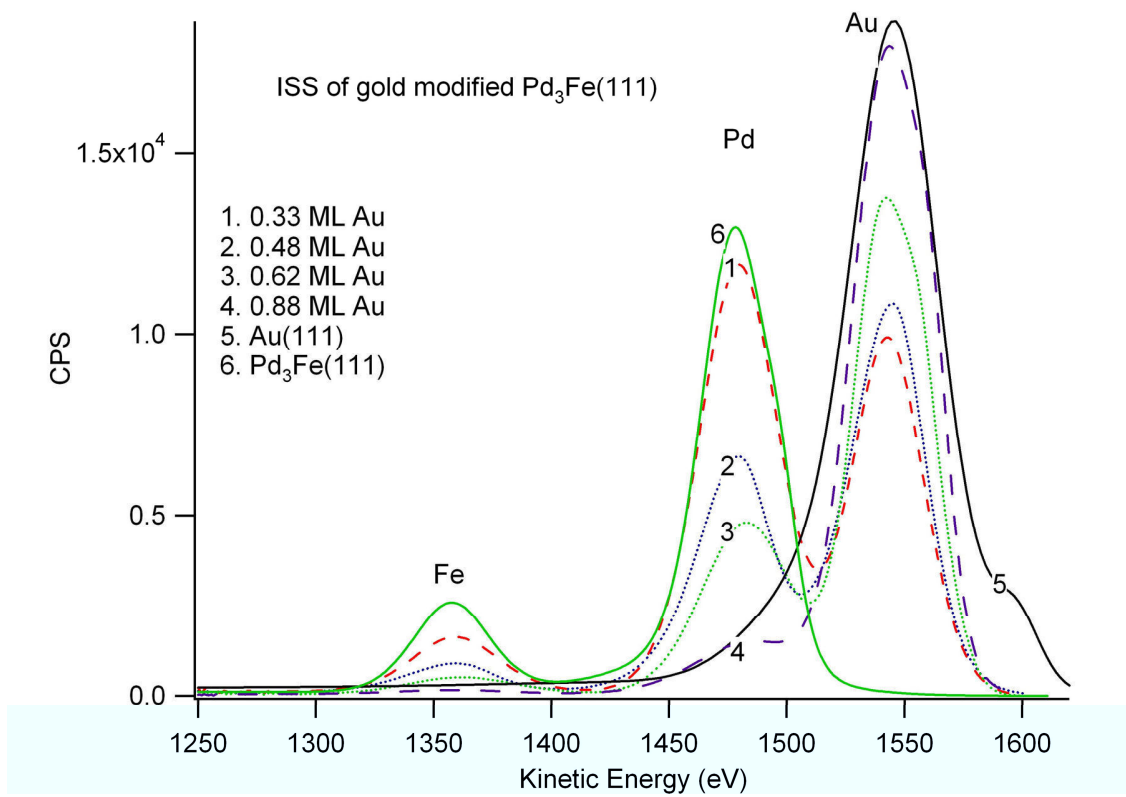


Figure 5.2 Au film growth on Pd₃Fe(111) monitored by XPS and LEIS. A. Pd 3d_{5/2} XPS spectra of Au-modified Pd₃Fe(111). B. Au 4f_{7/2} XPS spectra of Au-modified Pd₃Fe(111). C. LEIS of Au-modified Pd₃Fe(111). XPS parameters: Mg K α , 20 mA emission; pass energy, 46.75 eV. ISS parameters: 1.6 KeV Ar⁺, 10 nA, pass energy: 1127.1 eV.

5.3.2 Cyclic voltammetry (CV) measurements

CV scans were performed in Ar gas-purged, 0.1 M HClO₄ solution, cycled in potential between 0 and 1000 mV at a scan rate of 20 mV s⁻¹. Addition of Au to the surface completely changed the electrochemical properties as shown by the hydrogen adsorption/desorption (H_{ads/des}) features and surface-oxide formation/reduction (Oxide_{form/red}) features, which are displayed in the four paired CVs in Figure 5.3. The H_{ads/des} peaks are significantly reduced by adding Au. However, this change was not linearly correlated with the Au coverage. For example, the H_{ads/des} peak obtained at the surface with 0.33 ML Au was much smaller than that at the surface with 0.48 ML Au. The onset potentials for surface oxidation were shifted positively by a large amount, ~ 100 mV. As the Au film coverage approached one monolayer, its behavior became similar to that of bulk gold. There was no any surface oxide formation up to 1000 mV. The CVs for all the gold-modified surfaces were very stable for long scanning times in the Ar-purged solution (tested up to 200 cycles). However, after the ORR experiments, all the CVs were very different, as shown by the colored curves in Figure 5.3. There was a large change in H_{ads/des} peaks before and after the ORR measurements for all the gold-modified surfaces. The H_{ads/des} peaks recovered an intensity comparable to the H_{ads/des} peak obtained at Pd-Pd₃Fe(111). The Oxide_{form/red} features were also different before and after the ORR measurements for most Au-modified surfaces except those at high Au coverages, where the surface was still very inert and free of oxides at potentials up to 1000 mV. Apparently, all the surfaces experienced extensive reconstruction during the ORR measurements. The oxygen must play an important role for this reconstruction, because the surfaces were stable in the Ar-purged solutions. Figure 5.4 compares the CVs

of $\text{Au}_x/\text{Pd}/\text{Pd}_3\text{Fe}(111)$ and $\text{Pd}/\text{Pd}_3\text{Fe}(111)$ surfaces after the ORR measurements. The $H_{\text{ads/des}}$ peak of the surface without Au increased significantly in intensity after long scanning times (200 Cycles, 0~1100 mV). This behavior was likely caused by the dissolution of Fe into the electrolyte. After this loss of surface Fe, the surface behaved like pure Pd, and the near surface Pd layers could participate in hydrogen desorption and adsorption. The protecting role of surface Au is apparent since the $H_{\text{ads/des}}$ peaks after the reconstruction were stable for long scanning times. The Au-covered surfaces became less active when the coverage was close to one monolayer. In this case, the surfaces were not covered by OH species at all and the $H_{\text{ads/des}}$ peak was also very small. The large differences in $\text{Oxide}_{\text{form/red}}$ behavior observed for all Au covered surfaces may be important to determine their ORR activities as discussed below.

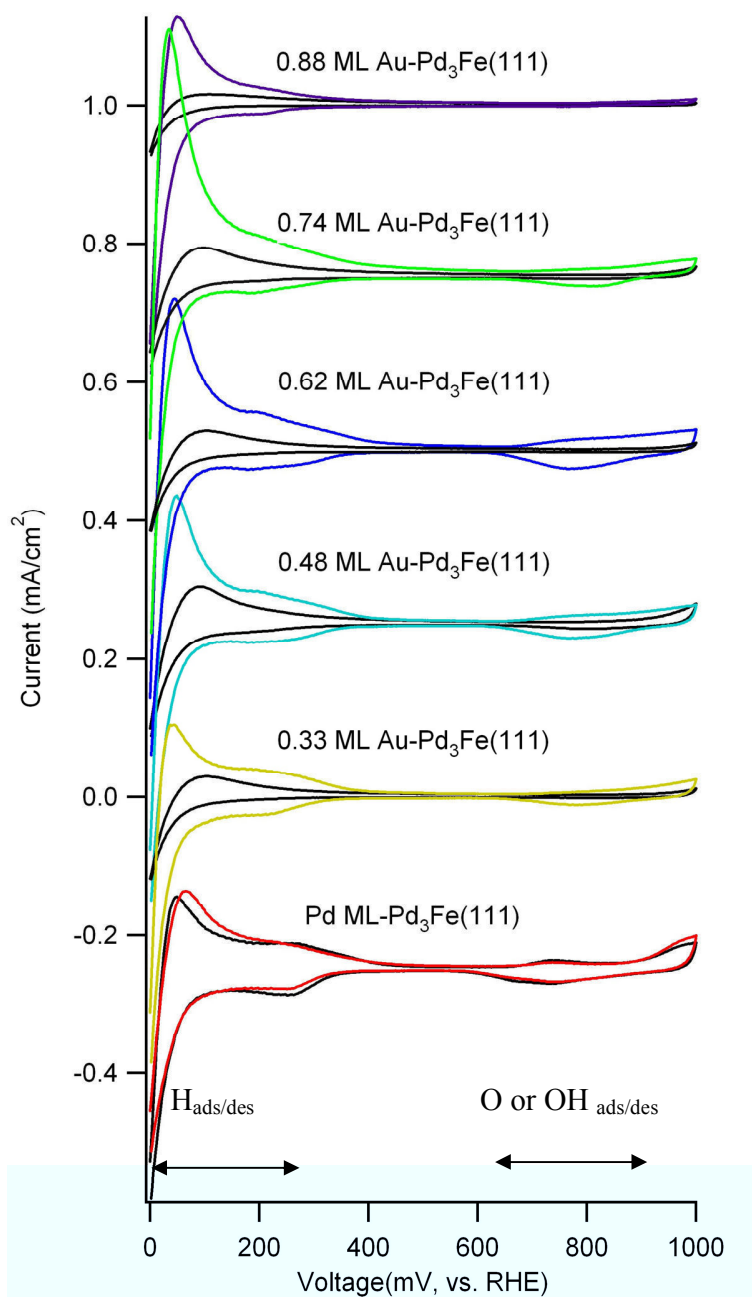


Figure 5.3 Linear sweep voltammetry curves for Au_x/Pd/Pd₃Fe(111) surfaces in Ar-saturated 0.1 M HClO₄ before (black) and after measurements of the ORR kinetics (colored). The arrows labeled the H_{ads/des} region and Oxides_{form/red} (or O/OH_{ads/des}) region.

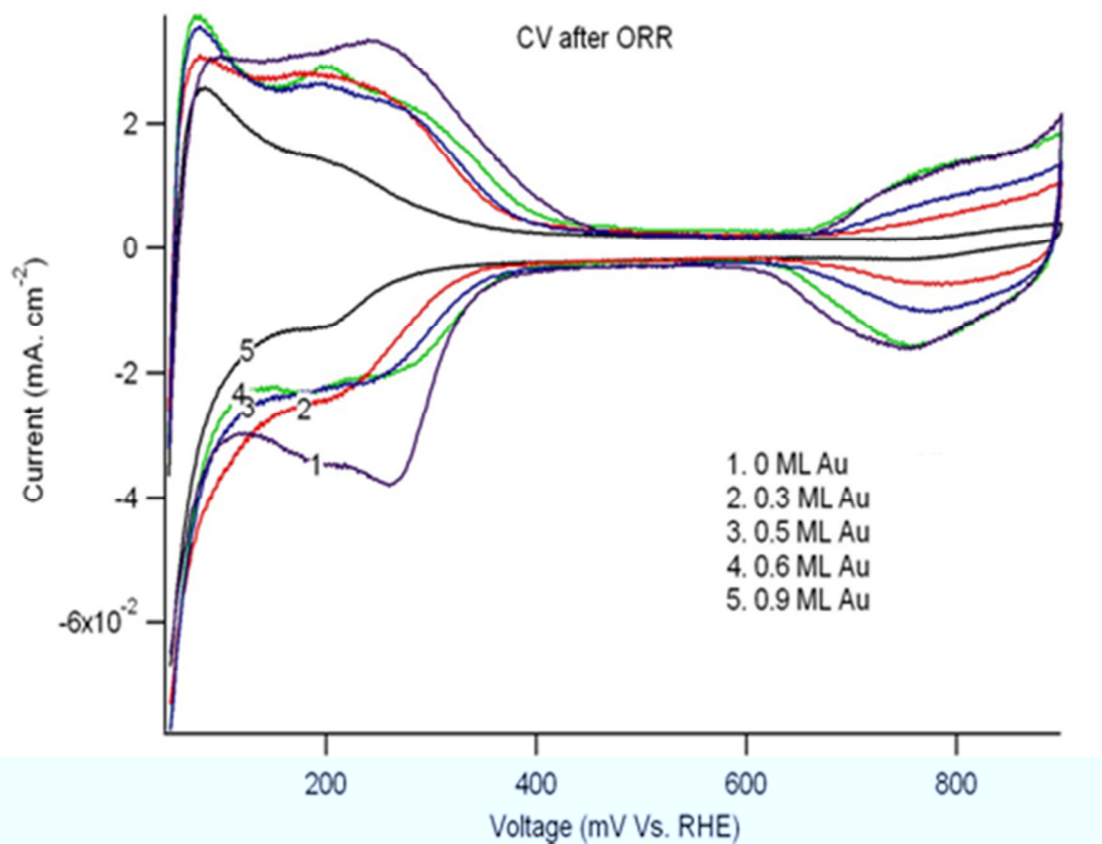


Figure 5.4 Comparison of CV curves for Au_x/Pd/Pd₃Fe(111) surfaces in Ar-saturated 0.1 M HClO₄ solution after polarization curves were obtained for measuring the ORR. Curve 1 was from the annealed Pd/Pd₃Fe(111) surface after 200 ORR scanning cycles. Larger H_{ads/des} peaks indicate the surface was not stable and the surface area increased after surface Fe was dissolved.

5.3.3 ORR kinetics

The ORR performance for all the $\text{Au}_x/\text{Pd}/\text{Pd}_3\text{Fe}(111)$ surfaces were examined in 0.1M HClO_4 solution at 300 K. Figure 5.4 shows a set of these ORR polarization curves. In general, the polarization curves clearly display two different regions, the well-defined limiting currents (j_D) in the potential region of 0.2 ~ 0.75 V and the mixed diffusion-kinetic control region of 0.75 ~ 0.95 V. Bulk gold doesn't have any ORR activity in the potential range of 0.2 ~ 0.95 V. All Au-modified Pd/Pd₃Fe(111) surfaces displayed much higher activity than Au(111). Their ORR activities were largely dependent on the Au coverage. However, the Au coverage doesn't affect the activity linearly. A volcano type of relationship between the activity and the Au coverage was shown in Figure 5.6, with the highest activity at 0.6 ML Au. All other kinetic parameters are shown in Table 5.1. We note that the ORR performance of 0.6 ML Au-modified Pd/Pd₃Fe(111) is better than Pt(111). All other kinetic data are listed in Table 5.1.

Generally speaking, in order to have fast ORR kinetics, the binding between oxygen and the active sites should be neither too strong nor too weak. On one hand, strong binding helps electron transfer between adsorbed O_2 and the surface, but it hinders O diffusion and desorption from the surface. The blocking effect by adsorbed oxygen slows down the ORR kinetics. On the other hand, weak binding helps with removal of oxygen, but hinders electron transfer. So, there is a volcano relationship between the ORR performance and the oxygen binding energy. The ORR performance of Au-covered surfaces provides a good example to clearly display this effect. We must realize that most Au modified surfaces should have weaker interaction with oxygen than that on Pd₃Fe(111).

As we have discussed, $\text{Oxide}_{\text{form/red}}$ behavior at these surfaces is affected by the Au coverage. The largest oxidation and reduction peaks were found at the surface with 0.6 ML Au, suggesting that this surface has stronger interaction with oxygen species than other surfaces. Therefore, all other Au-modified surfaces fall on one side of the volcano plot, characterized by a weak oxygen binding interaction. It is hard to understand why surface with less Au coverage (0.3 ML Au) is less active than surface with higher Au coverage (0.6 ML Au). It cannot be explained only by the inert properties of Au. In an attempt to understand the role of Au in this regard, we studied the surface structure and composition by XPS and LEIS in UHV after the electrochemical experiments.

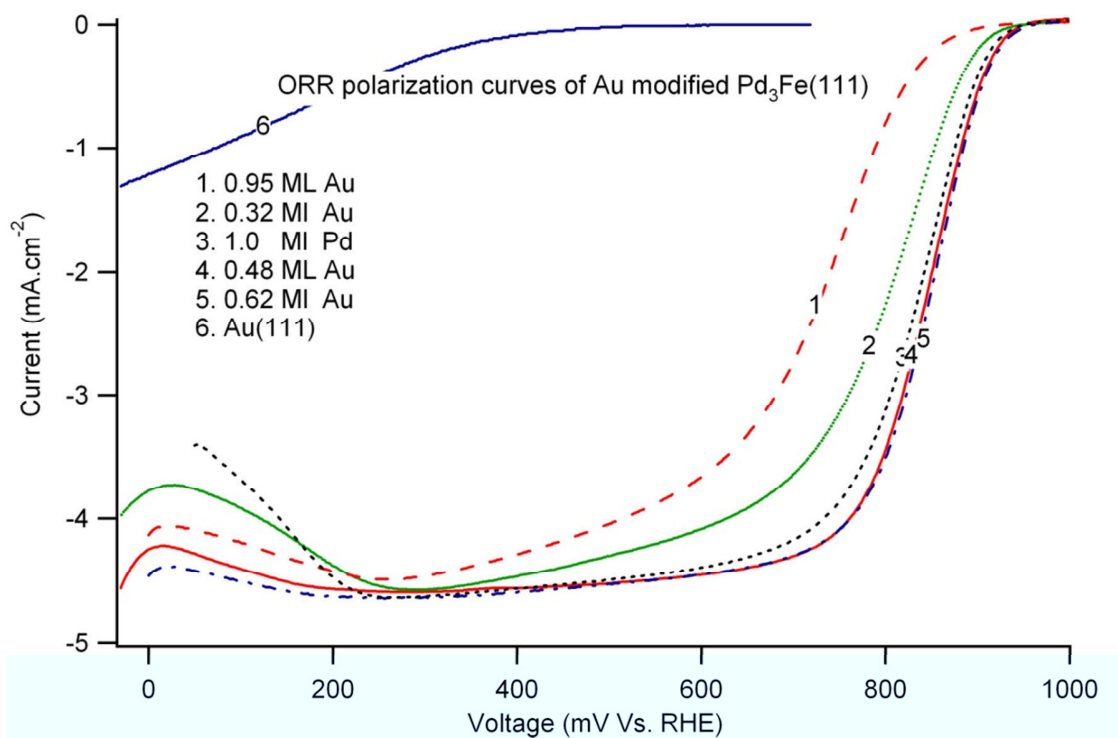


Figure 5.5 Comparison of ORR polarization curves for Au_x/Pd/Pd₃Fe(111), Pd/Pd₃Fe(111) and Au (111) surfaces. Polarization curves were obtained at 300 K in an O₂-purged 0.1 M HClO₄ solution with a sweep rate of 20 mV/s and rotation rate of 900 rpm.

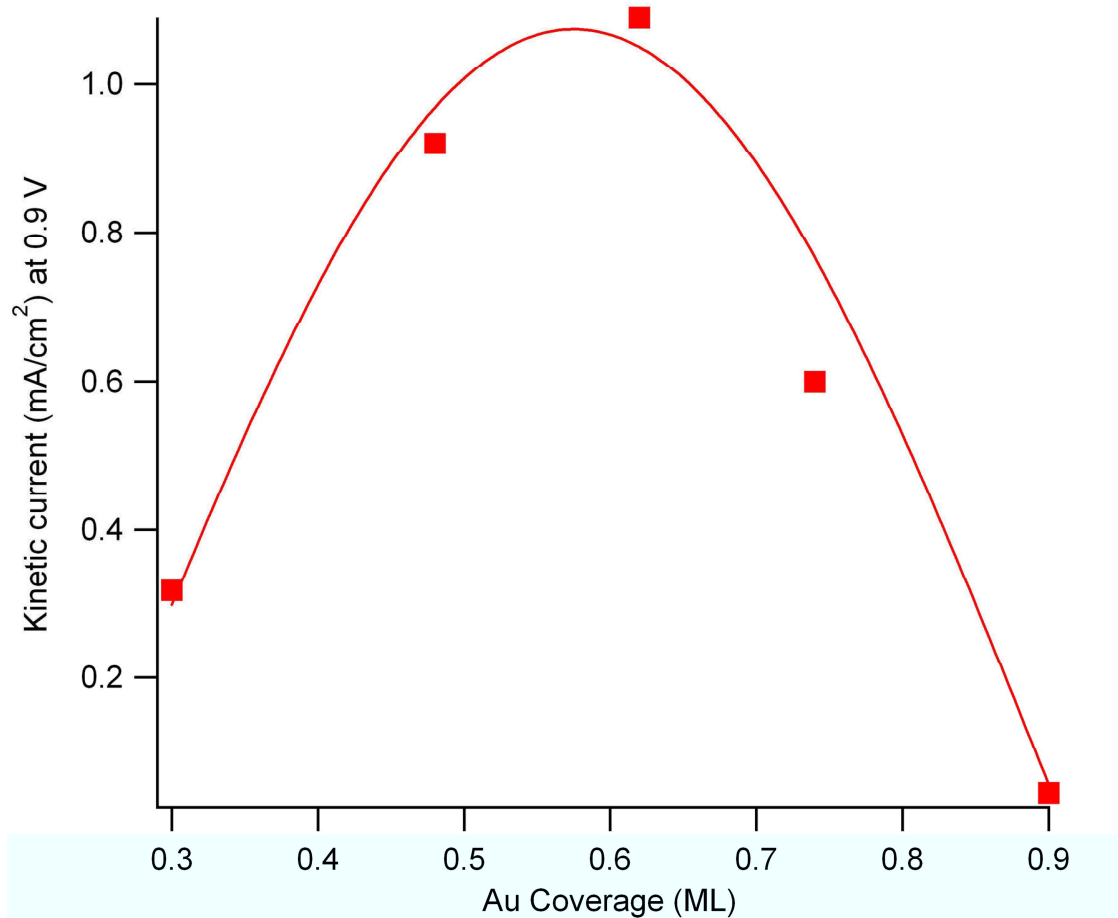


Figure 5.6 Influence of the Au film coverage on Pd/Pd₃Fe(111) on the ORR kinetic current at 0.9 V (vs. RHE). Measurements were obtained at 300 K in an O₂-purged 0.1 M HClO₄ solution with a sweep rate of 20 mV/s and rotation rate of 900 rpm.

Table 5.1. Kinetic parameters for the ORR of Pd ML-Pd₃Fe(111), Pt(111), and Au_x/Pd/Pd₃Fe(111) surfaces at 900 rpm.

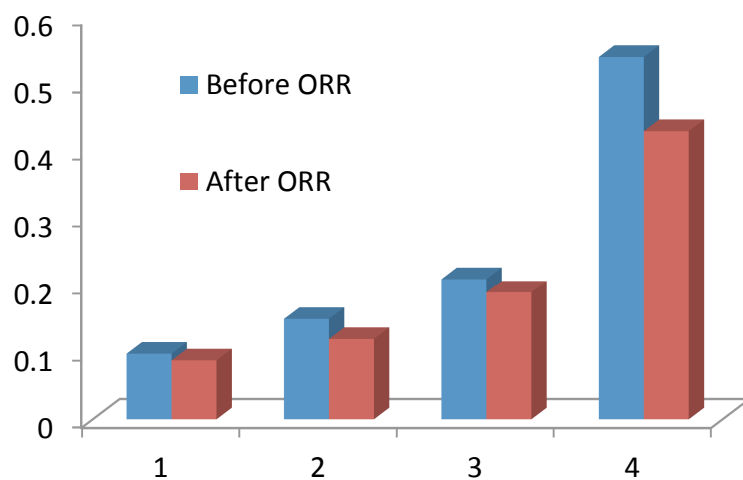
	$E_{1/2}$ (mV)	j_k (mA cm ⁻²)		
		@900m V	@850mV	@800mV
Pd ML-Pd ₃ Fe(111)	845	0.741	3.72	11.84
0.32 ML Au on Pd ₃ Fe(111)	810	0.318	1.85	5.33
0.48 ML Au on Pd ₃ Fe(111)	850	0.918	4.70	17.4
0.62 ML Au on Pd ₃ Fe(111)	860	1.09	5.65	18.9
0.90 ML Au on Pd ₃ Fe(111)	730	0.045	0.282	1.09
Pt (111)	850	0.921	3.94	16.2

5.3.4 Surface characterization after electrochemical analysis

To understand how the Au_x/Pd/Pd₃Fe(111) surface changes during the ORR measurements, all the surfaces were transferred back to the UHV chamber and measured by XPS and LEIS. The surface compositions from these measurements are plotted and compared in Figure 5.6. The relative composition of Au and Pd in the sample surface measured by XPS did not exhibit large differences, but the outermost layer compositions measured by LEIS were totally different. The Au intensities were reduced to one-half of their original values after the ORR measurements. This difference between XPS and LEIS is easy to understand since XPS usually analyzes several layers near the surface, which is specifically dependent on the mean free path of the photoemitted electrons and the detection angle.²⁰⁻²¹

There are two possible reconstructions, as shown schematically in Figure 5.8A and B, that are consistent with the observations by XPS and LEIS. In both cases, the total amount of gold at surface or in the near-surface layers is 0.6 ML. It can be expected that the XPS signal from the 0.6 ML Au film before ORR measurements would not be very different than that after ORR measurements for both of the illustrated cases of reconstruction. However, the LEIS signal for Au would be greatly reduced if the gold forms clusters or diffuses into the near surface layers. STM should be very helpful to distinguish these two situations. The STM image in Figure 5.8c shows large atomically flat terraces without a significant amount of clusters. This result supports the reconstruction occurring with the formation of a surface alloy as shown in Figure 4.8b. Therefore, it appears that a Au-Pd alloy is formed on the Pd₃Fe(111) surface at room temperature in the presence of oxygen and applied potentials (up to 1.0 V *versus* RHE).

A.



B.

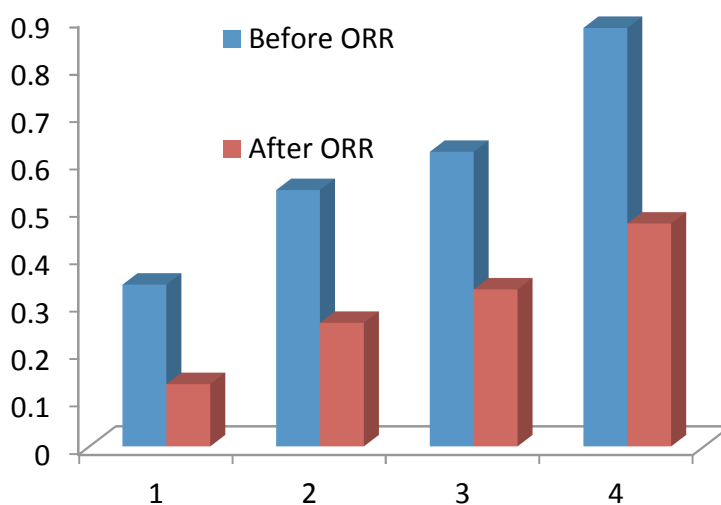


Figure 5.7 Characterization of Au_x/Pd/Pd₃Fe(111) surfaces by A. Au_{4f_{7/2}}/Pd_{3d_{5/2}} XPS peak area ratio, B. Au peak area measured by LEIS. Little Au concentration change in the near surface region was revealed by XPS, but the Au surface concentration measured by LEIS was reduced by about one-half after polarization curves were measured for the ORR performance. So, the Au_x/Pd/Pd₃Fe(111) surfaces reconstruct during ORR to form a Au-Pd surface alloy.

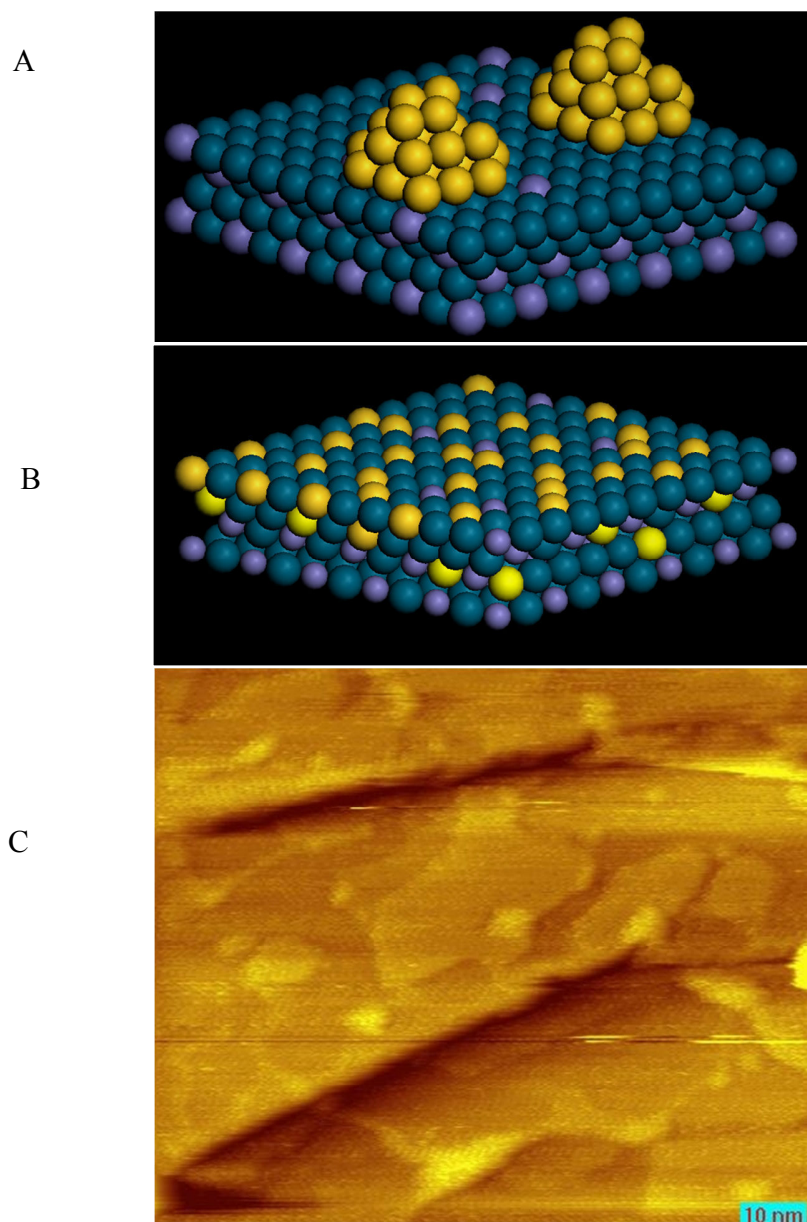


Figure 5.8 Schematic depictions of two possible reconstructions for $\text{Au}_x/\text{Pd}/\text{Pd}_3\text{Fe}(111)$ surfaces with 0.6 ML Au induced by polarization measurements of the ORR activity: A. Au nanocluster formation and B. Formation of a near surface Au-Pd alloy. C. STM image of the $\text{Au}_x/\text{Pd}/\text{Pd}_3\text{Fe}(111)$ surface after electrochemical measurements of the ORR. Image size: $100 \times 85 \text{ nm}^2$. Image conditions: -154 mV , 0.62 nA .

5.3.5 Importance of reactive sites and oxygen spillover in the reaction mechanism for the ORR on Au_x/Pd/Pd₃Fe(111) surfaces

We have shown the Au_{0.6}/Pd/Pd₃Fe(111) surface reconstructed to form a Au-Pd surface alloy with about 0.3 ML Au in the first layer during the electrochemical measurements of the ORR. A mechanism for the ORR on these surfaces is proposed in Figure 5.9. This proposal is based on the knowledge that the large difference in strength of Au-O and Pd-O bonding causes different roles for Pd and Au in the reduction of O₂ molecules. Specifically, O₂ molecules adsorb and dissociate at sites with Pd atoms. Surface-bound oxygen species are able to diffuse from Pd atoms to Au atoms fairly easily, where surface oxygen reacts with protons and desorbs from the surface as H₂O molecules. In Ch.4, a similar mechanism was discussed for Pd_{0.9}Fe_{0.1}/Pd₃Fe(111) surfaces, on which oxygen species interact with Pd and Fe differently. That mechanistic discussion was supported by DFT calculations. The mechanism proposed here seeks to explain the different roles of the surface Pd and Au atoms instead of focusing on the electronic structural changes due to alloying. It is difficult to prove this mechanism experimentally, but there is support provided for it by the surface composition analysis that showed all the surface Au atoms were covered by oxygen species. This is based on the observation that the Au peak only started to appear after the ion gun was on for 5 mins during an ion scattering experiment. The ions gradually sputter off the light species (OH) to expose the Au.

Analysis of this surface by XPS found no Au oxides or Pd oxides formed after the ORR measurements. Formation of stable oxides would not likely be benign to the ORR activity since the surface active sites would presumably be bonded to oxygen permanently and not available for additional O₂ adsorption and dissociation.

The process in which oxygen diffuses from Pd to Au sites is often discussed in heterogeneous catalysis as “oxygen spillover”.²² But this mechanism is barely discussed in electrocatalysis. We believe that this is an important phenomenon in electrocatalysis and that further investigation by theoretical calculations and surface science characterization of O₂ adsorption and spillover of oxygen species at the Pd/Au surface is important to elucidate and test this mechanism.

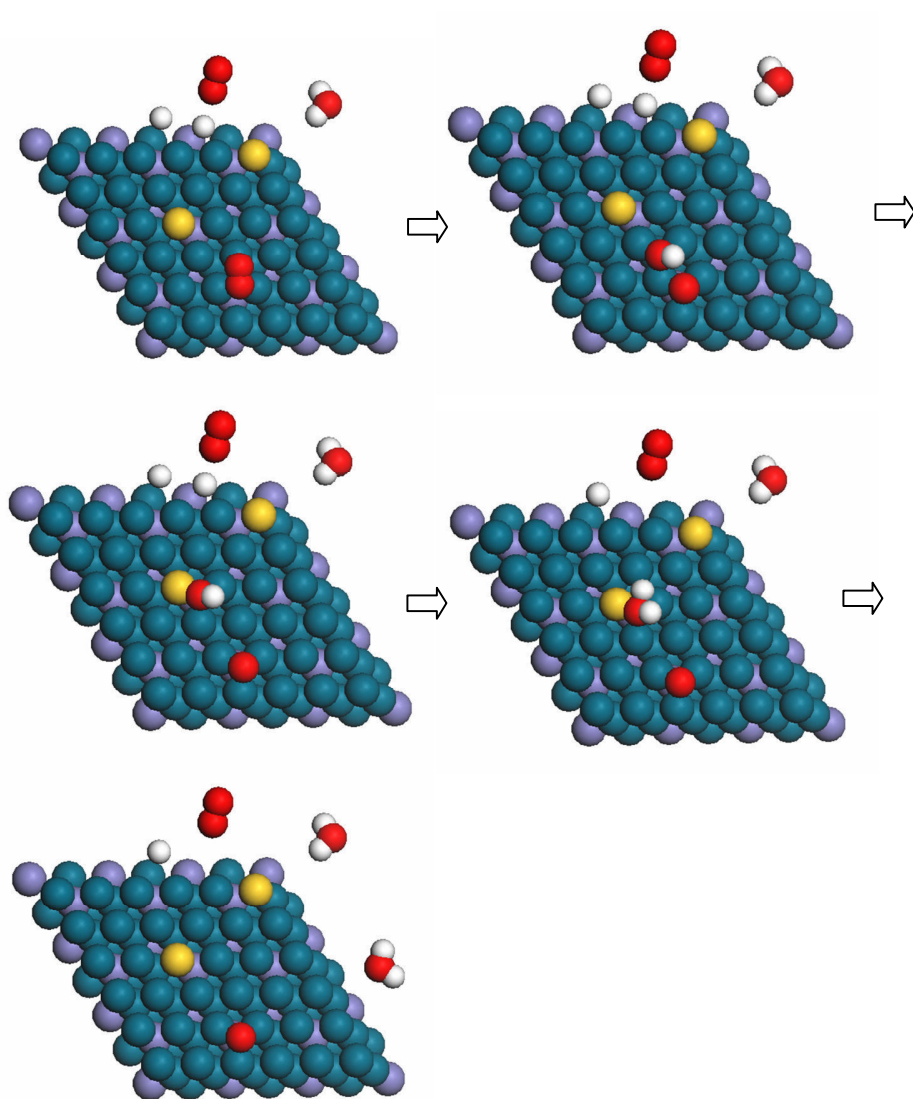


Figure 5.9 Schematic representation of the importance of reactive sites and oxygen spillover in the reaction mechanism of oxygen reduction on $\text{Au}_x/\text{Pd}/\text{Pd}_3\text{Fe}(111)$ surfaces. Atoms encoded as: Fe (purple), Pd (blue), Au (yellow), O (red), and H (white). In this mechanism, the O_2 tends to dissociate on the Pd atom and then O atom diffuses to nearby Au, where O atoms react with H^+ to become water.

5.4 Conclusions

The stability of cathode catalysts is extremely important for developing durable fuel cells with long lifespans. The high-temperature annealed Pd₃Fe(111) surface is highly active for the ORR, but it may suffer from activity loss due to the slow dissolution of the active metal, Fe. We have demonstrated a method to improve the stability while maintaining high activity involving adding a submonolayer amount of Au to the surface. The Au-modified surfaces underwent reconstruction to form a relatively stable Au-Pd surface alloy in the O₂-saturated acid electrolyte. While bulk gold is an oxidation-resistant and catalytically inactive material, submonolayer amounts of Au deposited on a Pd/Pd₃Fe(111) surface was discovered to be highly active. A surface with ~0.6 ML Au was twice as active as Pt(111). This study not only discovered a potential candidate for non-Pt catalysts to replace Pt cathode catalysts for the ORR, but also successfully identified conditions for activating gold for use in practical catalysts.

5.5 References

1. Zhou, W.-P.; Yang, X.; Vukmirovic, M. B.; Koel, B. E.; Jiao, J.; Peng, G.; Mavrikakis, M.; Adzic, R. R., Improving electrocatalysts for O₂ reduction by fine-tuning the Pt-support interaction: Pt monolayer on the surfaces of a Pd₃Fe(111) single-crystal alloy. *J. Am. Chem. Soc.* **2009**, *131* (35), 12755-12762.
2. Sasaki, K.; Naohara, H.; Cai, Y.; Choi, Y. M.; Liu, P.; Vukmirovic, M. B.; Wang, J. X.; Adzic, R. R., Core-protected platinum monolayer shell high-stability electrocatalysts for fuel-cell cathodes. *Angew. Chem. Int. Ed.* **2010**, *49* (46), 8602-8607.
3. Hirunsit, P.; Balbuena, P. B., Stability of Pt monolayers on Ir-Co cores with and without a Pd Interlayer. *J. Phys. Chem. C* **2010**, *114* (30), 13055-13060.
4. Adzic, R.; Zhang, J.; Sasaki, K.; Vukmirovic, M.; Shao, M.; Wang, J.; Nilekar, A.; Mavrikakis, M.; Valerio, J.; Uribe, F., Platinum Monolayer Fuel Cell Electrocatalysts. *Top. Catal.* **2007**, *46* (3), 249-262.
5. Zhang, J.; Lima, F. H. B.; Shao, M. H.; Sasaki, K.; Wang, J. X.; Hanson, J.; Adzic, R. R., Platinum monolayer on nonnoble metal-noble metal core-shell nanoparticle electrocatalysts for O₂ reduction. *J. Phys. Chem. B* **2005**, *109* (48), 22701-22704.
6. Zhang, J.; Mo, Y.; Vukmirovic, M. B.; Klie, R.; Sasaki, K.; Adzic, R. R., Platinum monolayer electrocatalysts for O₂ reduction: Pt monolayer on Pd(111) and on carbon-supported Pd nanoparticles. *J. Phys. Chem. B* **2004**, *108* (30), 10955-10964.
7. Shao, M.; Peles, A.; Shoemaker, K.; Gummalla, M.; Njoki, P. N.; Luo, J.; Zhong, C.-J., Enhanced oxygen reduction activity of platinum monolayer on gold Nanoparticles. *J. Phys. Chem. Lett.* **2010**, *2* (2), 67-72.
8. Matsuoka, K.; Miyazaki, K.; Iriyama, Y.; Kikuchi, K.; Abe, T.; Ogumi, Z., Novel anode catalyst containing gold nanoparticles for use in direct methanol fuel cells. *J. Phys. Chem. C* **2007**, *111* (7), 3171-3174.
9. Gong, J.; Mullins, C. B., Selective oxidation of ethanol to acetaldehyde on gold. *J. Am. Chem. Soc.* **2008**, *130* (49), 16458-16459.
10. Haruta, M.; Kobayashi, T.; Sano, H.; Yamada, N., Novel gold catalysts for the oxidation of carbon monoxide at a temperature far below 0 °C. *Chem. Lett.* **1987**, *16*, 405-408.

11. Hughes, M. D.; Xu, Y.-J.; Jenkins, P.; McMorn, P.; Landon, P.; Enache, D. I.; Carley, A. F.; Attard, G. A.; Hutchings, G. J.; King, F.; Stitt, E. H.; Johnston, P.; Griffin, K.; Kiely, C. J., Tunable gold catalysts for selective hydrocarbon oxidation under mild conditions. *Nature* **2005**, *437* (7062), 1132-1135.
12. Turner, M.; Golovko, V. B.; Vaughan, O. P. H.; Abdulkin, P.; Berenguer-Murcia, A.; Tikhov, M. S.; Johnson, B. F. G.; Lambert, R. M., Selective oxidation with dioxygen by gold nanoparticle catalysts derived from 55-atom clusters. *Nature* **2008**, *454* (7207), 981-983.
13. Franceschetti, A.; Pennycook, S. J.; Pantelides, S. T., Oxygen chemisorption on Au nanoparticles. *Chem. Phys. Lett.* **2003**, *374* (5-6), 471-475.
14. Raj, C. R.; Abdelrahman, A. I.; Ohsaka, T., Gold nanoparticle-assisted electroreduction of oxygen. *Electrochem. Commun.* **2005**, *7* (9), 888-893.
15. Prieto, A.; Hernández, J.; Herrero, E.; Feliu, J., The role of anions in oxygen reduction in neutral and basic media on gold single-crystal electrodes. *J. Solid State Electrochem.* **2003**, *7* (9), 599-606.
16. Chen, W.; Ny, D.; Chen, S., SnO₂-Au hybrid nanoparticles as effective catalysts for oxygen electroreduction in alkaline media. *J. Power Sources* **2010**, *195* (2), 412-418.
17. El-Deab, M. S.; Ohsaka, T., Electrocatalysis by design: Effect of the loading level of Au nanoparticles-MnOx nanoparticles binary catalysts on the electrochemical reduction of molecular oxygen. *Electrochim. Acta* **2007**, *52* (5), 2166-2174.
18. Zhang, J.; Sasaki, K.; Sutter, E.; Adzic, R. R., Stabilization of platinum oxygen-reduction electrocatalysts using gold clusters. *Science* **2007**, *315* (5809), 220-222.
19. Xing, Y.; Cai, Y.; Vukmirovic, M. B.; Zhou, W.-P.; Karan, H.; Wang, J. X.; Adzic, R. R., Enhancing oxygen reduction reaction activity via Pd-Au alloy sublayer mediation of Pt monolayer electrocatalysts. *J. Phys. Chem. Lett.* **2010**, 3238-3242.
20. Ratner, B. D.; Castner, D. G., Ch. 3 Electron Spectroscopy for Chemical Analysis. In *Surface Analysis—The Principal Techniques, 2nd Edition*, Vickerman, J. C.; Gilmore, I. S., Eds. John Wiley & Sons Ltd: Chichester, UK, 2009.
21. Taglauer, E., Ch. 6 Low-Energy Ion Scattering and Rutherford Backscattering. In *Surface Analysis -The Principal Techniques, 2nd Edition*, Vickerman, J. C.; Gilmore, I. S., Eds. John Wiley & Sons Ltd: Chichester, UK, 2009.

22. Teichner, S. J., Recent studies in hydrogen and oxygen spillover and their impact on catalysis. *Applied Catalysis* **1990**, 62 (1), 1-10.

Chapter 6 Investigation of A Pt Monolayer on Carbon-Induced Faceted Re(11 $\bar{2}$ 1) For the Hydrogen Evolution Reaction (HER)

6.1 Introduction

Rhenium-based catalysts are mainly used for petroleum processing. Recently, this system has also been investigated because Re-based catalysts exhibit high reactivity in many other important catalytic reactions, (*e.g.*, selective reduction of NO_x with NH₃, selective oxidation of methanol, thiophene hydrodesulfurization, and ammonia synthesis),¹⁻⁵. In these reactions, the reaction rate is sensitive to the catalyst surface structure.

It is known that two high index planes of a rhenium single crystal, Re (12 $\bar{3}$ 1) and Re(11 $\bar{2}$ 1) reconstruct significantly, and this can be induced by adsorbates such as oxygen and nitrogen.⁶ This reconstruction is caused by migration of a large amount of atoms, and is driven by the minimization of surface free energy. It is of interest to also determine if carbon can induce such reconstruction. Carbon is one of the most common impurities in metal catalysts, and the effect of surface carbon on the surface structure, and consequent modification of catalytic properties, is important for understanding correlations between the structure and catalytic activity of Re-based catalysts.

We expect that if reconstruction occurs, it would affect the electronic structure and reactivity of the surface. There has been success in recent years obtained by considering that the chemical activity of the surface is characterized by the *d*-band center

position, as the interaction between adsorbates and the surface is governed by the d-band center position.⁷ We know that the electronic properties of a surface monolayer can be modified by the substrate. In general, the *d*-band center of a surface layer is shifted due to the tension or compression induced by the lattice mismatch between the surface layer and the substrate.⁸ Specifically, higher electrocatalytic activity and stability were found when metals or alloys were used as supports for a Pt or Pd monolayer. For example, a Pt monolayer on Pd₃Fe(111) is more active than bulk Pt for the ORR⁹ and a Pt monolayer on WC is comparable to bulk Pt for the hydrogen evolution reaction (HER).¹⁰

In this chapter, studies of the influence of carbon on the surface structure of Re(11 $\bar{2}$ 1) are described. These investigations were carried out by using surface science techniques including LEED, XPS, AES, and STM. We found that the presence of surface carbon modifies the surface structure significantly, causing faceting of Re(11 $\bar{2}$ 1), *i.e.*, an initially planar Re(11 $\bar{2}$ 1) surface becomes "nanotextured" to expose new crystal faces on the nanometer scale. The fully faceted surface consists of three-sided nano-pyramids with well-defined surface structure and controlled size, which may serve as a nanoscale model catalyst. Specifically, a Pt monolayer was added on faceted Re(11 $\bar{2}$ 1) by PVD and the activity for catalyzing the HER was explored. At least two important factors may affect the activity of the faceted monolayer surface: i) modification of the electronic properties by the Re substrate, and ii) geometric effects due to the faceted reconstruction at the nanoscale. We found that the presence of a Pt monolayer at the surface was able to protect the Re substrate from dissolution, which is important since Re is active element in acid solution. The Pt monolayer on faceted Re (11 $\bar{2}$ 1) also exhibits much higher

reactivity than pure Pt. Because Re is only one-fifth the price of Pt, our results suggest significant advantages for using a Pt monolayer supported on Re as a catalyst for the HER in terms of activity and cost.

6.2 Experimental details

6.2.1 Preparation of a Pt monolayer on faceted Re(11 $\bar{2}$ 1)

The Re(11 $\bar{2}$ 1) crystal was cleaned by cycles of sputtering (1000 keV Ar⁺, 5.0×10^{-7} torr, 0.4 uA, 5 min) and annealing (1100 K, 2 min) in a UHV chamber with base pressure of 2.0×10^{-10} torr. Small oxygen exposures (5.0×10^{-9} torr, 1 min) on the substrate at 800 K were also needed to remove surface carbon. The clean and well-ordered Re(11 $\bar{2}$ 1) surface was characterized by a sharp and bright LEED pattern, as shown in Figure 6.1A. Auger electron spectroscopy (AES) was used to verify the surface cleanliness and was used to periodically verify that there were no detectable surface impurities following cleaning. A typical clean AES spectrum is shown in Figure 6.2A.

Faceting of the Re(11 $\bar{2}$ 1) surface was induced by dosing 0.3L of C₂H₂ on the surface at 700 K, followed by annealing at 1000 K for 60 s. Acetylene was dosed using a 0.05 in.-dia. stainless steel dosing tube 2 in. away aimed at the surface. The carbon coverage was measured by AES, as illustrated in Figure 6.2. The structure of the faceted Re surface was studied by LEED and STM.

A Pt monolayer was synthesized by PVD from a Pt doser in which Pt was evaporated from a hot W wire. The construction of Pt doser is the same as that of the Au doser (see the schematic drawing and picture of the doser, shown in Figure 5.1 in Chapter 5). The coverage of Pt was monitored by LEIS using Ar⁺ with an incident ion energy of

4.5 keV and a beam current of 1 nA. Since Ar^+ has a strong sputtered effect on Au, all the spectra were obtained in 10 seconds by setting the smallest scanning range (2500-2850 eV) and high pass energy of 1127.1 eV on the energy analyzer. Calibration of the Pt coverage and determination of the formation of a Pt ML was done by dosing Pt on $\text{Re}(11\bar{2}1)$ and monitored by LEIS. A full monolayer of Pt is defined as the amount of Pt which fully eliminates the Re peak signal in LEIS. A typical LEIS spectrum of the Pt monolayer is shown in Figure 6.7A.

6.2.2 Electrochemical measurements

After surface preparation in the UHV chamber, the crystal was transferred to an electrochemical cell for electrochemical analysis. As discussed above, the sample holder could be attached to a rotating disc electrode rotator (RDE, Pine). A quick transfer of the sample between the main UHV chamber and the electrochemical cell was accomplished with the aid of a small high-pressure antechamber/load lock attached directly to the UHV chamber. Before the sample transfer, this antechamber was backfilled with high purity N_2 (99.998 % purity, Airgas) to a pressure of 1.5 atm and N_2 flew during sample transfer. The UHV-prepared Pt ML-C/ $\text{Re}(11\bar{2}1)$ surfaces were protected by a droplet of high pure water (with a glass pipette, HPLC grade water, Fisher) on the surface immediately after opening the port to the antechamber and immediately transferred into an electrochemical cell and immersed in a 0.1 M HClO_4 solution for electrochemical measurements. A hanging meniscus rotating disc technique was used and the height of the meniscus was carefully controlled to prevent the side of the crystal from wetting. A standard three-

electrode electrochemical cell with a Pt-wire counter electrode and a hydrogen reference electrode was used, as described previously in Ch. 1.

6.3 Results and discussion

6.3.1 Preparation and characterization of C/Re(11 $\bar{2}$ 1)

The (1 \times 1) LEED pattern of clean, planar (unfacetted) Re(11 $\bar{2}$ 1) is shown in Figure 6.1A. All the LEED spots converged to the center as the incident electron energy was increased, indicating the surface was planar. The symmetry of the LEED pattern was identical to the symmetry of the ideal Re(11 $\bar{2}$ 1) plane because the LEED pattern from (11 $\bar{2}$ 1) resembles its lattice pattern in real space rotated by 90°. New features appeared after the surface at 700 K was exposed to 0.3 L C₂H₂ (5.0×10^{-9} torr, 60 s), followed by annealing at 1100 K for 1 min. These new LEED spots converged to three different centers as the incident electron energy was increased, indicating that the surface facets into three different planes. The surface was initially only partially faceted, as shown in Figure 6.1B, since some of the LEED spots still converged to the screen center. Further annealing caused the planar LEED spots to completely disappear. The surface could be made fully faceted as shown in Figure 6.1C. It has been reported that two-sided faceting was induced by oxygen on the Re(11 $\bar{2}$ 1) surface. Therefore, our results demonstrate that the faceting reconstruction is affected by the adsorbate used. AES spectra were taken to confirm the existence of surface carbon, which was created by acetylene decomposition on the surface. Figure 6.2 compares the difference in AES spectra of the planar and faceted surfaces; the carbon peak only appears on the faceted surfaces. This result confirms that carbon produces the faceted surface.

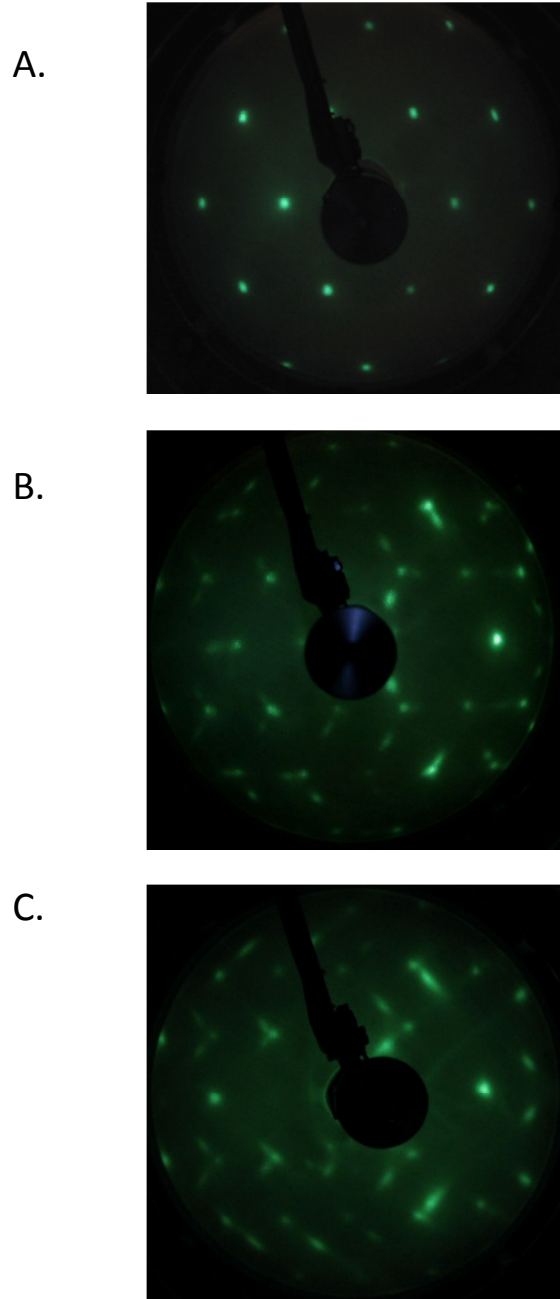


Figure 6.1 LEED patterns from $\text{Re}(11\bar{2}1)$. A. Planar $\text{Re}(11\bar{2}1)$ at $E_i = 60$ eV. B. Partially faceted $\text{C}/\text{Re}(11\bar{2}1)$ at $E_i = 90$ eV. C. Fully faceted $\text{C}/\text{Re}(11\bar{2}1)$ at $E_i = 90$ eV.

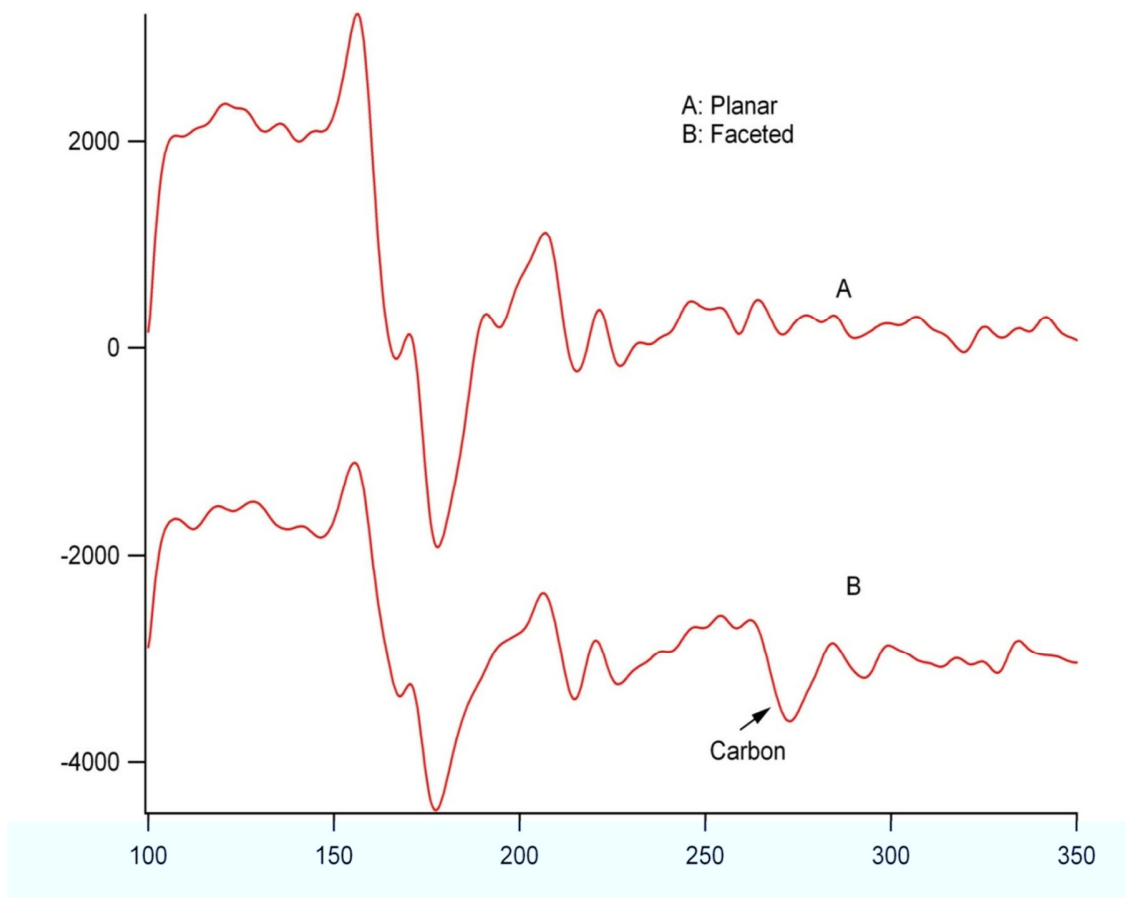
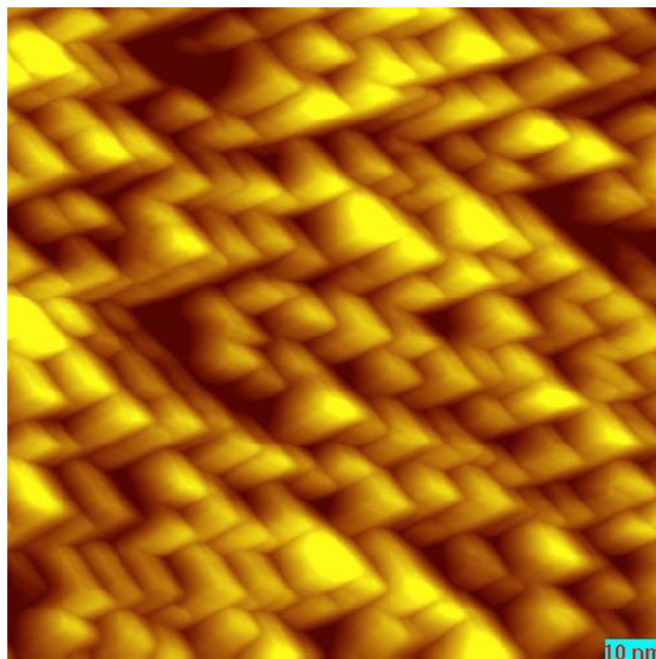


Figure 6.2 AES spectra of planar and C-induced faceted $\text{Re}(11\bar{2}1)$. A. Planar $\text{Re}(11\bar{2}1)$. B. Faceted $\text{Re}(11\bar{2}1)$ after 0.3 L C_2H_2 exposure at 700 K followed by annealing in vacuum at 1100 K for 1 min.

The structure of the faceted $\text{Re}(11\bar{2}1)$ surface was studied by STM under UHV conditions using the instrument and procedures discussed in Ch. 1. Basically, the STM images display three-sided pyramids with sizes of 2-10 nm, consistent with the LEED observations. We also find that different morphologies of the faceted surface can be found for different annealing conditions. Figures 6.3, 6.4 and 6.5 illustrate three types of faceted surfaces. The LEED patterns for these surfaces appeared to be the same (Figure 6.1C), indicating that all three of these surfaces were fully faceted to form three planes. These three-sided pyramids shown in Figure 6.3 were uniform in size (~ 10 nm) and “flat” for each of the faceted planes. Increasing the annealing time from 1 to 3 min didn’t change the pyramid size, but created a new feature at each pyramid. It is clearly shown in Figure 6.4 that the large pyramids are made of small pyramids (~ 1 nm). Further extending the annealing time up to 5 min caused the pyramids to significantly reconstruct, reducing in size (2-5 nm) and becoming less uniform. This observation is different from the previously observed behavior of the growth of faceted islands on $\text{Re}(12\bar{3}1)$ induced by oxygen.⁶ We observed that carbon tended to segregate to the surface after annealing. This behavior leads us to believe that the surface carbon concentration may play a role in affecting the faceted pyramid size. Furthermore, it is clear that the carbon concentration must be less than one monolayer for the surface to be faceted, which was concluded from analysis by LEIS and LEED. All faceted surfaces were only partially covered by carbon. If carbon completely covered the surface, the LEED pattern became diffuse or disappeared. However, the determination of an accurate coverage of carbon for the faceted surface has not been completed and more experiments are planned.

A.



B.

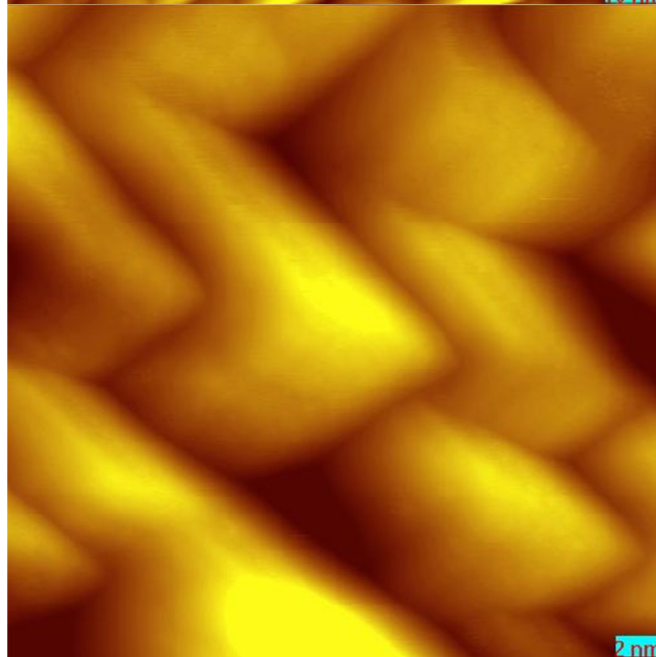
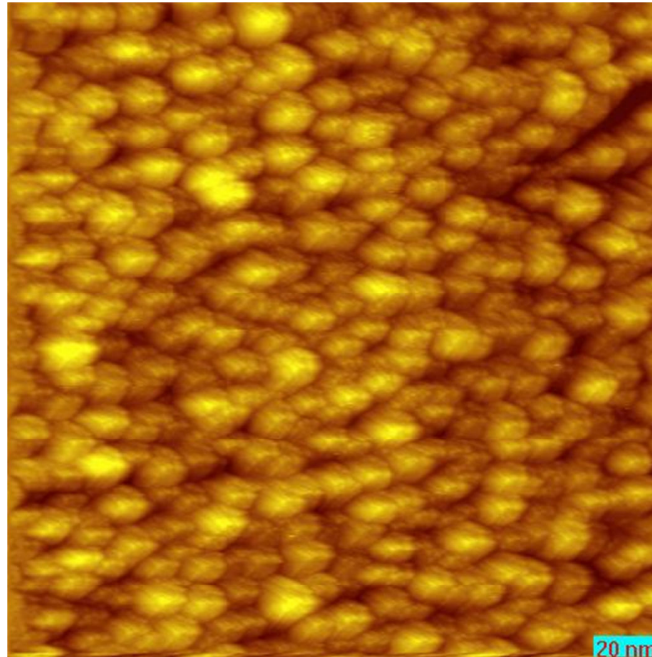


Figure 6.3 Constant current STM images of faceted $\text{Re}(11\bar{2}1)$ induced by exposure of $\text{Re}(11\bar{2}1)$ at 700 K to 0.3 L C_2H_2 and then heating to 1100 K in vacuum for 1 min. A. $(120 \times 120) \text{ nm}^2$, B. $(30 \times 30) \text{ nm}^2$, -1.8 V, 430 pA

A.



B.

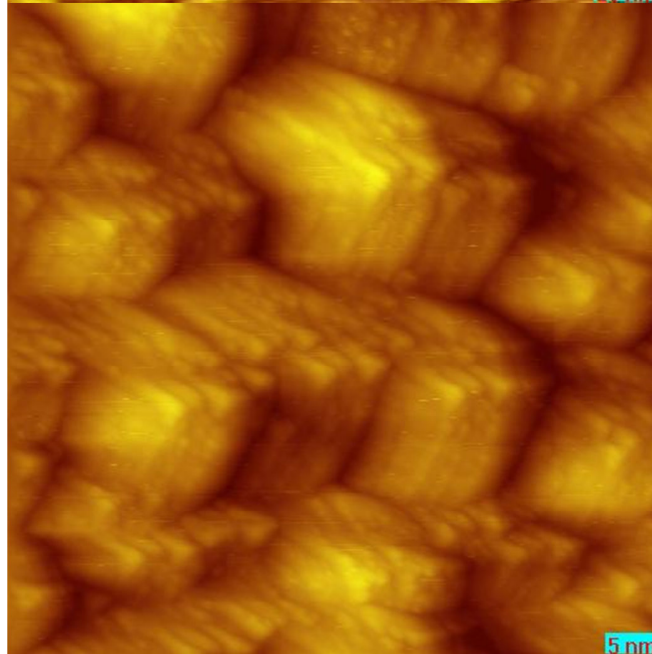


Figure 6.4 Constant current STM images of faceted Re(11 $\bar{2}$ 1) induced by exposure of Re(11 $\bar{2}$ 1) at 700 K to 0.3 L C₂H₂ and then heating to 1100 K in vacuum for 3 min. A. (200 × 200) nm². B. (60 × 60) nm², -2.08 V, 434 pA.

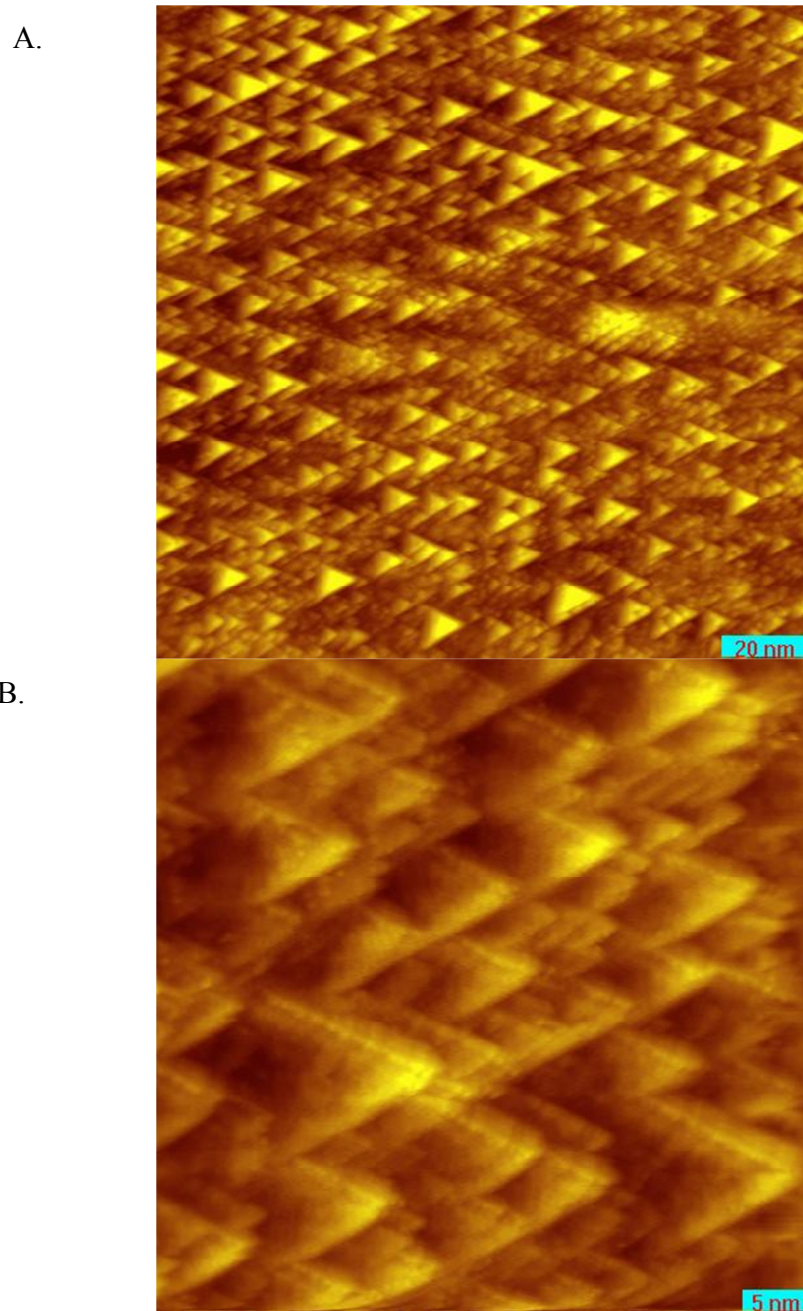
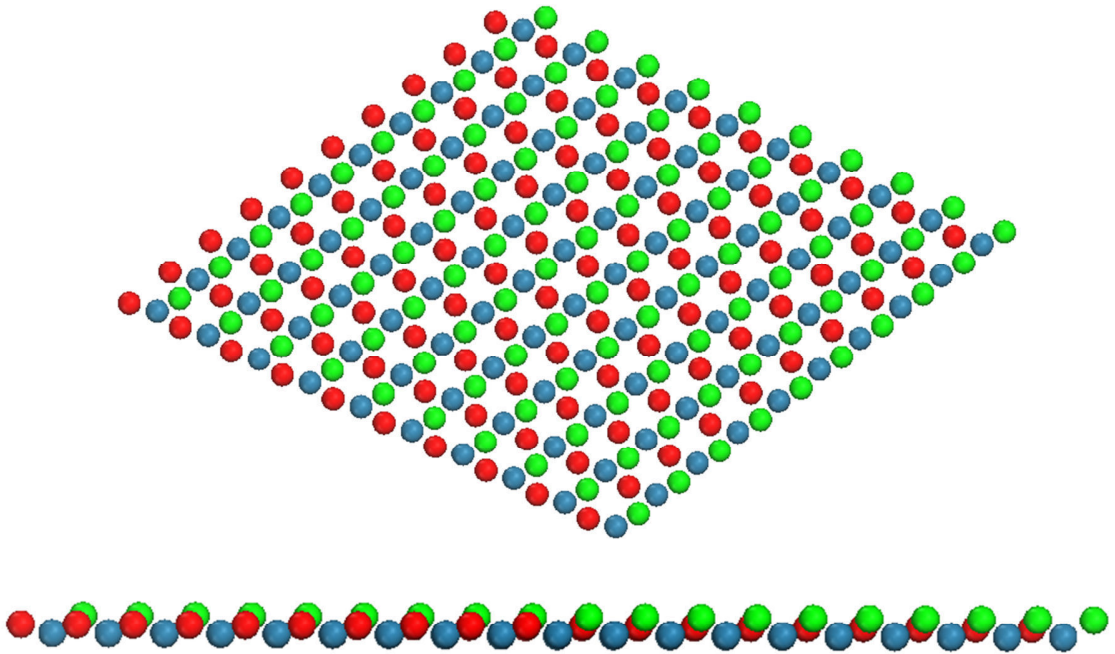


Figure 6.5 Constant current STM images of faceted $\text{Re}(11\bar{2}1)$ induced by exposure of $\text{Re}(11\bar{2}1)$ at 700 K to 0.3 L C_2H_2 and then heating to 1100 K in vacuum for 5 min. A. $(150 \times 150) \text{ nm}^2$. B. $(50 \times 50) \text{ nm}^2$, -1.95 V, 330 pA.

A.



B.

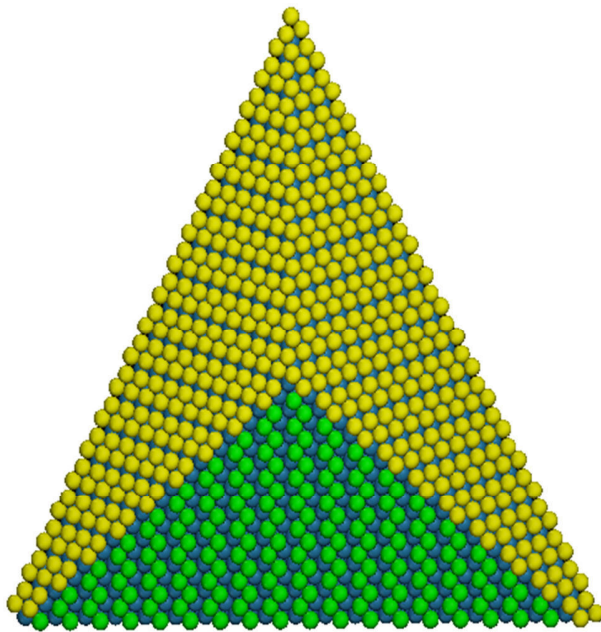


Figure 6.6 Schematic illustrations providing top views of a hard-sphere model of A. a planar $\text{Re}(11\bar{2}1)$ surface with three geometrical layers exposed, top view and side view, Green-1st layer, Red-2nd layer and Blue-3rd layer and B. a single pyramid from a faceted $\text{Re}(11\bar{2}1)$ surface. Facet orientations were determined by kinematic LEED simulations performed by our collaborator, Dr. Hao Wang at Columbia University. The faceted planes are $(01\bar{1}1)$, $(10\bar{1}1)$ and $(11\bar{2}0)$ for the left, right, and bottom facets, respectively. Yellow- the exposed layers on the faceted plane $(01\bar{1}1)$, $(10\bar{1}1)$, Green the exposed layer on the faceted plane $(11\bar{2}0)$, Blue-bulk.

6.3.2 Preparation of a Pt monolayer on C/Re(11 $\bar{2}$ 1)

Pt was evaporated on the Re substrate and the Pt coverage was monitored by LEIS and XPS. The Pt doser operating conditions (9 V, 8 A) were determined using LEIS from conditions that resulted in a Pt monolayer deposited on the faceted Re(11 $\bar{2}$ 1) surface in 5 min. As we discussed in Ch.2, LEIS is able to analyze the elemental composition of the outermost atomic layer of the surface. As shown in Figure 6.7, the LEIS spectrum only displays a Pt peak and a negligible Re peak, which establishes that the Pt coverage was at least one monolayer. Careful measurements with increasing Pt deposition time titrated the amount of Pt to be just sufficient to eliminate the Re signal and thus just form only a Pt monolayer. The Pt-covered faceted Re sample was then transferred from the UHV chamber to the electrochemical cell for testing for the HER.

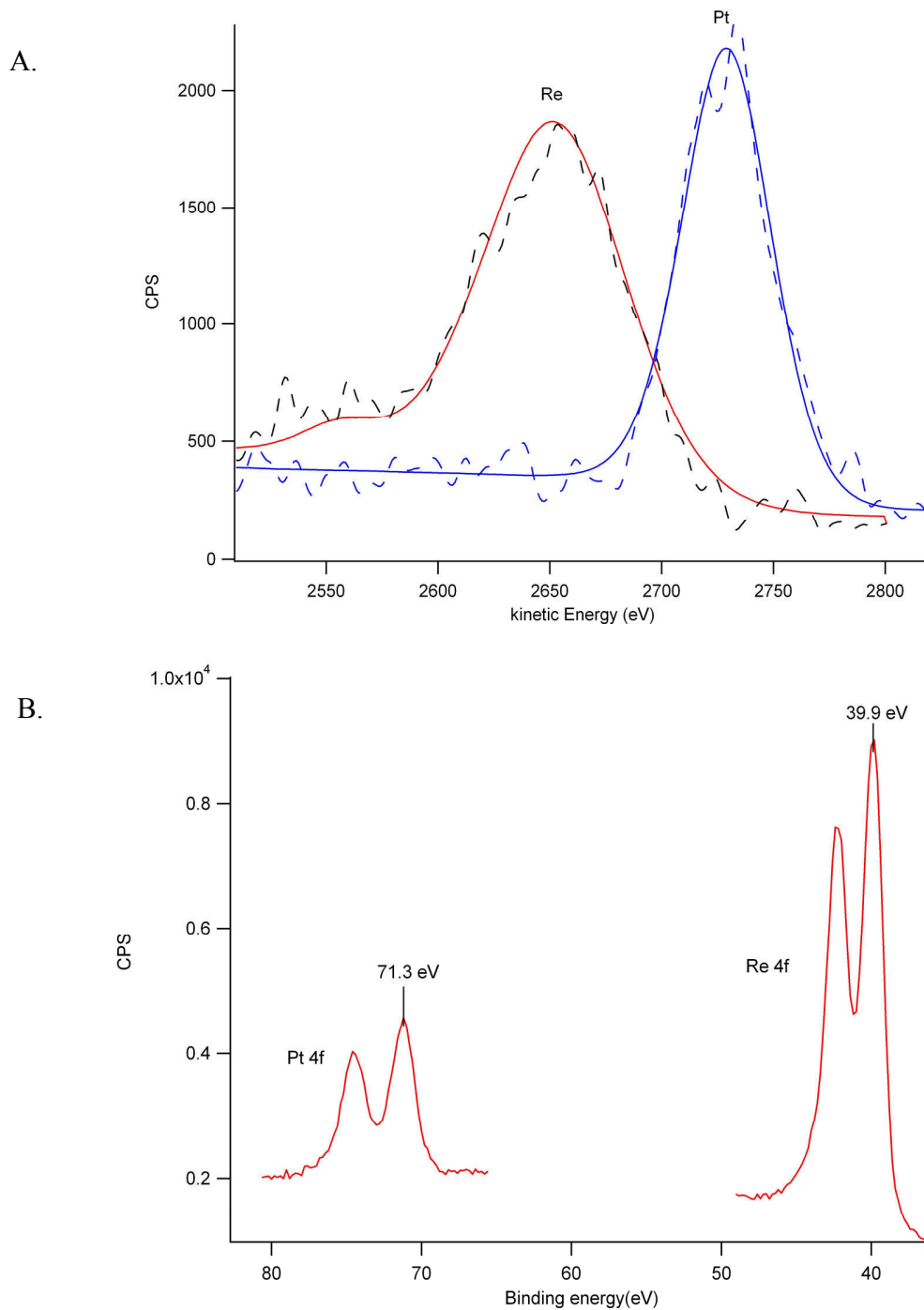


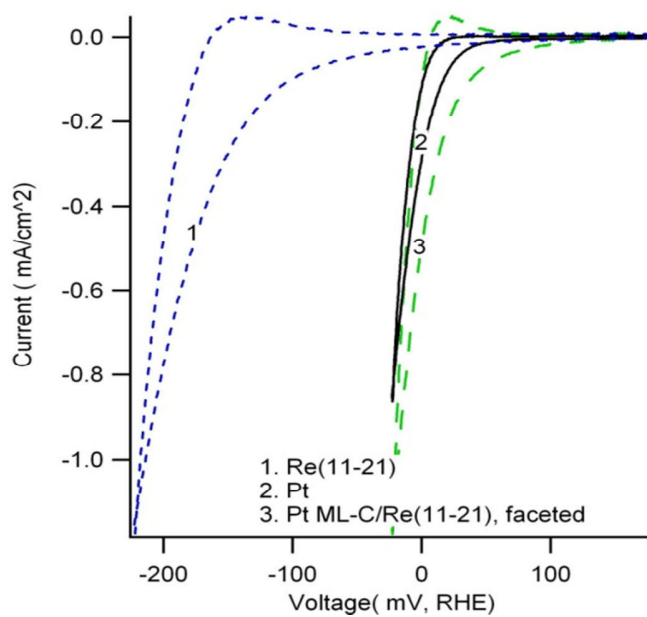
Figure 6.7 Surface characterization of Pt monolayer by LEIS and XPS. A. Red-Clean Re($11\bar{2}1$) and Blue-Pt ML on Re($11\bar{2}1$). 4.5 keV Ar^+ , 3 nA, pass energy:1127.1 eV B. Pt ML on Re($11\bar{2}1$). XPS: Mg $\text{K}\alpha$, 20mA emission, 46.75 eV pass energy.

6.3.3 Catalytic activity of the Pt ML-C/Re(11 $\bar{2}$ 1) surface

Polarization scans for hydrogen evolution using Re(11 $\bar{2}$ 1), Pt(111) and Pt ML-C/Re(11 $\bar{2}$ 1) samples were performed in an Ar-purged 0.1 M HClO₄ solution at a scan rate of 2 mV/s. In Figure 6.8, the HER overpotentials are plotted as a function of the logarithm of the current density to produce the Tafel curves. The activity of Re(11 $\bar{2}$ 1) was much lower than Pt(111) as can be observed by the large overpotential. However, the Pt ML-C/Re(11 $\bar{2}$ 1) sample had significantly improved activity and even better performance than Pt(111). The exchange current (j_0) values for Pt ML-C/Re(11 $\bar{2}$ 1) and Pt(111) were 6.30×10^{-4} and 3.98×10^{-4} A/cm², respectively.

Previous studies have shown a volcano type of relationship between the hydrogen adsorption energy and the HER.⁷ Pt monolayers on several substrates have been studied for improved ORR performance.^{8, 11-14} We believe a similar role for the faceted Re substrate exists, such that the Pt ML supported on C/Re(11 $\bar{2}$ 1) should have different electronic properties (d -band center position) from Pt(111). However, our results also include the potentially important effect induced by the nano-scale faceting of the substrate. It is still not clear how this nano-structure plays a role in this reaction and this needs more fundamental study including theoretical modeling of the electronic properties of the nanoscale pyramids and examining the reactivity of related surfaces and other reactions.

A.



B.

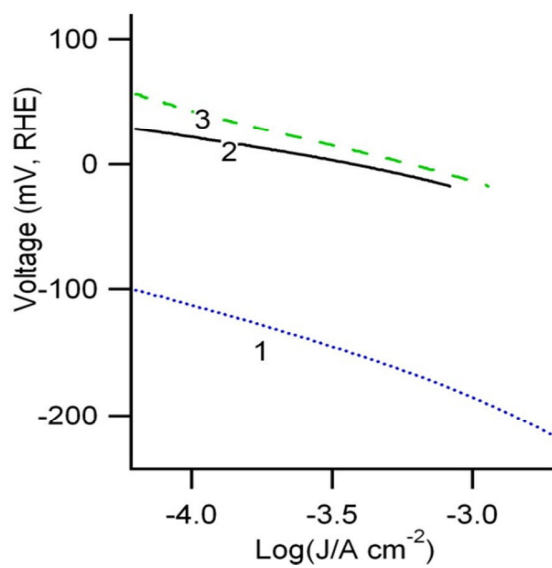


Figure 6.8 A. Hydrogen evolution polarization curves in 0.1 M HClO₄, B. Tafel plots for (1) Re(11 $\bar{2}$ 1), (2) Pt(111) and (3) Pt ML-C/Re(11 $\bar{2}$ 1). Scan rate is 2 mV/s.

6.4 Conclusions

In this study, a special faceted surface, C/Re(11 $\bar{2}$ 1), was prepared by introducing carbon on the surface and annealing to high temperature (1000 K). This faceted surface was characterized by three-sided pyramids with a size of 2-10 nm. These nanoscale pyramids with a well-defined structure can serve as good model catalysts or as templates for synthesizing related model catalysts. We added one monolayer of Pt on the faceted C/Re(11 $\bar{2}$ 1) surface and investigated its performance for the HER. This Pt ML-C/Re(11 $\bar{2}$ 1) surface displayed higher activity for the HER than pure Pt. Rhenium is only one-fifth the price of Platinum and our work shows the advantage of using a Pt ML on faceted C/Re as an electrocatalyst for the HER. This study is also the first case to successfully utilize a nanoscale faceted surface as a template for electrocatalyst synthesis. It is of great interest to explore further the catalytic activity of such special template surfaces for different reactions and understand the various effects (size, orientation, and low-coordination sites) that are induced by the nanoscale template.

6.5 Reference

1. Kojima, R.; Enomoto, H.; Muhler, M.; Aika, K.-i., Cesium-promoted rhenium catalysts supported on alumina for ammonia synthesis. *Appl. Catal., A* **2003**, *246* (2), 311-322.
2. Wachs, I. E.; Deo, G.; Andreini, A.; Vuurman, M. A.; de Boer, M., The Selective Catalytic Reduction of NO_x with NH₃ over Titania Supported Rhenium Oxide Catalysts. *J. Catal.* **1996**, *160* (2), 322-325.
3. Liu, J.; Zhan, E.; Cai, W.; Li, J.; Shen, W., Methanol Selective Oxidation to Methyl Formate over ReO_x/CeO₂ Catalysts. *Catal. Lett.* **2008**, *120* (3), 274-280.
4. Bussell, M. E.; Gellman, A. J.; Somorjai, G. A., Thiophene hydrodesulfurization over transition metal surfaces: Structure insensitive over molybdenum and structure sensitive over rhenium. *J. Catal.* **1988**, *110* (2), 423-426.
5. Asscher, M.; Carrazza, J.; Khan, M. M.; Lewis, K. B.; Somorjai, G. A., The ammonia synthesis over rhenium single-crystal catalysts: Kinetics, structure sensitivity, and effect of potassium and oxygen. *J. Catal.* **1986**, *98* (2), 277-287.
6. Wang, H.; Chen, W.; Madey, T. E., Morphological evolution in oxygen-induced faceting of Re(12-31). *Phys. Rev. B: Condens. Matter* **2006**, *74* (20), 205426.
7. Norskov, J. K.; Bligaard, T.; Logadottir, A.; Kitchin, J. R.; Chen, J. G.; Pandelov, S.; Stimming, U., Trends in the Exchange Current for Hydrogen Evolution. *J. Electrochem. Soc.* **2005**, *152* (3), J23-J26.
8. Nilekar, A. U.; Mavrikakis, M., Improved oxygen reduction reactivity of platinum monolayers on transition metal surfaces. *Surf. Sci. Lett.* **2008**, *602*, L89.
9. Zhou, W.-P.; Yang, X.; Vukmirovic, M. B.; Koel, B. E.; Jiao, J.; Peng, G.; Mavrikakis, M.; Adzic, R. R., Improving electrocatalysts for O₂ reduction by fine-tuning the Pt-support interaction: Pt monolayer on the surfaces of a Pd₃Fe(111) single-crystal alloy. *J. Am. Chem. Soc.* **2009**, *131* (35), 12755-12762.
10. Esposito, D. V.; Hunt, S. T.; Stottlemeyer, A. L.; Dobson, K. D.; McCandless, B. E.; Birkmire, R. W.; Chen, J. G., Cover picture: Low-cost hydrogen-evolution catalysts based on monolayer platinum on tungsten monocarbide substrates *Angew. Chem. Int. Ed.* **2010**, *49* (51), 9787-9787.

11. Xing, Y.; Cai, Y.; Vukmirovic, M. B.; Zhou, W.-P.; Karan, H.; Wang, J. X.; Adzic, R. R., Enhancing oxygen reduction reaction activity via Pd–Au alloy sublayer mediation of Pt monolayer electrocatalysts. *J. Phys. Chem. Lett.* **2010**, 3238-3242.
12. Shao, M.; Peles, A.; Shoemaker, K.; Gummalla, M.; Njoki, P. N.; Luo, J.; Zhong, C.-J., Enhanced oxygen reduction activity of platinum monolayer on gold Nanoparticles. *J. Phys. Chem. Lett.* **2010**, 2 (2), 67-72.
13. Shao, M.; Liu, P.; Zhang, J.; Adzic, R., Origin of enhanced activity in palladium alloy electrocatalysts for oxygen reduction reaction. *J. Phys. Chem. B* **2007**, 111 (24), 6772-6775.
14. Adzic, R.; Zhang, J.; Sasaki, K.; Vukmirovic, M.; Shao, M.; Wang, J.; Nilekar, A.; Mavrikakis, M.; Valerio, J.; Uribe, F., Platinum Monolayer Fuel Cell Electrocatalysts. *Top. Catal.* **2007**, 46 (3), 249-262.

Chapter 7 Summary

As the global community considers how to develop alternative energy sources to supplement, extend, and replace traditional fossil-based energy resources, fuel cells have drawn much attention due to their large inherent efficiency for energy conversion. Polymer electrolyte membrane (PEM) fuel cells have existed for a long time, and while there has been significant development, there are still major drawbacks that limit further development and applications of fuel cells on a large scale. First, fuel cells are expensive partly due to the use of costly Pt-based catalysts, and the natural abundance of Pt is too low to support large scale use of fuel cells with Pt as an electrocatalyst. Second, Pt-based catalysts are poisoned by impurities such as CO, H₂S, NH₃, *etc.*, in fuels, and these impurities seriously reduce the activity of catalysts, thus shortening their lifespan. Third, the sluggish oxygen reduction reaction (ORR) kinetics at the cathode (due to the large overpotential) causes relatively low current density and thus limits the power of fuel cells. Fourth, while direct ethanol fuel cells would benefit from the advantages in fuel production, transportation, storage, and volumetric energy density of ethanol over hydrogen, no catalyst can completely oxidize ethanol in high efficiency. Solutions to these problems rely on the discovery and tailoring of an optimal catalyst with attributes of high activity, durability, low cost, and resistance to negative effects of impurities in the fuel.

Our research focuses on the study of non-Pt catalysts and Pt monolayer (ML) model electrocatalysts relevant for advanced electrodes for fuel cells. This work seeks insights and the discovery of new materials by establishing clear structure-activity

relationships in electrocatalysis. Catalyst surface structures and electronic properties are characterized by employing multiple surface science techniques such as low energy electron diffraction (LEED), Auger electron spectroscopy (AES), low energy ion scattering (LEIS), X-ray photoelectron spectroscopy (XPS), and scanning tunneling microscopy (STM) under ultrahigh vacuum (UHV) conditions. Electrochemical measurements on these same surfaces determine electrocatalytic reactivity for the ORR, and hydrogen evolution reaction (HER) We have fabricated three types of model electrocatalysts: (i) Pd₃Fe(111), (ii) Au/Pd₃Fe(111), and (iii) Pt on a faceted C/Re(11 $\bar{2}$ 1) nanotemplate.

Pd₃Fe(111) model electrocatalyst for ORR

Annealing a clean Pd₃Fe(111) crystal at high temperatures (>1000 K) caused significant Pd segregation to the surface layer, up to 0.9-ML Pd as measured by LEIS. The surface structure is temperature dependent, with Pd monomer and dimer adatoms formed at temperatures above 1200 K and flat random substitutional alloy surfaces formed at lower annealing temperatures (1000 K). These surfaces are good electrocatalysts for the ORR that occurs at the cathode in PEM-fuel cells. Excellent electrochemical properties of Pd monomer and dimer adatoms were found with a strong correlation with the presence of surface Fe. A synergistic effect exists taking advantage of the capability of Fe sites for strong oxygen adsorption/dissociation and the capability of the Pd layer for fast removal of oxygen species by protonation. This study not only demonstrates Pd-Fe to be a possible candidate to replace Pt as the cathode electrocatalyst

but also points out the important role of a small amount of an active element in non-Pt alloy electrocatalysts.

Au/Pd₃Fe(111) model electrocatalyst for ORR

The stability of cathode catalysts is extremely important for developing durable, long lifespan fuel cells. The Pd₃Fe(111) surface is highly active for ORR, but it suffers from activity loss due to slow dissolution of the active metal, Fe. We found a way to improve the stability without sacrificing electroactivity by depositing a submonolayer of Au on the surface. The Au-covered surfaces reconstructed to form a stable surface alloy in the O₂-saturated acid electrolyte. Bulk gold is an oxidation-resistant and catalytically inactive material. However, Au deposited on Pd₃Fe(111) formed a highly active surface that was dependent on the Au coverage. Surfaces with 0.5-0.6 ML Au were twice as active as Pt(111). This work not only led to the discovery of a non-Pt catalyst that could be used for replacing Pt cathode catalysts, but also led to identification of conditions for activating gold as a practical electrocatalyst.

Pt on a faceted C/Re(11 $\bar{2}$ 1) nanotemplate model electrocatalyst for HER

Nano-faceting of Re(11 $\bar{2}$ 1) can be induced by adding a small amount of surface carbon (*e.g.*, by exposure to C₂H₂ at elevated temperatures). These nano-faceted surfaces can be routinely prepared in UHV and serve as ideal model supports for metals such as Pt and Pd to study the relationship between reactivity and structure. As one example, we added a Pt ML on these faceted surfaces and determined the reactivity for HER. HER is a prospective way to electrocatalytically produce H₂ from water for use in H₂ fuel cells.

Traditional catalysts for this reaction are primarily based on Pt. We found that a Pt ML on a faceted C/Re(11 $\bar{2}$ 1) surface exhibited much higher reactivity than pure Pt. Since Re is only one-fifth the price of Pt, our results demonstrate the advantages of using Pt supported on a C/Re nanotemplate as an electrocatalyst for HER.

In summary, we investigated a range of non-Pt and ultrathin-Pt film model electrocatalysts that we fabricated under UHV conditions with precise control of composition and structure and fully characterized by modern surface science tools. In experiments that directly measured their reactivity in electrochemical reactions, such as the oxygen reduction reaction (ORR) and hydrogen evolution reaction (HER), we find many of these materials more active than pure Pt. These studies provide a more thorough understanding of the origin of high catalytic activity of these systems and builds the foundation for the controlled modification of surface structure and chemical properties required for optimization of new and improved electrocatalysts needed for developing high performance, inexpensive and durable PEM fuel cells.

Curriculum Vitae

Xiaofang Yang

Bethlehem, PA 18015; 215-410-8747; xiy206@lehigh.edu

Education

- 2006-2011 Ph. D in Chemistry
Lehigh University, Bethlehem, PA, USA
- 2002-2006 M. S. in Textile Science
University of Georgia, Athens, GA, USA
- 1994-2001 B.S and M. S. in Applied Chemistry
School of Chemistry and Chem. Engineering, China Textile
University, Shanghai, China

Research Experience

- 2006-2011 **Graduate Research Assistant**, Department of Chemistry
Lehigh University, Bethlehem, PA, USA
Research in electrochemistry and surface science:
- Study of Pd-based alloys electrocatalysts for the oxygen reduction reaction
 - Study of Pt monolayer supported on polycrystalline Hf₃Ir for oxygen reduction reaction and ethanol oxidation
 - Study of Au monolayer supported on Pd₃Fe(111) for oxygen reduction reaction
 - Study of Pt monolayer on faceted Re(11-21) for the hydrogen evolution reaction
 - XPS, LEIS and STM study of carbon-induced Re faceting
 - Study of adsorption of phosphoric acid on Pt single crystal surfaces and its inhibiting effect on oxygen reduction reaction at the cathode
 - LEIS, XPS and STM study of the structure of a Pd₃Fe(111) alloy surface and oxygen-induced surface segregation
 - XPS and LEIS study of segregation at a polycrystalline Hf₃Ir alloy surface
 - XPS study of acetylene adsorption and reaction on Pt(111) and a Pt₃Sn(111) alloy
- 2005-2006 **Research Assistant**, USGS Patuxent Wildlife Research Center, Athens, GA
Research on the toxicity of phosphate ion in waste water
- 2002-2005 **Graduate Research Assistant**, Department of Textiles
University of Georgia, Athens, GA
Research on the biodegradation of dye with fungi

Honors and Awards

- June 2011 Kokes Award for the 22nd North American Catalysis Society (NACS) meeting, Detroit, MI
- 2008-2009 Constance N. Busch Graduate School Fellowship, Lehigh Univ., Bethlehem, PA
- 2004-2005 AATCC Foundation Student Research Grant, Univ. of Georgia, Athens, GA

Membership

- 2006- present American Chemical Society (ACS)
- 2009- present Materials Research Society (MRS)
- 2011- present American Vacuum Society (AVS)

Publications

9. "High activity sub-monolayer Au at Pd₃Fe(111) for the oxygen reduction reaction", **X. Yang** and B.E. Koel, *J. Am. Chem. Soc.*, to be submitted.
8. "A novel CuFe based cathodic catalyst for oxygen reduction reaction in high pH environment", Q.He, **X. Yang**, X. Ren, B. Koel, S. Mukerjee, R. Kostecki, *J. Power Sources*, 2011, accepted.
7. "Monolayer Pt electrocatalysts for oxygen reduction reaction and hydrogen evolution: Bridging the materials gap", **X. Yang**, H. Wang, W. Chen, B.E. Koel and R.A. Bartynski, *J. Amer. Chem. Soc.*, to be submitted.
6. "Role of surface Fe in enhanced activity for the oxygen reduction reaction on a Pd₃Fe(111) single crystal alloy", **X. Yang**, J. Hu, JJ. Fu, R. Wu, and B. E. Koel, *Angew. Chem. Internat. Ed.*, 2011, submitted.
5. "Formation of Pd monomers and dimers on single crystal Pd₃Fe(111) surface", **X. Yang**, J. Hu, R. Wu, B. Koel, *J. Phys. Chem. Lett.*, **2010**, 1(16), 2493–2497.
4. "Influence of phosphate anion adsorption on the kinetics of oxygen electroreduction on low index Pt(hkl) single crystals", Q. He, **X. Yang**, W. Chen, S. Mukerjee, B. Koel, and S. Chen, *Phys. Chem. Chem. Phys.*, 2010, 12(39), 12544-55.

3. “Surface Structure of Pd₃Fe(111) and Effects of Oxygen Adsorption”, **X. Yang**, L. A. Welch, J. Fu and B. E. Koel, in *Catalytic Materials for Energy, Green Processes and Nanotechnology*, edited by C-Y. Mou, J. Liu, H.H. Kung, S. Dai (Mater. Res. Soc. Symp. Proc. Vol. **1217**, Warrendale, PA, 2010), 1217-Y08-43.
2. “Improving electrocatalysts for O₂ reduction by fine-tuning the Pt – support interaction: Pt monolayer on the surfaces of a Pd₃Fe(111) single-crystal alloy,” W.P. Zhou, **X. Yang**, M.B. Vukmirovic, B.E. Koel, J. Jiao, G. Peng, M. Mavrikakis, and R.R. Adzic, *J. Amer. Chem. Soc.*, 2009, 131, 12755–12762.
1. “Investigation of the chemical nature of alkaline scouring and its effect on cotton seed coat fragments”, **X. Yang**, M.S. Dissertation, University of Georgia, Athens, GA, May 2006.